

Synthesis, Characterization, and Applications of Visible Light Active Metal-Organic Frameworks

Thèse N° 7382

Présentée le 30 octobre 2019

à la Faculté des sciences de base

Laboratoire de simulation moléculaire

Programme doctoral en chimie et génie chimique

pour l'obtention du grade de Docteur ès Sciences

par

Samantha Lynn ANDERSON

Acceptée sur proposition du jury

Prof. A. Züttel, président du jury

Prof. B. Smit, Dr K. Stylianou, directeurs de thèse

Prof. R. Morris, rapporteur

Dr J. Vitillo, rapporteuse

Prof. P. Dyson, rapporteur

2019

ACKNOWLEDGEMENTS

Firstly, I would like to express my sincere gratitude to Professor Berend Smit for the support, patience, and guidance over the course of my Ph.D. I would also like to thank my co-supervisor Dr. Kyriakos Stylianou for his help, knowledge and motivation during my studies.

I would also like to thank all the professors that have collaborated with us during projects. Namely, Prof. Andreas Züttel for the access to his laboratory, tools and equipment, all of which were necessary to gain insights into new potential applications for our materials.

From the Laboratory of Molecular Simulations, I would like to thank Dr. Peter Boyd, Dr. Davide Tiana, Dr. Gloria Capano, and Dr. Olga Syzgantseva for the simulation work done which helped us gain insights into how our materials behaved, and new experiments we could do for potential applications. I would also like to thank Dr. Christopher Ireland for all the experimental help over the course of my Ph.D, and for answering (and tolerating) the endless list of questions I've had.

I've had the pleasure of sharing the office with some of the best students and post-docs I've ever met, and to Chris, Arun, Dr. Dre (Andrzej), P-Diddy (Pelin), Bardiya, Aliner (Alina), Tu, and Mishmash (Mish), thank you. A Ph.D is never supposed to be easy, but sharing an office and laboratory with you guys made the bad days feel good, and the good days great. The adventures we've had outside of the office will always be some of the best memories I have.

Moving across the world to a new country is never an easy task, and adding on the pressures associated with a Ph.D thesis sometimes made it feel like I was drowning. I don't know if I could have made it through this without my friends and family. To Volker, Zarha, Manon, Clement, Gard, Jean, Love, and Abhik, thank you all so much. The adventures, game nights, debates, support, advice and help were nothing short of amazing. To Suzie, Steve and Kevin, even though my studies took me from Winnipeg, to Kingston, to Switzerland, thank you for the support during my masters, Ph.D and through life in general.

I have to thank my parents, Robert and Lynn, for their understanding, support and advice throughout every big idea (no matter how stupid). Mom and dad, you've kept me grounded, and been there for every step of every project, and for that thank you can't even express how grateful I am for you both.

Last but not least, thank you to my husband Mitchell, who has been there for every up and down, and has continued to push me to be my best through every obstacle and challenge I've faced, regardless of how stubborn about it I was. The endless support and love has made these last 4 years feel like the greatest adventure, and I am so excited about our future. You are my sun and my moon.

ABSTRACT

Gaining insights into chemical transformations in metal-organic frameworks (MOFs), and their structure property relationship(s) promotes a deeper fundamental understanding of these materials. Taking advantage of such insights, can allow greater control of material formation, and application development. In this thesis, through the combination of techniques and *in situ* studies, we studied the chemical transformation of two MOFs **SION-1** and **SION-2**, their familial isostructural optical properties, as well as the applications of two new MOFs **SION-19** and **SION-9**.

Understanding how crystalline materials are assembled is important for the rational design of MOFs. Controlling their formation can allow researchers to streamline the synthesis of new materials as well as control their properties for targeted application. In the first chapter of this thesis we report the construction of two 3-dimensional Tb^{III} based MOFs (**SION-1** and **SION-2**). Here, **SION-2** acts as a metastable MOF and intermediate phase that partially dissolves and transforms into the thermodynamically stable MOF, **SION-1**. This chemical transformation occurs in a *N,N*-dimethylformamide (DMF)/water solvent mixture, and is triggered when additional energy is provided to the reaction. *In situ* studies reveal the partial dissolution of the metastable phase after which the MOF components are reassembled into the thermodynamically stable phase. The marked difference in thermal and chemical stability between the kinetically and thermodynamically controlled phases is contrasted by their identical chemical building unit composition.

Following the understanding of this transformation, an isostructural family of **SION-1** and **SION-2** had been constructed using lanthanide metal salts, where **Ln^{III}-SION-1** is comprised of Ce, Nd, Eu, Gd, Tb, Dy, Ho, Er, Yb and Lu and **Ln^{III}-SION-2** is formed using Ce, Nd, Eu, Gd, Tb and Yb. The electronic properties of lanthanide based MOFs have not been extensively studied due to the general cognizance that Ln^{III} ions behave as isolated free ions as their 4f orbitals do not contribute to bonding. Here, we systematically studied the electronic properties (UV-vis) of **Ln^{III}-SION-1** and **Ln^{III}-SION-2** and show that the higher the intensity of this absorption band in **Ln^{III}-SION-1** is due to the better overlap between Ln(5d) and ligand(π^*) orbitals and reveals that the lowest unoccupied crystalline orbitals are dispersed over an energy range and can be considered as a conduction band. We validated this observation by the non-linear *I-V* curves collected on **Ce^{III}-SION-1** and **Yb^{III}-SION-1**, both of which display dielectric properties.

In the second chapter of this thesis, we rationally design a novel biologically derived MOF (**SION-19**) featuring unobstructed Watson-Crick faces of adenine (Ade) pointing towards the MOF

cavities. We show, through a combined experimental and computational approach, that thymine (Thy) molecules diffuse through the pores of the MOF and become base-paired with Ade. The Ade-Thy pair binding at 40-45% loading reveals that Thy molecules are packed within the channels in a way that fulfill both the Woodward-Hoffmann and Schmidt rules, and upon UV irradiation, Thy molecules dimerize into Thy<>Thy. This study highlights the utility of accessible functional groups within the pores of MOFs, and their ability to ‘lock’ molecules in specific positions that can be subsequently dimerized upon light irradiation, extending the use of MOFs as nanoreactors for the synthesis of molecules that are otherwise challenging to be isolated.

Concluding this thesis, a biologically derived multimodal sensor MOF is synthesized and a formed into a device. The MOF, named **SION-9**, is comprised of Ade and a porphyrin based ligand, and has tuneable conductive properties ranged from $2.69\text{-}4.20 \times 10^{-8}$ - $7.43\text{-}7.34 \times 10^{-6}$ S/cm. **SION-9** is sensitive to both pressure and temperature simultaneously, and demonstrated both fast response times (< 60 ms) and a long shelf life (> 6 months). This proof-of-concept study provides new insights into the development of conductive bimodal bio-MOF sensors using cost effective materials.

KEYWORDS

Metal-Organic Framework - Optical - Tunable - Dimerization - Carotid - Health Monitoring - Application discovery

RESUME

Obtenir des informations sur les transformations chimiques dans les structures métal-organiques(MOF) et sur les relations entre leurs propriétés et structures favorise une compréhension fondamentale plus profonde de ces matériaux. Profiter de ces connaissances peut permettre un meilleur contrôle de la formation du matériau et du développement des applications. Dans cette thèse, par la combinaison de techniques et d'études in situ, nous avons étudié la transformation chimique de deux MOFs **SION-1** et **SION-2**, leurs propriétés optiques isostructurales, ainsi que les applications de deux nouveaux MOFs **SION-19** et **SION-9**.

Comprendre comment les matériaux cristallins sont assemblés est important pour la conception rationnelle des MOFs. Contrôler leur formation peut permettre aux chercheurs de rationaliser la synthèse de nouveaux matériaux et de contrôler leurs propriétés pour une application ciblée. Dans le premier chapitre de cette thèse, nous rapportons la construction de deux MOFs tridimensionnels basés sur Tb^{III} (**SION-1** et **SION-2**). **SION-2** agit ici comme un MOF métastable et une phase intermédiaire qui se dissout partiellement et se transforme en le MOF thermodynamiquement stable, **SION-1**. Cette transformation chimique se produit dans un mélange de solvants *N,N*-diméthylformamide (DMF) / eau et se déclenche lorsque de l'énergie supplémentaire est fournie à la réaction. Des études in situ révèlent la dissolution partielle de la phase métastable, à la suite de laquelle les composants MOF sont réassemblés dans la phase thermodynamiquement stable. La différence marquée de stabilité thermique et chimique entre les phases contrôlées cinétiquement et thermodynamiquement est contrastée par leur composition chimique identique.

Suite à la compréhension de cette transformation, une famille isostructurale de **SION-1** et **SION-2** a été construite en utilisant des sels métalliques de lanthanides, où Ln^{III} -**SION-1** comprennent Ce, Nd, Eu, Gd, Tb, Dy, Ho, Er, Yb et Lu et Ln^{III} -**SION-2** sont formés à l'aide de Ce, Nd, Eu, Gd, Tb et Yb. Les propriétés électroniques des MOF à base de lanthanide n'ont pas fait l'objet d'études approfondies, car les ions Ln^{III} se comportent généralement comme des ions libres isolés, leurs orbitales 4f ne contribuant pas à la liaison. Ici, nous avons étudié systématiquement les propriétés électroniques (UV-vis) de Ln^{III} -**SION-1** et Ln^{III} -**SION-2** et avons montré que l'intensité plus élevée de cette bande d'absorption dans Ln^{III} -**SION-1** est due au meilleur chevauchement entre les orbitales Ln(5d) et ligand(π^*) et révèle que les orbitales cristallines les plus basses vacantes sont dispersées sur une plage d'énergie et peuvent être considérées comme une bande de conduction. Nous avons validé cette observation par les courbes *I-V* non linéaires recueillies sur Ce^{III} - et Yb^{III} -**SION-1**, qui présentent toutes les deux des propriétés diélectriques.

Dans le deuxième chapitre de cette thèse, nous concevons rationnellement un nouveau MOF biologiquement dérivé (**SION-19**) comportant des faces Watson-Crick non obstruées d'adénine (Ade) pointant vers les cavités du MOF. Nous montrons, par une approche combinée expérimentale et computationnelle, que les molécules de thymine (Thy) diffusent à travers les pores du MOF et deviennent appariées en bases avec Ade. La paire Ade-Thy se liant à une charge de 40 à 45% révèle que les molécules de Thy sont encombrées dans les canaux de manière à respecter à la fois les règles de Woodward-Hoffmann et de Schmidt, et lors de l'irradiation UV, ces molécules se dimérisent en Thy<>Thy. Cette étude met en évidence l'utilité de groupes fonctionnels accessibles dans les pores des MOF et leur capacité à "verrouiller" les molécules dans des positions spécifiques qui peuvent ensuite être dimérisées lors d'une irradiation lumineuse, ce qui étend l'utilisation des MOF comme nanoréacteurs pour la synthèse de molécules difficile d'être isolées autrement.

En conclusion de cette thèse, un capteur multimodal biologiquement dérivé MOF est synthétisé appelé **SION-9**. C'est composé d'Ade et d'un ligand à base de porphyrine et présente des propriétés conductrices ajustables comprises entre $2,69-4,20 \times 10^{-8}$ et $7,43-7,34 \times 10^{-6}$ S/cm. **SION-9** est sensible à la fois à la pression et à la température et présente des temps de réponse rapides (< 60 ms) et une longue durée de vie (> 6 mois). Cette étude de validation fournit de nouvelles informations sur le développement de capteurs bimodaux bio-MOF conducteurs utilisant des matériaux rentables.

MOTS-CLES

Structure métal-organique - Optique - Réglable - Dimérisation - Carotide - Surveillance de l'état de santé - Découverte d'application

TABLE OF CONTENTS

Acknowledgements	ii
Abstract.....	iii
Resume.....	v
List of Figures.....	ix
List of Tables.....	i
List of Equations	xii
Chapter 1 Introduction to Metal-Organic Frameworks.....	11
1.1 Introduction	1
1.2 The Formation of Metal-Organic Frameworks	1
1.3 Ligand Design for the Formation of New Metal-Organic Frameworks	6
1.3.1 Adenine Based Metal-Organic Frameworks.....	7
1.4 Optical Properties of Metal-Organic Frameworks	13
1.4.1 Luminescence	13
1.4.2 Lanthanide Based Luminescence	20
1.5 Electrically Conductive Metal-Organic Frameworks.....	23
1.5.1 General Design and Measurement Techniques	23
1.6 Electrochemical Impedance Spectroscopy	27
1.7 Outlook.....	29
Chapter 2 Formation Pathway and Optical Properties of SION-1 and SION-2	31
2.1 Introduction	31
2.2 Structural Description, Stability and Bulk Characterization of SION-1 and SION-2.....	32
2.3 Effects of Time and Solvent Concentration of the Formation of SION-2 and SION-1, and the Transformation of SION-2 to SION-1	38
2.4 The Partial Dissolution of SION-2.....	40
2.5 Structural Transformation of SION-2 and SION-1	44
2.6 Optical properties of Ln-SION-2 and Ln-SION-1	45
2.7 Conclusions	51
Chapter 3 SION-19: Nucleobase Pairing and Photodimerization in a MOF Nanoreactor	53
3.1 Introduction	53
3.2 Crystal Structure Determination and Bulk Characterization of SION-19	54
3.3 Thymine loading and dimerization	60

3.4	Conclusions	65
Chapter 4 SION-9: Multimodal Sensor for Real Time Health Monitoring		67
4.1	Introduction	67
4.2	Structural Description, Stability and Bulk Analysis of SION-9	69
4.3	Multimodal Response of SION-9 to Variable Temperature and Pressure.....	72
4.4	Electrochemical Impedance Spectroscopy and Origin of Conductivity of SION-9.....	73
4.5	Real Time Health Monitoring Using SION-9.....	74
4.6	Conclusions	77
Chapter 5 Future Work and Outlook		79
Appendix		81
References.....		131
Curriculum Vitae		141

LIST OF FIGURES AND SCHEMES

Chapter 1 Introduction to Metal-Organic Frameworks1

Figure 1-1: General MOF components	1
Figure 1-2: High Throughput Screening	2
Figure 1-3: MOF-5.....	3
Figure 1-4: Hofmeister Series.....	3
Figure 1-5: Formation of MIL-96(Al), MIL-100(Al) and MIL-110(Al) crystal integrated units..	4
Figure 1-6: ZIFs compared to SiO ₄	5
Figure 1-7: Families of organic linkers used to make MOFs	6
Figure 1-8: Adenine structure.....	7
Figure 1-9: The electromagnetic spectrum.....	13
Figure 1-10: Basic photo physical processes represented in a Jablonski diagram.....	14
Figure 1-11: Molecular orbital diagram of potential excitation pathways	15
Figure 1-12: Possible mechanism of electron transport within a MOF with LLCT	16
Figure 1-13: Antennae effect from Ln ^{II} or Ln ^{III} luminescence	18
Figure 1-14: Sum of Ln-O bond lengths against the number of f-electrons.....	21
Figure 1-15: Electronic excited-state energy levels for Ln ^{III} ions.....	22
Figure 1-16: Through bond approach to charge transfer	25
Figure 1-17: Complex impedance plane	28

Chapter 2 Formation Pathway and Optical Properties of SION-1 and SION-2

Figure 2-1: Crystal structure of SION-2	32
Figure 2-2: Crystal structure of SION-1	34
Figure 2-3: Network topologies of SION-1 and SION-2	34
Figure 2-4: PXRD of SION-2 and SION-1	36
Figure 2-5: PXRD of SION-2@H ₂ O and SION-1@H ₂ O	36
Figure 2-6: TGA of the SION MOFs.....	37
Figure 2-7: Crystal Structures of SION-2@H ₂ O and SION-1@H ₂ O	37
Figure 2-8: PXRD of SION-2 and SION-1 reflecting the effects in changing the solvent concentration and reaction time	38
Figure 2-9: PXRD of the transformation in air from SION-2 to SION-1	39
Figure 2-10: PXRD of the transformation in fresh solvent (DMF : H ₂ O 2.0 : 0.5 mL) using preformed SION-2	39
Figure 2-11: ¹ H NMR of the transformation of SION-2 to SION-1	41
Figure 2-12: Analysis of ¹ H NMR shifts and influence of Tb	41

Figure 2-13: VT-PXRD and lattice parameter analysis of the transformation	43
Figure 2-14: Proposed transformation mechanism	44
Figure 2-15: PXRD of Ln^{III} -SION-1	46
Figure 2-16: PXRD of Ln^{III} -SION-2	47
Figure 2-17: UV/Vis spectra the Ln^{III} -SION-1 and Ln^{III} -SION-2 families	48
Figure 2-18: Projected density of states (pDOS) and crystalline orbitals	49
Figure 2-19: Current-Voltage curves	50

Chapter 3 SION-19: Nucleobase Pairing and Photodimerization in a MOF

Nanoreactor

Scheme 3-1: Method for the synthesis of cyclobutane Thy photodimers using UV light and water	54
Figure 3-1: Structural representation of SION-19	56
Figure 3-2: Underlying net of SION-19	57
Figure 3-3: PXRD, MAS NMR, and N_2 isotherm of SION-19 and SION-19'	57
Figure 3-4: Isotherms of SION-19'	58
Figure 3-5: XPS of SION-19	59
Figure 3-6: Solution thymine isotherms in SION-19' and probability of Adenine-Thymine pairing and Thymine-dimerization	60
Figure 3-7: PXRD, N_2 Isotherm and IR of SION-19@Thy	61
Figure 3-8: MAS ^1H - ^{13}C NMR	62
Figure 3-9: Schematic representation of thymine loading, location and dimerization within SION-19'	63

Chapter 4 SION-9: Multimodal Sensor for Real Time Health Monitoring

Figure 4-1: Crystal structure of SION-9	69
Figure 4-2: PXRD, VT-PXRD, TGA, ^{13}C CP-MAS, and EPR of SION-9	71
Figure 4-3: Conductivity summary of SION-9	72
Figure 4-4: DOS and frontier orbitals of SION-9	73
Figure 4-5: Location and wave form of the Carotid Artery	74
Figure 4-6: Device construction	75
Figure 4-7: Tap Tests of devices and their response times	76

LIST OF TABLES

Chapter 1 Introduction to Metal-Organic Frameworks1

Table 1-1: Coordination mode(s) of Ade to different metals9

Table 1-2: Ade based MOFs, and their applications12

Chapter 3 SION-19: Nucleobase Pairing and Photodimerization in a MOF

Nanoreactor

Table 3-1: Binding energies of the fitted components for the XPS N1s spectra59

LIST OF EQUATIONS

Chapter 1 Introduction to Metal-Organic Frameworks1

Equation 1-1: Temperature dependent data to Arrhenius equation.....24

Equation 1-2: Equation for the measurement of electrical conductance26

Chapter 4 SION-9: Multimodal Sensor for Real Time Health Monitoring

Equation 4-1: Evaluation of conductivity72

Chapter 1 Introduction to Metal-Organic Frameworks

1.1 Introduction

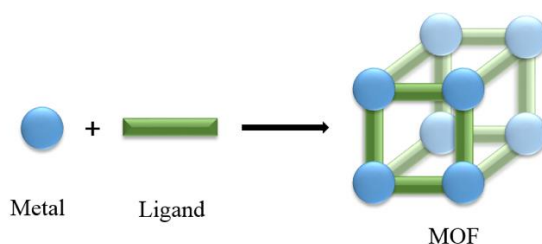


Figure 1-1: General MOF components. Combination of ligands and metal ions or metal ion clusters can lead to the formation of MOFs.

Metal-organic frameworks (MOFs) are crystalline coordination based materials consisting of an infinite network of metal-ions, or metal-ion clusters, bridged by organic ligands through coordination bonds into porous or nonporous 1-, 2- or 3-dimensional extended structures (Figure 1-1).^{1, 2} The judicious selection and combination of metal and ligands has led to the discovery of a broad array of MOFs with various topologies, compositions and properties such as record-breaking internal surface areas (up to 7000 m²/g),³ high void volumes (up to 90%),⁴ and low densities (as low as 0.126 g/cm³).⁵ These materials are tunable, either through the introduction of new metals into a family of MOFs, or through pre-/post-synthetic modification of the ligand or pore surface, allowing researchers to create new efficient materials for applications such as gas separations and storage, catalysis, and sensing.⁶ However, despite the wide variety of applications MOFs can be used for, the mechanism in which they form is unknown.

1.2 The Formation of Metal-Organic Frameworks

Typically, the self-assembly of metal ions or clusters with ligands to form MOFs can be achieved through classical coordination chemistry methods (<100 °C),^{1, 7} mechanochemistry,⁸ solvothermal synthesis (>100 °C),⁹ microwave synthesis,^{10, 11} or high-throughput techniques (Figure 1-2).¹²⁻¹⁴

It should be noted that sections from our publication "Anderson, L. Samantha; Stylianou, C. Kyriakos. Biologically Derived Metal-Organic Frameworks, *Coord. Chem. Rev.* **2017**, 349, 102-128" have been reused for this thesis chapter.

Currently, MOFs can be discovered through a trial-and-error or an automated approach, rather than through a fundamental understanding of the underlying mechanism.¹⁵⁻¹⁷ New MOFs can be hypothesized through computational studies,¹⁸ or through geometric assembly based on the secondary building units (SBUs),¹⁹ however while these predicated frameworks might be thermodynamically stable, they may not be kinetically accessible.²⁰ Ultimately, there are three aspects designing a new MOF that need to be considered: *i.* the solvent *ii.* the anion *iii.* the role of the metal and *iv.* temperature and pressure used during the experiment, which has been highlighted in the systematic work coming from the LSMO group and in this thesis.

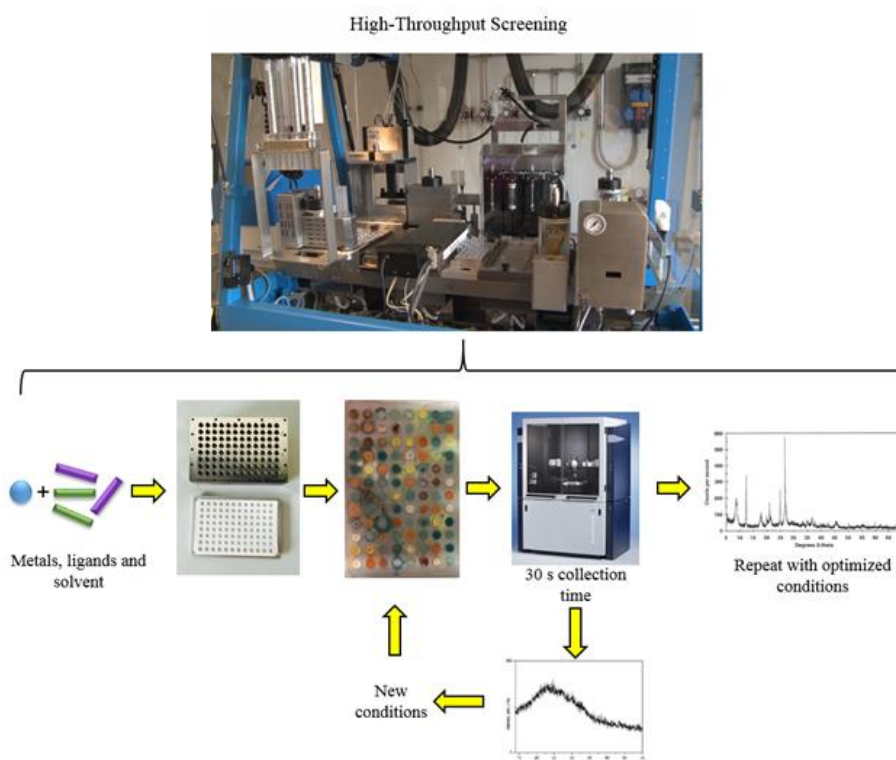


Figure 1-2: High Throughput Screening. Typical routine used for high-throughput screening used in the development of new MOFs.

The solvent chosen has been shown to be a significant parameter in the crystallization kinetics, network topology and crystal topology.²¹ The ability of a solvent to direct the structure formation of a MOF was previously demonstrated in a Cd^{II} -4,4'-dipyridyl sulfide framework, in which a 1-, 2-, or 3-dimensional structure can be obtained depending on if a DMF-DCM, MeCN-DCM, or MeOH-DCM solvent system is chosen (where DMF = dimethylformamide, DCM = dichloromethane, and MeOH = methanol).²² Solvent can also act as a non-coordinating structure directing agent, as seen by Dastidar et al. who showed that polar solvents lead to Cd^{II} based MOFs, but solvents with less polarity only formed coordination complexes.²³

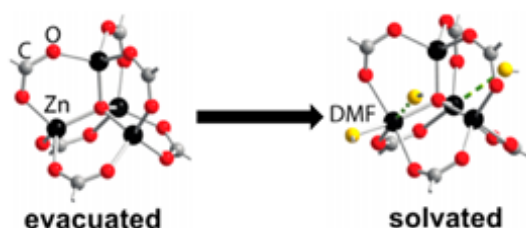


Figure 1-3: MOF-5. Solvated MOF-5 in which DMF is coordinated on average to one Zn^{II} . Adapted with permission, copyright © 2015 American Chemical Society.²⁶

The role of the solvent was further examined through the use of time resolved monochromatic high energy X-ray diffraction and Rietveld analysis. *In-situ* crystallization of $[\text{Yb}_2(\text{BDC})_3(\text{DMF})_2] \cdot \text{H}_2\text{O}$ (MOF-5) in a $\text{H}_2\text{O}/\text{DMF}$ mixture (BDC = benzene-1,4-dicarboxylate) revealed a topochemical replacement of coordinated solvent, where initially coordinated H_2O molecules were replaced with DMF as the reaction proceeded.²⁴ In addition, through the use of multinuclear solid-state nuclear magnetic resonance (NMR), mass spectrometry (MS) and first-principle molecular dynamics, it was revealed that the MOF-5 framework was not rigid as originally proposed. Instead Zn^{II} binds the DMF solvent molecules, increasing its coordination number, followed by their decoordination from the framework, with an average of one Zn^{II} in each cluster coordinating to at least one DMF molecule (Figure 1-3).^{25, 26} Taking advantage of this behaviour, the authors developed a rational low temperature cation exchange approach, allowing them to synthesize metastable Co^{II} substituted MOF-5 analogues, which had previously been unavailable through typical high-temperature synthetic routes.^{25, 26}

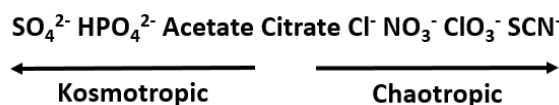


Figure 1-4: Hofmeister Series.

Just as the ability of the solvent to play multiple roles, so too does the metal anion. The influence of the anion on the final topology has been regularly observed,^{27, 28} and apart from acting as mineralizers which can enhance the crystallinity, they can also act as structure-directing agents.²⁹ This was eloquently shown in an ethylenediaminetetrapropionitrile (EDTPN) Ag-MOF, where the choice of $\text{Ag}(\text{NO}_3)$, $\text{Ag}(\text{CF}_3\text{SO}_3)$ or $\text{Ag}(\text{ClO}_4)$ lead to three different crystal structures ($\text{P2}_1/\text{c}$, $\text{P2}_1/\text{n}$ and Pccn , respectively).³⁰ The authors also reported on the possibility to induce crystal-to-crystal rearrangements upon ion exchange, in which a reversible transformation between the two monoclinic structures ($\text{Ag}(\text{NO}_3)$, $\text{P2}_1/\text{c}$ and $\text{Ag}(\text{CF}_3\text{SO}_3)$, $\text{P2}_1/\text{n}$) was observed.³⁰ However, upon transformation

to the orthorhombic structure using $\text{Ag}(\text{ClO}_4)$, the rearrangement was subsequently rendered irreversible. The irreversible transformation could be due to the Ag -EDTPN coordination polymer having a greater affinity to the ClO_4^- anion, while the NO_3^- - CF_3SO_3^- exchange proceeds through blocking a coordinative site and/or changing coordination geometry through ligand coordination.²¹ The authors further demonstrated that the anion affinity followed the trend of: $\text{ClO}_4^- > \text{NO}_3^- > \text{CF}_3\text{SO}_3^- > \text{Cl}^-$ which is in agreement with the Hofmeister Series (Figure 1-4), which ranks the relative influence of anions on macromolecules.³⁰ Here, the Hofmeister series has kosmotropes and chaotropes, which describe the ability of the anion to alter the hydrogen-bonding network of water.³¹ For example, kosmotropes have been shown to stabilize the ‘water structure’ and salt out/stabilize protein macromolecules.³¹ Unfortunately, while MOFs tend to follow this series, it is nothing more than a guideline as both anti- and non-Hofmeister selectivity’s in MOFs has been observed.³²

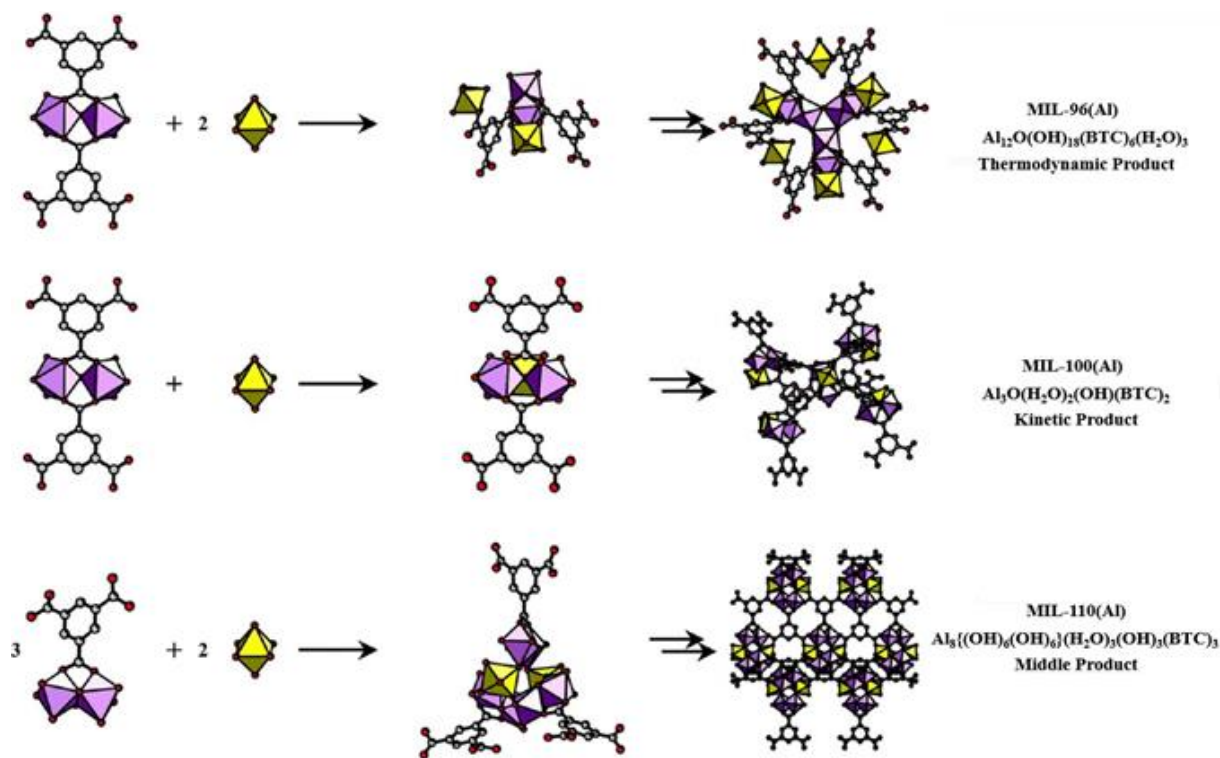


Figure 1-5: Formation of MIL-96(Al), MIL-100(Al) and MIL-110(Al) crystal integrated units. Here, the reaction of the dimeric Al_2 -BTC complexes, and the mono Al^{III} cation, lead to nanoaggregation, condensation/networking, and finally crystallization. Adapted with permission,³³ © 2012 American Chemical Society.

While there are a wide variety of metals available for MOF synthesis, many transition metals with d^{10} configurations are employed. Metals such as Zn^{II} are commonly used due to Zn 's ability to

hold many different coordination geometries (tetrahedral, pentagonal bipyramidal,³⁴ octahedral,³⁵ trigonal bipyramidal,³⁶ square pyramidal,³⁷ etc.), its relative ease of handling, and for some applications its low toxicity. Lanthanide metals (Ln) are also used in MOF synthesis, and while the coordination geometries are even more unpredictable, interesting environments such as square antiprisms³⁸ and supercubanes³⁹ have been reported. Isostructural families of lanthanides are typically constructed using the Ln +3 oxidation state. To examine this overall unpredictability of metal ions, a family of Al based MOFs, MIL-96(Al), MIL-100(Al) and MIL-110(Al) (MIL = Matériel Intitut Lavoisier) were studied. Here, all three are comprised of the same components, Al and BTC (BTC = benzenetricarboxylate), however only in MIL-96(Al) and MIL-100(Al) is an $\text{Al}_3(\mu_3\text{-O})(\text{BTC})_6\text{L}_3$ SBU found, with its connectivity residing in the hexagonal chains of MIL-96(Al), or in the “super tetrahedron” found in MIL-100(Al) (Figure 1-5).³³ MIL-110(Al) is comprised of two types of clusters, six with terminal hydroxide ligands, and two with no terminal ligands, which make up a large Al_8 octagonal SBU, leading to hexagonal channels.³³ Haouas et al. subsequently performed *in situ* NMR, and found that dinuclear Al-BTC complexes form early, with kinetic/thermodynamic effects leading to the formation of the three different products: *i.* MIL-100(Al) is the kinetic product; *ii.* MIL-96(Al) is the thermodynamic product; and *iii.* MIL-110(Al) is somewhere in the middle.³³ The authors further showed that they can control the final product formation via heating the thermodynamically stable product to either the middle, or kinetic product.

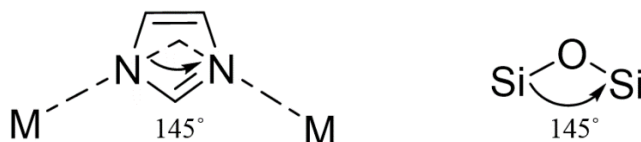


Figure 1-6: ZIFs compared to SiO_4 . Metal (M) ion coordination geometry in zeolitic imidazolate frameworks (ZIFs) where the ligand holds a similar angle to the Si-O-Si found in SiO_4 .

Similar to MOFs, zeolitic imidazolate frameworks (ZIFs) have also been constructed where the metal-organic domain mimics zeolites through a tetrahedrally coordinated ion and imidazolate bridging ligand.^{40, 41} In ZIFs, the metal ion coordination geometry resembles SiO_4 , while the ligand has a similar Si-O-Si angle (145°), leading to the formation of material with zeolite topology (Figure 1-6). The pathway in which these materials crystallize has somewhat been elucidated, and in one case has been demonstrated to follow a similar mechanism for high-silica zeolites.⁴² This is compared to MOFs, in which the transition metal chemistry governs “serendipitous self-assembly”.

While we currently still do not have a full fundamental understanding on how to predict the self-assembly of MOFs, progress is being made.

1.3 Ligand Design for the Formation of New Metal-Organic Frameworks

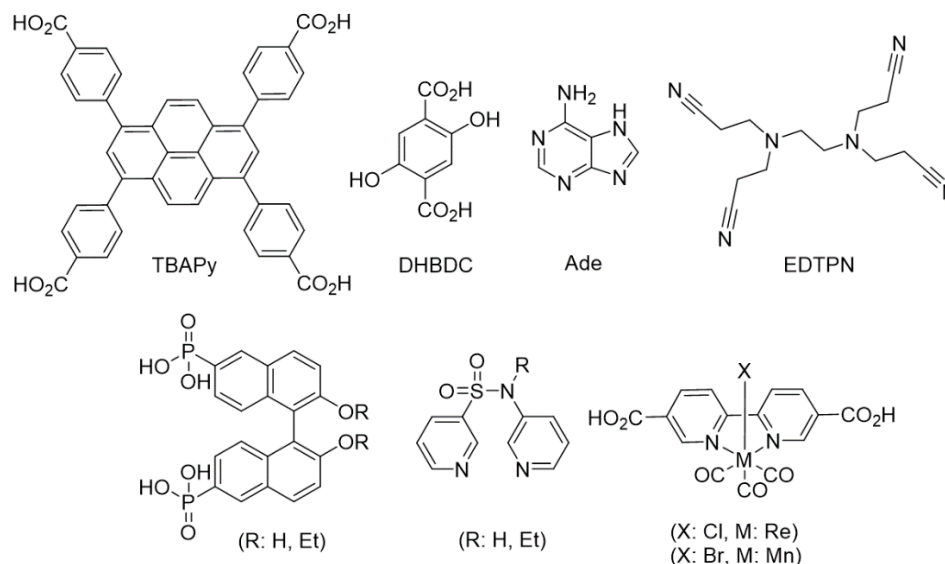


Figure 1-7: Families of organic linkers used to make MOFs. Organic ligands from each family used to construct MOFs such as carboxylic acid containing ligands (TBAPy, DHBDC), nitrogen containing ligands (Ade), cyano ligands (EDTPN), phosphonic acids ligands, ligands based on mixed functional groups, sulfonyl ligands and metal-bearing ligands

While the judicious choice of metal ions, and solvent(s) is important for the formation of new MOFs, so are the ligand(s) used as this creates vertices that hold the nodes into place, which can further influence the properties that the material has. Generally, rigid organic ligands are preferred (over flexible) since the resulting MOFs can be robust and/or porous.⁴³⁻⁴⁵ Commonly used organic ligands within MOFs are divided into families such as: *i.* carboxylic acid containing ligands, *ii.* nitrogen containing ligands (pyridyl, pyrrol, imidazolyl, etc.), *iii.* cyano ligands, *iv.* phosphonic acids ligands, *v.* ligands based on mixed functional groups, *vi.* sulfonyl ligands and *vii.* metal-bearing ligands (Figure 1-7).^{46, 47} While cationic ligands are less common in the synthesis of MOFs (low affinity to coordinate to metal cations), both neutral and charged molecules can be used.⁷ Functionalities pointing towards their internal pore surface are often utilized to introduce strong interactions with a target molecule and can influence the frameworks structure.⁴⁶ In addition, they may have interconnecting functions, which could extend the coordination motifs, creating secondary interactions such as hydrogen bonding (H-bonding) and aromatic stacking.^{46, 48} Replacing the organic ligands in a MOF with units that are topologically similar or identical, but instead increasing in length,

can extend the pore size creating new isorecticular (IRMOFs) families of MOFs with unique properties.¹⁷

While there are a variety of ligands available for MOF synthesis, biologically related ligands (i.e. nucleobases, porphyrins, etc.), or bio-ligands, offer researchers the ability to buy any combination of chirality, aromaticity, cyclic or aliphatic features desired, or the ability to purchase the necessary backbone and synthetically alter it. Adding to their attractive features, bio-ligands are generally low cost, commercially available and environmentally benign, allowing them to be used in MOFs for drug delivery.⁴⁹ It's not surprising that these ligands have found their way into the same applications that other well-known MOFs (e.g. HKUST-1, MOF-74) have been known for such as carbon capture and storage.⁵⁰

1.3.1 Adenine Based Metal-Organic Frameworks

Nucleobases are suitable bio-ligands for the design and synthesis of metal-organic supramolecular arrays due to their large number of oxygen and nitrogen donor sites of different basicity. This is a strong motivation to employ nucleobases for the formation of biologically derived MOFs, or bio-MOFs, as they have the potential to form numerous interactions, including coordination bonds, hydrogen-bonds and π - π stacking interactions. The multifunctionality and a variety of binding modes in nucleobases within a structure can give rise to structural flexibility as seen in biological molecules such as proteins and peptide based frameworks. Transition metal complexes containing nucleobases have also been studied in order to explore the DNA metal binding processes which are vital for the development of new biologically active metallodrugs. With the added benefits of being biologically and environmentally friendly, they are also naturally abundant and easy to produce, thereby keeping industrial costs low. To date, the most commonly reported bio-MOFs constructed from nucleobases contain Adenine (Ade).⁵¹⁻⁵⁸

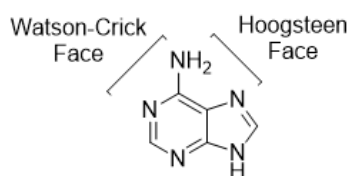
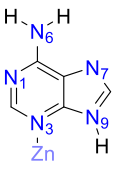
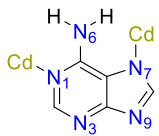

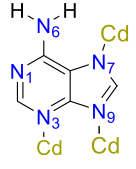

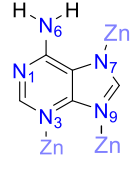
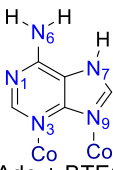
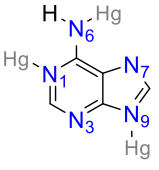
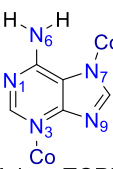
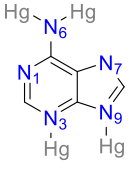

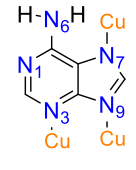
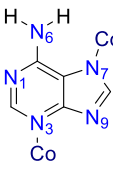
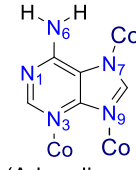
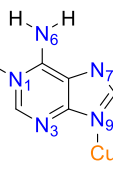
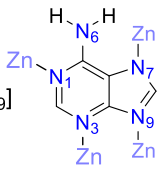


Figure 1-8: Adenine structure. The structure of Adenine highlighting both the Watson-Crick and Hoogsteen Faces.

Nucleobases, such as Ade, have the ability to bind to metals through a variety of different donor atoms, leaving the non-coordinated atoms open, which can in turn be used to enhance the interactions within the pores of MOFs. For the spatial host-guest binding within the pores of a framework, two prerequisites must be fulfilled: *i.* the pores have to be guest accessible, and *ii.* the Watson-Crick faces have to be available, and unobstructed (Figure 1-8).⁵⁹ Purine ligands are well-known for their ability to build dinuclear complex *via* their [N3] and [N9] bridging modes, and previous literature has demonstrated that adeninate ligands can form paddle-wheel complexes, with the entities self-assembling *via* Watson-Crick ([N6]-H, [N1]) and Hoogsteen faces ([N6]-H, [N7]) through π - π stacking.⁶⁰ Despite the advantages, bio-MOFs containing nucleobases are not exhaustive, which may be the result of the lack of control over their binding modes to metal ions, and their inherent lack of symmetry which inhibit packing in the formation of crystalline materials. Most of the examples reported in the literature highlight the rich coordination modes of Ade leading in the formation of highly porous bio-MOFs. Ade has five N atoms with different basicity; two pyrimidinate N1 and N3, two imidazolate N7 and N9 and one amino group N6 and all are available for metal coordination. Ade can be then mono-, bi-, tri-, or tetradentate coordinating ligand within the bio-MOF structure through [N3], [N9], [N3, N9], [N7, N9], [N1, N9], [N1, N7], [N3, N7], [N3, N7, N9], [N1, N6, N9], [N2, N6, N9] or [N1, N3, N7, N9] (Table 1-1).⁶¹⁻⁷⁰

Rosi et al. demonstrated that the use of a symmetric Zn adeninate SBU can overcome problems such as undesired coordination modes between Ade and metal ions, while increasing symmetry. The first nucleobase bio-MOF with formula of $[\text{Zn}_8(\text{Ade})_4(\text{BPDC})_6\text{O}\cdot 2\text{Me}_2\text{NH}_2]\cdot 8\text{DMF}\cdot 11\text{H}_2\text{O}$ (Bio-MOF-1) was composed with eight Zn^{II} ions linked to four Ade ligands *via* [N1], [N3], [N7] and [N9] coordination modes, and infinite Zn^{II} Ade columns made of apex sharing Zn^{II} Ade octahedral cages.⁵¹ This is compared to $[\text{Co}_2(\text{Ade})_2(\text{CO}_2\text{CH}_3)_2]\cdot 2\text{DMF}\cdot 0.5\text{H}_2\text{O}$ (Bio-MOF-11), which consists of Co^{II} –Ade–acetate paddlewheel clusters made of two Co^{II} ions bridged by Ade *via* N3 and N9 coordination, and two acetate ligands.^{52, 71} $[\text{Co}_2(\text{Ade})_2(\text{CO}_2\text{CH}_3)_2]\cdot 2\text{DMF}\cdot 0.5\text{H}_2\text{O}$ is built by further linking the clusters to Ade *via* [N7] coordination, and has cavities that are periodically distributed.

Table 1-1: Coordination/bridging mode(s) of Ade to different metals.

Entry	Metal	Coordination Mode	Ref.	Entry	Metal	Coordination Mode	Ref.
1	Zn	[N ₃] 	[54]	9	Cd	[N ₁ , N ₇] 	[65]
2	Cu	[N ₉] 	[62]	10	Cd	[N ₃ , N ₇ , N ₉]  (Ade + isonictiaic)	[71]
3	Ni	[N ₃ , N ₉] 	[63]	11	Zn	[N ₃ , N ₇ , N ₉]  (Ade + BTC or pyrazole)	[58]
4	Co	[N ₃ , N ₉]  [Ade + BTEC]	[60]	12	Hg	[N ₁ , N ₆ , N ₉] 	[67]
5	Co	[N ₃ , N ₇]  [Ade + TCPB]	[60]	13	Hg	[N ₃ , N ₆ , N ₉] 	[68]
6	Zn	[N ₇ , N ₉]  (Ade + Imidazole)	[63]	14	Cu	[N ₃ , N ₇ , N ₉] 	[54]
7	Co	[N ₃ , N ₇] 	[60]	15	Co	[N ₃ , N ₇ , N ₉]  (Ade + ligands)	[57, 69]
8	Cu	[N ₁ , N ₉] 	[64]	16	Zn	[N ₁ , N ₃ , N ₇ , N ₉] 	[51, 81]

The versatility of Ade as an organic ligand has continually proven itself to be a key in designing multidimensional frameworks. In combination with aliphatic monocarboxylic acids and Cu^{II} , the 3-dimensional, robust open frameworks $[\text{Cu}_2(\mu_3\text{-Ade})_2(\mu_2\text{-OOC}(\text{CH}_2)_n\text{CH}_3)_2]_3 \cdot x\text{H}_2\text{O}$ [n from 0 (acetate) to 5 (pentanoate)] can be constructed using inexpensive reagents.⁷² The basic building unit of these bio-MOFs is a center symmetric dimer where two carboxylic ligands and two Ade ligands ([N3] and [N9] atoms) are coordinated to two Cu^{II} atoms forming a paddlewheel unit.⁷² Ade displays a tridentate coordination mode [N3, N7, N9], due to the cross-linking of units through the coordination of the [N7] atom in the adeninato ligand to four adjacent entities with a 5.97 Å Cu--Cu separation across the imidazole N9/N7 bridge. Hydrogen bonding interactions between the [N6]–H6Ade group of the Hoogsteen face of the nucleobase and the coordinated O atom of the carboxylic ligand reinforces the linkage.⁷²

Kang and Wang reported a new 3-dimensional bio-MOF $[\text{Cd}_2(\text{Ade})_2(\text{IN})_2(\text{DMF})(\text{H}_2\text{O})] \cdot \text{DMF}$ (IN = isonicotinic acid) with a Cd-adeninate paddlewheel subunit.⁷³ Within $[\text{Cd}_2(\text{Ade})_2(\text{IN})_2(\text{DMF})(\text{H}_2\text{O})] \cdot \text{DMF}$, there are two Cd (Cd1 and Cd2) atoms; one is square-pyramidal (Cd1) with four different nitrogen atoms (Ade) and one oxygen atom (IN), while the other (Cd2) is octahedrally coordinated with three oxygen atoms (one H_2O , one DMF molecule and one carboxylate from IN), and three nitrogen atoms ([N7, N3, N9] from Ade, and N from IN).⁷³ Ade acts independently as a μ_3 -linker to bridge three Cd atoms, and the structure consists of a cadmium-Ade paddle-wheel units, in which two Cd1 atoms are bridged by four Ade.⁷³ The $\text{Cd}_2(\text{Ade})_4$ units are further bridged by Cd2 atoms to form a chain along the *a*-axis.⁷³ The axial position is occupied by two pendent IN ligands, while one links two adjacent Cd2 atoms to form a chain, and the other coordinates a Cd1 atom by acting as a pendent ligand.⁷³

To overcome the disadvantage of low symmetry, the introduction of a highly symmetric co-ligand has proven to be a useful strategy for the introduction of nucleobases into MOFs.⁷⁴ Within $\text{Zn}_3[\text{Zn}_2(\mu_2\text{-H}_2\text{O})]_3(\text{Ade})_6(\text{TATB})_4(\text{DMF})$, two distinctive building units were identified in the structure due to the multiple binding modes of Ade. The first building unit contains two Ades which are linked by a four-coordinated Zn^{II} via the imidazolate [N7] atoms and two carboxylates.⁷⁴ In the second building unit, the binuclear Zn^{II} unit is bridged by two Ade ligands through [N3, N9], at the two equatorial positions, while two carboxylates coordinate at the two axial positions.⁷⁴ One-dimensional Zn-adeninate chains were formed with Ade connected to both building units in a 1:1 ratio.⁷⁴ In each adeninate, it should be noted that the [N7] donors coordinate to the first building unit, the [N3], and [N9] coordinate to the second building unit and the [N1] and [N6] atoms were uncoordinated.⁷⁴

Using Co^{II} , Ade and aromatic tetracarboxylic acids H_4TCPB and H_4BTeC , 3-dimensional bio-MOFs were composed.⁶¹ $[\text{Co}_3(\mu_6\text{-TCPB})(\mu_4\text{-H}_2\text{TCPB})(\text{Ade})_2]\cdot\text{H}_2\text{O}$ is a compact network, in which three Co^{II} ions are bridged by two bidentate Ade ligands through [N3] and [N9].⁶¹ $[\text{Co}_2(\text{Ade})(\mu_6\text{-BTeC})(\mu\text{-H}_2\text{O})(\text{H}_2\text{O})_2]\cdot 4(\text{H}_2\text{O})$ is comprised of bidentate Ade ligands forming binuclear Co^{II} clusters through both the [N3] and [N7] sites, leading to 1-dimensional Co^{II} -Ade chains.⁶¹ The latter structure is shown to have reversible structural transformations upon removal and addition of H_2O , giving a color change from pink to purple, respectively.⁶¹ The indication of a color change implies a change in the coordination geometry of Co^{II} from an octahedral to tetrahedral upon removal of coordinated H_2O .⁶¹

While the extensive list of Ade, and other nucleobase based bio-MOFs, their coordination modes, and subsequent applications is out of the scope of this thesis, we would like to reference the readers to Table 1-2 and the recent review written by Anderson et al. for more details.⁵⁸

Table 1-2: Ade based MOFs, and their applications.

Formula	MOF name	BET surface area (m ² /g)	Application	Ref.
[Zn ₈ (Ade) ₄ (BPDC) ₆ O ₂ ·2Me ₂ NH ₂]·8DMF·11H ₂ O	Bio-MOF-1	1700	1) Drug loading via cation exchange (Procainamide). 2) CO ₂ adsorption via cation exchange (TMA, TEA, and TBA). 3) Encapsulation and sensitization of visible and near-infrared emitting lanthanide cations. 4) Eu @ Bio-MOF-1: VOC detection. 5) Enhancement of CO ₂ adsorption via cation exchange (GND ⁺ , AmGND ⁺ , DiAmGND ⁺).	51, 75-78
Zn ₈ (Ade) ₄ (BPDC) ₆ O ₂ ·4Me ₂ NH ₂ ·49DMF·31H ₂ O	Bio-MOF-100	4300	CO ₂ adsorption, selective CO ₂ adsorption over N ₂ .	52, 71
[Co ₂ (Ade) ₂ (CO ₂ CH ₃) ₂]·2DMF·0.5H ₂ O	Bio-MOF-11	1148		
Zn ₃ (Ade)(BTC) ₂ (H ₂ O)·(CH ₃) ₂ NH ₂ ·xDMF·yH ₂ O	ZnBTCA	3057.5	1) PfH ⁺ and MB ⁺ adsorption (DNA staining agents). 2) Ade-Thy base pairing.	59
[Cu ₂ (μ-Ade) ₄ (Cl) ₂] ²⁺ ·2MeOH [Cu ₂ (μ-Ade) ₄ (μ-Cl) ₂ (Cl) ₂] ²⁺ ·2MeOH [Cu ₂ (μ-Ade) ₄ (μ-Br) ₂ (Br) ₂] ²⁺ ·2PrOH	SMOF-1 SMOF-2 SMOF-3	14-26	Selective gas adsorption and separation (CO ₂ , N ₂ , CH ₄ , H ₂)	60
[Co ₃ (μ ₆ -TCPB)(μ ₄ -H ₂ TCPB)(Ade) ₂]·H ₂ O [Co ₂ (Ade)(μ ₆ -BTcC)(μ-H ₂ O)(H ₂ O) ₂]·4(H ₂ O)	---	---	Hydrochromic behavior for H ₂ O sensing.	61
[Zn(Im) ₃ (L2) _{2-x} (L2= (Ade)(Int))	TIF-A1	718	CO ₂ /N ₂ separation.	64
[Cu ₂ (Ade) ₄ Cl ₂]Cl ₂ [Cu ₂ (Ade) ₄ (TiF ₆) ₂]	MPM-1-Cl MPM-1- TIFSIX		CO ₂ /N ₂ and CO ₂ /CH ₄ separation	72, 79
[Cd ₂ (Ade) ₂ (IN) ₂ (DMF)(H ₂ O)]·DMF	---	---	Only structural details reported.	73
Zn ₃ [Zn ₂ (μ ₂ -H ₂ O)] ₃ (Ade) ₆ (TATB) ₄ (DMF)	PCN-530	---	DNA coated biosensors.	74
[Co ₂ (Ade) ₂ (C ₂ H ₅ CO ₂) ₂]·2.25DMF·0.3H ₂ O [Co ₂ (Ade) ₂ (C ₃ H ₇ CO ₂) ₂]·1.1DMF·0.6H ₂ O [Co ₂ (Ade) ₂ (C ₄ H ₉ CO ₂) ₂]·0.6DMF·0.6H ₂ O	Bio-MOF-12 Bio-MOF-13 Bio-MOF-14	1008 412 17	CO ₂ adsorption, selective CO ₂ adsorption over N ₂ .	80, 81
[Cu ₂ (μ ₃ -Ade) ₂ (μ ₂ -OOC(CH ₂) _n CH ₃) ₂] ₃ ·xH ₂ O N= 0 for acetate to 5 for pentanoate	---	500-8.9	Antiferromagnetic behavior reported.	82
Zn ₈ (Ade) ₄ (BPDC) ₆ O ₂ ·4Me ₂ NH ₂ ·49DMF·31H ₂ O Zn ₈ (Ade) ₄ (ABDC) ₆ O ₂ ·4Me ₂ NH ₂ ·49DMF·31H ₂ O Zn ₈ (Ade) ₄ (NH ₂ -TCPD) ₆ O ₂ ·4Me ₂ NH ₂ ·49DMF·31H ₂ O	Bio-MOF-101 Bio-MOF-102 Bio-MOF-103	4410 3222 2704	Only porosity details reported.	83
[Ni ₃ (pzdc) ₂ (7Hade) ₂ (H ₂ O) ₄]·(H ₂ O) _{1.5}	---	165 (CO ₂) 124 (N ₂)	CO ₂ /CH ₄ separation.	84
[NH ₂ (CH ₃) ₂][Zn ₃ (4-Pca) ₃ (Ade)]·10DMF·8H ₂ O	---	418.6	Adsorption of C ₁ to C ₃ paraffin's.	85
[Ni ₂ (BTC)(Ade)(H ₂ O) ₅]·3H ₂ O [Ni(IPA)(3Hade)] [Ni ₂ (BTEC)(7Hade) ₂ (H ₂ O) ₂]·4H ₂ O [Cu ₃ (PZDC) ₂ (1Hade)(H ₂ O) ₄] [Zn ₂ (BTC)(Ade)(H ₂ O) ₂]	SION-31 SION-32 SION-33 SION-34 SION-35	---	Fundamental study of the HAd location in different Ade based MOFs.	70
a. [Zn ₃ (TCPPZn)(Ade)(HAd)O _{0.5}] ·guest molecules b. [Zn _{1.5} O _{0.25} (Ade)(TBAPy) _{0.5}]·(NH ₂ Me) _{0.5} ·1.7DMF·4H ₂ O	a. SION-9 b. SION-19	a. --- b. 563	a. Electrical conductivity b. Thy adsorption and dimerization	This work

1.4 Optical Properties of Metal-Organic Frameworks

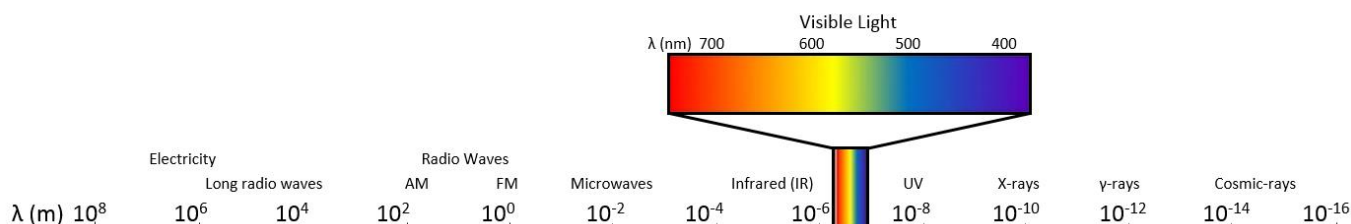


Figure 1-9: The electromagnetic spectrum.

While MOFs have been studied for a wide variety of applications, their optical properties and their ability to interact with light has led to interesting applications such as photocatalytic hydrogen generation⁸⁶ and organic reactions within their pores.⁸⁷ Within the electromagnetic spectrum (Figure 1-9) visible light falls within the range of ~380-700 nm, while wavelengths from ~100-400 nm fall into the ultraviolet (UV) region, which is divided up into UV-A (~315-400 nm), UV-B (~280-315 nm) and UV-C (~100-280 nm), and wavelengths from ~700 nm - 1 mm are considered as infrared (IR) radiations. When light interacts with a MOF, photophysical processes can occur, such as absorption and emission such as fluorescence or phosphorescence, which will be referred to under an umbrella term of luminescence. Depending on the crystal structure of the MOF, non-linear optical effects or upconversion can occur. While these processes will not be commented on in this thesis, it should be noted that a recent review by our group has been published covering these topics in detail.⁸⁸

1.4.1 Luminescence

Luminescent MOFs have gained attention since around the early 2000s, and since then more than 200 articles have been published.⁸⁹ Typically, luminescence is used as an umbrella term to encompass observed emissive processes such as fluorescence and phosphorescence.

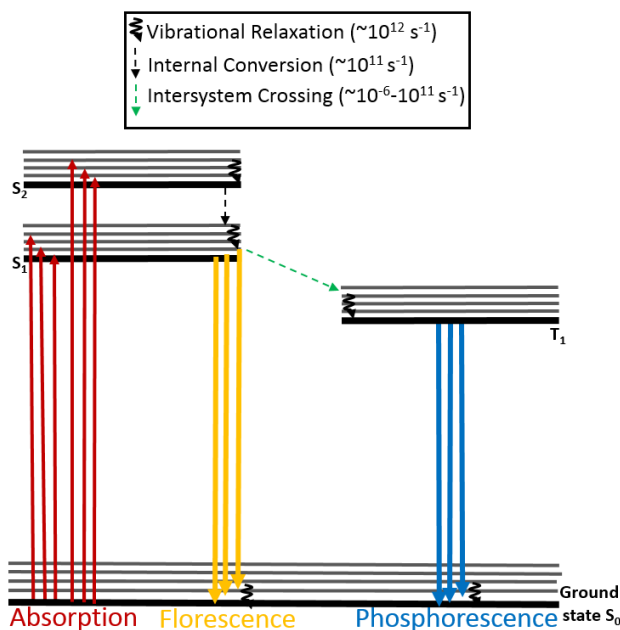


Figure 1-10: Basic photophysical processes represented in a Jablonski diagram. Here, S denotes a singlet state and T a triplet state.⁹⁰

Typically fluorescence is distinguished from phosphorescence via a direct re-emission of absorbed light, whereas phosphorescence includes delayed emissions due to processes like intersystem crossing (ISC) (Figure 1-10).⁹⁰ Ligand fluorescence corresponds to a radiative transition from the first singlet state S_1 , to the ground singlet state S_0 ($S_1 \rightarrow S_0$), which is spin-allowed.⁹¹ The radiative transition from a triplet state T_1 , to S_0 ($T_1 \rightarrow S_0$), which is spin-forbidden, is called phosphorescence and can have a lifetimes from microseconds to seconds. This rule (the Spin rule), consequently makes phosphorescence a weaker emission than fluorescence. While the concept is straight forward and theoretically they can be distinguished from each other, experimentally it is much more difficult as time-dependent investigations using a defined energy source for selective excitation (e.g. a pulsed laser) is required to determine the decay time of the luminescence process and intensity.⁹⁰ Due to this, and the cost associated with such set ups, these experiments are often left out of literature reports.

Due to the inorganic-organic hybrid nature of MOFs, a wide range of emissive phenomena that can be found and is dependent of the framework of the material. Typically, luminescence in MOFs can arise from: a) ligand-based luminescence, which includes ligands-centered (LC), ligand-to-ligand charge transfer (LLCT), ligand-to-metal charge transfer (LMCT) and metal-to-ligand charge

transfer (MLCT); b) metal-centered emissions (MC); c) antennae effects; d) adsorbate-based emission and sensitization; e) excimer and exciplex emissions; f) surface functionalize and g) scintillation.⁸⁹

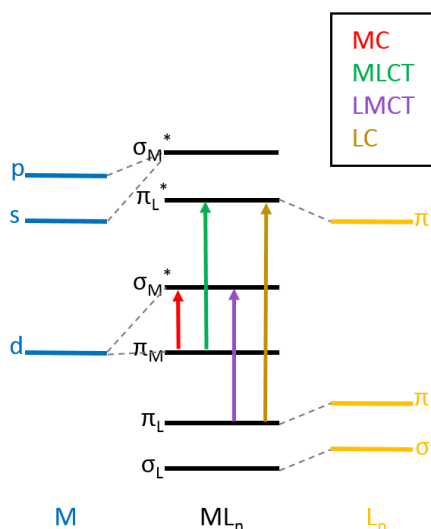


Figure 1-11: Molecular orbital diagram of potential excitation pathways. Molecular orbital diagram for possible excitations in a transition metal complex ML_n .⁹⁰ Here, MC is metal-based emission; MLCT is metal-to-ligand charge transfer; LMCT is ligand-to-metal charge transfer; and LC is ligand-based emission.

A basic description of these process is shown using a molecular orbital diagram as depicted in Figure 1-11. For MOFs, π -extended ligands are often employed in their construction due to their ability to form rigid frameworks. Often, these ligands contain a mixture of functional groups, such as carboxylates or heterocyclic groups, for coordination to metal ions. Ligand-based emission is derived from highly conjugated ligands which absorb in the UV and visible regions, and in some cases more than one competing process can be observed. Ultimately, the luminescence of a MOF is dependent on the crystal structure. Here, the orientation of the linkers, the highest occupied molecular orbital (HOMO) and lowest unoccupied molecular orbital (LUMO) of the linkers vs the accessible states of the metal units, and the electronic configuration of the metal and its bonding geometry all play roles in dictating which type of emission is observed.⁸⁹

Ligand-centered emission (LC), has been described for a variety of transition and alkaline earth metals which have closed shells such as d^0 or d^{10} , resulting in no d-d transitions, or group 13 or 14 metal cations such as In^{III} or Sn^{IV} .^{89, 90} Frameworks with LC emissions often show effects such as guest dependent luminescence as observed in reported in structures such as $[In_2(OH)_2(TBAPy)]$

·(guests) (TBAPy = 1,3,6,8-Tetrakis(benzoic acid)pyrene).⁹² Here, the authors reported a red shift of 34 nm in emission spectra in the desolvated material which is attributed to the increased interactions between the optically active TBAPy ligands, which can be regenerated after exposure to DMF. Frameworks comprised of LC emissions are often sensitive to solvatochromic effects in the fluorescence emission spectra, which can be dependent on the polarity of the solvent molecules. The authors further noted that the structure was unable to be regenerated after exposure of the desolvated material to other guest molecules such as H₂O, toluene and dioxane, with polar guest molecules affording a greater influence on the structure and fluorescence vs non-polar.⁹²

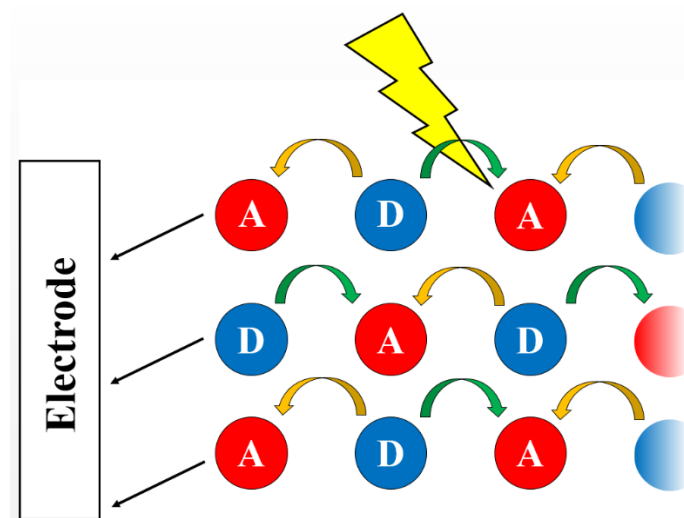


Figure 1-12: Possible mechanism of electron transport within a MOF with LLCT. Here A is the acceptor, and D is the donor, while the electron and hole movement is characterized by green and yellow arrows, respectively.⁹³

Ligand-to-ligand charge transfer (LLCT) has been studied less than other charge transfer processes, such as MLCT and LMCT, due to the fact that the MOF has to be constructed with two different ligands. The metal (M) has to be coordinated with an electron donor (D) and acceptor (A), with the caveat that the acceptor should be before the D-A and the M-A or M-D separation (Figure 1-12).^{93, 94} The charge transfer results in a $D^0A^0 \leftrightarrow D^{\delta+}A^{\delta-}$ ionic form due to possible charge distributions, which can link to physical properties of electron/hole transports, magnetic ordering, and dielectric responses at the bulk level.⁹⁴ Targeting MOFs with LLCT requires careful selection of the D and A ligands. The use of ligands such as tetrathiafulvalene (TTF) has been successfully reported in charge-transfer compounds,^{95, 96} and recently combined with 4,4'-bipyridine (4,4'-bpy), 1,2-bis(4-pyridyl)ethane (BPE), 1,2-bis(4-pyridyl)ethane (BPA) and a Mn metal ion resulting in a framework where the intensity of the charge transfer (CT) was related to the bipyridyl conjugation.⁹³ Metal

complexes can act as D and/or A, and it has been suggested to choose redox-active such as Mn^{II} or Ru^{II} , however it should be noted that this is not easy because molecular control of the ionization potential of the D, and the electron affinity to A is required to control the CT in addition to the already complicated design of the system.^{94, 96}

Energy transfer between different ligands can also be observed for those MOFs constructed with two different organic components. Both the BOB and BOP MOFs, which were assembled using a pyridyl-functionalized boron dipyrromethane (BODIPY) ligand, a tetratopic carboxylic acid, and Zn^{II} showed ligand-to-ligand energy transfers shifting the emission from green to red when the acid was replaced by a porphyrin.⁹⁷

Ligand-to-metal charge transfer (LMCT) and metal-to-ligand charge transfer (MLCT) arises from easily oxidized ligands and reducible metal, or vice versa for MLCT, in MOFs containing transition metal cations.⁹⁰ LMCT has been demonstrated in a wide variety of Zn^{II} and Cd^{II} MOFs, such as $\text{Zn}_3(1,4\text{-BDC})(1,3,5\text{-BTC})_2(\text{NH}(\text{CH}_3)_2)_2(\text{NH}_2(\text{CH}_3)_2)_2$ which emits at 430 nm and has a BTC ligand absorption feature at 370 nm.⁹⁸ Commonly, these MOFs exhibit LMCT when combined with benzene derived ligands such as BDC, BTC and other terephthalates. Similarly, MLCT occurs with benzene derived ligands and d^{10} metals such as Cu^{I} and Ag^{I} . Here, the difference is that the valence orbitals of these metals enables MLCT, whereas the Zn^{II} and Cd^{II} have core-like orbitals.⁸⁹ If the metal is instead paramagnetic, such as d^9 Cu^{II} , ligand-based luminescence can be quenched. For example, comparing the uranyl complex $\text{UO}_2(\text{C}_5\text{H}_2\text{N}_2\text{O}_4) \cdot \text{H}_2\text{O}$ with a Cu^{II} -doped analogue $\text{UO}_2(3,5\text{-pyrazole dicarboxylate})(\text{H}_2\text{O})$, the former complex exhibits a characteristic UO_2^{2+} emission spectra, whereas the MOF has no emission.⁹⁹ Copper based MOFs have the potential to form structures which three-, four-, five- or six- coordinate Cu geometries, all with interesting luminescent properties. For example, mixed valence MOFs such as $[\text{Cu}(1,2\text{-propanediamine})_2][\text{Cu}_2(\text{CN})_4]$ and $[\text{NEt}_4][\text{Cu}_2(\text{CN})_3]$ have MLCT emissions which arise from the Cu-CN transfer, and was demonstrated to be stronger in the later species.¹⁰⁰

Metal-centered (MC) luminescence is found in MOFs comprised of lanthanides or actinides, but has been seen in transition (d-d transitions) and main group metals (s-p-transitions).^{90, 101} Unfortunately for transition metals, there are problems with observing this weak luminescence due to the d-d transitions, and therefore low temperatures are required. Metals used to observe MC luminescence are Pb^{II} and Bi^{III} however there is still some difficulties in clearly assigning the emissions. For example, $\text{Bi}(\text{pydc})_2(\text{H}_3\text{O})(\text{H}_2\text{O})_{0.83}$ (pydc2- = pyridine-2,5-dicarboxylate) displays a broad blue emission at 481 nm, whereas the free ligand afford a green emissions at 518 nm. While this is a relative-

ly simple system comprised of one ligand, it has been suggested that the emission comes from LMCT and/or s-p transitions.¹⁰²

Lanthanide MC luminescence is attributed to the shielded nature of the f-electrons, resulting in predictable MC f-f transitions, with narrow emissions, that have very little influence from the environment of the lanthanide ion.⁹⁰ Due to the parity-forbidden nature, the absorption coefficients for these f-f transitions is low, giving poor luminescence. However, trivalent lanthanides have a diverse luminescence of colors and characteristics, such as Tb^{III} and Eu^{III}, which have green and red 4f-4f emissions respectively, and energy gaps large enough between their main emissive and receives states that avoids vibrational quenching.⁹⁰ Ions such as Ce^{III} are not just restricted to MC f-f luminescence, and have been show to 5d-4f-transitions which are highly dependent on the coordination environmental of the metal as the energetic level of the d states is reduced via ligand and crystal fields. This can also be seen for divalent lanthanides such as Eu^{II}, which can access 5d energy levels in luminescent processes.

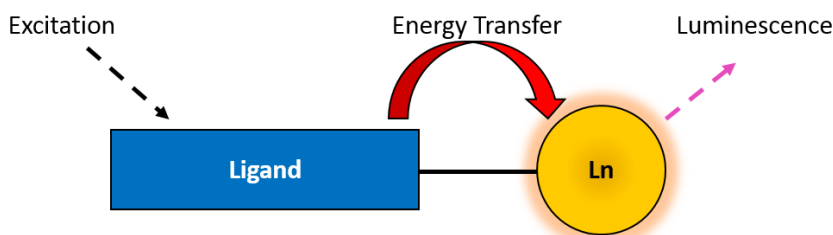


Figure 1-13: Antennae effect from Ln^{II} or Ln^{III} luminescence.

To avoid low light absorption attributed to f-f transitions, ligands which can transfer energy to the lanthanide after excitation have been used in a process called an antennae effect (Figure 1-13). Ligands which have been reported are functionalized symmetric or unsymmetrical benzene rings such as terephthalic acid, 4,4'-bipy, isonicotinic acid and extended triazines, as well as non-aromatic ligands such as oxalic acid, fumaric acid, adipic acid, and nitrilotriacetic acid.⁸⁹ However, a synergistic effect between the Ln and ligand is required, which was demonstrated by Huang et al. who shows that in five isostructural Ln-(3-nitrophthalic acid MOFs) (Ln = Pr, Eu, Gd, Tb, Dy) only the Eu complex exhibited Ln emissions, while the others only showed ligand fluorescence.¹⁰³ It should be noted that the energy transfer mechanism involved is of interested, however not easily elucidated. In the case for the Eu-(3-nitrophthalic acid) MOF, the authors original suggestion that the energy transfer rate is proportional to energy gap was an insufficient explication, due to additional factors that should be considered such as the extent of the Franck-Condon (FC) overlap between the two excited states.⁸⁹

The antennae effect can also be achieved through doping Ln^{III} ions into frameworks, as was shown in a $[\text{Zn}(\text{NDIC}) \cdot 2\text{H}_2\text{O}] \cdot 2\text{H}_2\text{O}$ (NDIC = 5-(5-Norbornene-2,3-dicarboximide)Isophthalic acid) which was doped with Tb^{III} and Eu^{III} for luminescence sensing of Ag^{I} , Pb^{II} , Mg^{II} , Cd^{II} , K^{I} , Zn^{II} , Ni^{II} , Co^{II} , and Fe^{III} .¹⁰⁴ The as made Ln^{III} doped material showed strong green and red luminescence under UV-light, attributed to the Tb^{III} and Eu^{III} ions, with good quantum yields and lifetimes reported for the Tb doped material (42.67%, 0.587 ms, respectively).¹⁰⁴ Luminescence decreases at 545 nm were seen when Fe^{III} , K^{I} , Zn^{II} , Ni^{II} , Mg^{II} , and Co^{II} , were added, while an increase in luminescence was observed for Pb^{II} , Cd^{II} ions.

Adsorbate-based emission and sensitization plays off of a frameworks porosity, and its ability to incorporate emissive molecules for the purpose of molecular detection and structural probing, however there are only a few examples in the literature in which the luminescence is fully examined. Here, a MOF derived structure consisting of Tb^{III} ions and triazine-1,3,5-(4, 4', 4''-trisbenzoate) was shown to have two distinct pore shapes (3.9 nm and 4.7 nm diameters), a BET of 3855 m^2/g , and gave a bright green sensitized luminescence characteristic of Tb^{III} .¹⁰⁵ Introducing ferrocene into the material induced a reversible color change from green to dark brown, and a decrease in Tb emission intensity, which was restored following removal. The authors suggest that the inclusion of ferrocene introduced a non-radiative energy transfer-pathway to quench the Tb emissions.

Depending on the orientation of the ligand groups within a framework, and how they respond to the absorption of a photon, or the interaction of the framework with a guest molecule, exciplexes (heterodimer in an excited state) or excimers (dimer in an excited state), respectively, can be formed resulting in a broad featureless emission at red-shifted wavelengths from the original ligand.⁸⁹ Emissions are dependent on the orientation of the ligand/group, as cofacial arrangements have been hypothesized to be more favorable for excimer formation. Electronic modeling has also suggested that there is a strong dependence on separation distances, as strong face-to-face interactions have been predicted for stilbene dimers with distances less than 5 Å.¹⁰⁶ Exciplexes in MOFs have been only observed in a few cases, such as $(\text{Zn}(4,4'\text{-bipy})_{1.5}(\text{NO}_3)_2 \cdot \text{CH}_3\text{OH} \cdot 0.5\text{pyrene})_n$ in which the 4,4'-bipy ligand is in a cofacial arrangement with the pyrene molecule.^{107, 108} In the structure, the pyrene molecules are not coordinated to the Zn ions, but are instead trapped within the matrix to form a 2 : 1 4,4'-bipy-pyrene exciplex.¹⁰⁸

Using a MOF as a template to generate core-shell and hollow shell nanoparticles is a method that has been explored for MOF luminescence via surface modification. Nanoscale MOFs (NMOFs) comprised of $\text{Ln}(1,4\text{-BDC})_{1.5}$ were used to template NMOF rods with polyvinylpyrrolidone (PVP) and coated with a Si shell.¹⁰⁹ Doping the material with 5 % Eu leads to an NMOF material which

can be used for sensing. Altering the Si to Tb-bound EDTA monosiloxylamide yields a dual Ln competitive sensors which can detect various bacterial spores.¹¹⁰

If a framework emits light when it is irradiated with ionizing radiation such as gamma rays, neutrons or alpha particles, it is known as luminescence via scintillation. This arises from using conjugated ligands such as SDC (SDC = stilbene dicarboxylate), and Zn.^{111, 112} Experiments were conducted using a 3 MeV beam of protons which simulates the interaction between the neutrons with a hydrogen-containing material, which causes ‘recoil protons’ to be produced.¹¹¹ Scintillation luminescence produced by MOFs through this method are comparable to their commercial organic counterparts.

1.4.2 Lanthanide-based MOF Luminescence

Due to the hard Lewis acid nature of Ln^{III} ions, lanthanide based MOFs (Ln-MOFs) are typically constructed using ligands with hard, negatively charged donor atoms such as carboxylic acids, compared to softer bases such as nitrogen.¹¹³ Lanthanide (Ln^{III}) doped or based MOFs are of great interest due to their wide range of applications in areas such as photonics,¹¹⁴ and white light emitting diodes (LEDs).¹¹⁵ The current challenges researchers face when engineering new luminescent materials are:¹¹⁶

- i.* Increasing the brightness (target : 10^2 cd/m²), emission quantum yield (>0.50 for excitation in the deep UV/blue), enhanced absorption cross-section (5-6 orders of magnitude larger than upon intra-4f excitation), and broad excitation range (>100 nm);
- ii.* Synthesis of more environmentally friendly phosphors which would allow for cheaper and safer LEDs;
- iii.* Under UV/blue irradiation, increased photo stability with no degradation before 20 hrs (organic and hybrid materials);
- iv.* New electroluminescent materials with a brightness of at least 10^2 cd/m² for applied voltages of <10 V;
- v.* Synthesis of new multifunctional systems, for example porous materials with light emission properties.

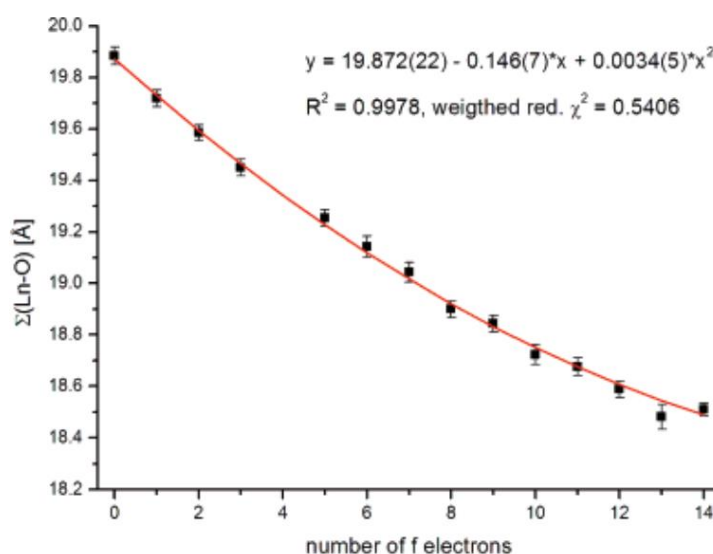


Figure 1-14: Sum of Ln-O bond lengths against the number of f-electrons. Here, the quadratic fit in red, with χ^2 as the weighting factor σ^{-2} .¹¹⁷ Reprinted with permission, © 2009 American Chemical Society.

The advantages of using lanthanides instead of other metals is due to the nature of the group itself. Studying families of MOFs using Ln-MOFs is typically easier than transition metals, as lanthanides have similar chemical properties such as common oxidation states and ionic radius, whereas transition metals can vary. Furthermore, properties such as the decrease in atomic radii of Ln's across the series (known as the lanthanide contraction) have been previously studied and used to fine tune materials.¹¹⁷ In 2007, this concept was revisited and studied via a 1-dimensional polymeric isostructural series of Ln-complexes (La-Lu, except Pm). Each lanthanide was eight-coordinate, with a distorted trigonal-dodecahedral environment, eight unique oxygen atoms, and was the first example of a complete series with a ligand of denticity greater than two. The authors went on to show a quadratic decrease in the sum of all distances for Ln-X (X = N, O), and that the decrease follows Slaters model for calculating ionic radii (Figure 1-14). Here, the model utilizes a set of rules for shielding by the nuclear charge (Z) from electrons in a particular orbital by the inner shell electrons.¹¹⁷

Another benefit of using Ln-based MOFs for luminescent applications, is the unusual spectroscopy properties that Ln^{III} ions can contribute to a framework. Trivalent lanthanide ions display absorption and emission bands that correspond to Laporte-forbidden f-f transitions, which results in line-like optical bands characteristic of each metal.¹¹³ In a centrosymmetric environment, transi-

tions between the s-s, p-p, d-d and f-f orbitals are forbidden when $\Delta l = 0$ (Laporte rule or Orbital rule, $\Delta l = \pm 1$). Therefore, for example, in an octahedral molecule (centrosymmetric) these transitions would be forbidden, whereas for a tetrahedral molecule (non-centrosymmetric) these transitions may appear stronger because small amounts of mixing between the orbitals can occur.¹¹⁸ Due to these rules, and the consequence of parity, these absorptions have lower intensities, however this can be circumvented by using an antennae ligand.

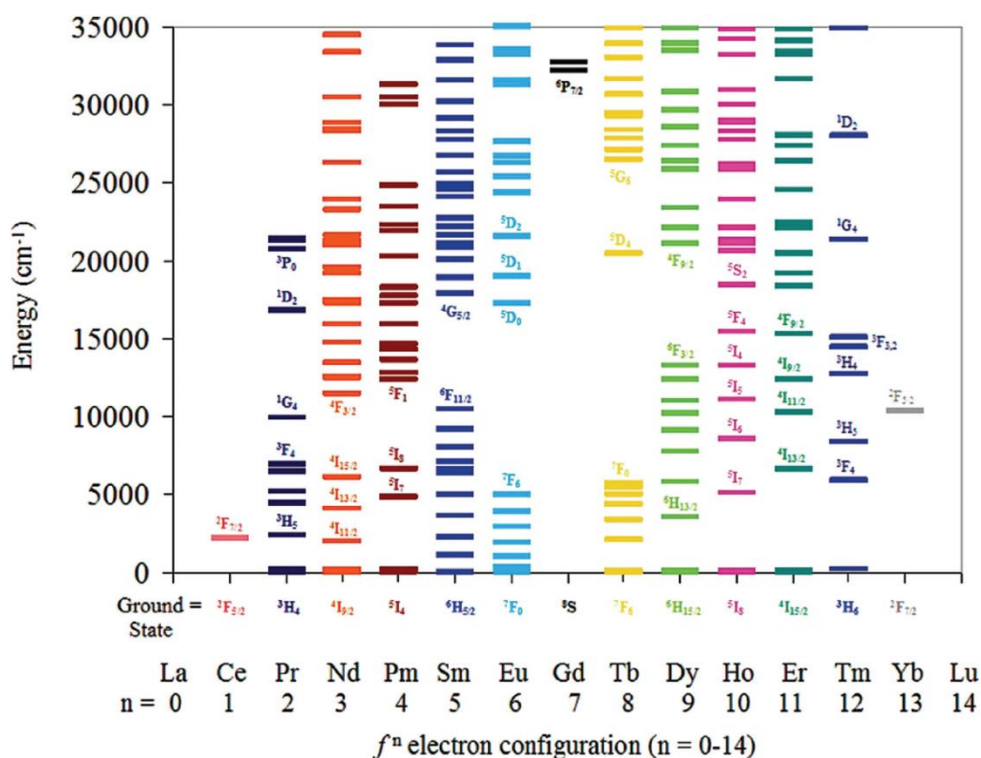


Figure 1-15: Electronic excited-state energy levels for Ln^{III} ions.¹¹³ Reprinted with permission, © 2009 American Chemical Society.

Illustrated in Figure 1-15 is the ground and excited states of Ln^{III} ions, and shows the energy gaps between adjacent levels. Those early (Ce-Pm) and late (Ho-Yb) have relatively small energy gaps when compared to the central (Sm-Dy) ions, particularly Gd.¹¹³ For the early and late ions, non-radiative deactivation pathways processes (e.g. coupling to solvent vibrational modes) are efficient, rendering the ions only weakly emissive. This is compared to the central group, in which the electronic transitions involve a change in spin multiplicity, giving long lived luminescence.¹¹³

1.5 Electrically Conductive Metal-Organic Frameworks

The typical approach of constructing MOFs relies on hard metal-ions and redox-active organic ligands that coordinate via their oxygen or nitrogen atoms.¹¹⁹ This, unfortunately leads to insulating MOFs (conductivity $<10^{-10}$ S/cm) as no low-energy pathways are available for charge transport or free charge carriers.¹²⁰ Since 2010, researchers have realized new approaches that allow for electrically conductive MOFs to be form. It should be noted that for the scope of this thesis proton conductivity¹²¹ will not be discussed.

1.5.1 General Design and Measurement Techniques

Electrical conductivity (σ) is dictated by the density (n) and mobility (μ) of the electrons (e) and holes (h) within a framework. To achieve high conductivity values, both high charge density and high charge mobility are needed. Achieving high charge density requires the material to have a high concentration of loosely bound charge carries (10^{15} cm⁻³), which can be either as free carriers (metallic conductors) or thermally activated (semiconductors).¹²⁰ The components of the framework can act as a source of charge carriers, with metals such as square planar d⁹ Cu^{II} or octahedral d⁶ Fe^{II}, and stable radical containing or redox-active ligands commonly employed. Here, these choice of metals should provide the framework with a source of high-energy electrons/holes, while the ligands can either provide a source of unpaired electrons and/or enable a facile charge transfer between the metal ions.¹²⁰

Depending on how the framework is constructed, depends on if the material will be a metallic or semiconducting. According to band theory, in which the energy levels in a material form continuous energy bands, metallic conductors have a conduction band which is filled up to the Fermi level (E_F), which lies in the middle of the band, and is not completely filled. The electrons in the conduction band are free charge carries, resulting in a charge density $>10^{20}$ cm⁻³, affording conductivity values that are >100 S/cm.¹²² This is different than semiconductors, in which the E_F lies between the valence and conduction band (VB and CB, respectively). At 0 K, the VB is completely filled, while the conduction band is completely empty.¹²⁰ The activation energy of the material arises from the difference between the E_F , and the VB maximum (E_{VBM}) or the conduction band minimum (E_{CBM}). Thermally promoting electrons to the CB, leaving holes in the VB, results in free charge carriers, and charge density is therefore determined by the E_a (activation energy). Here, the smaller the E_a , the larger the charge density at a given temperature.¹²⁰ If the MOF is undoped (intrinsic semiconductor), then the E_F level is at the center of the band gap, a narrow band gap is preferred and therefore redox matching is required between the components of the material to achieve

this. If a MOF is doped (extrinsic semiconductor), the E_F is shifted towards the VB or CB giving either n-type or p-type semiconductors, respectively.¹²³ For semiconductors, the E_a is generally obtained by fitting temperature dependent data to the Arrhenius equation:

$$\sigma = \sigma_0 \cdot \exp (-E_a/k \cdot T) \quad (1-1)$$

where σ_0 is a prefactor, and charge mobility is required to be constant in the range of temperatures used for this measurement. The E_a can also be used to derive the fundamental band gap (E_g) through the formula $E_g = 2E_a$, and E_g can be determined from the difference between the VBM and CBM.¹²⁰ It should be noted that this relationship is only valid for undoped semiconductors, and that for MOFs, ultraviolet photoelectron spectroscopy (UPS) and inversion photoemission spectroscopy (IPES) should be used to measure the difference between the VBM and CBM as it gives exact energy levels, whereas UV-vis-NIR (NIR = near infrared) does not.

Theoretically, the charge transportation can be broken up into either a hopping or band transport mechanism, both of which require good spatial and energetic overlap between their orbitals, which improves the transportation pathway and increases charge mobility. In the hopping transport mechanism, the charge carriers (electrons and/or holes) are found in localized specific sites and have discrete energy levels, allowing them to hop between neighboring sites.¹²⁴ This is compared to the band transportation mechanism where the charge carriers are delocalized, and depend on the curvature of the band.¹²² Achieving high mobility unfortunately at the moment is not entirely controllable, as factors such as crystal lattice symmetry and unit cell parameters control how well a band is dispersed which fundamentally is a result of the orbital overlap.¹²⁰ Unfortunately, both of these pathways are absent in the majority of MOFs, and instead, a “through-bond” or “through-space” approach should be considered instead, both of which can theoretically lead to a hopping or band transport mechanism.¹²⁵

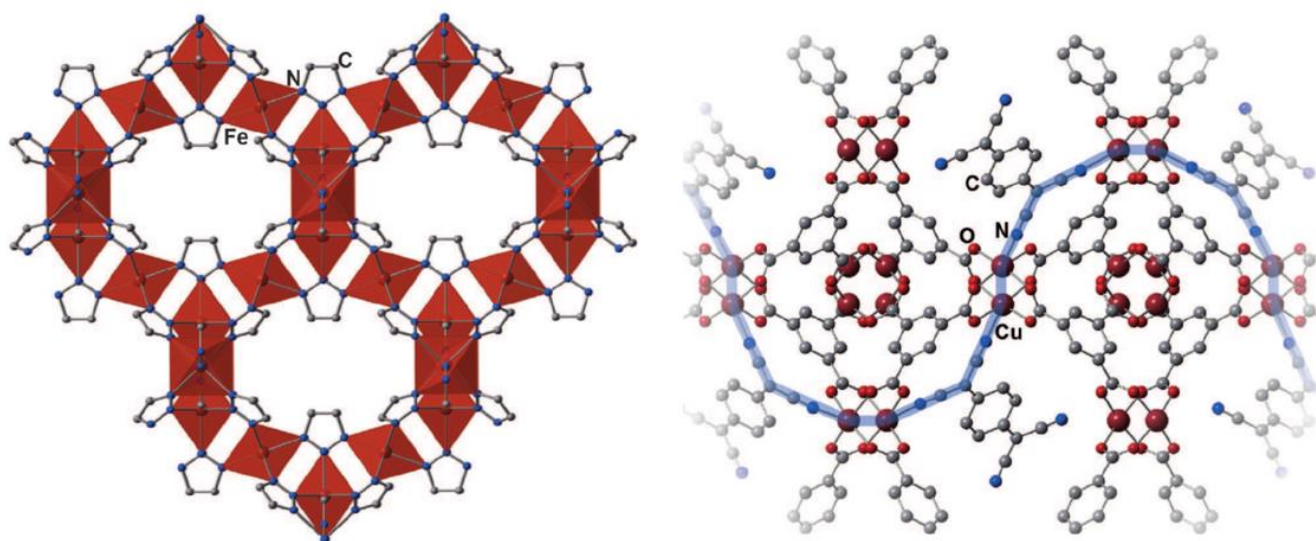


Figure 1-16: Through bond approach to charge transfer. Structures highlighting two strategies to develop a through-bond approach to electrically conductive MOFs. **Left:** The structure of Fe(1,2,3-triazolate)₂, which shows a continuous covalent network of Fe-N bonds. **Right:** TCNQ adsorbed into Cu₃(BTC)₂, with the covalent charge pathway highlighted in blue.¹²⁰ Reprinted with permission, © 2016 John Wiley and Sons.

In the through-bond approach, charge transport is achieved through favorable spatial and energetic overlap of frameworks components (Figure 1-16 left). For example, it's common for these frameworks to have 1-dimensional metal chain complexes which afford the desired charge transport mechanism. Strategically, metals with loosely held electrons, conjugated ligands, and frameworks that have mostly covalent bonding interactions between the metal ions and ligand.¹²⁰ Metals such as Cu^I, Cu^{III}, Fe^{II}, and Mn^{II}, have been employed with ligands such as 2,3-pyrazinedithiolate (pdt),¹²⁶⁻¹²⁹ 2,5-dihydroxybenzene-1,4-dicarboxylate (DOBDC),¹³⁰⁻¹³³ 2,5-disulphydrylbenzene-1,4-dicarboxylic acid (DSBDC),¹³⁴ and benzene-1,3,5-tricarboxylate (BTC)¹³⁵ have been used. For these frameworks, conductivity values ranged between 10⁻¹² S/cm for Mn₂(DSBDC) to 0.07 S/cm for TCNQ doped Cu₃(BTC)₂ (HKUST-1). Interestingly, as made HKUST-1 has a recorded conductivity of 10⁻⁸ S/cm, however when doped the conductivity increases. Theoretical calculations suggest that the TCNQ molecule (on molecule per MOF pore) binds to two open metal Cu sites forming a new continuous covalent network (Figure 1-16 right). This is ultimately achieved through redox matching and orbital overlap between the HKUST-1 framework and TCNQ molecule, in which the VBM of HKUST-1 and the LUMO of TCNQ give rise to a $E_a = 0.041$ eV, resulting in a partial charge transfer (0.3-0.4 electrons) which affords loosely bound charge carriers.^{120, 136} The creation

of loosely bound electrons can also be achieved through I₂ doping in frameworks such as SION-8,¹³⁷ and Cu[Ni(pdt)₂].¹²⁷

Similar to organic conductors and semiconductors such as TTF-TCNQ (TTF = tetrathiafulvalene)¹³⁸ and polythiophene,¹³⁹ a through-space approach has also been successfully used to create electrically conducting MOFs via non-covalent interactions such as π - π stacking. For this approach to work, a rigid MOF framework is required, as stacking between the conjugated organic ligands should be approximately ~3.3-3.6 Å so that an extended charge pathway can be created with sufficient orbital overlap between adjacent ligands.¹⁴⁰ Generally, the ligands used should be stable organic radical ligands because they can provide free charge carriers and improve the charge density.¹²⁰ Ligands that have been previously reported are tetrathiafulvalene tetrabenzoate (TTFTB),¹⁴¹⁻¹⁴³ hexahydroxytriphenylene (HHTP),¹⁴⁴ benzenhexathiol (BHT),¹⁴⁵ hexathiotriphenylene (HTTP),^{145, 146} hexaaminotriphenylene (HATP),¹⁴⁷ and hexaiminotriphenylene (HITP),^{147, 148} with metals such as Mn^{II}, Co^{II}, Zn^{II}, Cd^{II}, Co^{II}, Ni^{II}, Pt^{II}, Pd^{II}, and In^{III}. Conductivity values for MOFs utilizing these metals and ligands range from 10⁻⁶ S/cm for Pt₃(HTTP) to 40 S/cm for Ni₃(HITP)₂.

Once a MOF has been made, testing it for electrical conductivity can get tricky. These measurements depend not only on the framework, but also the method in which is used to measure conductivity, the quality of the instrument, and materials used for the device's fabrication such as electrical leads, contact pastes, and substrates.¹²⁰ To measure conductivity, measurements of the electrical conductance, the length (*l*) and area (*A*) are required:

$$\sigma = (I/V) \cdot (l/A) \quad (1-2)$$

Where:

V= voltage

I= current

Conductivity follows Ohms law ($I = V/R$, where *R* is resistance), which states that the current between two points of a conductor is proportional to the *V* across the two points, where the proportionality is *R*.¹⁴⁹ Measurements taken between the *I* and the *V* are then fitted to a (typically) linear *I*-*V* curve. However, depending on the form of your sample also depends on the method used, for example for single crystals and pressed powders a four-contact probe or two-contact probe can be

used whereas thin films require a four-point probe or van der Pauw method. Both the four-probe and van der Pauw method eliminate the resistance of contacts and wires, so these methods are often used with materials that have higher conductivity values. Generally, for most 3-dimensional MOFs, their conductivity is below 10^{-3} S/cm, with resistance of more than 1 k Ω in their conduction channels, which is significantly larger than contacts and wires (1-10 Ω).¹²⁰ For these samples then, the two-point probe method is sufficient enough to give meaningful conductivity values.

As stated earlier, an important concern in measuring the conductivity of a MOF, is the form in which the MOF is present as each form can give different conductivity values. In an ideal set up, a single crystal would be measured through a four-probe or van der Pauw method, in constant temperature, in vacuum and in the dark, however often these experimental conditions are not always feasible. For many MOFs, obtaining single crystals large enough to measure can be nearly impossible, and also difficult to handle. Therefore, powders can offer an attractive advantage as they're easy to handle and can be pressed into pellets using standard laboratory equipment. Fundamentally however, powder pellets have a high number of grain boundaries which can present the study of intrinsic charge transport properties, and the random orientation of crystallites within the pellet can mask any potential anisotropy of charge transport.¹²⁰ An alternative method is to use polycrystalline films, as they're often denser than pellets and have shown higher conductivity values, but overall suffer from the same drawbacks as pressed powders. Combining pressed pellets with Electrochemical Impedance Spectroscopy (EIS) measurements however offers the advantage of understanding complex material variables such as mass transport, and gives insights into defects, microstructures, and compositional influences.¹⁵⁰ Due to the ease at which these measurements can be taken, material can also be measured under the influence of different temperatures and/or pressures.

1.6 Electrochemical Impedance Spectroscopy

Evaluating the electrochemical behavior of a material is typically done in a cell with two identical electrodes, which are in contact with the faces of the sample in either a circular cylinder or a rectangular parallelepiped. The sample can be tested under conditions such as vacuum, a neutral atmosphere (e.g. argon) or under a normal/O₂ enriched atmosphere (e.g. oxidizing atmospheres). Once the cell is connected to a voltage source, electrical stimulus can be applied and a response is subsequently recorded. Application of electrical stimulus to the material results in: *i.* the transportation of electrons through the conductors; *ii.* the transfer of electrons via the electrode-material interface to/from charged/uncharged species or components of the material; *iii.* flow of charged atoms/atom agglomerates through the defects in the material, where the flow rate is called the charge,

and is dependent on the ohmic resistance of the electrodes and the reaction rate at the electrode-material interface.¹⁵⁰ The properties of the material are assumed to be time-invariant, and through the use of EIS, the relationship of the material to controllable variables such as temperature, oxygen partial pressure, applied hydrostatic pressure and applied static voltage can be deduced.¹⁵⁰ It should be noted that the flow of charge throughout the cell can be impeded or influenced by the contacts and the material being measured. While it's assumed that the electrode-material interface is smooth, in reality it isn't. The interface is rough, the powdered material doesn't have a perfect crystal orientation, grain boundaries are present, and there will be defects in the bulk of the material.

While there are many methods to determine the conductivity of a material, impedance spectroscopy is useful because any intrinsic property that influences the system can be studied. There are two categories that can be used to classify the information gained through this study, *i.* information in regard to the material itself such as, conductivity, dielectric constant, charge mobility, equilibrium concentration of charge species, and bulk generation-recombination rates, and *ii.* information regarding the electrode-material interface such as adsorption-reaction rate constants, capacitance of the interface region, and diffusion coefficient of the neutral species in the electrode itself.¹⁵⁰

When a measurement is performed, a monochromatic signal $v(t) = V_m \sin(\omega t)$, which has a single frequency $\nu = \omega/2\pi$ is applied to a cell, and the steady state current $i(t) = I_m \sin(\omega t + \theta)$ is measured, where ω is the angular frequency, t is time, and θ is the phase difference between the voltage and the current, which is zero for a purely resistive behavior.¹⁵⁰ Following measurements, data is displayed as the magnitude and direction of a planar vector in the first quadrant of Cartesian system, and are commonly expressed as the vector sum of the components a and b along the axis.¹⁵⁰

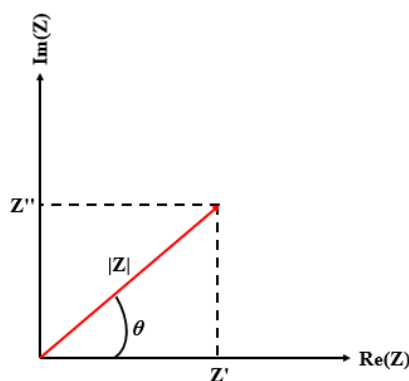


Figure 1-17: Complex impedance plane. Here, the complex impedance plane shows both the real, $\text{Re}(Z)$, and imaginary, $\text{Im}(Z)$ axis's.

Here, the real part of Z ($\text{Re}Z$, or Z'), along the a -axis, is direction along the real axis, where b represents a direction along the imaginary axis ($\text{Im}Z$, or Z''). The real and imaginary parts of the axis are commonly denoted as Z' and Z'' , respectively. An impedance then of $Z(\omega) = Z' + jZ''$ is a vector quantity and can be plotted with a phase angle of $\theta = \tan^{-1}(Z''/Z')$, as seen in Figure 1-17.

It should be noted that there are impedance related function generically called immittances which can play a roles in impedance spectroscopy. These concepts combine **impedance** and **admittance** of a system, and refer to complex numbers of either the impedance or the admittance of the system. However, for the electrode-material systems present throughout this thesis, only impedance will be discussed for the sake of relevancy, clarity and consistency.¹⁵⁰ Furthermore, it should be noted that the conductivity of the samples is taken directly from the data, and that while an equivalent circuit can be fit, it will not be discussed in this body of work.

1.7 Outlook

The following thesis will explore MOFs through functional applications based on tuning their properties, and through bridging fields such as organic chemistry and health monitoring. More specifically, in the next chapter we explore the chemical transformation of **SION-2** to **SION-1**, which proceeds through the loss of a ligand upon continuous heating. As mentioned in this introductory chapter, developing insights into these transformations can be difficult due to the lack of instrumentation available to monitor *in-situ* solution crystal transformations. Following this work, we developed an isostructural family of **Ln-SION-1** and **Ln-SION-2** materials, and explored their tunable optical properties and potential use as dielectric materials.

In the third chapter of this thesis, we developed a novel Ade based MOF, **SION-19**, which can be used as a MOF nanoreactor to absorb and dimerize thymine molecules within its pores. The use of MOFs as nanoreactors is an emerging field that bridges both the materials and organic chemistry fields, allowing researchers to obtain organic molecules with specific conformations or functionalities which may be difficult to synthesize through typical synthetic pathways.

In the final chapter of this work, we synthesized a new MOF (**SION-9**) using a porphyrin based ligand with a free electron and Ade, to construct an electrically conductive MOF. Here, our goal was to develop a new, multimodal sensing MOF that could detect pressure and temperature changes simultaneously and allow us to construct a cheap health monitoring device using common hobby shop items. We hope that this work highlights that MOFs can be used to make cost effective health monitoring devices, without using complicated device fabrication steps.

Through this work, we hope to demonstrate both the fundamental insights we have gained through the synthesis and analysis of new MOFs, while also showing their ability to bridge other fields such as organic chemistry, conductivity, and health.

Chapter 2 Formation Pathway and Optical Properties of SION-1 and SION-2

2.1 Introduction

The ability for a chemical compound to exist in two or more solid forms has been demonstrated by researchers since the 19th century. Compounds such as calcium carbonate minerals can exist in anhydrous forms such as calcite, aragonite, and vaterite,¹⁵¹ while other compounds like TiO₂, can exist in either the well-known forms such as rutile, anatase and brookite, or the less well-known columbite structure.¹⁵² For these structures, it's typically reported that specific phases exist either as a kinetic, thermodynamic or metastable phase. Examples of the metastable phases for calcium carbonate and TiO₂ are the aragonite/vaterite and anatase/brookite structures, respectively, while the thermodynamically stable phases are calcite and rutile.¹⁵³ These metastable phases can be formed through the addition of additives, or changes in the reaction conditions,^{26, 154, 155} and for many practical applications it is important to determine the correct conditions for the formation of the desired phase. However, understanding the underlying mechanism that guides the formation of these phases is limited, thereby restricting access to materials that otherwise may be difficult to form through traditional methods.²⁶ The self-assembly of the components in MOFs is a dynamical non-equilibrium process, evolving from an initially disordered state, towards an ordered stable state by the completion of the reaction.¹⁵⁶ This process can proceed through various pathways, where structures can either be described as under kinetic or thermodynamic control.¹⁵⁶⁻¹⁶⁰ Revealing the pathways in the synthesis of MOFs remains a challenge, since there are limited experimental methods available that can provide high quality *in situ* data.^{154, 155, 161-167} We are only beginning to reveal the dynamic nature of these reactions, as recent studies have challenged the conventional view that once the MOF crystal is formed it remains stable in solution.^{24, 25, 33, 168,}

It should be noted that our publication "Anderson, L. Samantha; Gładysiak, Andrzej; Boyd, G. Peter; Ireland, P. Christopher; Miéville, Pascal; Tiana, Davide; Vlasisavljevich, Bess; Schouwink, Pascal; Van Beek, Wouter; Gagnon, J. Kevin; Smit, Berend; Stylianou, C. Kyriakos. Formation pathways of metal–organic frameworks proceeding through partial dissolution of the metastable phase, *CrysEngComm*.**2017**, 19, 3407-3413" has been reused for this thesis chapter.

A key issue hindering the fundamental insights into the formation of MOFs is the lack of model systems in which different frameworks composed of the same chemical components can be systematically studied. This work presents two 3-dimensional Tb^{III} based MOFs utilizing a DHBDC (DHBDC = 2,5-dihydroxybenzene-1,4-dicarboxylate) ligand; **SION-1** and **SION-2** (SION refers to MOFs synthesized at the EPFL Valais in Sion, Switzerland). Uniquely, this systematic study reveals tuneable conditions favouring the formation of one phase or the other, and in-situ ¹H NMR and powder X-ray diffraction (PXRD) studies on how **SION-2** transforms to **SION-1**. This tunability arises from the addition of more energy allowing the kinetic and metastable **SION-2** to partially dissolve and undergo a structural rearrangement into the thermodynamically stable **SION-1**.

2.2 Structural Description, Stability and Bulk Characterization of SION-1 and SION-2

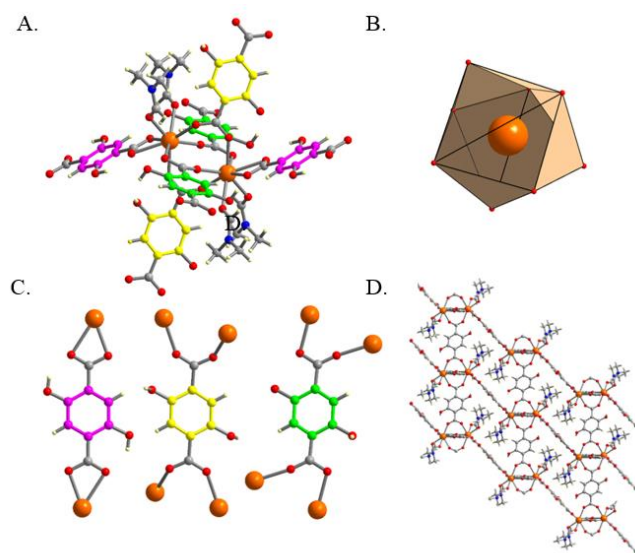


Figure 2-1: Crystal structure of SION-2. **a)** Tb₂-cluster **b)** antiprismatic coordination geometry of Tb^{III}, **c)** coordination modes of the three distinct ligands with η^2 chelating (purple) and $\eta^1:\eta^1$ bridging (yellow and green) modes and **d)** the packing along the crystallographic [100] direction with coordinated DMF molecules occupying the accessible void space. Atom colours: orange, Tb; red, O; blue, N; grey, C; pale yellow, H.

The reaction of Tb(NO₃)₃·6H₂O with H₂DHBDC in DMF:H₂O solvent mixture at 120 °C for 24 hours yielded gold coloured crystals of **SION-2**. **SION-2** crystals were analysed using single crystal X-ray diffraction (SCXRD) and its formula is based on [Tb₂(DHBDC)₃(DMF)₄]₂DMF (general formula M₂L₃, where M = Tb^{III} and L = DHBDC). **SION-2** crystallizes in the triclinic space group

$P\bar{1}$ and is composed of a binuclear $\text{Tb}_2(\text{COO})_6$ cluster interconnected by three distinct DHBDC ligands with η^2 chelating and $\eta^1:\eta^1$ bridging modes (Figure 2-1a). Each of these ligands possess a centre of symmetry which is retained within the crystal structure. The Tb_2 -clusters are centrosymmetrical as well, and each 8-coordinated Tb^{III} displays a square antiprismatic geometry (Figure 2-1b), which is completed via coordination of two fully ordered DMF molecules, two carboxylate O-atoms from a η^2 chelating DHBDC ligand, and the remaining four carboxylate O-atoms from two symmetrically distinct DHBDC with $\eta^1:\eta^1$ bridging modes (Figure 2-1c). Here, the hydroxyl groups of the DHBDC ligands do not participate in metal binding. **SION-2** possesses rectangular channels running along the crystallographic direction of [100] which are filled with coordinated to Tb^{III} and guest DMF molecules (Figure 2-1d), the latter being disordered over two sites with unequal occupancies. We note that **SION-2** is isomorphous to the structures of $[\text{Ln}_2(\text{DHBDC})_3(\text{DMF})_4] \cdot 2\text{DMF}$ ($\text{Ln} = \text{La}, \text{Ce}, \text{Pr}, \text{Nd}, \text{Sm}, \text{Gd}, \text{Er}$) reported previously.^{169, 170} Topological analysis of **SION-2** using the TOPOS4.0 software package designates this material as the *xah* topology, using the three-letter notation of O’Keeffe.¹⁷¹

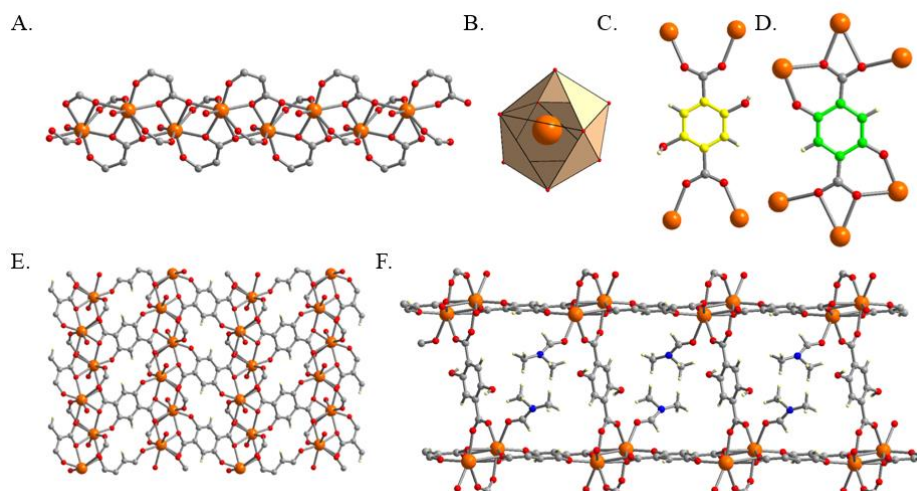


Figure 2-2: Crystal structure of SION-1 **a)** 1-dimensional Tb-O chains running along the crystallographic [010] direction, **b)** distorted dodecahedron geometry of Tb^{III} **c)** and **d)** coordination schemes of DHBDC and DOBDC ligands in **SION-1** ($\eta^1:\eta^1$ bridging – yellow and $\eta^1:\eta^2:\eta^2$ bridging – green, respectively), **e.** the coordination of DOBDC with Tb^{III} leads in the formation of 2-dimensional layered sheets ($\bar{1}01$) which are interlinked by DHBDC to form **f)** the 3-dimensional **SION-1**, with pores along the [010] direction which are occupied by coordinated DMF molecules. Atom colours: orange, Tb; red, O; blue, N; grey, C; pale yellow, H.

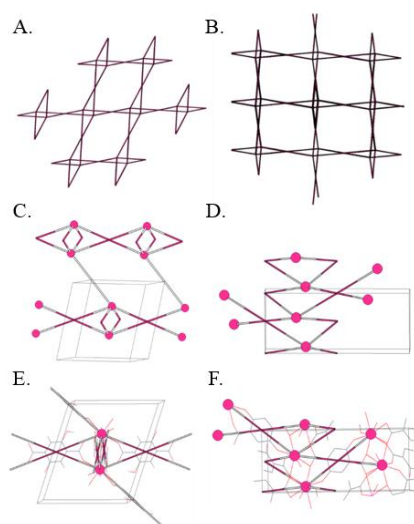


Figure 2-3: Network topologies of SION-1 and SION-2. Network topologies of **a)** *lvt* of **SION-1**, **b)** *xah* of **SION-2** along the *c*-axis, **c)** projection of the *xah* net approximately along the *a*-axis, **d)** projection of the *lvt* net approximately along the *a*-axis, **e)** the *xah* net with **SION-2** superposed in the background, **f)** the *lvt* net with **SION-1** superposed in the background. Tb^{III} ions are represented as purple balls, while the organic ligands are represented as purple and white lines.

The reaction of $\text{Tb}(\text{NO}_3)_3 \cdot 6\text{H}_2\text{O}$ with H_2DHBDC in $\text{DMF}:\text{H}_2\text{O}$ solvent mixture at 120°C for 72 hours gave rise to red single crystals of **SION-1**. **SION-1** has a formula of $[\text{Tb}_2(\text{DHBDC})(\text{DOBDC})(\text{DMF})_2]$, (where: DOBDC = 2,5- dioxidobenzene-1,4-dicarboxylate), or a general formula of M_2L_2 , and possesses a higher monoclinic symmetry (space group $P2_1/n$). The DHBDC and DOBDC ligands are symmetrically independent and their centres of gravity sit on crystallographic inversion centres. The main building unit of **SION-1** consists of 2_1 - symmetrical chains of alternating Tb^{III} and O atoms that are running along the $[010]$ direction (Figure 2-2a). Visually, the structure appears to resemble a ladder, and within these ladder-like arrays, the coordination number of each Tb^{III} is 8 with a distorted dodecahedron geometry, where only one out of eight coordination sites is occupied by DMF molecules (Figure 2-2b), which are disordered over two sites with unequal occupancies. The DHBDC ligands with protonated hydroxyl groups bind to Tb^{III} in a similar coordination mode with the $\eta^1:\eta^1$ bridging ligands in **SION-2**, demonstrating a similar partial disorder over the two pendant hydroxyl groups (Figure 2-2c-d). However, the fully deprotonated DOBDC has a $\eta^1:\eta^2:\eta^2$ bridging mode and binds to Tb^{III} in a similar way as observed in MOF-74.¹³⁰ This highly-connected coordination mode allows for the formation of 2-dimensional puckered sheets consisting of Tb^{III} and O-atoms (Figure 2-2e) which are interlinked by the DHBDC to form a 3-dimensional structure with 1-dimensional channels running along $[010]$ (Figure 2-2f).

Deriving the structural topology of **SION-1** into discrete secondary building units of 1-dimensional Tb-O chains is challenging and has been acknowledged previously for MOFs with similar coordination schemes to 1-dimensional Tb^{III} -O chains, such as in MOF-74 analogues.^{171, 172} For the topological analysis of **SION-1**, we treated each Tb^{III} ion in the 1-dimensional Tb^{III} -O chains as a separate node, and using this method ultimately resulting in the net *lvt* for **SION-1** (Figure 2-3). Here, the DHBDC and DOBDC ligands are described as connected to four separate Tb^{III} nodes. We note that the DOBDC ligands in **SION-1** are coordinated to six Tb^{III} ions (Figure 2-3d) however, for conceptual symmetry with the ligand binding in **SION-2** we have severed two of these connections in the topological description, corresponding to the terminal carboxylate O- Tb^{III} bond on the opposite side of the oxido group.

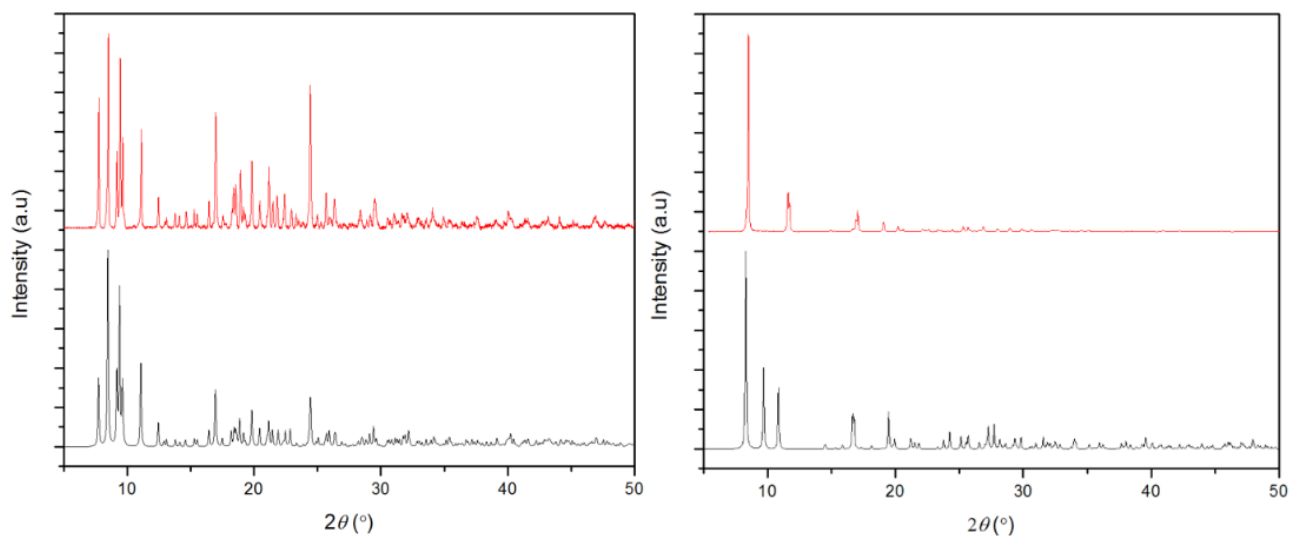


Figure 2-4: PXRD of SION-2 and SION-1. Left, **SION-2**; right, **SION-1**. Color scheme: black, theory; red, experimental.

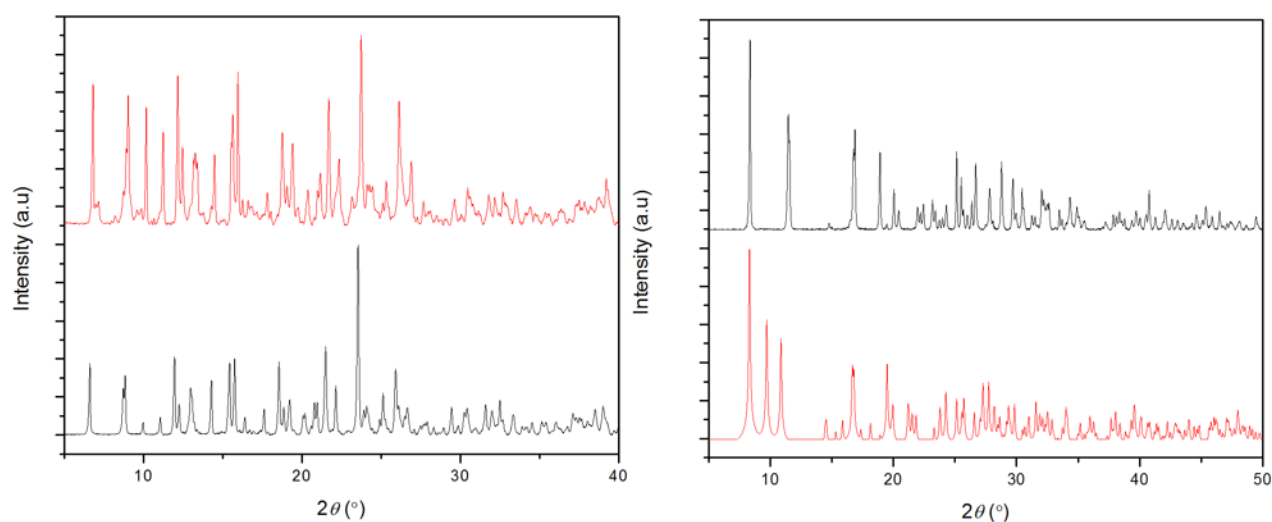


Figure 2-5: PXRD of SION-2@H₂O and SION-1@H₂O. Left, **SION-2 @ H₂O**, color scheme: black, theory; red, experimental. Right, **SION-1@ H₂O**, color scheme: red, theory; black, experimental.

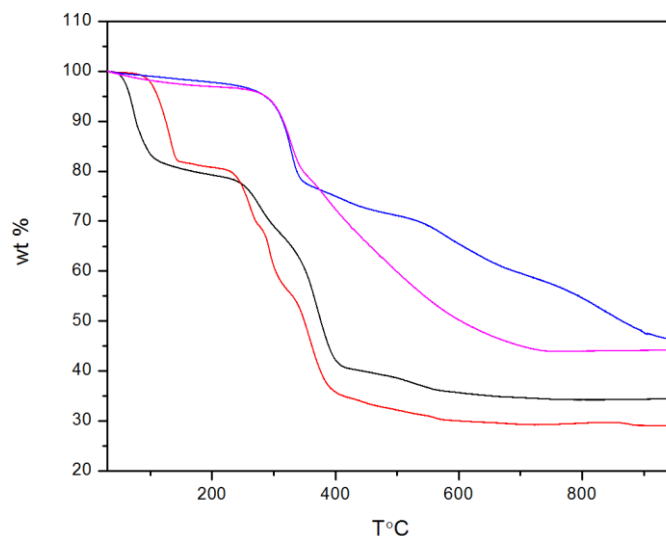


Figure 2-6: TGA of the SION MOFs. Color scheme: **SION-2**, red; **SION-2@H₂O**, black; **SION-1**, blue; **SION-1@H₂O**, pink.

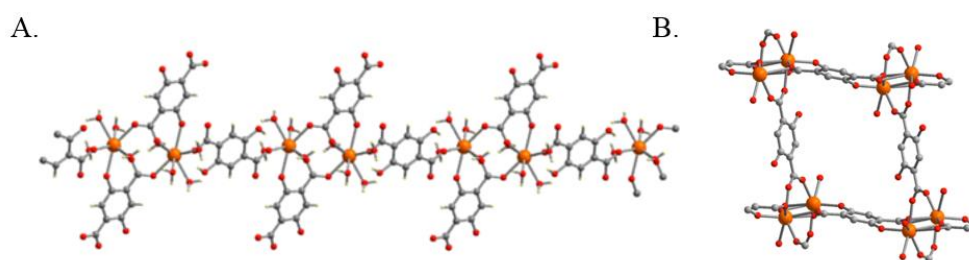


Figure 2-7: Crystal Structures of SION-2@H₂O and SION-1@H₂O a) 1-dimensional chains of **SION-2@H₂O**, b) structure of **SION-1@H₂O**. Atom colours: orange, Tb; red, O; grey, C; pale yellow, H.

The bulk phase and elemental purity of **SION-1** and **SION-2** is confirmed by PXRD (Figure 2-4-5), infra-red spectroscopy and elemental analysis, whereas their thermal stability was evaluated by TGA (Figure 2-6). Both **SION-1** and **SION-2** are stable standing in air for long periods of time, however their stability in H₂O is different. The PXRD patterns of the H₂O loaded **SION-1@H₂O** and **SION-2@H₂O** (Figure 2-5) suggested that although they are still crystalline, structural changes have occurred; an observation that was visually confirmed by the change of their colour from gold to beige for **SION-2**, and red to orange for **SION-1**.¹⁷³ Both **SION-1@H₂O** and **SION-2@H₂O** structures were solved using SCXRD (Figure 2-7). We found that **SION-1@H₂O** does not undergo substantial structural changes compared to **SION-1**, however, the 3-dimensional structure of **SION-2** collapses into binuclear Tb₂-clusters aligned in 1-dimensional chains.

2.3 Effects of Time and Solvent Concentration of the Formation of SION-2 and SION-1, and the Transformation of SION-2 to SION-1

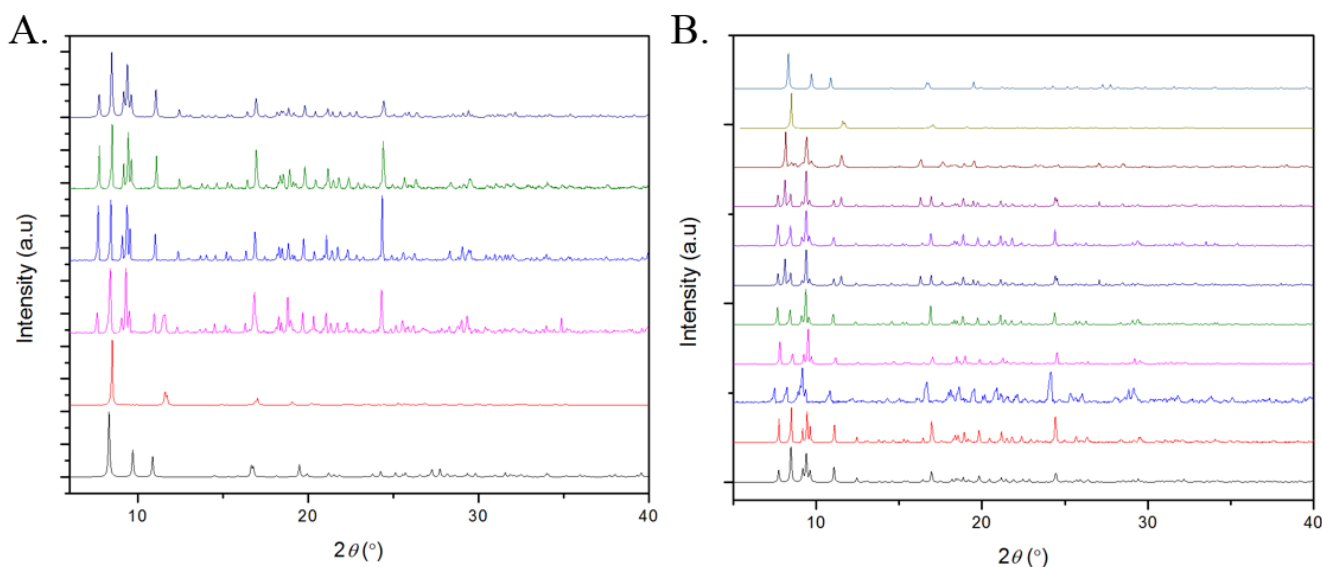


Figure 2-8: PXRD of SION-2 and SION-1 reflecting the effects in changing the solvent concentration and reaction time. a) Effects of concentration of DMF on the formation of **SION-1** and **SION-2**, here all vials contain 0.5 mL of H₂O. Color scheme: black, **SION-1** theory; red, 2.0-2.2 mL DMF; pink, 1.5-1.7 mL DMF; Blue 1.0-1.3 mL DMF; green, **SION-2**; navy blue, **SION-2** theory, b) Effects of time on the formation of **SION-1** and **SION-2**. Color scheme: black, **SION-2** theory; red, 12 hrs; blue, 24 hrs; pink, 48 hrs; green, 52 hrs; grey, 62 hrs; purple, 65 hrs; dark yellow, 72 hrs (**SION-1**); brown, **SION-1** theory.

During synthesis, it was observed that both crystals of **SION-2** and **SION-1** could be formed together in the same reaction vial. Therefore, **SION-2** was further examined as an intermediate to **SION-1**, as it appeared to form in shorter amounts of times. **SION-2** was synthesized using different solvent ratios of DMF : H₂O for 72 hours at 120 °C under the same solvothermal previously used for its formation (Figure 2-8a). It was observed that outside of the optimal 2.0 : 0.5 mL DMF : H₂O ratio, led to various ratios of both MOFs. Subsequently, the time required to form each MOF was studied (Figure 2-8b), and found that short reaction times (< 48 hrs) gave predominately **SION-2**, reactions between 48-62 hrs gave mixtures of both, and reaction times longer than 68 hrs gave **SION-1**.

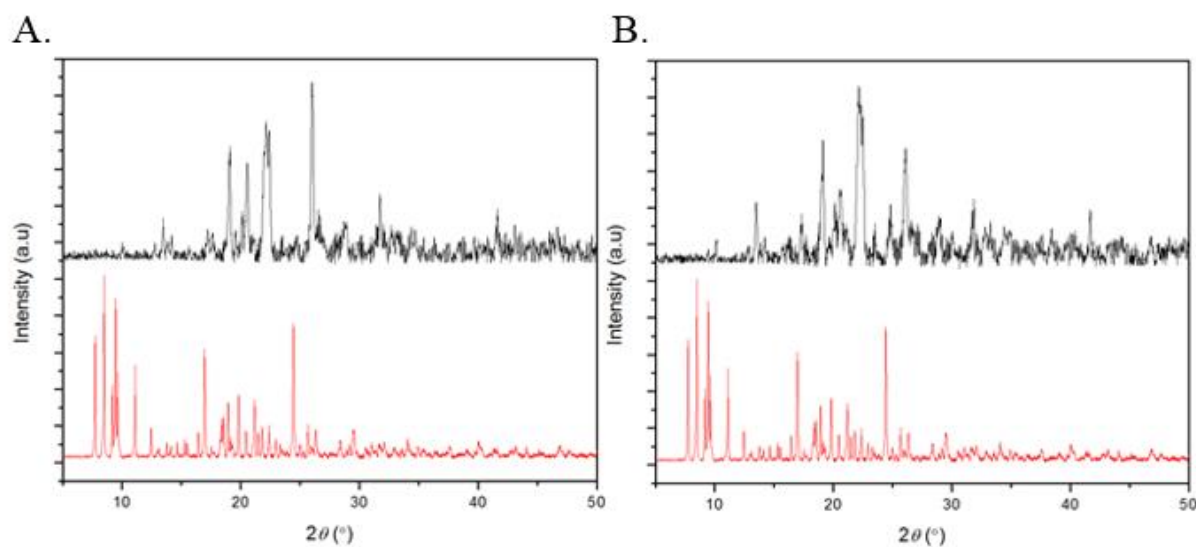


Figure 2-9: PXRD of the transformation in air from SION-2 to SION-1. Here, material had been a) previously dried b) and material that had been just removed from solvent (“wet”) but not dried. Color scheme: **SION-2** Theory, red; dry/wet material after heating, black.

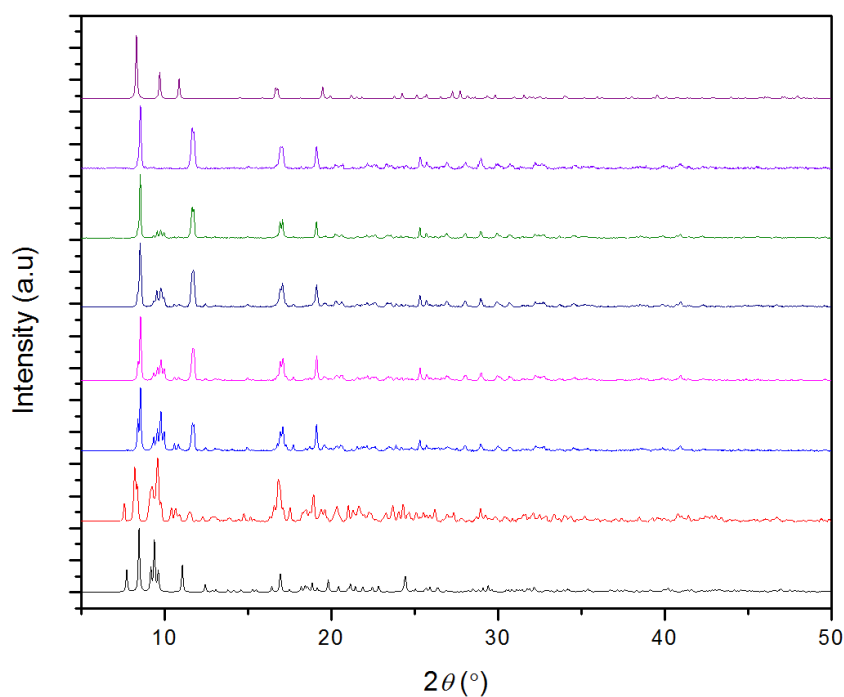


Figure 2-10: PXRD of the transformation in fresh solvent (DMF : H₂O 2.0 : 0.5 mL) using preformed SION-2. Color scheme: black, **SION-2** theory; red, 5 hrs; blue, 10 hrs; pink, 14 hrs; green, 18 hours; dark blue, 20 hrs; purple, 24 hrs; dark purple, **SION-1** theory.

To rule out a single-crystal to single-crystal transformation between **SION-2** to **SION-1**, preformed **SION-2** was made and either dried, or kept in submerged in solvent. Placing dry, or wet crystals of **SION-2** in the oven for 72 hours at 120 °C lead to a breakdown of the crystal structure and no single-crystal transformation (Figure 2-9). This transformation was also unobservable after heating if single crystals of **SION-2** were submerged in anhydrous DMF. Using preformed **SION-2** crystals, the original solvent in the vial was replaced with a fresh mixture of DMF : H₂O 2.0 : 0.5 mL, and placed back into the oven for varying amounts of time at 120 °C (Figure 2-10). It was found that a reaction time of 24 hrs was required for the chemical transformation of **SION-2** to **SION-1** to take place, and therefore, the irreversible transformation only occurs when **SION-2** is submerged in a DMF/H₂O solvent mixture and heated.

2.4 The Partial Dissolution of SION-2

Due to the requirements for this chemical transformation to occur, we were experimentally limited on methods that could be used to study this phenomenon. *In-situ* ¹H NMR was chosen, as we could monitor the changes within the solvent to determine if any ligand or Tb were leached into the solution during this process. However, paramagnetism in NMR often leads to difficulty in interpreting spectra due to: *a.* signal broadening through nuclear relaxation from the electronic magnetic moment, and *b.* hyperfine chemical shifts that are dependent on the topological and geometrical locations of each proton with respect to their position from the paramagnetic center.¹⁷⁴ While challenging, structural and electronic information can be revealed through the understanding of these NMR spectra.¹⁷⁴

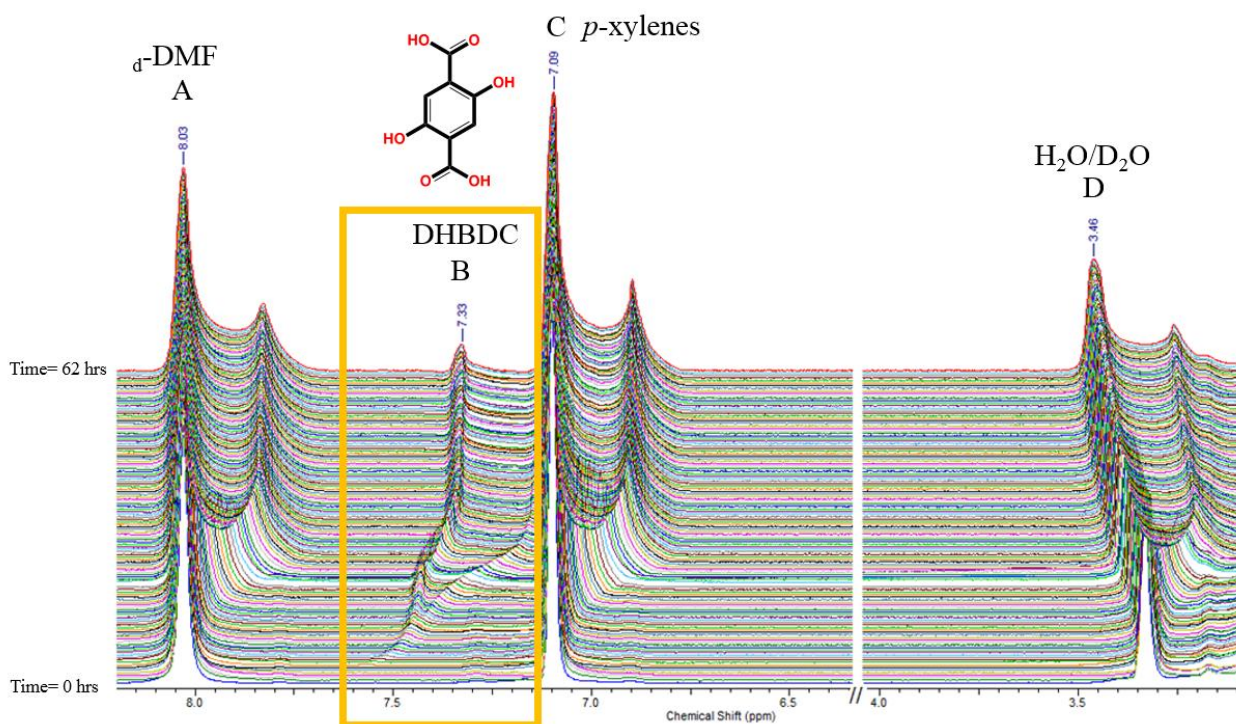


Figure 2-11: ^1H NMR of the transformation of SION-2 to SION-1. Here, 30-minute interval scans are shown. A: d -DMF, B: DHBDC evolution, C: p -xylene, D: $\text{D}_2\text{O}/\text{H}_2\text{O}$. Branched/split peaks correspond to the presence of small amounts of paramagnetic material leaching into the NMR solvent.

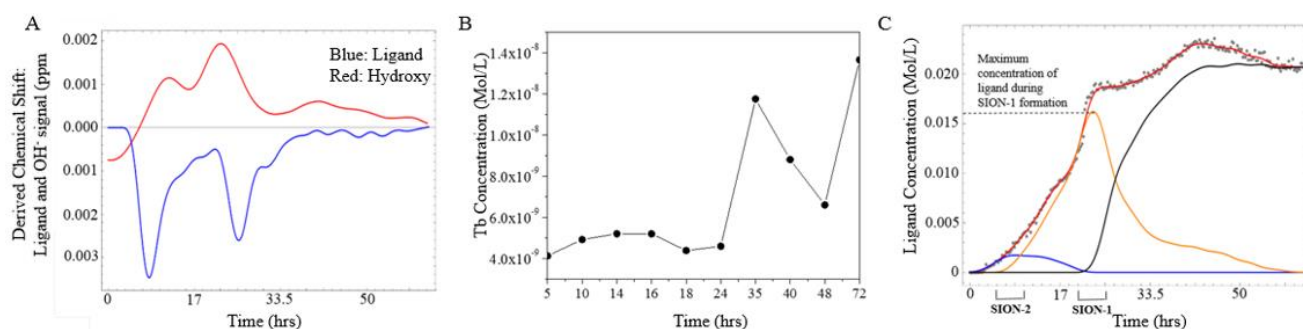


Figure 2-12: Analysis of ^1H NMR shifts and influence of Tb. a) Deviation of chemical shift in the ^1H NMR spectrum of both the aromatic DHBDC (blue) and hydroxy (red) signals, b) ICPMS indicating negligible amount of free $\text{Tb}(\text{III})$ is released in the liquor during the transformation, c) Aromatic ^1H DHBDC integral as a function of time. Grey dots: experimental integration determined using Mestre GSD algorithm; red line: is the interpolated function, blue and orange: DHBDC in close proximity to Tb^{III} , black: free DHBDC. Vertical axis gives the calculated ligand concentration in mol/L based on p -xylene integration.

In-situ ^1H NMR experiments were utilized to probe the formation pathway from **SION-2** to **SION-1** by analysing the composition of the d_4 -DMF/ D_2O solution during heating. Crystals of **SION-2** were immersed in d_4 -DMF/ D_2O in a sealed NMR tube and heated at 120°C for 62 hrs (Figure 2-11). After 4.25 hrs an appearance of a peak at 7.60 ppm was observed corresponding to the release of the ligand, followed by a gradual shift to 7.44 ppm (after 12.25 hrs), after which the peak appears to split and continues to shift until reaching 7.33 ppm where it stabilizes (after 38 hrs) for the remaining time. To understand if the cause of the peak splitting is due to the evolution of another DHBDC by-product or a change in the chemical environment of the aromatic H of DHBDC, variations in the chemical shift of both DHBDC and OH (from $\text{H}_2\text{O}/\text{D}_2\text{O}$) signals were compared. Figure 2-12a shows that the changes in both of these occur at approximately the same time, suggesting a simultaneous modification throughout the whole system. The release of ligand within the liquor indicates that **SION-2** is partially disassembled and therefore free Tb^{III} could be potentially released as the structure rearranges itself. ICP-MS was therefore utilized and confirms the presence of free Tb^{III} in extremely low quantities (less than 0.1 % of Tb^{III} after 72 hrs) (Figure 2-12b), and as Tb^{III} is paramagnetic, the split of all the peaks in the ^1H NMR spectrum is attributed to its release. Since the concentration is significantly lower than that of DHBDC, the formation of a molecular complex is ruled out, and instead, we observed a dynamic change from deprotonated DHBDC to protonated H_2DHBDC .

Analysis of the ^1H NMR spectra using the Mestre GSD algorithm reveals the signal of the aromatic proton on the ligand as a function of time, with the ligand concentration determined through the integration of an internal standard (*p*-xylene, Figure 2-12c). The use of ~12 mg of **SION-2** consists of 0.043 mol/L (2.7×10^{-5} mols, 0.625 mL of solvent used) of DHBDC ligand. Combining the *in-situ* ^1H NMR for the analysis of the solution media with the PXRD patterns, a number of observations have been recorded: a. **SION-2** is still present after 5-10 hours of heating but there are traces of ligand leaching into the liquor, b. between 10-20 hours there is a mixture of **SION-1** and **SION-2** and after 24 hours, there is 0.016 mol/L (1.0×10^{-5} mols) of ligand released corresponding to 37% release of the total ligand; c. **SION-1** is formed after a duration of 24 hours, and e. after 24 hours, the ligand released into the solution adopts a new form (protonated H_2DHBDC). A release of 37% ligand, represents the loss of approximately 1/3 of the ligands in the M_2L_3 (**SION-2**) general formula resulting in M_2L_2 (**SION-1**). Therefore, **SION-2** is indeed acting as an intermediate phase for the generation of **SION-1** and the transformation from **SION-2** to **SION-1** occurs through a

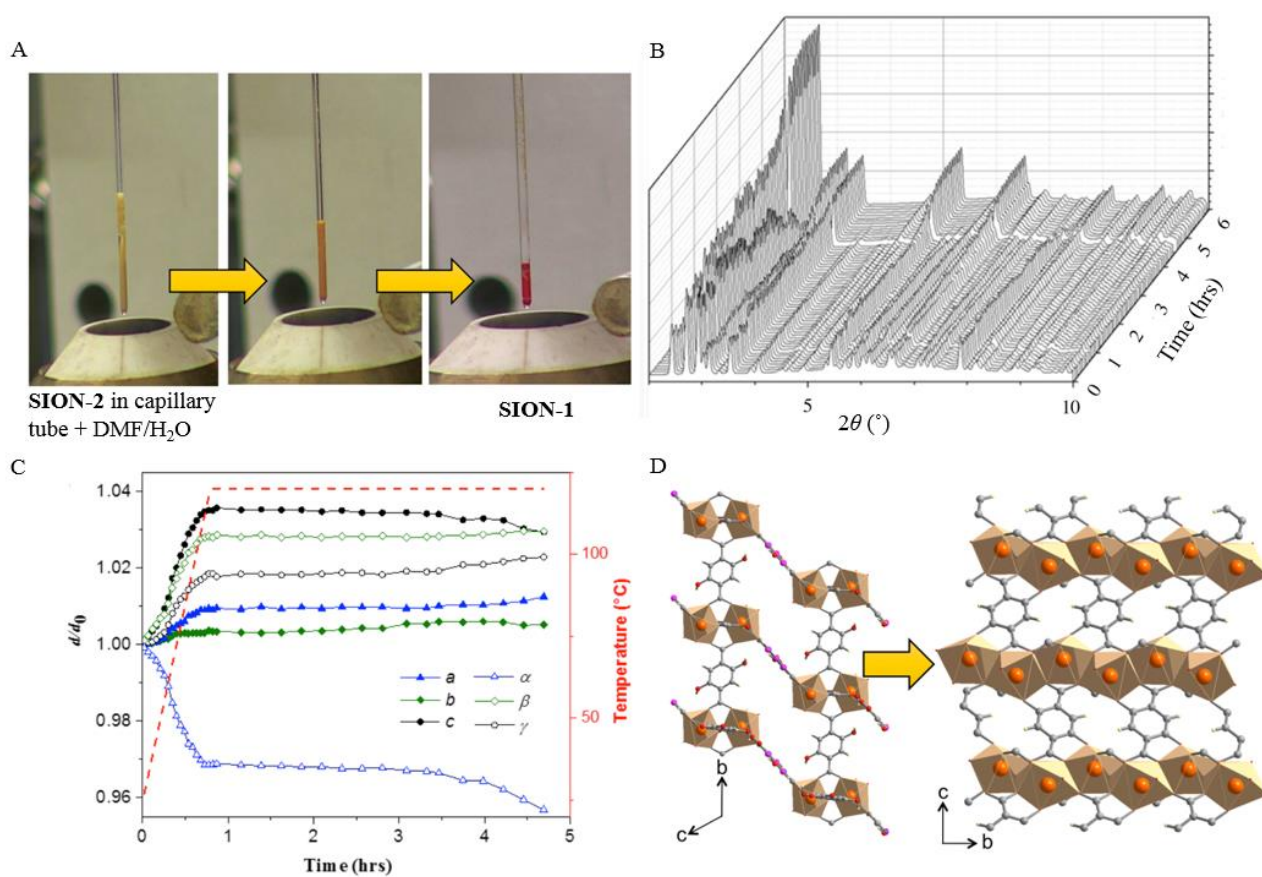


Figure 2-13: VT-PXRD and lattice parameter analysis of the transformation. a) SION-2 crystalline powder was immersed in DMF : H₂O and packed in a quartz capillary. The reaction was heated at 120 °C for over a period of 6 hrs and as can be seen, the golden colour of SION-2 changed to red upon heating, indicating that SION-1 is formed, b) PXRD patterns collected throughout the reaction evolution. SION-2 could be fully transformed to SION-1 within 6 hours, c) Temperature dependent evolution of lattice parameters of SION-2 as a function of time. After 4.7 hours no SION-2 lattice parameters cannot be longer extracted from the PXRD data, d) General view of the SION-2 to SION-1 transformation emphasising the removal of one η_2 -chelating DHBDC ligand (shown in purple) and the re-organisation of Tb₂ clusters (shown as pairs of orange spheres along with coordination polyhedra) into Tb-O chains.

partial dissolution pathway.

The chemical transformation from SION-2 to SION-1 was further monitored with an *in-situ* powder X-ray diffraction study. SION-2 in the form of crystalline powder was immersed in a mixture of DMF :H₂O, packed in a quartz capillary and heated at 2 °C min⁻¹ to 120 °C, then held at 120 °C for 6 hours, with collection time of 60 secs per PXRD pattern (Figure 2-13a-b). Fitting the

PXRD data according to the Le Bail method provided us with insights on the evolution of unit cell parameters as a function of temperature and time (Figure 2-13c). Anisotropic thermal expansion upon heating to 120 °C is followed by the actual time-dependent transformation. As can be seen in Figure 2-13c, the largest magnitude of thermal expansion occurs along the *c*-axis, which suggests a structural instability along the [001] direction of **SION-2** related to the presence of Tb₂ dimers and η^2 -chelating DHBDC ligands (as summarised in Figure 5d, upon the chemical transformation of **SION-2** to **SION-1**, discrete Tb₂ clusters reorganise into infinite Tb–O chains, and one out of three DHBDC ligands is removed). Once the temperature of 120 °C is attained, the unit-cell parameters of **SION-2** are stabilised (Figure 2-13c), however, after 1.6 hours, we have observed new Bragg reflections evolving which can be indexed with the unit cell of **SION-1**. Subsequently, as the **SION-1** Bragg reflections gain in intensity whereas the diffraction from **SION-2** becomes increasingly weaker and completely disappears after 4.7 hours. There are no additional peaks or amorphous phases present that would indicate the deconstruction of **SION-2** and between 1.6 to 4.7 hours we have observed that the X-ray diffraction patterns consist both phases **SION-1** and **SION-2**. Therefore, the transformation from **SION-2** to **SION-1** occurs without losing crystallinity, and can be followed by the colour change of the samples from gold to red (Figure 2-13a).

2.5 Structural Transformation of SION-2 to SION-1.

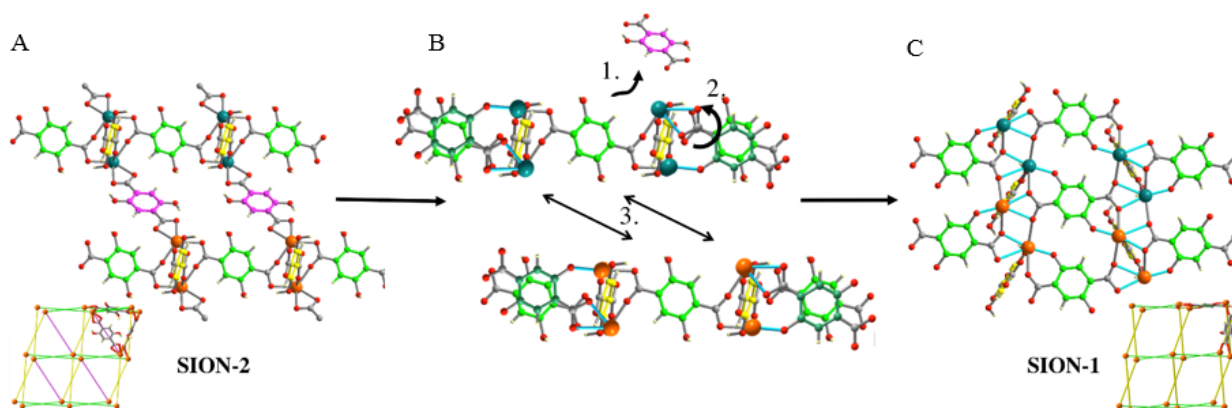


Figure 2-14: Proposed transformation mechanism. a-c) The chemical transformation from **SION-2** (a) to **SION-1** (c) through **b1**, partial dissolution of SION-2 and release of the η^2 -chelating DHBDC ligand (purple), **b2**, rotation of the green DHBDC, and **b3**, shift of the structure leading to the formation of 1-dimensional Tb–O chains upon coordination of the oxido O-atom of DOBDC to the neighboring Tb^{III}. The transformation can be also rationalized by their network topologies of *xah* of **SION-2** (a, bottom) and *lvt* of **SION-1** (c, bottom).

Combining the information gained from the *in-situ* studies with the structural topologies of **SION-2** to **SION-1**, the formation pathway of **SION-1** can be proposed (Figure 2-14a-c). The projection of the topologies of **SION-2** along [001] and **SION-1** along [010] shows significant similarities. It is apparent that the *lvt* network can be recovered from the *xah* by simply eliminating the purple edge, which corresponds to the η^2 -chelating DHBDC ligand. Figure 2-14a shows a layer of **SION-2** projected along [010] where the purple DHBDC ligand corresponds to the purple line in the *xah* network topology. From this structure, **SION-1** can be formed (Figure 2-14c) through the completion of the following steps presented in Figure 2-14b. Firstly, the purple η^2 -chelating DHBDC ligand is eliminated, followed by a 180° rotation of the green DHBDC ligands and slight tilt along the [100] direction, which can be achieved by severing one of the Tb-O bonds and, following rotation, forming two new Tb-O bonds, including one with the oxido group of DOBDC. Finally, the isolated Tb₂-clusters, represented in separate layers as dark cyan and orange balls (Figure 2-14a-c), join together to form the 1-dimensional Tb-O chains present in **SION-1**. This is achieved by forming new Tb-O bonds with nearby carboxylate O- and oxido O-atoms of the green DOBDC ligands and central (coloured grey and red) ligands, respectively. DFT calculations support this mechanistic hypothesis as the purple η^2 -chelating DHBDC in **SION-2** has a bond energy (-41.347 kcal/mol) which is smaller than the $\eta^1:\eta^1$ bridging DHBDC ligands (-59.888 and -65.745 kcal/mol) in **SION-2**, highlighting that their lability is the initial driving force for the transition from **SION-2** to **SION-1**.

2.6 Optical properties of the Ln-SION-2 and Ln-SION-1 series.

Lanthanide-based MOFs (Ln^{III}-MOFs) have drawn increasing interest due to the intrinsic nature of Ln^{III} ions, which exhibit relatively large magnetic moments, strong spin-orbit coupling and high coordination numbers.^{116, 175, 176} Most Ln-MOFs can be obtained isostructurally throughout the Ln^{III} series, allowing for a systematic study of their sensing and magnetic properties.^{177, 170} Despite their potential in sensing applications, the electronic properties of Ln^{III}-MOFs have been rarely studied due to the fact that Ln^{III} ions behave as isolated free ions as the 4f orbitals do not contribute to bonding.¹⁷⁵ Therefore, there is a limited orbital overlap and charge interaction with their local environment.¹⁷⁸ Additionally, the hard-acid nature of Ln^{III} ions requires the use of highly electronegative ligands such as carboxylates, which often localize their unpaired electrons.¹⁷⁹ However, by manipulating the Ln^{III}-ligand interactions in Ln^{III}-MOFs, their overall electronic structure can be tuned for specific applications including those relying on photoabsorption and conductivity.^{89, 180}

In MOFs, after photoabsorption, the electrons are excited from the Highest Occupied Crystalline Orbitals (HOCOs) to the Lowest Unoccupied Crystalline Orbitals (LUCOs); or in band-structure terms, from the valence band (VB) to the conduction band (CB). These frontier orbitals can consist of either metal or ligand orbitals, or a mixture of both, thereby creating a hybrid metal/ligand orbital.^{181, 182}

Developing strategies to tune the electronic properties of MOFs can aid in the discovery of materials that can have potential in applications such as photocatalytic hydrogen generation, solar cells, and capacitors.¹⁸³⁻¹⁸⁵ In order to effectively accomplish this, an interplay between experimental and theoretical techniques is required for a total understanding of the materials properties.^{183, 186-190} Following the structural investigation and transformation of **SION-2** to **SION-1**, we reported a systematic study of two isostructural families of **Ln^{III}-SION-1** and **Ln^{III}-SION-2** families.¹⁹¹ Both families display different colors, with **Ln^{III}-SION-2** possessing a gold color, while **Ln^{III}-SION-1** is red, thus having different absorption properties. The phase purity of the isostructural **Ln^{III}-SION-1** (Ln^{III}: Ce, Nd, Eu, Gd, Tb, Dy, Ho, Er, Yb and Lu) and **Ln^{III}-SION-2** (Ln^{III}: Ce, Nd, Eu, Gd, Tb and Yb) series was confirmed by powder X-ray diffraction (PXRD) in respect to the **Tb^{III}-SION-1** and **Tb^{III}-SION-2** (Figure 2-15-16).⁸⁹

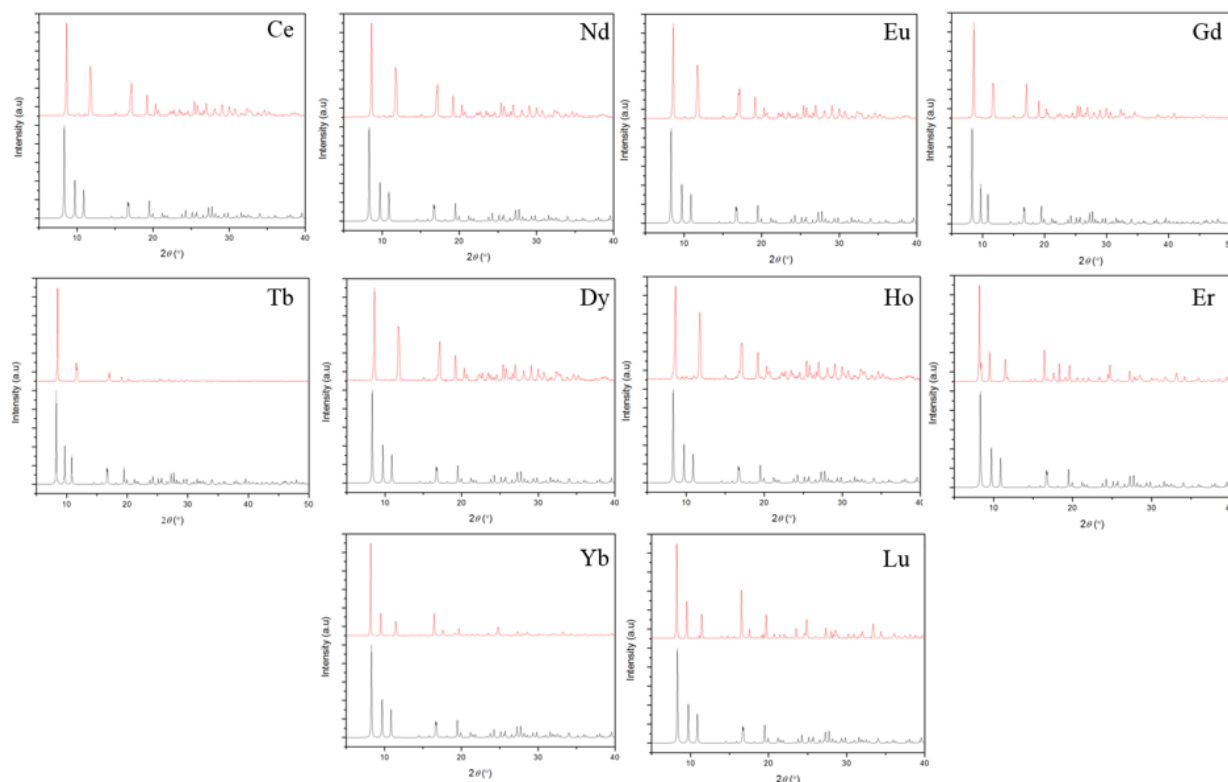


Figure 2-15: PXRD of Ln^{III}-SION-1. Color scheme: black, theory; red, experimental. Please note these patterns can be seen in a higher resolution in the appendix.

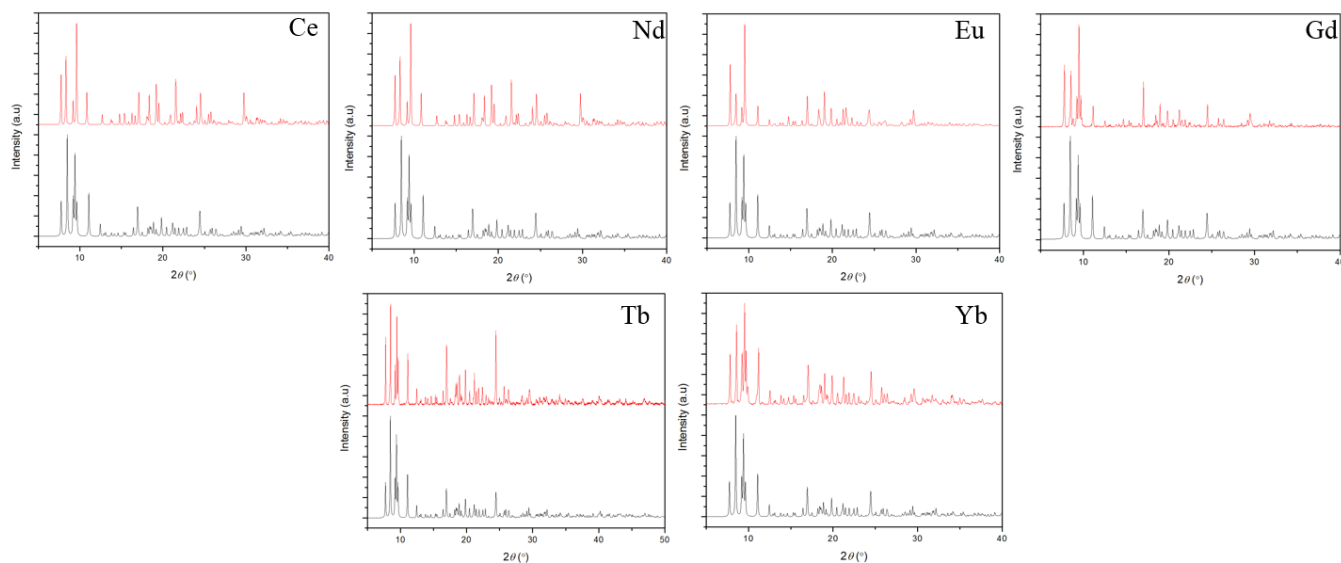


Figure 2-16: PXRD of Ln^{III} -SION-2. Color scheme: black, theory; red, experimental Please note these patterns can be seen in a higher resolution in the appendix.

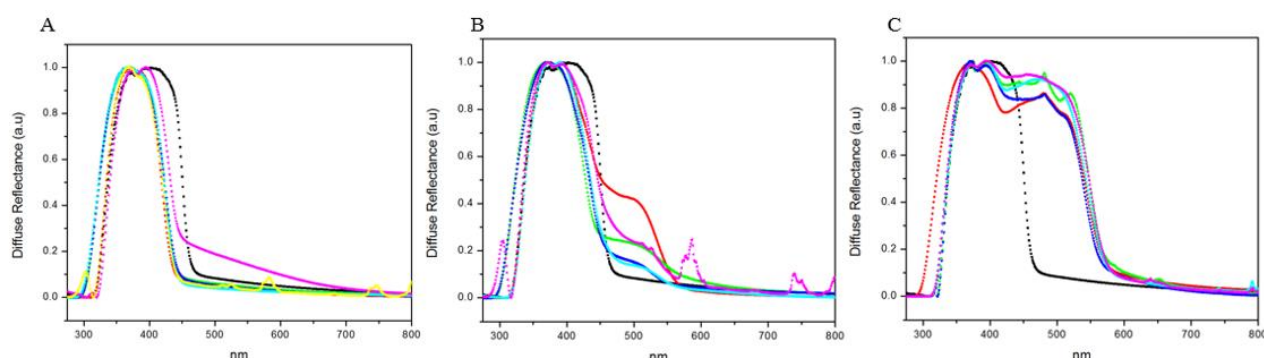


Figure 2-17: UV/Vis spectra the Ln^{III} -SION-1 and Ln^{III} -SION-2 families. a) Ln^{III} -SION-2, color scheme: black, ligand; light blue, Ce; yellow, Nd; blue, Eu; pink, Gd; red, Tb; green, Yb. b). Ln^{III} -SION-1, color scheme: black, ligand; blue, Ce; pink, Nd; green, Eu; light blue, Gd; red, Tb. and c) Ln^{III} -SION-1, color scheme: black, ligand; light blue, Dy; pink, Ho; green Er; red, Yb; dark blue, Lu.

Following PXRD characterization, the difference in the optical properties between H_2DHBDC , Ln^{III} -SION-1 and Ln^{III} -SION-2 was investigated by UV/vis spectroscopy (Figure 2-17). The free H_2DHBDC displays a strong absorption band in the UV to visible spectral region up to 470 nm (2.76 eV). Figure 2-17a shows that the diffuse reflectance spectrum of Ln^{III} -SION-2 displays a comparable absorption band with that of the free H_2DHBDC ligand. Changing the Ln^{III} within the Ln^{III} -SION-2 family affords no significant effect on its absorption properties. For Ln^{III} -SION-1, an additional absorption feature beginning at ~ 580 nm (~ 2.14 eV) was observed in addition to the ab-

sorption band attributed to the H₂DHBDC, indicating an interaction between the Ln^{III} and the ligand (Figure 2-17b-c). In addition, we observed that by changing the Ln^{III} ions within the **Ln^{III}-SION-1** structure – from Ce^{III} to Lu^{III}, the intensity of this feature increases.

To explore the link between the absorption properties and electronic structure of **Ln^{III}-SION-1** and **Ln^{III}-SION-2**, we performed electronic structure calculations using Quantum Espresso Suite.¹⁹² To optimize the geometry, the PBEsol functional was used, which is known to give a good description of the structure of MOFs.¹⁹³ To describe the energy gap accurately, a hybrid (Gau-PBE) exchange and correlation functional was employed. These calculations show that the HOCOs and LUCOs in **Ln^{III}-SION-2** correspond to the π and π^* orbitals of the DHBDC ligand, respectively. There is no noticeable overlap between the Ln(5d) and the ligand(π^*) orbitals as the arrangement of ligands and binuclear Ln₂-clusters prevent the physical orbital mixing to occur. The calculated projected density of states (pDOS) show that the LUCOs have no contributions from the unoccupied Ln(5d) orbitals, revealing that the absorption spectra of **Ln^{III}-SION-2** is due to an intraligand $\pi \rightarrow \pi^*$ transition.

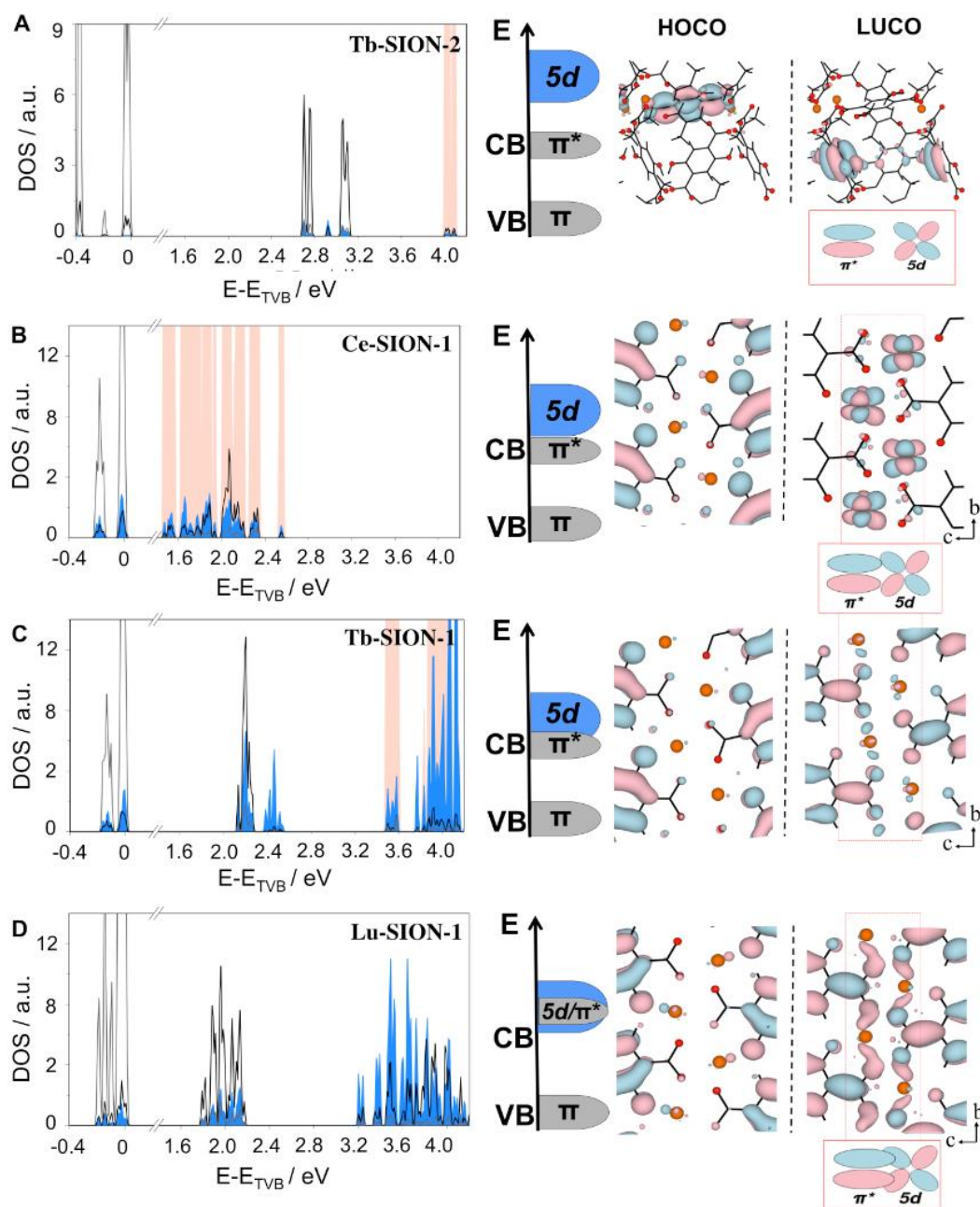


Figure 2-18: Projected density of states (pDOS) and crystalline orbitals. a) **Tb^{III}-SION-2**. Here, the HOCO and LUCO of **Tb^{III}-SION-2**, which have respectively π and π^* character, are centered on different DHBDC ligands, lying on crystal planes perpendicular to each other, b) **Ce^{III}-SION-1**, c) **Tb^{III}-SION-1**, and d) **Lu^{III}-SION-1**. The behavior of the **Ln^{III}-SION-1** differs; the pDOS of the LUCOs show a mixed Ln(5d)/DOBDC(π^*) character, that increases while moving along the lanthanide series (Ce→Lu). Color scheme for pDOS plots: gray, carboxylate O 2p; black, oxido O 2p orbitals; beige, Ln 4f orbitals; blue, Ln 5d orbitals. Color scheme for the orbital plots: red, O; orange, Tb; black, C. The representation of each electronic structure (HOCO/LUCO; molecular orbital overlap) is shown on the right.

While both DHBDC and DOBDC ligands are present within the structure of **Ln^{III}-SION-1**, the frontier orbitals are composed with those of DOBDC and Ln^{III} ions, and there is no contribution from the orbitals of DHBDC (Figure 2-18b and d). **Ce^{III}-SION-1** and **Lu^{III}-SION-1** were used as representatives of the early and late Ln^{III} ions, and their electronic structures were studied. The calculated electronic structure of **Ce^{III}-SION-1** shows that the HOCOs correspond to the π orbitals of DOBDC ligand, while the LUCOs have a predominantly 4f character (Figure 2-18b) which are similar in energy to the 5d- π^* orbitals as shown by the composition of the pDOS.¹²⁰ From one side, the Ln(4f) orbital spatial distribution is contracted and so does not mix with the π^* orbitals of the ligand; while on the other side, the Ln(5d) orbital spatial distribution is diffuse, allowing for some mixing with the π^* orbitals, giving rise to the observed transition at ~ 580 nm ($\pi \rightarrow \pi^*/5d$) in the diffuse reflectance of **Ce^{III}-SION-1**. Due to the filling and weaker shielding of the inner 4f orbitals through the Ln^{III} ion series, their ionic radii decrease and therefore the bond length between the Ln^{III} and oxido O atom of DOBDC shortens (this is confirmed by DFT-calculations). This has the effect of extending the overlap of the π^* and 5d orbitals within the 1-dimensional chains, accounting for the observed increase of the absorption feature intensity seen with **Tb^{III}-SION-1** and more dramatically with **Lu^{III}-SION-1**.

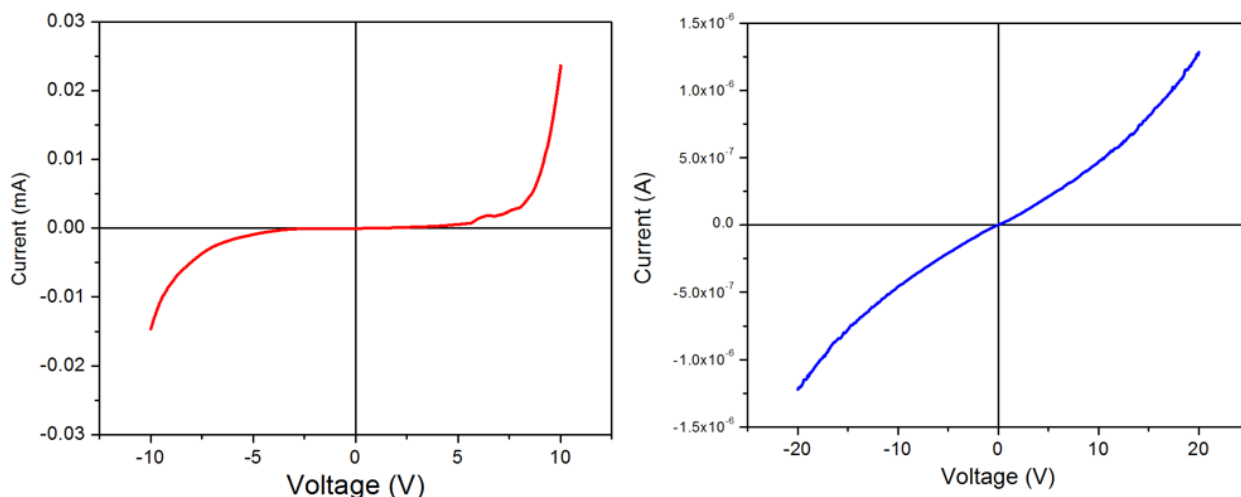


Figure 2-19: Current-Voltage curves. Current-Voltage (I-V) curves measured from of device using ITO/PEDOT.PSS/Active Layer/InGa in the dark: left, **Ce-SION-1**; right, **Yb-SION-1**.

The orbital overlap dictates that the LUCOs are dispersed over an energy range, and therefore it can be considered as a conduction band. Conduction band dispersion calculations show values of 0.04, 0.25 and 0.18 eV for **Ce^{III}-**, **Yb^{III}-** and **Lu^{III}-SION-1**, respectively. To examine this, current-

voltage (I - V) measurements were performed with the help of Prof. Kevin Sivula for **Ce^{III}-** and **Yb^{III}-SION-1** under inert and dark conditions (Figure 2-19). The observed non-linear I - V curves indicate a dielectric behaviour of both materials. Non-null electron mobility in **Ce^{III}-** and **Yb^{III}-SION-1** has been shown indirectly through photocatalytic H₂ generation experiments.^[13] **Ce^{III}-SION-1** produced no H₂ and this is thought to be due to the inefficient electron mobility and migration to the crystal surface and transportation to the co-catalyst responsible to reduce water into H₂. This is in contrast with **Yb-SION-1**, which has the highest dispersion band in the series and produces H₂ (detectable levels of H₂, with a measureable peak on the GC).

In summary, based on the UV/vis absorption spectra, degree of orbital overlap and pDOS seen in **Ln^{III}-SION-1** and **Ln^{III}-SION-2**, three conclusions can be drawn: *i.* **Ln^{III}-SION-2**: the orbitals of Ln^{III} and DHBDC do not overlap due to their large energy difference, *ii.* **Ce^{III}-to-Gd^{III}-SION-1**: a partial orbital overlap is observed and their LUCOs have a predominantly Ln(5d)/ligand(π^*) character, and *iii.* **Tb^{III}-to-Lu^{III}-SION-1**: the Ln(5d) and ligand(π^*) orbitals can be mixed energetically and match geometrically. Overall, the LUCOs in **Ln^{III}-SION-1** are dispersed and thus these materials exhibit dielectric behavior and non-null electron mobility as determined through the non-linear I - V curves and photocatalytic H₂ generation experiments, respectively.

2.7 Conclusions

In conclusion, we have observed through multiple analysis that the chemical transformation from the metastable kinetic phase **SION-2** to the stable thermodynamic phase **SION-1** occurs through the partial dissolution of **SION-2**. This is triggered by the loss of the η^2 chelating DHBDC ligand, followed by internal structural changes resulting in the formation of **SION-1**. To the best of our knowledge, this is the first example of a lanthanide based MOF that is chemically transformed in a solvent mixture, which does not rely on the removal of solvent coordinated to the metal, commonplace for single-crystal to single-crystal transformations occurring under dry conditions.^{194, 195} Understanding how MOFs are formed can promote greater control on the assembly of the metal ions or clusters with the ligands and can lead in the identification of stable materials with improved properties compared to the kinetically favoured MOF materials.

This work also shows that the formation of binuclear Ln clusters in Ln-MOFs can permit long-range electronic communication and charge mobility. Structurally designing a MOF with π - π stacking, donor-acceptor pairings, and 1-dimensional chains with short metal-to-metal distances are a few strategies that can be used achieve these MOFs with these desired electrical properties. Overall, controlling the metal-ligand frontier orbital overlap and energy matching between the Ln(5d) and

ligand(π^*) orbitals has been proven as a facile method to develop new Ln-MOFs with desired electronic structures. Furthermore, work demonstrates that by harnessing both experiments and computations, the structure-to-electronic property relationship can be elucidated and can lead in the discovery of new dielectric materials that can be used in electronic, optoelectronic and photocatalysis applications.

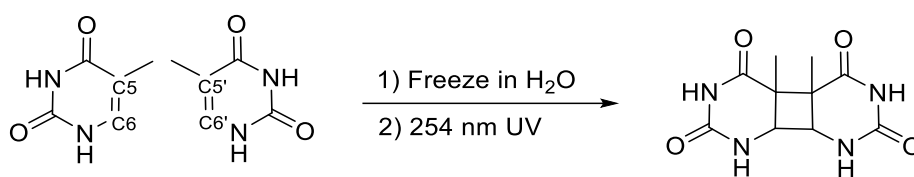
Chapter 3 SION-19: Nucleobase Pairing and Photodimerization in a MOF Nanoreactor

3.1 Introduction

The structural versatility, permanent porosity, tuneable pore surfaces and periodic nature of metal-organic frameworks (MOFs) provide a unique opportunity to study their potential in applications ranging from gas storage and separation, to UV-induced coupling, catalysis and sensing.^{77, 196-202} Biologically derived MOFs (bio-MOFs) based on ligands such as amino acids, nucleobases and oligosaccharides have shown a great potential in many research areas as they can be used as models for bio-mimicking and catalysis.^{57, 58} There is a significant interest in observing biological phenomena in porous bio-MOFs, as we can gain insights into their response upon the inclusion of guest molecules and how guest molecules behave within these confined spaces.^{1, 50, 57, 58, 203-207} These insights can ultimately lead into the generation of novel bio-MOFs with tuneable pore functionalization, allowing one to target specific chemical reactions and isolate desired products.^{59, 208-210} This has the potential to open up a new field of research related to drug design, discovery, delivery, and catalysis.^{49, 211}

Exploiting functional pore surface in MOFs has recently been utilized in carbohydrate separation and labelling and photochemical transformations.^{199, 212, 213} Intrigued by the pore surface interactions with guest molecules, and the use of functional groups as structure-directing agents, herein we investigated the Watson-Crick (W-C) face of adenine (Ade) within a new MOF (hereafter called as **SION-19**) for nucleobase pairing with thymine (Thy), and solid-state photodimerization of Thy to Thy<>Thy, a molecule that is related to skin cancers such as melanoma.²¹⁴ For this concept, two prerequisites govern both the ability of the MOF to act as a nanoreactor, and the ability of Thy to undergo dimerization.

It should be noted that our publication "Anderson, L. Samantha; Boyd, G. Peter; Gładysiak, Andrzej; Nguyen, N. Tu; Palgrave, G. Robert; Kubicki, Dominik; Emsley, Lyndon; Bradshaw, Darren; Rosseinsky, J. Matthew, Berend; Stylianou, C. Kyriakos. Nucleobase Pairing and Photodimerization in a Biologically Derived Metal-Organic Framework Nanoreactor, *Nat. Commun.* **2019**, 10, 1612" has been reused for this thesis chapter.



Scheme 3-1: Method for the synthesis of cyclobutane Thy photodimers using UV light and water.

First, the strength of Ade-Thy nucleobase pairing within the pores of the MOF is determined by its pore shape and size. Thy not only needs to be able to fit within the pore, but an optimal distance of $< 3 \text{ \AA}$ between Ade-Thy is required to allow for the formation of H-bonds via the W-C face of Ade.²¹⁵ Here, the structure directing ability of Ade within **SION-19** can ‘lock’ Thy into a position close enough to another Thy for photodimerization to occur. Second, for successful dimerization, both the Woodward-Hoffmann and Schmidt rules would have to be fulfilled.²¹⁶⁻²¹⁸ This implies that the C5-C6 and C5'-C6' (Scheme 3-1) double bonds of Thy (according to its conventional atom numbering scheme) have to be $< 4.2 \text{ \AA}$ apart (centre-to-centre)²¹⁸ and the molecular orbital symmetry has to be conserved.²¹⁷ Ultimately, an overall balance between these requirements is needed, as pores too large or of improper shape can disfavour Ade-Thy base-pair interaction, while incorrect packing of Thy within the pores can affect their ability to dimerize due to poor orientation of the C5-C6 and C5'-C6' double bonds.

MOFs with unobstructed W-C faces of Ade reported in the literature are scarce and the generation of materials with a precise pore aperture for Thy uptake has proven to be challenging.^{52, 59, 81} In addition, the dimerization of Thy and formation of Thy \rightleftharpoons Thy has only been achieved either in liquid systems such as freezing water, in the presence of sensitizers such as acetone or when Thy is ordered in DNA struts.²¹⁹⁻²²¹ Inspired by this challenge, and in order to highlight the structural tunability of MOFs, we demonstrate for the first time, that Ade-Thy binding can be achieved within the pores of **SION-19**, and Thy can be dimerized to Thy \rightleftharpoons Thy in solid state at 40-45 % Thy-loadings.

3.2 Crystal Structure Determination and Bulk Characterization of SION-19

The reaction of $\text{Zn}(\text{NO}_3)_2 \cdot 6(\text{H}_2\text{O})$, 1,3,6,8-tetrakis(p-benzoic acid) pyrene (H_4TBAPy)^{92, 222} and Ade in a solvent mixture of DMF/ H_2O / HNO_3 at 120°C for 72 hrs leads in the generation of yellow truncated rhombic bipyramid crystals. Single-crystal X-ray diffraction (SCXRD) reveals that anionic **SION-19**, with formula of $[\text{Zn}_{1.5}\text{O}_{0.25}(\text{Ade})(\text{TBAPy})_{0.5}](\text{NH}_2\text{Me}_2)_{0.5} \cdot (\text{DMF})_{0.6} \cdot (\text{H}_2\text{O})_{4.0}$, crystallizes in an ortho-rhombic unit cell with the *Ccce* space-group symmetry and cell parameters of $a = 10.7402(3) \text{ \AA}$, $b = 30.6236(7) \text{ \AA}$, $c = 42.6282(11) \text{ \AA}$, $\alpha = \beta = \gamma = 90^\circ$ with $V = 14020.6(6) \text{ \AA}^3$. Within **SION-19**, octahedral

cages are constructed by four Ade ligands and six Zn^{II} tetrahedral ions, four of which are in the equatorial plane ($\text{Zn}^{\text{II}}_{\text{eq}}$) and two at the apical positions ($\text{Zn}^{\text{II}}_{\text{ap}}$) (Figure 3-1a). The $\text{Zn}^{\text{II}}_{\text{eq}}$ link the cages by Zn_4O clusters forming the adeninate columnar building units running along the a -axis. The tetrahedral geometry of $\text{Zn}^{\text{II}}_{\text{eq}}$ is provided by the N3 and N9 atoms from Ade, one $\mu_4\text{-O}$ bridge and one carboxylate O from a TBAPy ligand. For $\text{Zn}^{\text{II}}_{\text{ap}}$, the tetrahedral coordination environment is owed to two N7 atoms from two adjacent Ade ligands, as well as two monodentate carboxylate O atoms from two consecutive TBAPy ligands (Figure 3-1b). Within **SION-19**, Ade acts as a deprotonated and bridging tridentate ligand, while the fully deprotonated and disordered TBAPy ligand coordinates in a monodentate fashion from each carboxylate. The TBAPy ligands, inclined with respect to the a -axis, link the Zn^{II} -based columnar units to yield a structure expanding in three dimensions. However, due to the geometrical features of these building units and TBAPy, infinite channels endowed with two markedly different chemical character are formed along the a -axis. These pores are classified as the acid-pore and the base-pore (Figure 3-1c-d). The acid-pore in which the free carboxylate O atoms from the TBAPy ligand are pointing in, has a pore dimension of $7.9 \times 4.9 \text{ \AA}$ (including van der Waals radii), while the base-pore contains the unobstructed W-C faces of Ade and its dimensions are $5.4 \times 6.9 \text{ \AA}$ (Figure 3-1e). Four Ade ligands attached to the same Zn_4O cluster point to four different channels, while two Ade linked to the same $\text{Zn}^{\text{II}}_{\text{ap}}$ ion are arranged in the antiparallel fashion; therefore, even though all Ade are grouped relatively close to each other within the crystal structure, their spatial orientation allows for all of their W-C faces to be exposed to the channels. These pores, in turn, are occupied by disordered guest solvent molecules and cations that show no indication of preferred location. The accessible volume of **SION-19** is 31.3%, and combining the accessible volume with the density of the static structure results in a pore volume of $0.287 \text{ cm}^3/\text{g}$. Topological analysis of **SION-19** using the TOPOS4.0 software package reveal a new 4,4,8-c net with the point symbol $\{4^2 \cdot 6^4\}4 \cdot 4^4 \cdot 6^{14} \cdot 8^{10}\}$.²²³ This net has been registered in the Topos Topological Database (TTD) collection as *kcsI* (Figure 3-2).

Powder X-ray diffraction (PXRD), elemental analysis (EA), thermogravimetric analysis (TGA) (Figure 3-3), and solid state ^{13}C CP/MAS NMR confirmed the purity and the structural stability of **SION-19**. Le Bail fit of the PXRD pattern of **SION-19** collected at 298 K gives refined cell parameters of $a = 10.965(7) \text{ \AA}$, $b = 30.811(2) \text{ \AA}$, $c = 42.261(6) \text{ \AA}$, $\alpha = \beta = \gamma = 90^\circ$, $V = 14277.5 \text{ \AA}^3$ (Cc space-group symmetry, and fit indicators: $R_{\text{wp}} = 4.7 \%$ and $\chi^2 = 1.9$) which are in good agreement with the cell parameters obtained by SCXRD (Figure 3-3a and 3c).

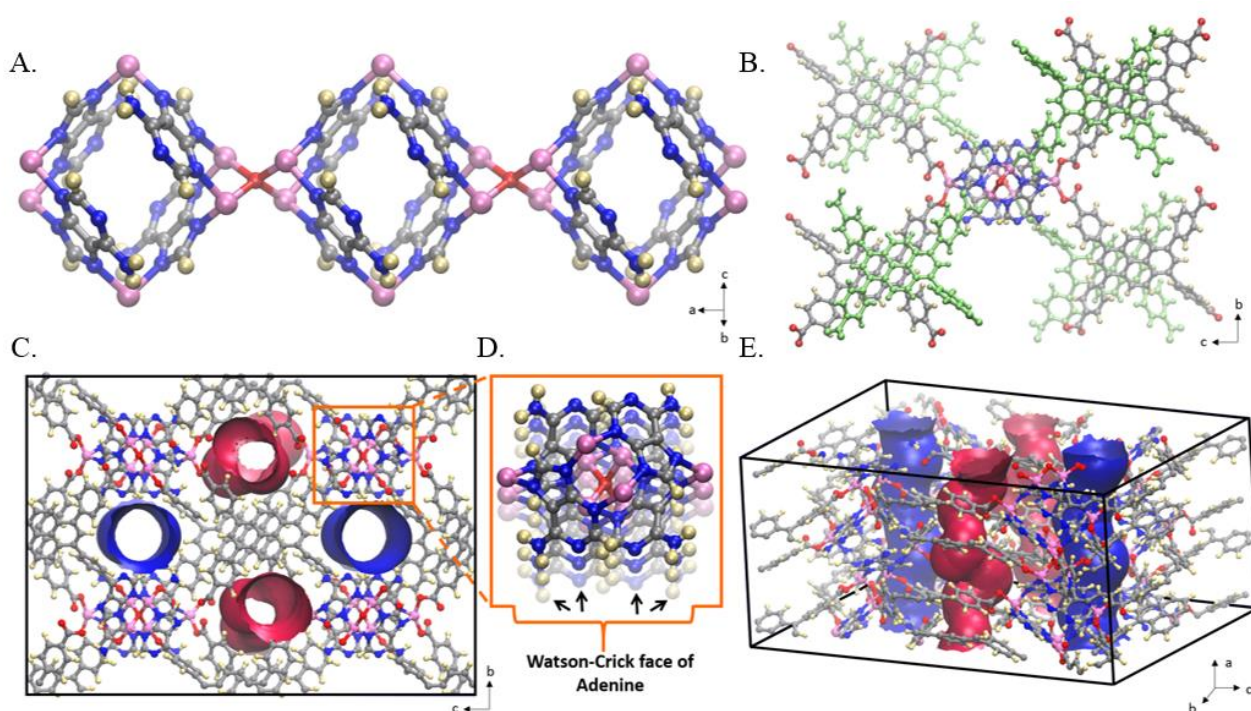


Figure 3-1: Structural representation of SION-19. **a)** A Zn^{II}(adeninate) octahedron cage is coordinated to six Zn^{II} ions, four at the corners of the equatorial plane (Zn^{II}_{eq}), and two at the apical positions (Zn^{II}_{ap}). The Zn^{II}(adeninate) cages are linked to each other via the Zn^{II}_{eq} to form 1-dimensional columnar building blocks, **b)** The Zn^{II}(adeninate) columnar building blocks are linked to each other via fully deprotonated TBAPy ligands – grey TBAPy is bound to Zn^{II}_{ap} whereas the lime green is bound to Zn^{II}_{eq}, **c-d)** Connolly surface representation of **SION-19** viewed along the *a*-axis, revealing that the coordination of TBAPy ligands to the Zn^{II}(adeninate) columns leads in the formation a 3-dimensional structure possessing two distinct types of 1-dimensional pores: the base-pore (blue) and the acid-pore (red). Highlighted in **d)** are the Watson-Crick faces of Ade which point into the base pore and **e)** Connolly surface representation of **SION-19** in a 3-dimensional view. Atom color code: pink, Zn; red, O; blue, N; grey, C; light yellow, H.

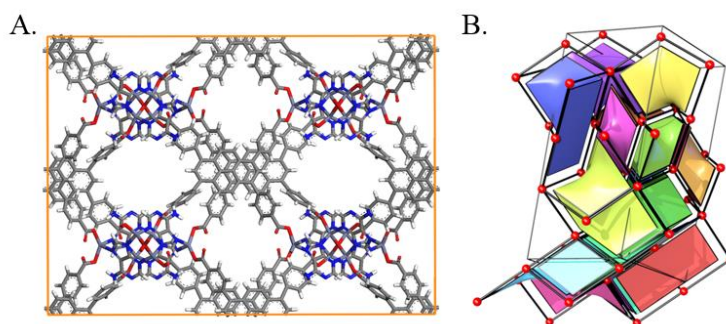


Figure 3-2: Underlying net of SION-19. Reducing the **SION-19** structure **a)** to the underlying ‘kcs1’ net, **b)** TOPOS 4.0 was used with the cluster simplification method to obtain the net in **b).**²²³

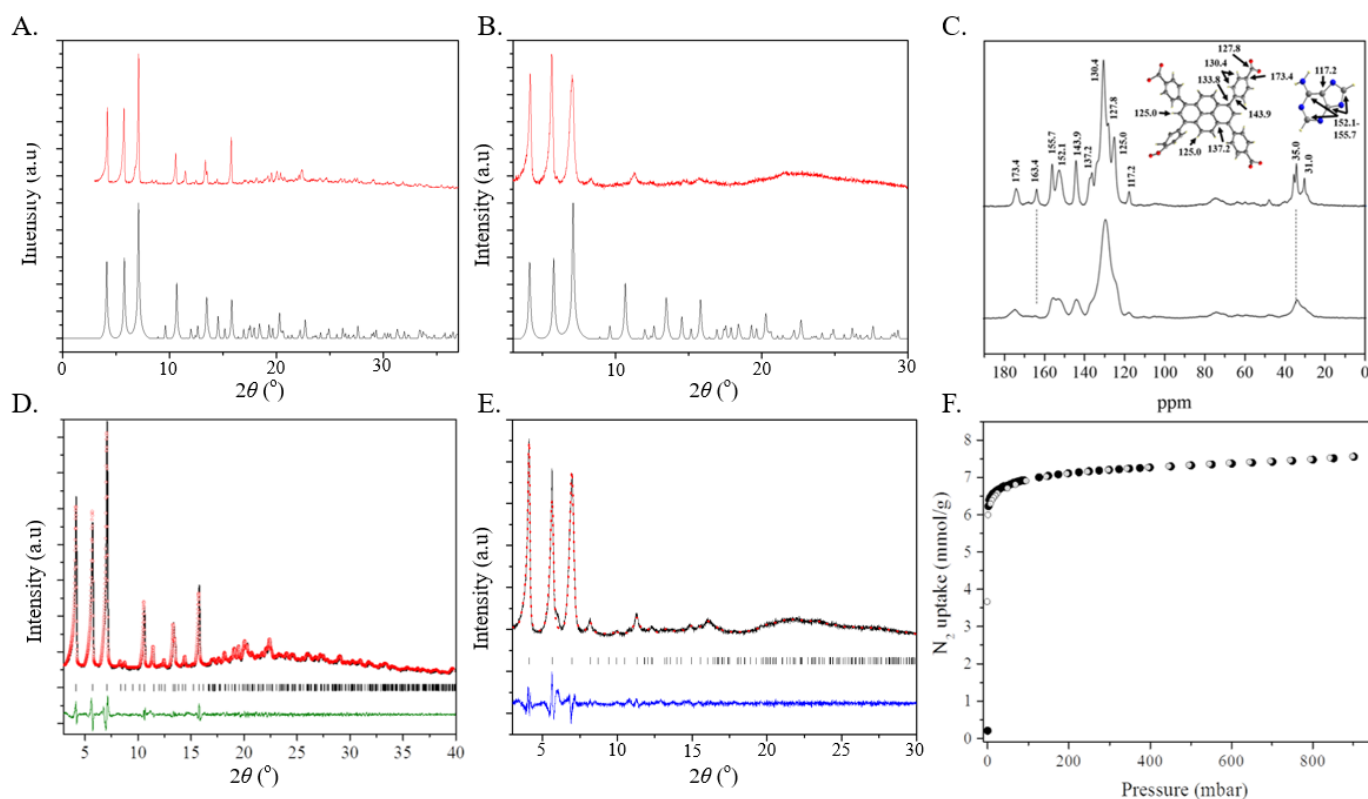


Figure 3-3: PXRD, MAS NMR, and N_2 isotherm of SION-19 and SION-19'. **a-b)** PXRD patterns for **SION-19** (a) and **SION-19'** (b). Color scheme: red, theory; black, experimental. **c)** Solid-state ^{13}C CP MAS NMR spectra of (top) **SION-19** and (bottom) **SION-19'** collected at 298 K. The assignment peaks in **SION-19** are consistent with TBAPy, Ade, DMF and $[\text{NH}_2\text{Me}_2]^+$. **d-e)** Final fit (Rietveld refinement) for a rigid-body structural refinement of the PXRD pattern of **SION-19** (d) and **SION-19'** (e) (final observed: red o, calculated: solid black lines, and difference: solid green line), and **f)** Type I N_2 isotherm measured on **SION-19'** at 77 K and 1 bar (filled symbols: adsorption, empty: desorption).

The EA revealed that the guest solvent molecules comprise 26.9 % of the mass of **SION-19**, which is consistent with the TGA mass loss of 27.9 %. **SION-19** is stable up to 450 °C. Full activation of **SION-19** can be achieved upon heating at 110 °C under dynamic vacuum (10^{-6} mbar) for 12 hours, giving rise to **SION-19'**. As can be seen in Figure 3-3b and 3-3d, **SION-19'** loses its crystallinity to a significant degree but its PXRD pattern can still be indexed with cell parameters $a = 11.048(9)$ Å, $b = 31.268(9)$ Å, $c = 43.140(1)$ Å, $\alpha = \beta = \gamma = 90^\circ$, $V = 14902.6$ Å³, Cc space-group symmetry, and fit indicators of $R_{wp} = 4.8\%$ and $\chi^2 = 2.3$. In order to probe any structural changes upon full activation of **SION-19**, ¹³C CP/MAS NMR was utilized. The complete removal of the guest molecules from **SION-19** is confirmed by: *i.* the broadening of the C-signals corresponding to the TBAPy and Ade ligands and *ii.* the absence of the carbonyl carbon of DMF at 163.4 ppm (Figure 3-3c). The NMR spectrum of **SION-19'** shows that aliphatic carbons of $[\text{NH}_2\text{Me}_2]^+$ are still present at 31.0 and 35.0 ppm as broad peaks. Combining our findings, it is apparent that the structural backbone of **SION-19** is maintained when is activated to **SION-19'**.

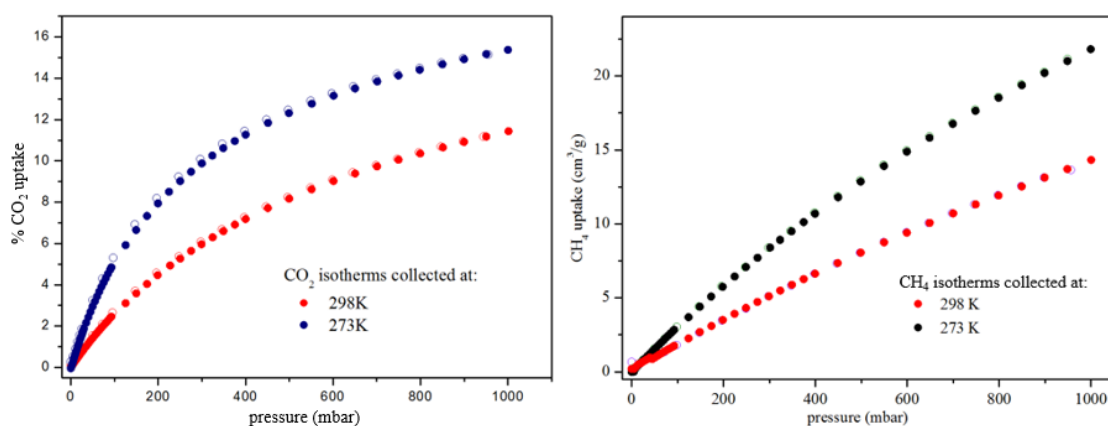


Figure 3-4: Isotherms of SION-19'. CO₂ (left) and CH₄ (right) isotherms collected on **SION-19'** at 298 and 273 K.

The permanent microporosity of **SION-19'** was demonstrated by the type I N₂ adsorption isotherm collected at 77K and 1 bar (Figure 3-3f), and it was also found that **SION-19'** is porous to CO₂ and CH₄ at 273 or 298 K and 1 bar (Figure 3-4). The BET surface area and Dubinin–Radushkevich pore volume of **SION-19'** were calculated to be 562(8) m²/g and 0.246 cm³/g, respectively (for BET surface area considerations please see the note in Section S1 of the appendix). These values are in agreement with the molecular simulations, when $[\text{NH}_2\text{Me}_2]^+$ species are placed in the acid pores of **SION-19'**. Dynamic N₂-probed properties of this simulation report an average void volume of 0.213 cm³/g and a surface area of 672 m²/g. This also confirms the presence of $[\text{NH}_2\text{Me}_2]^+$ in the acid-pore and thus they will not compete with other guest molecules for Ade binding in the base pore.

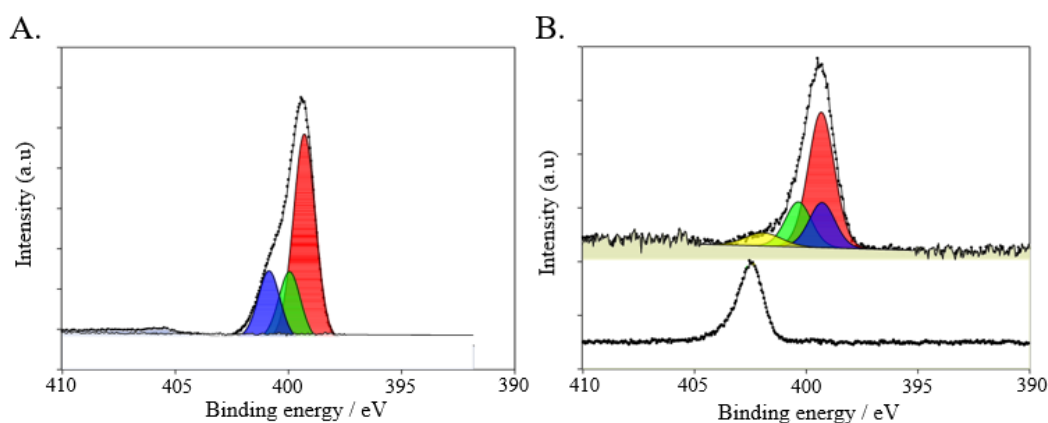


Figure 3-5: XPS of SION-19. Top: XPS N1s region of solid state Ade; Right, top: XPS N1s region of SION-19; Bottom, bottom: N1s XPS of $\text{NH}_2\text{Me}_2\text{Cl}$.

Both EA and X-ray photoelectron spectra (XPS) collected on H9Ade, $[(\text{Me})_2\text{NH}_2]\text{Cl}$ and SION-19' confirm the presence of $[\text{NH}_2\text{Me}_2]^+$ in the pores (Figure 3-5, Table 3-1) which were unable to be directly observed through SCXRD or TGA analyses.¹³⁷ To further resolve the location of cations within the pores of SION-19, we performed classical molecular dynamics (MD) simulations which show a clear preference for the $[\text{NH}_2\text{Me}_2]^+$ to localize near the carboxylate groups in the acid-pores of SION-19. This is further supported by the time-averaged energy difference of 14 kcal/mol/cation in favor of the acid-pore over the base-pore.

Table 3-1: Binding energies of the fitted components for the XPS N1s spectra. Compounds A, B and C were constrained to have the same FWHM, and the peak areas were constrained to a ration of A:B:C of 3:1:1. ^aValues in brackets are the differences of binding energies from component A.

	Binding Energy (eV) of Component			
	A	B	C	D
9HAde	399.30	399.96 (+0.66) ^a	400.87 (1.57) ^a	---
SION-19	399.33	400.46 (-0.113) ^a	399.33 (0) ^a	402.2
NH_2Me_2^+	---	---	---	402.1

3.3 Thymine loading and dimerization

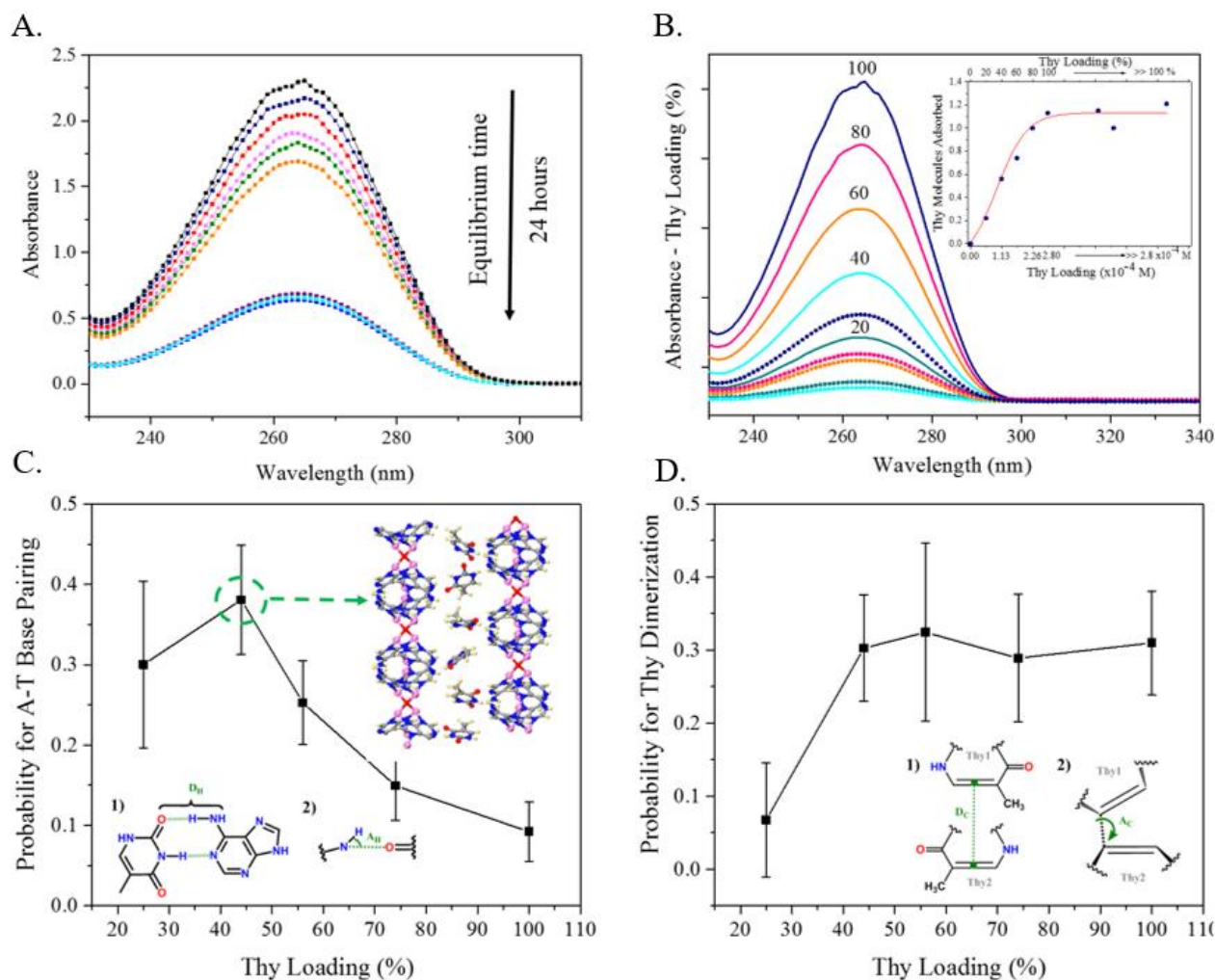


Figure 3-6: Solution thymine isotherms in SION-19' and probability of Adenine-Thymine pairing and Thymine-dimerization. **a)** Time dependency for Thy to reach equilibrium when loaded into SION-19', **b)** Solution isotherms of 20-100% (0.56-2.80 $\times 10^{-4}$ M) Thy loaded into the pores of SION-19'. Inset: maximum uptake of Thy (~1.1 molecules). Here, multiple Thy concentrations (blue circles – above 100 % loading) were used to determine the saturation limit of Thy into the pores of SION-19'. **c)** Frequency of observed Ade-Thy base pair formation from MD simulations – Insets 1) and 2) show the metrics used for H-bonding formation between Ade-Thy from the MD simulations and **d)** the frequency in which Woodward-Hoffmann and Schmidt rules are satisfied for Thy dimerization in the MD simulations at different loadings. Insets 1) and 2) show the metrics used for satisfying the Woodward-Hoffmann and Schmidt rules.

Based on the structural uniqueness of **SION-19** and accessibility of the W-C face of Ade pointing towards the base-pore, room temperature Thy solution isotherms were performed in a mixture of EtOH : MeCN solution (20 : 80) with loadings ranging from 20-100 %. These loadings were calculated based on the accessible volume of each formula unit in **SION-19** (242.0 \AA^3) and the volume of Thy (142.2 \AA^3). Following a loading of 100 %, the equilibrium was established *via* UV/vis spectroscopy to be for 24 hours (Figure 3-6a-b).²²⁴ **SION-19'** can uptake ~ 1.1 molecules of Thy at 100% loading (Figure 3-6b inset), and this is in agreement with the formula derived from EA: $[\text{Zn}_{1.5}\text{O}_{0.25}(\text{Ade})(\text{TBAPy})_{0.5}](\text{NH}_2\text{Me}_2)_{0.5} \cdot (\text{Thy})_{0.95} \cdot 1.1\text{EtOH} \cdot 1.5\text{H}_2\text{O}$.

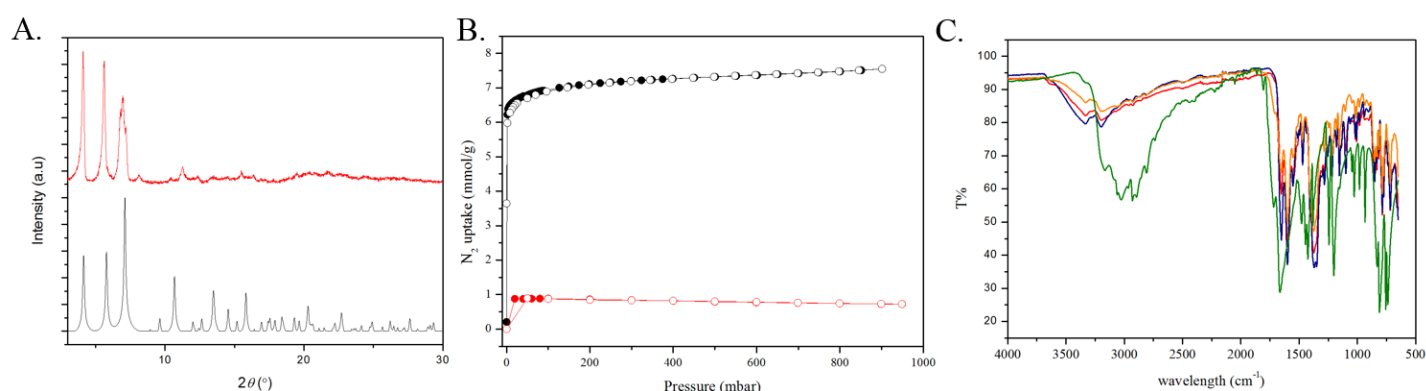


Figure 3-7: PXRD, N_2 Isotherm and IR of **SION-19@Thy.** a) PXRD of **SION-19@Thy**. Color scheme: black, theory; red, experimental. b) Type I N_2 isotherm measured on **SION-19'** (black) and **SION-19@Thy** (red) at 77 K and 1 bar (filled symbols: adsorption, empty: desorption). c) IR. Colour scheme: Blue, **SION-19**; red, **SION-19'**; orange, **SION-19@Thy**; green, Thy.

Although the crystals of **SION-19'** lose their singularity which precluded the use of single-crystal X-ray diffraction for the purpose of **SION-19@Thy** structure determination, the reduced BET surface area (Figure 3-7a-b): $79(4) \text{ m}^2/\text{g}$, FT-IR (free Thy carbonyl at 1702 cm^{-1} , and at 1699 cm^{-1} when present in **SION-19**), and solid state ^{13}C MAS NMR and ^{15}N CP NMR, which showed Thy shifts in **SION-19@Thy** of δ 156.1701 ppm (N3), and δ 126.5180-130.8505 ppm (N1) confirmed the diffusion of Thy within the pores of **SION-19'** (Figure 3-8a-b). We note that in Figure 3-7a, the experimental PXRD shows a peak at approximately 7° with multiple components compared to the same theoretical peak. This is likely due to the presence of Thy within the framework causing shifts or defects that cause **SION-19** to lose singularity as previously mentioned, or due to the measurements of **SION-19@Thy** as a flat powder on a Si holder

and not in a capillary tube. Using DFT calculations, EtOH molecules were simulated in the pores of **SION-19'** and shown to preferentially reside in the acid pores (where no Ade-Thy H-bonding can occur) by 3.3 kcal/mol. This is due to favourable interactions with the charge-balancing cations $[\text{NH}_2\text{Me}_2]^+$ present in the acid pores.

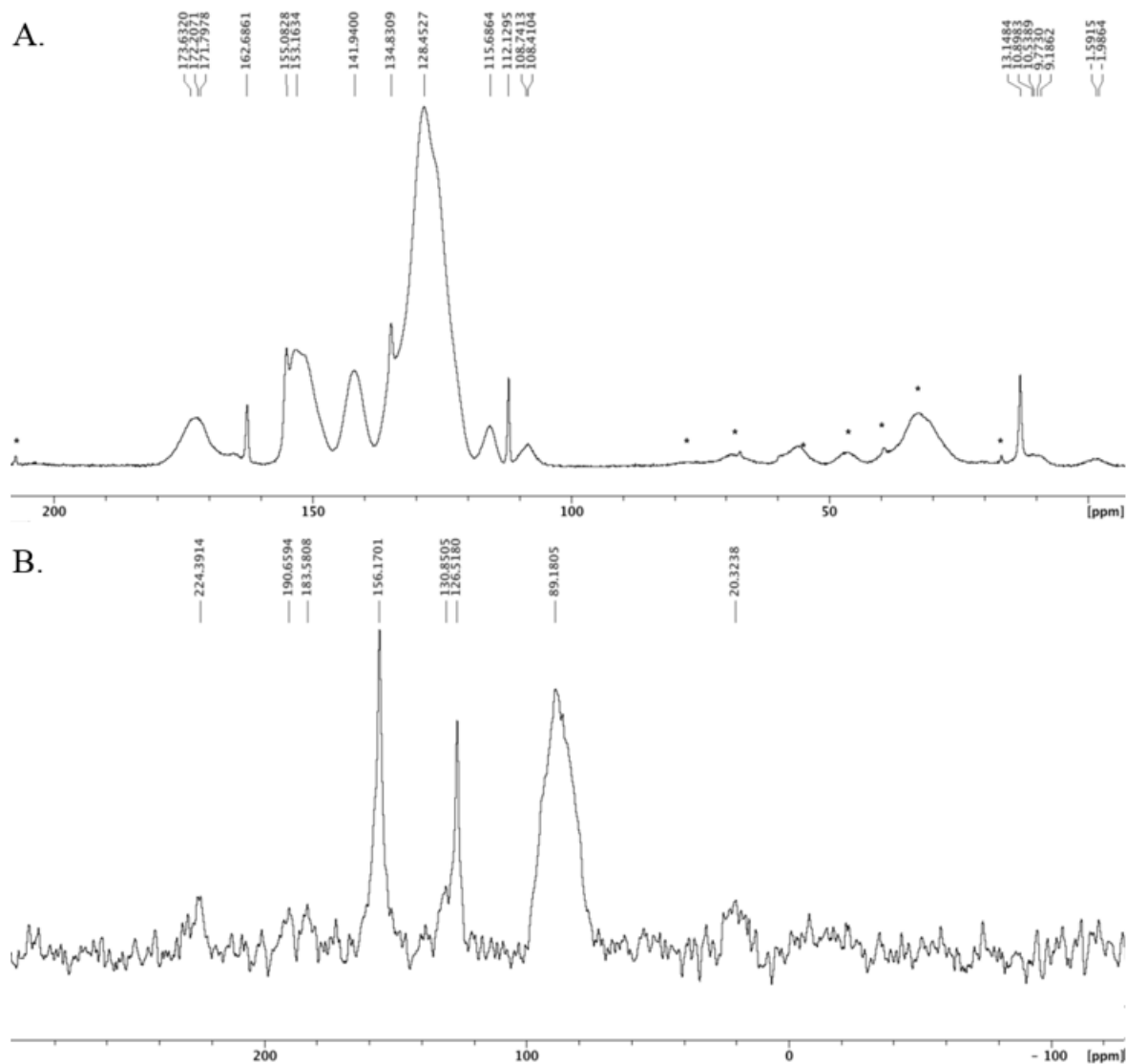


Figure 3-8: MAS ^1H - ^{13}C NMR. a) MAS ^1H - ^{13}C NMR of **SION-19@Thy, 103K, 12000 Hz. b) MAS ^1N CP NMR of **SION-19@Thy**, 100K, 12000 Hz. Peaks correspond to: δ Thy (N3), 156.1701; Thy (N1) 126.5180-130.8505; and Ade (NH_2) 89.1805.**

The nature of the Ade-Thy base pair formation in **SION-19'** was examined through DFT optimization of one Thy near Ade.⁵⁹ The optimized distances between H-bonding donors and acceptors are 2.72 Å ($N_{\text{Ade}}-N_{\text{Thy}}$) and 3.00 Å ($N_{\text{Ade}}-O_{\text{Thy}}$), and are comparable with the experimentally measured distances of 2.82 Å and 2.95 Å, respectively.²²⁵ In addition, Bader population analysis shows a slight charge polarization of 0.06 e^- on the heavy atoms,²²⁶ indicative of H-bonding formation between Thy and Ade in **SION-19'**. The DFT binding energy for a single Thy in **SION-19'** is calculated to be -18.2 kcal/mol, which has higher absolute value compared to the \sim -12 kcal/mol binding energy reported for pure Ade-Thy interactions in both experimental and theoretical calculations.^{227, 228} Dynamic, finite temperature behavior of Thy within the pores of **SION-19'** was investigated with classical MD simulations at room temperature (298 K). In these simulations, base-pair H-bonding was modeled using three-bodied potentials using parameters designed for accurate H-bonding in bio-molecules.²²⁹ With this potential, we observe a good energetic agreement with the DFT binding energy computed for Ade-Thy in **SION-19'**, being 1.4 kcal/mol higher in energy (-19.6 kcal/mol vs -18.2 kcal/mol).

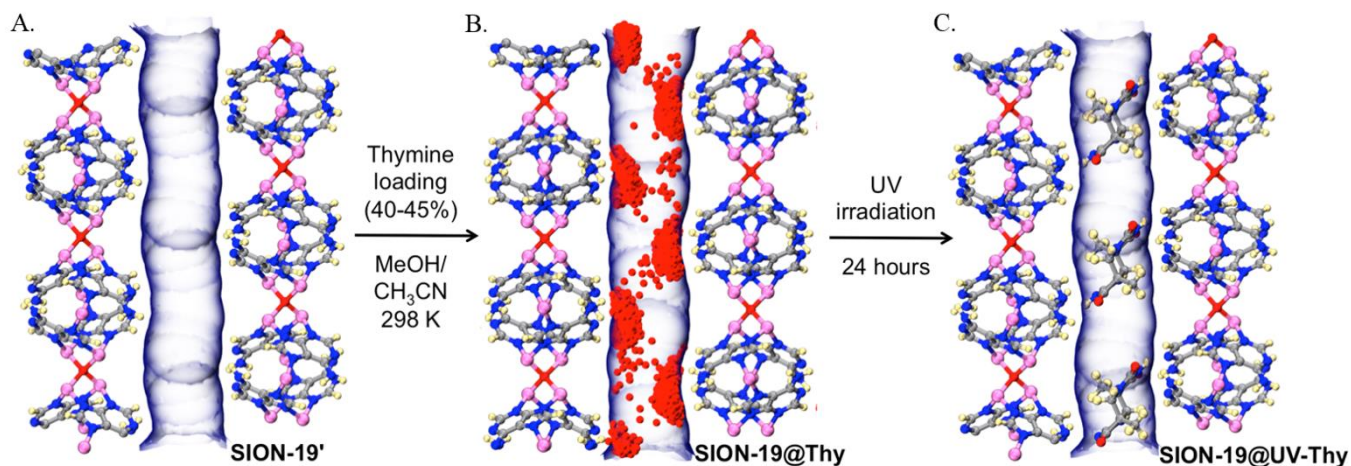


Figure 3-9: Schematic representation of thymine loading, location and dimerization within SION-19'. a) 1-dimensional base-pore surface for **SION-19'** prepared using HOLE2, b) Thy snapshots (red dots) from an MD trajectory of 44% thymine loading in the base pore of **SION-19**. Here, Ade acts as a structure directing agent that ‘locks’ Thy molecules into positions close enough to another Thy molecule for photodimerization to occur. c) DFT optimized positions of Thy<->Thy dimers arising from a 44% loading of Thy. Atom color code: pink, Zn; red, O; blue, N; grey, C; light yellow, H.

Exposure of pyrimidine nucleobases like Thy to UV light can induce a [2+2] cycloaddition between the C5-C6 and C5'-C6' double bonds of two pyrimidine rings (Scheme 3-1).²²⁰ While dimerization of Thy in a liquid medium is a viable method to afford Thy<>Thy, its solid-state dimerization has not been fully studied. To confirm this, Thy crystals were exposed to UV light (254 nm) for 24 hrs and ¹H NMR revealed that no Thy<>Thy was obtained. To investigate the atomistic features of the Thy loading experiments in **SION-19'**, room temperature MD simulations were performed at loadings of 25, 44, 56, 74, and 100 %. Due to the relatively tight pores, and the strong H-bonding potentials used in the simulation, 5 cycles of 2 ns annealing were performed at each loading. Statistics on the orientations of Thy with respect to themselves, and Ade in **SION-19'** were collected over the span of 10 ns at intervals of 2 ps. It was hypothesized that in order to enable the formation of Thy<>Thy, the Thy molecules must resemble the transition state of a [2+2] cycloaddition, and follow the Schmidt rules. That is, the C5-C6 and C5'-C6' must be nearly parallel, and separated by <4.2 Å.²¹⁸ Thus, the trajectories for the potential formation of a four-membered ring were analysed, specifically when the C5-C6 double bond of adjacent Thy molecules were: *i.* within 4.2 Å of each other, and *ii.* nearly aligned, by determining the dihedral angle formed between C5-C6 and C5'-C6' is below 30°.²¹⁸ Figures 3-6c-d and 9 demonstrate that Thy molecules appear to be more favourably oriented for dimerization at 44% loading and above. This is compared to the peak in base-pair formation, which occurs at a 44% loading and then subsequently deteriorates. At higher Thy loadings, Thy packs in a dense sterically unfavourable manner within the base pore disfavours base-pair formation (Figure 3-6c). This correlation suggests that the Ade ligands within **SION-19'** are structure-directing agents, which fix the position of Thy within the pores, and can allow for Thy<>Thy formation from two nearby 'locked' base-paired Thy molecules. A plot of the trajectories at a 44% loading show that Thy molecules form base pairs with Ade that are two Ade units apart along the *a*-axis, and on opposite sides of the pore (Figure 3-6d). To validate this experimentally, samples of **SION-19@Thy(20-80%)** were continuously exposed to UV for 24 hrs.²³⁰ The formation of Thy<>Thy was determined via ultra-high performance liquid chromatography coupled with electrospray ionization mass spectrometry (UHPLC-EIS/MS). Samples of **SION-19@UV-Thy(20-30, 50-80%)** showed no presence of product, while **SION-19@UV-Thy(40-45%)** afforded Thy<>Thy in a non-quantitative yield (58.5 %). The non-quantitative nature of this dimerization is thought to be due: *i.* to the low population of an excited state (singly excited, ¹SE), which proceeds through an internal conversion, and requires overcoming an energy barrier,²¹⁶ and *ii.* to the poor penetration of light throughout the solid material, and thus some Thy molecules do not have enough energy to overcome this barrier and dimerize. Here, this mechanism is governed by both conformational control, and electronic effects.²¹⁶⁻²¹⁸ The inability of lower Thy loadings (20-

30%) to dimerize might be due to the increased spatial distance between Thy molecules as they slowly diffuse through the channels, while at higher loadings (50-80%), there is a decrease of H-bonding stabilization between the framework Ade and Thy, leading to an unfavourable packing within the base-pore.

To further confirm the structural uniqueness of **SION-19** to 'lock' Thy into a specific orientation and transfer energy for dimerization, Thy loading and dimerization in the pores of adenine-containing Bio-MOF-1 as well as HKUST-1 and Zn-MOF-74, which are not adenine-based, were attempted, and in all cases no traceable amounts of Thy<>Thy were observed. These results further confirm that not only the presence of the W-C faces of Ade, but also the optimal Ade-Thy binding ratio and the subsequent electronic effects/conformation control, play an important role in the dimerization process. That is, the stabilization of Thy via W-C H-bonding with Ade in **SION-19** allows it to conform to both the Schmidt and Woodward-Hoffmann rules.

In conclusion, we synthesized a novel biologically derived MOF, **SION-19**, possessing a new *kcs1* topology and Ade-functionalized pore surface, that acts as a nanoreactor for the dimerization of Thy *via* site-specific binding to Ade. We successfully showed that the orientation of Ade within **SION-19** permits Thy binding (40-45% loading) that resembles the transition state of [2+2] cycloaddition required for Thy dimerization. Thy loading and dimerization in the pores of **SION-19**, and the specific relationship between Ade-Thy binding demonstrate that taking advantage of functional groups that decorate the pore surface of MOFs can be used as an effective strategy for their utilization as nanoreactors for photo-induced organic reactions.

3.4 Conclusions

The ability to photo-induce the dimerization of solid state Thy within the constrained pores of **SION-19** can ultimately provide new fundamental insights on the governing mechanism of this process. Our approach can be applied to a variety of MOFs or other porous materials with comparable structural features to 'lock' molecules in specific positions, and can open up new avenues for the synthesis of organic molecules that may otherwise be difficult to obtain through traditional routes. Furthermore, using bio-MOFs as nanoreactors to form biologically relevant molecules can bridge multiple research disciplines, which can aid in the development of new methods for drug discovery and delivery. These strategies can offer an opportunity for interdisciplinary work, that is, to develop new synthetic methodologies and study the activity of new bio-related products.

Chapter 4 SION-9: Multimodal Sensor for Real Time Health Monitoring

4.1 Introduction

The development of new conductive polymeric materials is of great importance for nanotechnology, and to date, they have shown potential in biomedical applications as biosensors, drug delivery systems, biomedical implants and tissue engineering.²³¹ Apart from unimodal sensors (e.g. pressure sensors), multimodal sensors can detect simultaneous changes in stimuli such as pressure and temperature, and are highly desired in health diagnostics to monitor the influence of temperature on the pulse pressure of a patient.²³²⁻²³⁵ Their specific use in this field can lead to the generation of new smart bio-functional devices for real time health monitoring,^{235, 236} the development of artificial fingers and electronic skin which are required to feel the temperature, discern surface texture, and the hardness of the objects simultaneously.^{232, 233, 237}

Designing and synthesising new materials with conductive properties however, is a challenging task, as high charge density and mobility have to be achieved within their structures. This is correlated to the components used to generate the material (organic ligands and/or metal ions), the connectivity between them, and their spatial arrangements in 3-dimensions.^{88, 120, 238} MOFs have recently emerged as a promising class of conductive materials, and typically there are three strategies which can be used to form MOFs with conducting properties: *i.* through-bond, *ii.* through-space and *iii.* guest molecule doping.¹²⁰ The first utilizes metal ions such as Cu^{II} , Mn^{II} , or Fe^{II} with electron rich organic ligands like 2,3-pyrazinedithiolate, and 2,5-disulfhydrylbenzene-1,4-dicarboxylic acid.^{126, 134} The through-bond approach results in modest covalent bonding interactions, affording the overall observed conductivity in the framework. If instead for example, the ligands incorporated in the MOF structure have a π - π stacked motif, the resulting orbital overlap can create an extended pathway for conductivity known as the through-space approach.¹²⁰ Here, ligands such as tetrathiafulvalene tetrabenzoate, and hexahydroxytriphenylene with metals such as Mn^{II} , Co^{II} , Zn^{II} , Cd^{II} and Ni^{II} have been shown to afford conductive MOFs.^{120, 141, 144, 232, 239} However, the reali-

zation of the through bond and through space strategies is challenging as the conductivity properties of MOFs rely on an ideal orbital-overlap, covalency, and/or ligand-to-ligand distances which are difficult to control during the MOFs synthesis.¹²⁰ Finally, due to the porous nature of MOFs, the introduction of guest molecules acting as charge carriers within the pores can result in conducting MOFs from previously non-conducting frameworks.^{135, 137} This strategy is limited to porous MOFs with channels that are large enough to accommodate the desired guest molecules, and a strong affinity between the guest molecules and MOF.

Moving into the future, conductive MOFs will have to prove their utility not just as unimodal sensors, but also as multimodal sensors that can detect multiple environmental changes such as temperature and pressure simultaneously.^{236, 240} Recently, these multimodal MOF sensors have only been reported following further processing such as carbonization and doping before the devices fabrication.^{236, 240} This requires that the MOF has to be structurally stable to the processing and fabrication steps, as well as still maintain its sensitivity, and be electrically controllable.^{241, 242} These devices have been reported to be competitive with graphene-oxide based devices which exhibit high sensitivity, flexibility, fast response times, and durability.^{243, 244}

Inspired by these challenges, herein we describe the synthesis of a novel conducting 3-dimensional MOF (hereafter named **SION-9**) based on Zn^{II} , tetra-(p-carboxylphenyl)-porphyrin (H_6TCPP) and adenine (Ade). Within **SION-9**, we have strategically employed an electron rich and paramagnetic ligand based on the porphyrin core which has been previously shown to exhibit strut-to-strut electron hopping,^{24, 25} and the nucleobase Ade,²⁶ which has been used as a dopant in super capacitor applications.²⁷ Due to the 3-dimensional arrangement of these components **SION-9** conducts and behaves as a multimodal sensor to both temperature and pressure changes. The fabricated sensor exhibits high sensitivity and fast response time, demonstrating its high potential for real time health monitoring applications.

4.2 Structural Description, Stability and Bulk Analysis of SION-9

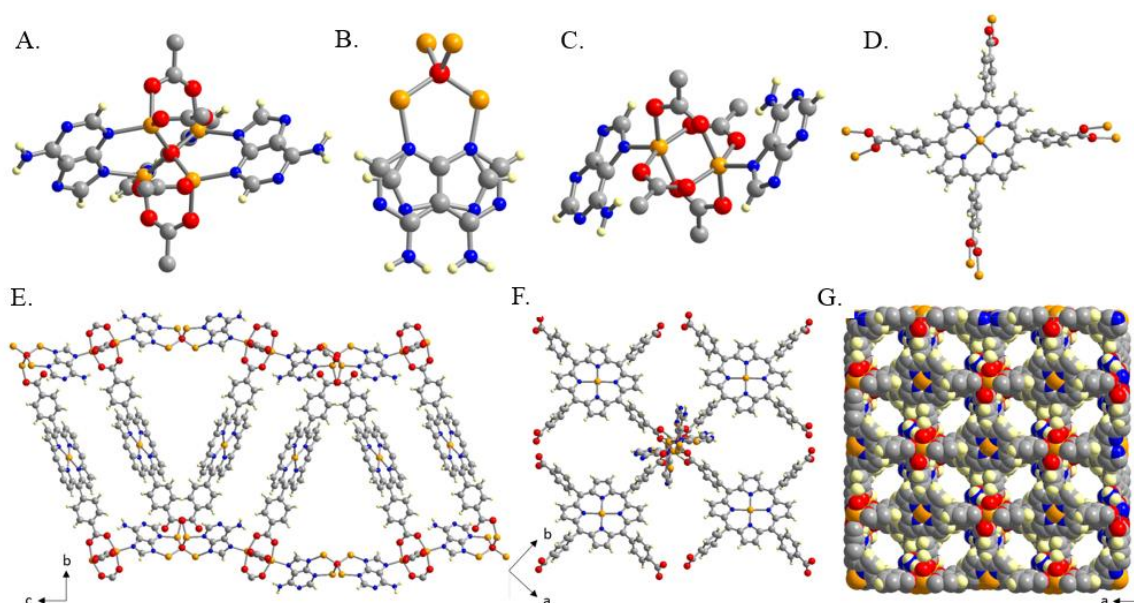


Figure 4-1: Crystal structure of SION-9. **a-d)** demonstrate the coordination environments of Zn^{II} metal centers present in the crystal structure of **SION-9** with **a)** showing the tetrahedron-shape unit formed by Zn1 and Zn2, **b)** showing the disordered HAd molecule attached to the Zn1Zn2 tetrahedron, but not contributing to the connectivity of the framework, **c)** the paddlewheel unit formed by a pair of Zn3 atoms related by symmetry, and **d)** the Asymmetric unit of **SION-9** with the Zn4 atom situated in the center of the TCPP^{6-} porphyrin ring. **e)** Zigzag-like 1D chains constituted by alternating Zn1Zn2 tetrahedra and Zn3 paddlewheel units lined by the $(\text{TCPPZn})^{4-}$ ligands, **f)** Planes of mutually parallel $(\text{TCPPZn})^{4-}$ ligand cores extending infinitely in one direction, **g)** the overall view of **SION-9** down the *c*-axis. Color scheme: orange, Zn; blue, N; red, O; grey, C; yellow, H.

Red square plate of **SION-9** $[\text{Zn}_3(\text{TCPPZn})(\text{Ade})(\text{HAd})\text{O}_{0.5}] \cdot \text{guest molecules}$ are afforded through the combination of $\text{Zn}(\text{NO}_3)_2 \cdot 6(\text{H}_2\text{O})$, H_6TCPP and Ade, in an acidic $\text{DMF}/\text{H}_2\text{O}/\text{HNO}_3$ solution (Appendix Section 5.1). Single crystal X-ray diffraction (SCXRD) reveals that **SION-9** crystallizes in the monoclinic space group $C2/c$. The asymmetric unit of **SION-9** comprises: *i.* one fully deprotonated TCPP^{6-} ligand with one Zn^{II} atom positioned in its center giving rise to $(\text{TCPPZn})^{4-}$, *ii.* three further bridging Zn^{II} atoms: Zn1, Zn2, and Zn3, *iii.* one fully deprotonated Ade^- molecule and a half of the neutral HAd molecule, and *iv.* one bridging O^{2-} atom occupying a special position with 0.5-occupancy. Zn^{II} atoms adopt three distinct coordination geometries. Zn1, Zn2 and their symmetry equivalents, each with the coordina-

tion number 4 and tetrahedral coordination geometry, form a tetrahedron-shape unit with the bridging O^{II} atom (O10) in its center (Figure 4-1a). Here, Zn1 ions are attached monodentately to the carboxylate group of the $(\text{TCPPZn})^{4-}$ ligand, as well as to the N3A of the bridging Ade^- , in which the N9A coordinates to the remaining Zn2 ions. The Zn2 ions are further bridged together by the disordered HAd e^- ligand (Figure 4-1b). Zn3 is found in the paddlewheel unit: it adopts a square pyramid coordination geometry. The paddlewheels contain four $\eta^1:\eta^1$ -bridging carboxylate groups, and a N7A-coordinated Ade^- found at their apices (Figure 4-1c). Zn4, in turn, is situated in the center of the TCPP^{6-} porphyrin ring; its coordination number is 4 and it is in a square planar geometry (Figure 4-1d). The ligands, $(\text{TCPPZn})^{4-}$, Ade^- and HAd e^- , serve as linkers between the Zn1, Zn2 and Zn3 atoms. The $(\text{TCPPZn})^{4-}$ ligand links with a $\eta^1:\eta^1$ -bidentate mode to two neighboring Zn3 paddlewheels and to one Zn1Zn2 tetrahedron. The mode of coordination to another Zn1Zn2 tetrahedron is η^1 -monodentate, although the Zn1–O2 contact of 2.635 Å is shorter than the sum of the respective van der Waals radii, 3.89 Å.¹⁴⁰ The deprotonated Ade^- molecule serves as a link between a Zn3 paddlewheel unit and a Zn1Zn2 tetrahedron, coordinating with N7A to the former and with N3A and N9A to the latter. On the other hand, the HAd e^- molecule is attached to the Zn1Zn2 tetrahedron only with N3B (and N9B sharing the same position), thus not contributing to the connectivity of the framework. This molecule is disordered over two components, whose 0.5-occupancy is imposed by the 2-fold axis relating one to the other. We note that due to the positional disorder it was not possible to assign the protonation site in HAd e^- .

The topological description of **SION-9** requires localizing the nodes of its underlying net. One of them is constituted by the porphyrin ring of the $(\text{TCPPZn})^{4-}$ ligand (node A), the second is the Zn1Zn2 tetrahedron (node B), while the Zn3 paddlewheel forms the third one (node C). Node A is 4-coordinated with the benzyldiene arms of the $(\text{TCPPZn})^{4-}$ ligand serving as links. Both nodes B and C are in turn 6-coordinated, and the linkage between them is realized through bridging Ade^- molecules. The 3-dimensional array of these nodes has the A_2BC stoichiometry and can be described by the Schläfli symbol $(4^3.5.6^2)_2(4^2.5^5.6^5.7^3)(4^4.5^4.6^6.7)$. This is the first time that such a net is found in a MOF. Two characteristic features come out from the topological analysis of **SION-9**: first, the presence of planes of mutually parallel $(\text{TCPPZn})^{4-}$ ligand cores extending infinitely in one direction with Zn3 paddlewheels connecting their centres and Zn1Zn2 tetrahedra linking their edges; the tetrahedra are the spots of the structure where one such plane is inclined towards the other under an angle of 44.76°. The second characteristic feature is the occurrence of infinite zigzag-like 1D chains constituted by alternating Zn1Zn2 tetrahedra and Zn3

paddlewheel units; the (TCPPZn)⁴⁻ ligand cores are parallel to these chains, also forming a zigzag array of pairs of mutually parallel units (Figure 4-1e-f).

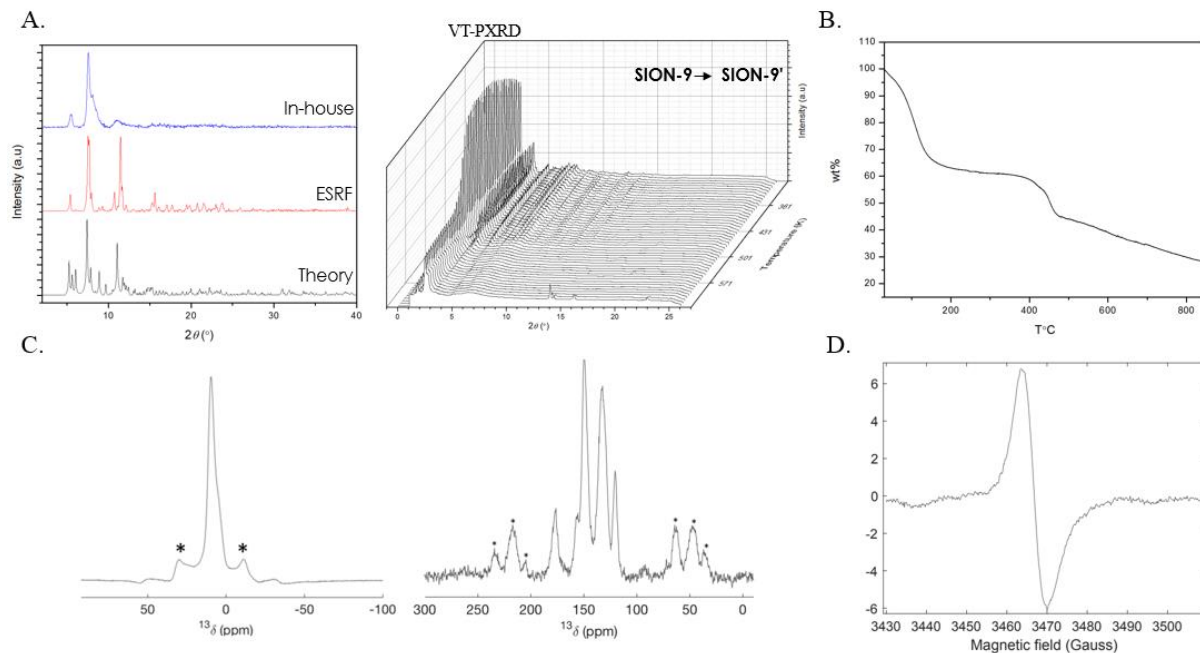


Figure 4-2: PXRD, VT-PXRD, TGA, ^{13}C CP-MAS, and EPR of SION-9. a) PXRD of SION-9 (left) and VT-PXRD of SION-9 to SION-9' b) TGA analysis of SION-9. c) SION-9' ^{13}C CP-MAS recorded at 700 MHz proton frequency. Rotor spinning at 15 kHz, contact time 4ms. Left: expanded spectrum; right: spectra from 0-300 ppm. Spinning sidebands indicated with a star. d) EPR of SION-9 as made material confirming the presence of an unpaired electron in the material.

Activation of SION-9 crystals to SION-9' can be achieved upon heating at 120 °C under dynamic vacuum (10^{-6} mbar) for 72 hours. Elemental and thermogravimetric analysis reveal that upon heating 38.0 % of the mass loss in SION-9 is attributed to guest molecules (DMF and H₂O) (Figure 4-2a-b). As can be seen in Figure 4-2a-b, SION-9 loses its crystallinity to a significant degree upon activation, however the integrity of the structural backbone of SION-9' remains intact compared to SION-9, as confirmed by ^{13}C CP/MAS NMR (Figure 4-2c). Following the structural analysis of SION-9, we performed electron paramagnetic resonance (EPR) experiments under light and dark conditions in order to confirm the presence of an unpaired electron from the TCPP ligand. As seen in Figure 4-2d, the presence of an unpaired electron was confirmed, and subsequently, EIS measurements were performed.²⁴⁵

4.3 Multimodal Response of SION-9 to Variable Temperature and Pressure

Following characterization of **SION-9**, conductivity measurements using EIS was performed on **SION-9** pellets as a function of temperature and pressure. The in-house designed cell in which the **SION-9** pellets were introduced in consists of two gold plated electrodes, both of which are 8 mm in diameter and the conductivity measurements were conducted at different applied mass (0, 995, 1592, and 1990 kg/cm² of pressure) and temperatures (5, 10, 25, 40, 45, 50, 55 and 60 °C) - (Appendix Section 5.4). Here, the evaluation of conductivity was based on equation 1:

$$\sigma = (1/\text{Re}Z) \cdot (h/A) \quad (4-1)$$

where h is the thickness and A is the surface area of the pellet (0.5024 cm based off of the cell dimensions). **SION-9** gave a modest conductivity value of 1.1×10^{-6} S/cm, with its structural integrity revealed to be intact following the powder press and measurements. The resulting Nyquist plots (Figure S37-59) displayed a semi-circle in the high frequency component and an inclined tail in the low frequency component. Overall, these features have been exhibited in impedance data of passive Ni^{III} phosphate buffer solutions,¹⁵⁰ three-dimensionally ordered macroporous gold film immunosensors,²⁴⁶ and themolyzed Pt- and Al-MOFs.²⁴⁷

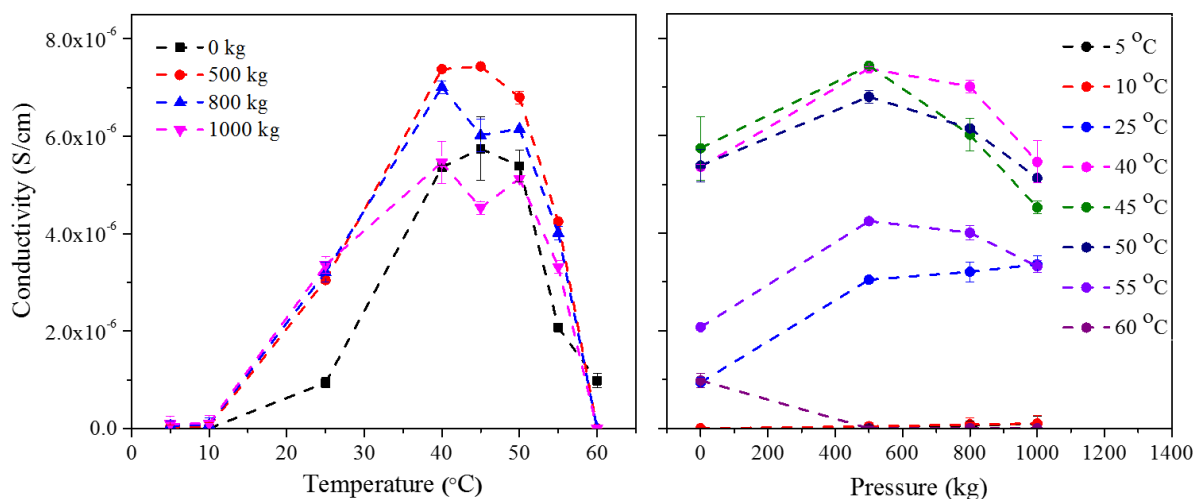


Figure 4-3: Conductivity summary of SION-9. Summary of the multimodal response to both temperature (right) and pressure (left) of **SION-9** pellets using electrochemical impedance spectroscopy measurements.

At different temperatures, the conductivity of **SION-9** is increased from $2.69\text{--}4.20 \times 10^{-8} \text{ S/cm}$ to $7.43\text{--}7.34 \times 10^{-6} \text{ S/cm}$ at $40\text{--}45^\circ \text{C}$ (995 kg/cm^2) (Figure 4-3). The sudden decrease in conductivity at temperatures greater than 45°C is thought to be attributed to the loss of guest molecules from the cavities of **SION-9**, leading to **SION-9** with structural disorder, and ultimately reflects the role that the solvent molecules play in the conductivity of **SION-9**.

4.4 Electrochemical Impedance Spectroscopy and Origin of Conductivity of **SION-9**

To understand the implication of electronic structure on the possible practical applications and the origins of conductivity in **SION-9**, we have performed a theoretical investigation of its electronic properties, accomplishing geometry optimization, molecular dynamics simulations, as well as electronic structure calculations within DFT and GW-BSE approaches, the computational details for which are given in the Supporting Information.

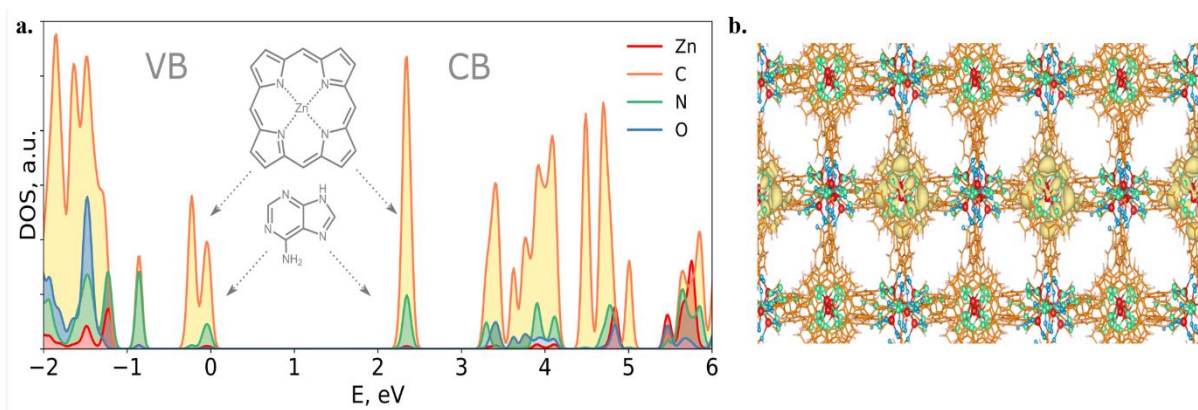


Figure 4-4: DOS and frontier orbitals of SION-9. a) Density-of-states in **SION-9**, b) Porphyrin and HAd frontier orbitals in **SION-9**.

The nature of states forming the valence and conduction band edges is depicted in Figure 4-4 using projected density-of-states and electron density isosurfaces. This analysis reveals that the bottom of the conduction band (CB), as well as the top of the valence band (VB) are constructed of porphyrin orbitals, along with some contribution from the protonated Ade species HAd, while contributions from Zn and O atoms lie further away from the band edges. The porphyrin and HAd orbitals create a detached manifold of almost degenerate states at the VB top and CB bottom, the highest occupied crystal orbital (HOCO)

and lowest unoccupied crystal orbital (LUCO) being centered on porphyrin rings of adjacent stacked layers (Figure 4-4) with HAd contributions. The nature of frontier electronic states suggests that the lowest excitations will take place between the stacked porphyrins that is consistent with the unpaired electron signal characteristic to porphyrin rings, observed in the EPR experiment.

4.5 Real Time Health Monitoring Using SION-9

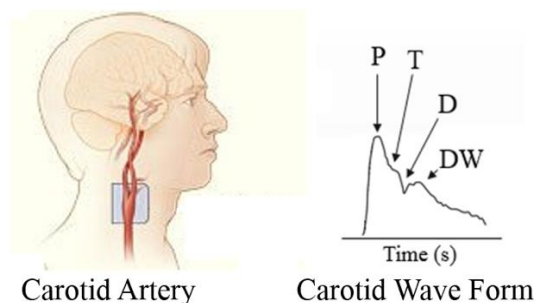


Figure 4-5: Location and wave form of the Carotid Artery. Here, P: percussion wave; T: Tidal wave; D: dicrotic notch; DW: dicrotic wave.

Following the conclusions of our computational and EIS studies, we began to hypothesize potential devices that could utilize the multimodal nature of **SION-9**. Wearable electronic devices that can provide information on a person's biological signal (i.e. heart beat) are useful for clinical diagnosis such as cardiovascular disease (Figure 4-5).^{240, 248-250} Ideally, these devices should be flexible, have a fast response time, and able to monitor biological signals such as the carotid artery pressure in real time.^{240, 248-250} To date, many of these devices comprised of nanocrystal arrays of MOFs,²⁴⁰ MOF derived porous carbon sensors,²³⁶ or graphene based.²³¹ While they all successful at real time health monitoring, extra steps are typically required to process the material into a functioning device.

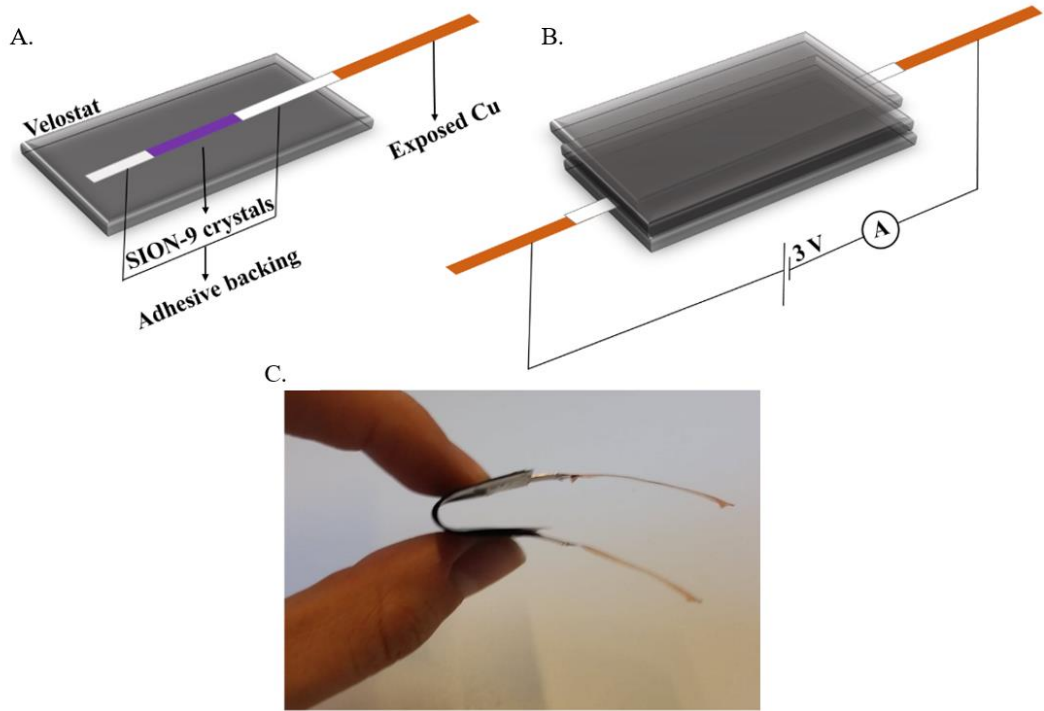


Figure 4-6: Device construction. a-b) construction of the **SION-9** device using Velostat, copper tape, and **SION-9** crystalline powder. c) the flexibility of the device.

To demonstrate the utility of **SION-9** as a pressure-based sensor for real time health monitoring, we constructed a cost effective sensor made out of components that could easily be acquired (Appendix Section S5.5, Figure 4-6). The standards in which we aimed for when fabricating our sensor were fast response times (< 65 ms) and the sensitivity to show the shape of the carotid artery wave pulse (CP) which indicates the variations in arterial blood pressure and volume with each cardiac cycle.²⁵¹ As the carotid arteries are large, and located near the heart, the CP signals resemble the pressure signals that are found at the root of the aorta.²⁵¹ Here, the CP sharply rises as blood enters the left ventricle to the ascending aorta, known as the percussion wave (P). Following this is the second wave known as the tidal wave (T), the dicrotic notch (D), which is caused by the aortic valve closing, and subsequently the dicrotic wave (DW) (Figure 4-5).²⁵¹ This pulse can vary depending on the position of the volunteer, for example standing vs sitting, and is sensitive to moving between the two positions.²⁵²

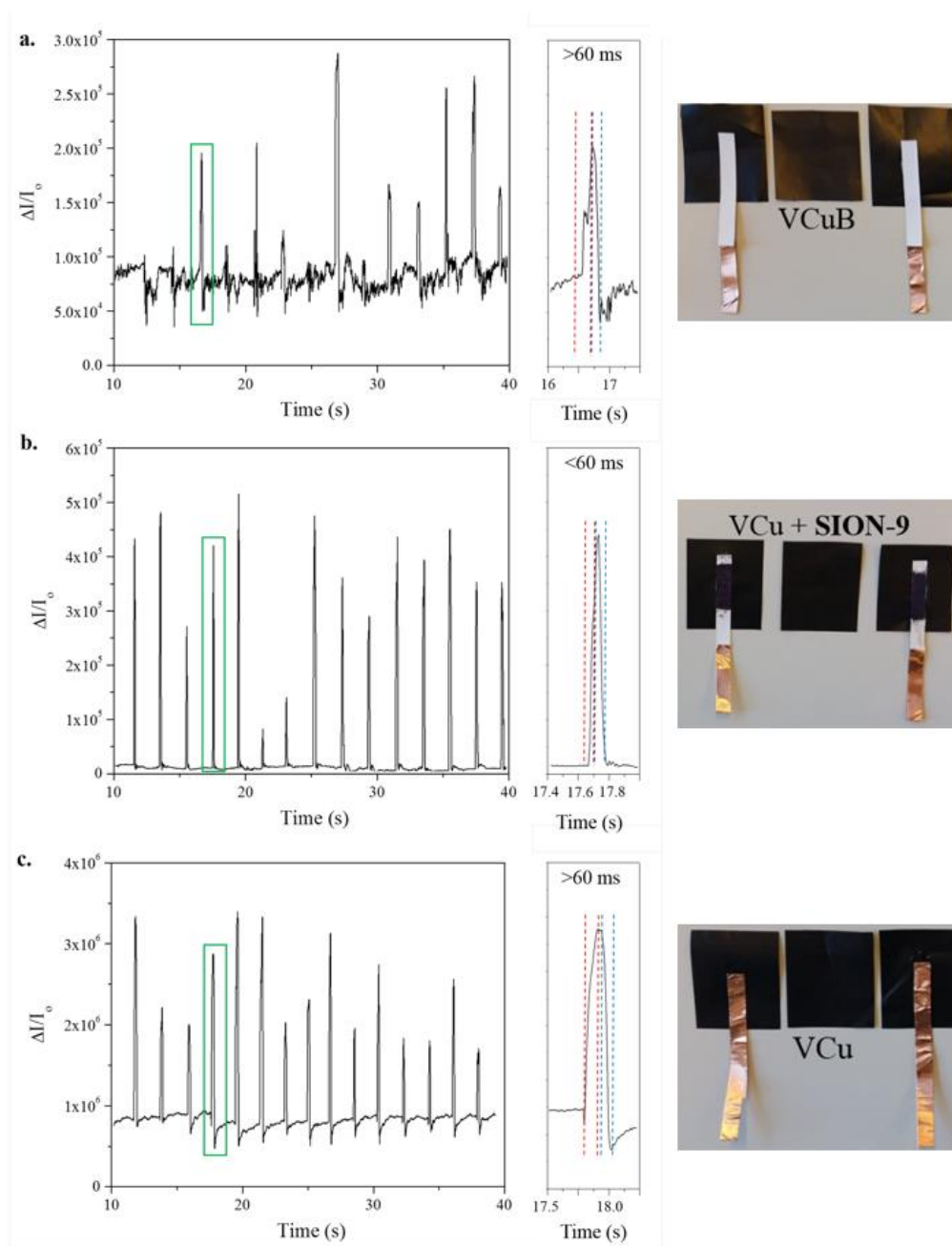


Figure 4-7: Tap Tests of devices and their response times. Tap tests of the device using different components of the device to find the response time. These tests were performed by tapping on the device while it was measuring current changes from the potentiostat/galvanostat PGSTAT302N. Here we used **a)** all of the components including the adhesive backing (VCuB) but without the addition of **SION-9**, **b)** the **SION-9** device (VCu + **SION-9**) and **c)** all of the components without adhesive backing (VCu) and **SION-9**. Blue and red dotted lines demonstrate the part of the response which was used to calculate the response time.

For the device construction, Velostat (V) and Cu adhesive tape (Cu) were used; the Cu tape was connected to the potentiostat/galvanostat PGSTAT302N with chronoamperometry module and resembles that of a piezoelectric system. Initial tap testing was performed on two equivalent **SION-9** free devices, one with just VCu and the other with VCu+ blocking agent (VCuB) to determine the response of the components to sudden changes in pressure (Figure 4-7). Here the test was performed by tapping on the device while it was measuring current changes on the potentiostat/galvanostat PGSTAT302N in intervals of approximately 2 seconds. The average response and relaxation time for the **SION-9** device was found to be < 60 ms, while the **SION-9** free device gave a much longer response time of > 75 ms. The fast response and relaxation time of a device is required for its applicability in real health time monitoring, as small changes in the increase, decrease, or signal shape of wave pulse is important for showing the heart beat in real time of a patient.²⁵² Due to the easy assembly of the device and the fact that **SION-9** is physically adhered without any other treatment, the lifespan of the device is simply limited by the shelf life of **SION-9**. Based off of these conclusions, the **SION-9** device will soon be tested to monitor the carotid artery in real time.

4.6 Conclusions

In summary, we have successfully synthesized a new conductive MOF sensor, named **SION-9**. The conductivity in **SION-9** is sensitive to the changes of temperature and strain, and can therefore be employed for creation of multimodal thermobaric detectors. Following the assessment of **SION-9**'s conductivity origins, we incorporated it into a flexible device consisting of components that are readily accessible (Velostat and Cu tape), and assembled without any additional heating or deposition steps. This device shows a great response time, highlighting the potential of **SION-9** for real health time monitoring. Overall, this proof-of-concept study provides new insights into the development of new smart materials, which can be used in the fabrication of cheap devices for biomedical applications.

Chapter 5 Future Work and Outlook

As described and shown in this thesis, MOFs can be used for a wide variety of research from giving us fundamental insights to application development. Understanding how MOFs form, transform, and how this changes their structural and electronic properties is necessary as we move forward with streamlining their synthesis and developing new materials for emerging applications such as artificial skin.

Compared to some porous solids like Zeolites, MOFs are a relatively new family of porous materials that have seen an exponential growth rate in both publications and patents. Moving from academic to industrialization, MOFs have been seen as a challenge for commercialization due to issues like low yields, expensive metals and ligands, as well as the solvents that are sometimes used in their synthesis. In the case of this thesis, looking realistically at the materials I have synthesized, their potential for commercialization is limited due to these exact reasons. One way to solve this is to move from metal nitrates to oxides to avoid potential hazards associated with scaling up reactions and using larger quantities of metals with nitrate or perchlorate counter ions which can be flammable or explosive. Also, new synthetic routes to decrease the cost of the linkers (TBAPy and TCPP) would possibly be required, along with optimizing the solvent : MOF yield ratio to increase product yield and decrease costs. It's also ideal to move from typical solvents such as DMF towards more environmentally friendly solvents such as water.

Moving forward into industrialization, many of these challenges have already been solved for MOFs such as HKUST-1 (Basolite), Al-fumate, and UiO-66 which have already found success through sales via companies such as BASF in 500 kg batches. Furthermore, taking advantage of the porous nature of MOFs to solve environmental challenges such as capture greenhouse gas emissions/CO₂ capture and storage is already being explored extensively. However new challenges have recently emerged regarding micro plastics in drinking water, which can be filtered using expensive systems such as reverse osmosis. For porous materials such as MOFs, this could provide a solution to the problem with their porous nature and the seemingly unlimited number of materials that can be

made and tailored to solve this problem. Similar to the MOFs that have already found commercial success, these micro plastic absorbing materials should be made using cost selective materials, synthesized on a kg or tonne scale, easily recyclable or readily absorb/desorb the plastic and selective to all types of micro plastics.

While MOFs can be used for a wide variety of applications, in some cases they may not be the appropriate material to use to solve a problem. Since MOFs are typically sensitive to solution or environmental changes, those applications which require material stability under harsh or a wide variety of conditions might benefit from using zeolites or metal-oxides instead. Taking our work into the future with the goal of solving global climate and plastic problems, knowing and understanding the alternatives to MOFs is ultimately ideal to solution discovery.

Ultimately, due to the porous nature and modular disposition, MOFs are materials that exist at the cross-roads of different disciplines. At the moment, they are accepted to excel in applications related to gas storage and separation, as porous electrical conductors, and as heterogeneous catalysts. The challenges and opportunities present for this field and these materials to grow is marked by their increasing literature, patent and commercial presence. The field of MOFs presents an interesting combination of future research that is still needed, from the fundamental (how do they form?), to their industrialization (how cheap and fast can we make them?), to solving global climate and greenhouse gas problems. These questions which span from traditional and modern aspects of the MOF field illustrate the ability of this field to continually expand and the subsequent bright future of MOF chemistry.

Appendix

Table of Contents

S1 Experimental Considerations	83
S2 Supplementary Information for SION-1 and SION-2.....	85
S3 Solid state Characterisation Ln-SION-1 and Ln-SION-2.....	86
S3.1 Synthesis of Ln-SION-1 and Ln-SION-2.....	86
S3.2 PXRD of Ln-SION-2 and Ln-SION-1	86
S3.3 UV/Vis of Ln-SION-2 and Ln-SION-1	91
S3.4 Computational Details for Ln-SION-1 and Ln-SION-2	93
S3.5 Electronic Transition.....	94
S3.6 Density of State of Ln-SION-1.....	97
S3.7 Optimized Bond Distances	101
S3.8 Electron mobility (H ₂ generation) and Current Voltage (I-V) Curves	103
S4 Supplementary Information for SION-19.....	106
S5 Supplementary Information for SION-9	107
S5.1 Synthesis of SION-9	107
S5.2 Crystal Structure	107
S5.3 Solid State Characterization	109
S5.3.1 SION-9 Characterization	109
S5.3.2 SION-9' Characterization.....	111
S5.3.3 EPR and Solid State NMR Experiments	112
S5.4 Conductivity of SION-9.....	113
S5.5 Device Fabrication.....	128

S1 Experimental Considerations

Chemicals: All chemicals were purchased from Sigma Aldrich, Carl Roth, and Fischer Scientific and used without further purification.

Elemental analyses (EA): performed on a Thermo Scientific Flash 2000 Organic Elemental Analyzer.

Infrared spectra (IR): collected in air on a Perkin Elmer FT-IR/FIR Frontier Spectrometer (ATR) from 400 to 4000 cm^{-1} measuring the neat (solid) MOF sample.

Thermogravimetric analysis (TGA): performed under N_2 on a TGA Q 500, V20.13 with a balance gas flow of 10 mL/min and a sample gas flow of 25 mL/min. All samples were analyzed with a ramp of 5 $^{\circ}\text{C}/\text{min}$. to 950 $^{\circ}\text{C}$ followed by an isothermal hold for 15 minutes before cooling down.

Powder X-ray diffraction (PXRD): data was collected in air on a Bruker D8 Advanced using $\text{Cu K}\alpha$ radiation ($\lambda = 1.5418 \text{ \AA}$, 50 kW/40mA) on flat back groundless Si holders (Bragg-Brentano geometry). Samples were rotated during data collection. Simulated powder X-ray diffraction patterns were generated from the single crystal data using Mercury 3.0.

Single crystal X-ray diffraction (SCXRD): data were collected on a Bruker D8 Venture using $\text{Mo K}\alpha$ ($\lambda = 0.71 \text{ \AA}$).

^1H - ^{13}C NMR and MAS NMR: spectra, *in-situ* experiments and MAS NMR were collected on a 400 MHz Bruker NMR. Please refer to the NMR details in each section for the deuterated solvents and conditions used for each sample.

Inductively coupled plasma mass spectrometry (ICPMS): was performed on a Perkin Elmer ICPMS nexION 350D spectrometer.

High resolution X-ray photoemission spectra (XPS): on neutral adenine (Ade), commercial available $\text{Me}_2\text{NH}_2\text{Cl}^+$ and **SION-19'** were recorded on a Scienta ESCA 300 spectrometer located at Daresbury Laboratory, UK, which incorporated a rotating anode Al K α ($h\nu = 1486.6 \text{ eV}$) X-ray source and has an effective instrument resolution of 400 meV. The spectrometer was calibrated regularly to set the Fermi edge of a silver reference sample at zero binding energy. Samples were mounted on adhesive tape and, to reduce charging, the samples were covered with a stainless steel mask, through which a small area of the sample was exposed. In addition, it was necessary to use an electron flood gun to stabilize the surface charge. Use of a flood gun shifts all spectral features to high kinetic energy, and photoelectron spectra were therefore charge calibrated using a weak C1s contaminant peak (present due to surface hydrocarbon contamination from vacuum pumps and other sources) which was assigned a binding energy of 285.0 eV. The integrity of the samples under the measurement conditions of high vacuum and x-ray irradiation was determined by collecting several sequential N1s region spectra. No changes over time were seen in any sample, suggesting that no significant sample degradation occurred during the measurements. Spectra were fitted using CasaXPS software. All fitted peak shapes were 70:30 Gaussian:Lorentzian convolutions, and linear backgrounds were used in all cases.

Gas sorption measurements: Carbon Dioxide, Nitrogen and Methane isotherms were collected on activated **SION-19'** using the Intelligent Gravimetric Analyser Instrument (IGA) from Hiden Isochema. CO_2 isotherms were collected at 195 K, 273 K and 298 K at 1 bar, while N_2 isotherms were collected at 77 K and 1 bar. CH_4 isotherms were measured at 273 K and 298 K at 1 bar.

UV/vis: was collected in solid state at room temperature in air on a Perkin Elmer Lambda 650S

UV/vis spectrometer equipped with Labsphere integrating over the spectral range 190–900 nm using BaSO₄ reflectance standards. The spectra for **SION-19** and **SION-19'** were collected using the solid-state holder containing with the same amount of solid; the holder for **SION-19'** was filled in the dry box. Fluorescence excitation and emission spectra and lifetimes were collected at room temperature on a Perkin-Elmer LS 55 fluorescence spectrometer. Excitation and emission spectra of **SION-19** and **SION-19'** (sealed in a capillary to prevent any re-absorption of H₂O moisture from the atmosphere from **SION-19'**) were collected in the range between 200-600 nm and 400-700 nm respectively with scan speed of 10 nm/min. Data obtained was collected in reflectance mode, and treated using the Kubelka-Munk function give the absorbance of the MOFs. Subsequently, the data collected was processed and normalized through Origin Pro 8.5 using the normalization function found within the software.

Ultra High Performance Liquid Chromatography (UHPLC): was carried out using a Acquity UPLC HSS T3, 1.8 μ m, 2.1 x 100 mm column from Waters, on a ThermoScientific Orbitrap Q Exactive HF equipped with H-ESI and AP-MADLI source.

Note - BET Surface Area: We would like to inform the reader that for MOFs where the surface area is discussed, by convention we only report the BET surface area instead of the Langmuir Surface area. Although there is a wide variety of literature discussion on the most accurate and ideal way to measure the surface area of a MOFs, such discussion is beyond the scope of this thesis. Here, surface area only is used to indicate porosity and instead the pore volume plays a more significant role and is more applicable to the discussions in this thesis.

S2 Supplementary Information for SION-1 and SION-2 studies

Please note that the supporting information for this chapter can be found in our publication:

Anderson, L. Samantha; Gładysiak, Andrzej; Boyd, G. Peter; Ireland, P. Christopher; Miéville, Pascal; Tiana, Davide; Vlaisavljevich, Bess; Schouwink, Pascal; Van Beek, Wouter; Gagnon, J. Kevin; Smit, Berend; Stylianou, C. Kyriakos. Formation pathways of metal–organic frameworks proceeding through partial dissolution of the metastable phase, *CrysEngComm*. **2017**, 19, 3407-3413

A note for PXRD patterns of SION-1 and SION-2: Following SCXRD, a theoretical PXRD pattern is generated which is compared to an experimental PXRD pattern of the material. The theoretical pattern, or simulated PXRD pattern, is calculated from the single crystal structure of a MOF, and provides a pattern of a pure crystalline form which is considered to be a reliable reference standard of a MOF. It should be provided when available with all experimental PXRD patterns to ensure that the bulk material of the powder reflects the purity of the pure single crystalline form. However, the experimental PXRD pattern can differ from that of the theoretical pattern, which is what is seen in the **SION-1**, **SION-2**, **Ln-SION-1** and **Ln-SION-2** patterns. Measurements of these samples were performed as flat powders on backgroundless Si sample holders, and so it is possible that the orientations of the crystallites within the powder cause minor discrepancies between the two patterns. To overcome this, samples can instead be measured in capillaries, or refinements/fits can be done on the experimental powder patterns to confirm the unit cell dimensions which can be then compared to the dimension obtained via SCXRD. In the cases of the PXRD patterns presented in this chapter, the unit cell dimensions were compared between the experimental PXRD patterns and SCXRD obtained data, which matched well.

A note for VT-PXRD pattern of the SION-2 and SION-1 transformation: A third potential form within this transformation, or any intermediates, were ruled as unlikely during the VT-PXRD which showed only the evolution of **SION-2** and **SION-1** peaks and no other Bragg reflections that would otherwise indicate the presence of a third form.

S3 Solid State Characterization of Ln-SION-2 and Ln-SION-1

S3.1 Synthesis of Ln-SION-1 and Ln-SION-2

Synthesis of **Ln-SION-2**: H₂DHBDC (20 mg) and Ln(NO₃)₃·6H₂O (20 mg) were mixed in a 12 mL vial. 2 mL of DMF was added, and stirred until the entire solution was clear. Following this, 0.5 mL of H₂O was added and the scintillation vial was capped, and shaken to ensure the solution is homogeneous. The vials were placed in an oven and heated at 120 °C, for 24 hrs with a temperature ramp of 2.0 °C, and cooling ramp of 0.2 °C.

Synthesis of **Ln-SION-1**: **Ln-SION-1** was synthesized following the same synthetic protocol with that of **SION-2** and the reaction was heated at 120 °C for 72 hrs (76 % yield based on Tb).

S3.2 PXRD of Ln-SION-2 and Ln-SION-1

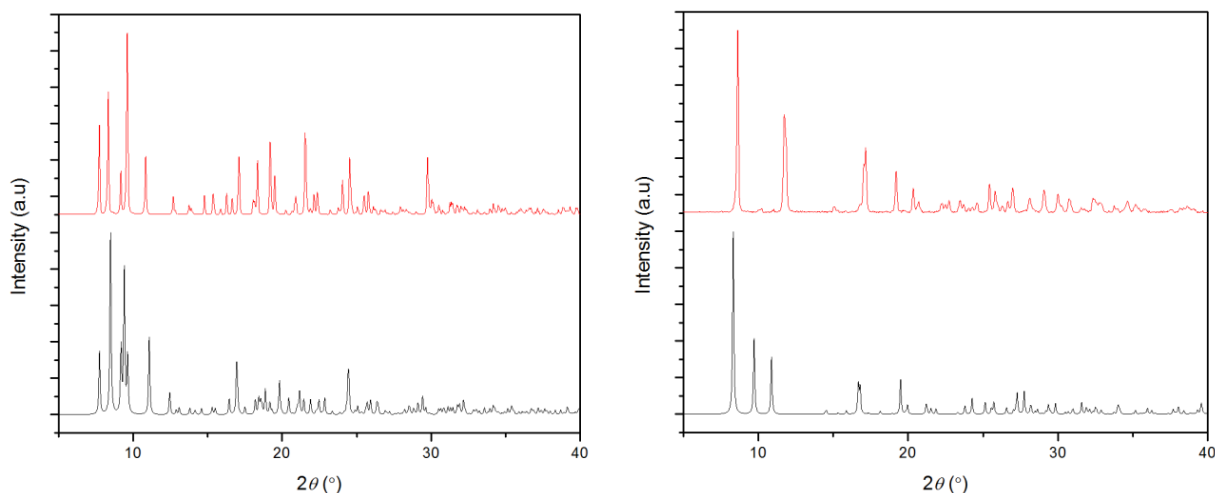


Figure S1- PXRD of Ce-SION2 and Ce-SION-1: Left, **Ce-SION-2**. Right, **Ce-SION-1**. Color scheme for both patterns: black, theory; red, experimental.

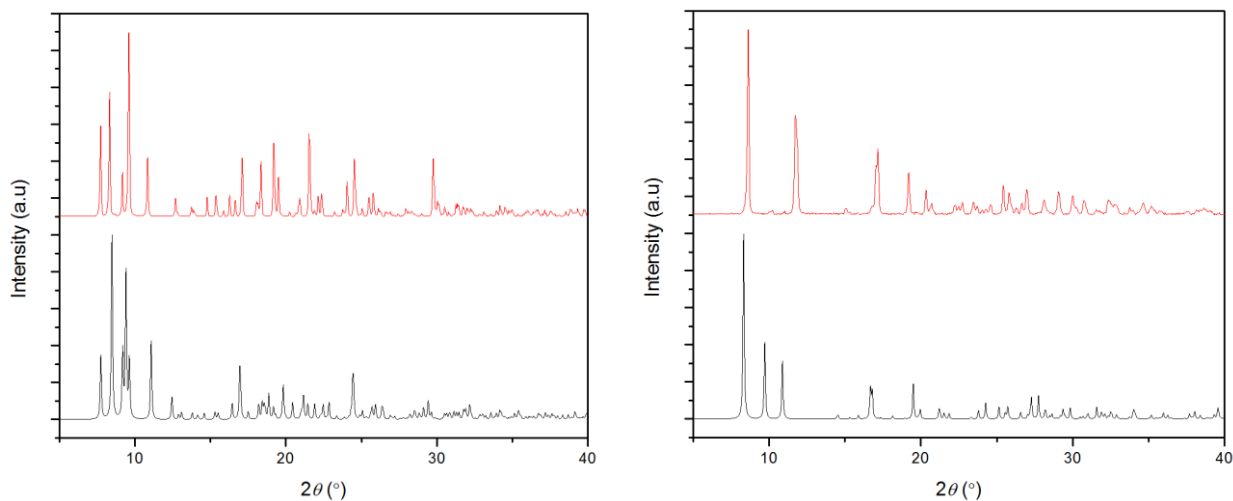


Figure S2- PXRD of Nd-SION2 and Nd-SION-1: Left, Nd-SION-2. Right, Nd-SION-1. Color scheme for both patterns: black, theory; red, experimental.

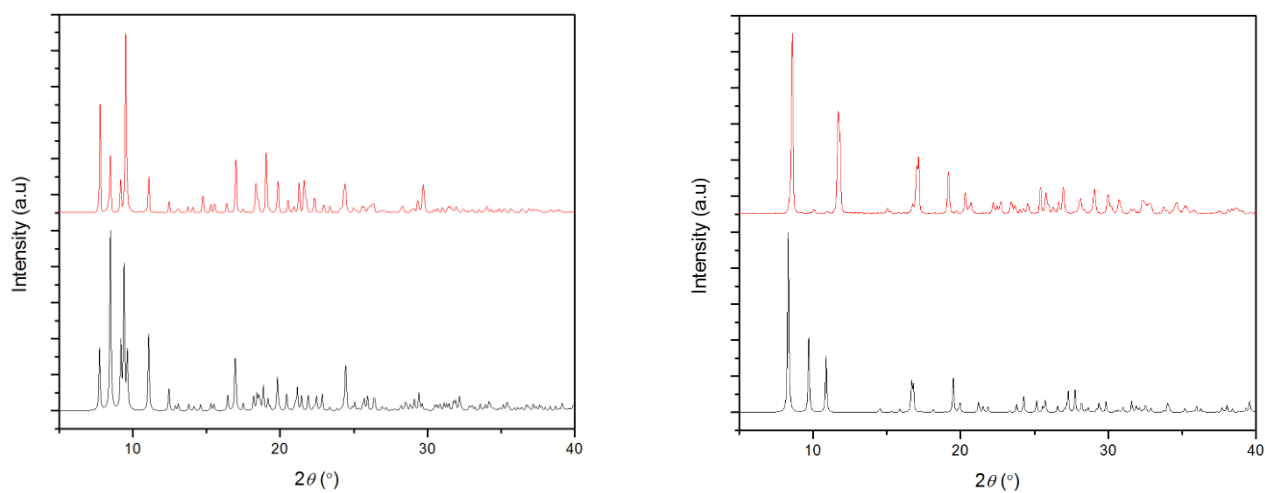


Figure S3- PXRD of Eu-SION2 and Eu-SION-1: Left, Eu-SION-2. Right, Eu-SION-1. Color scheme for both patterns: black, theory; red, experimental.

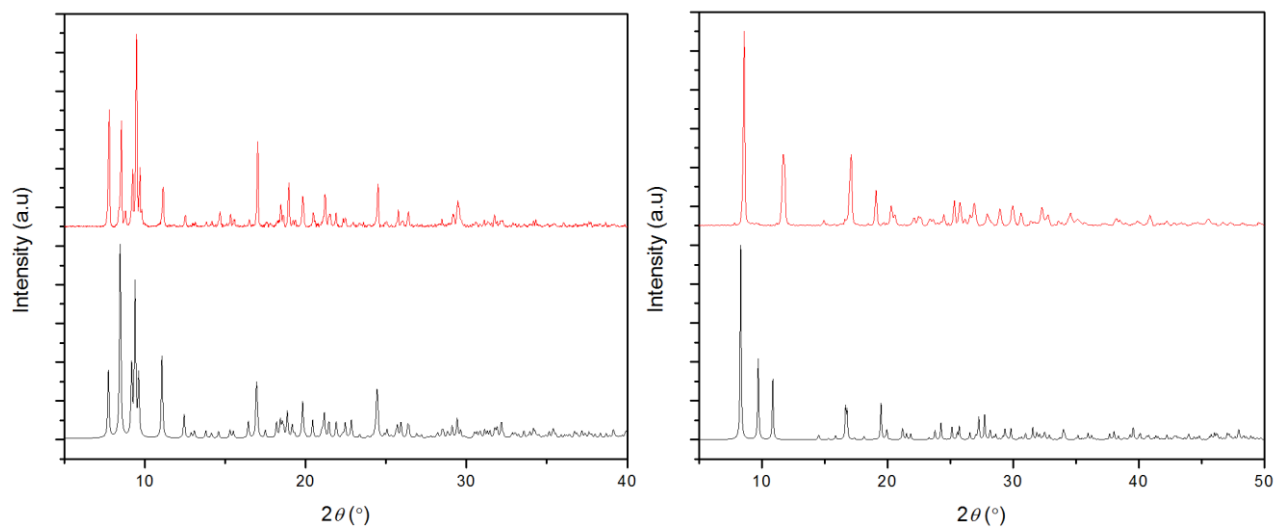


Figure S4- PXRD of Gd-SION2 and Gd-SION-1 : Left, **Gd-SION-2**. Right, **Gd-SION-1**. Color scheme for both patterns: black, theory; red, experimental.

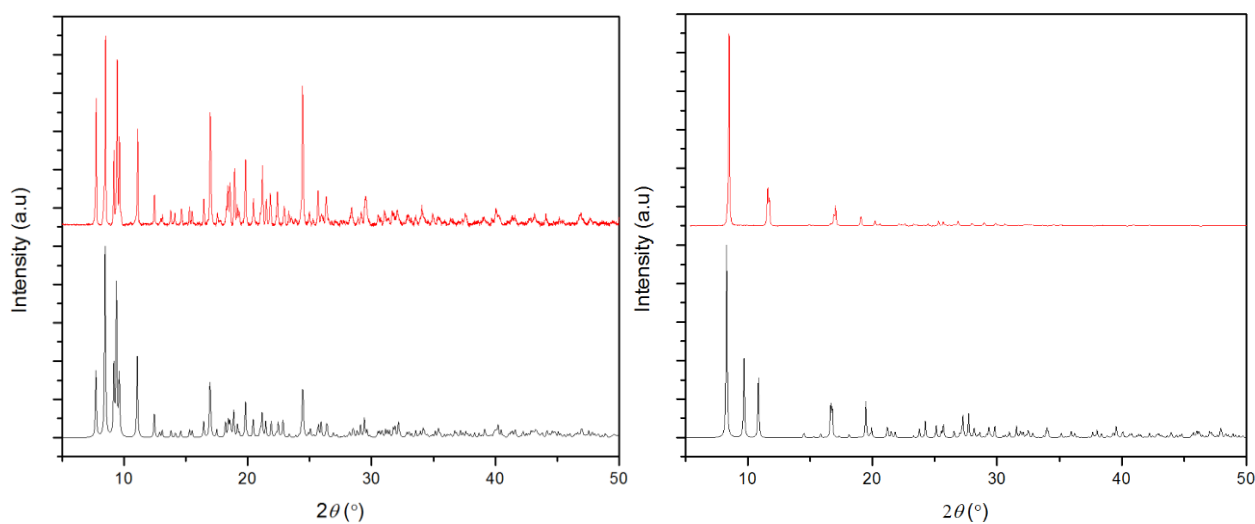


Figure S5- PXRD of Tb-SION2 and Tb-SION-1: Left, **Tb-SION-2**. Right, **Tb-SION-1**. Color scheme for both patterns: black, theory; red, experimental.

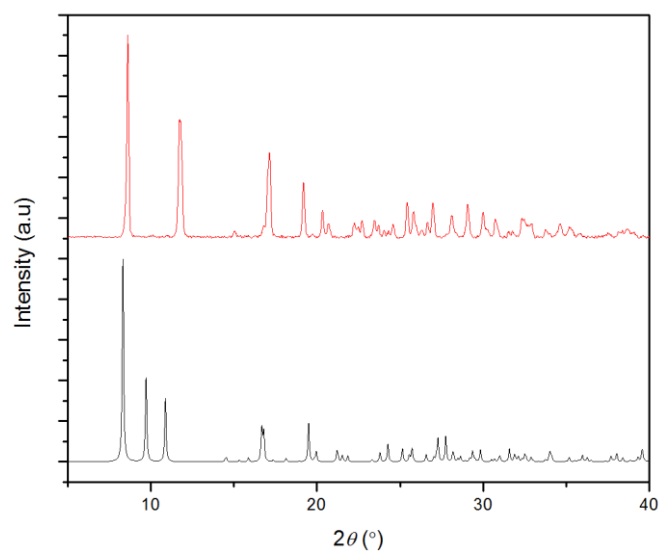


Figure S6- PXRD of Dy-SION-1. Color scheme: black, theory; red, experimental.

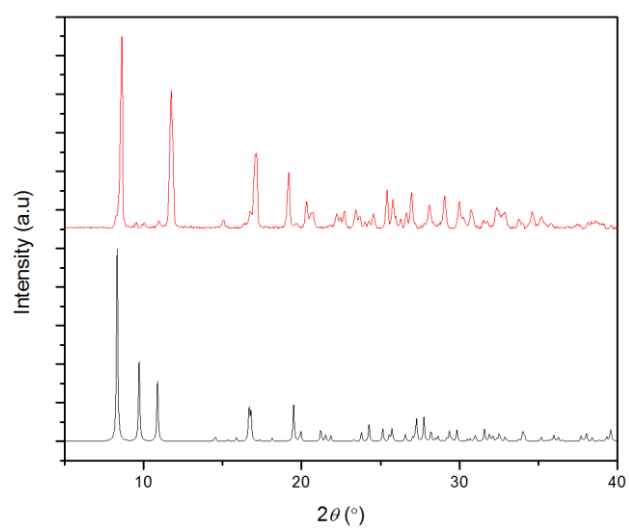


Figure S7- PXRD of Ho-SION-1. Color scheme: black, theory; red, experimental.

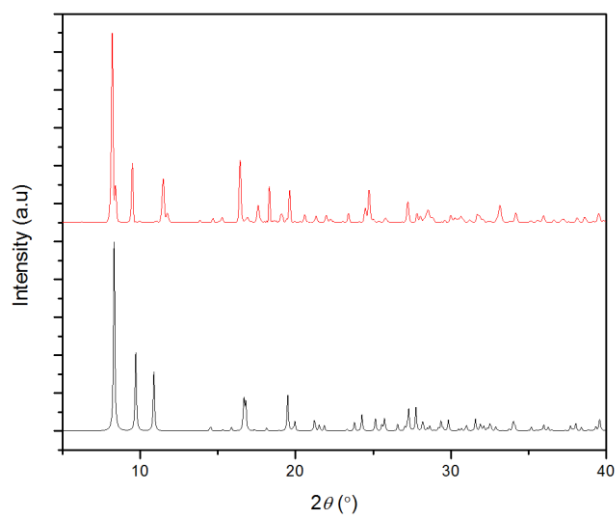


Figure S8- PXRD of Er-SION-1. Color scheme: black, theory; red, experimental.

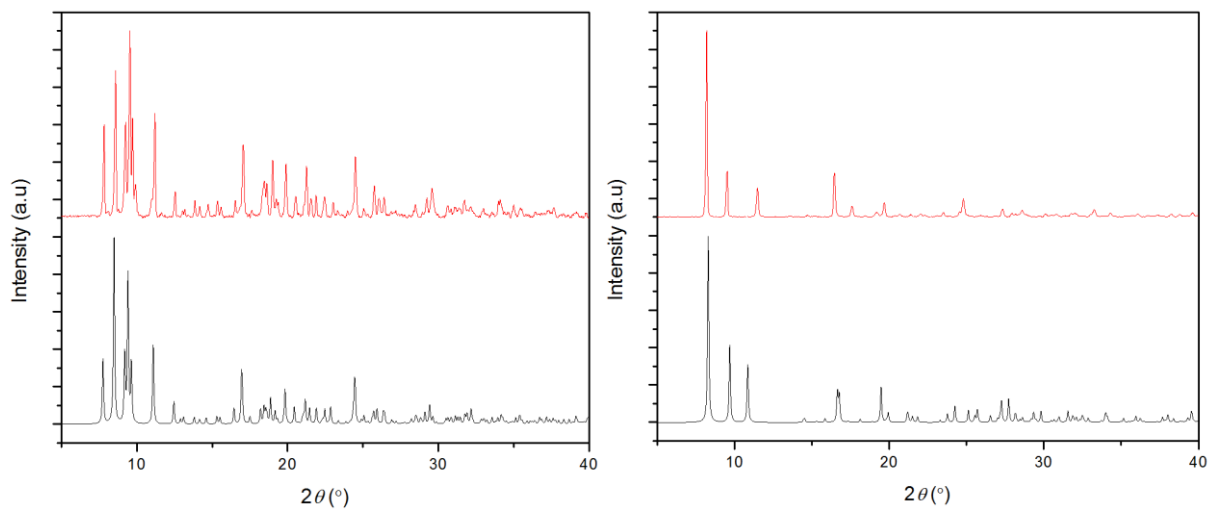


Figure S9- PXRD of Yb-SION2 and Yb-SION-1: Left, Yb-SION-2. Right, Yb-SION-1. Color scheme for both patterns: black, theory; red, experimental.

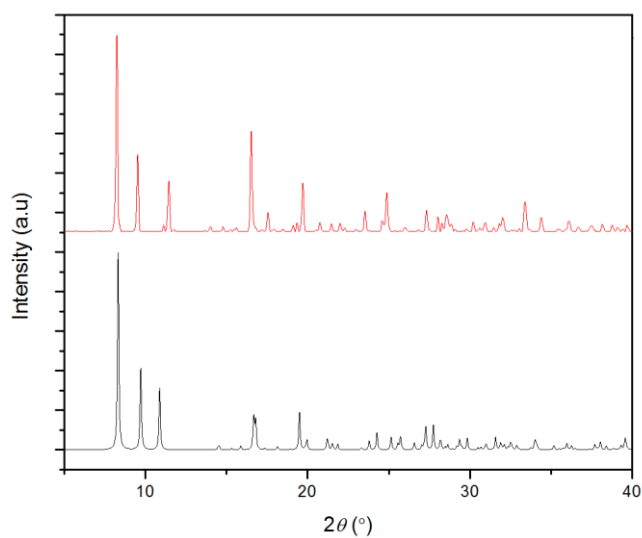


Figure S10- PXRD of Lu-SION-1. Color scheme: black, theory; red, experimental.

S3.3 UV/Vis of Ln-SION-2 and Ln-SION-1

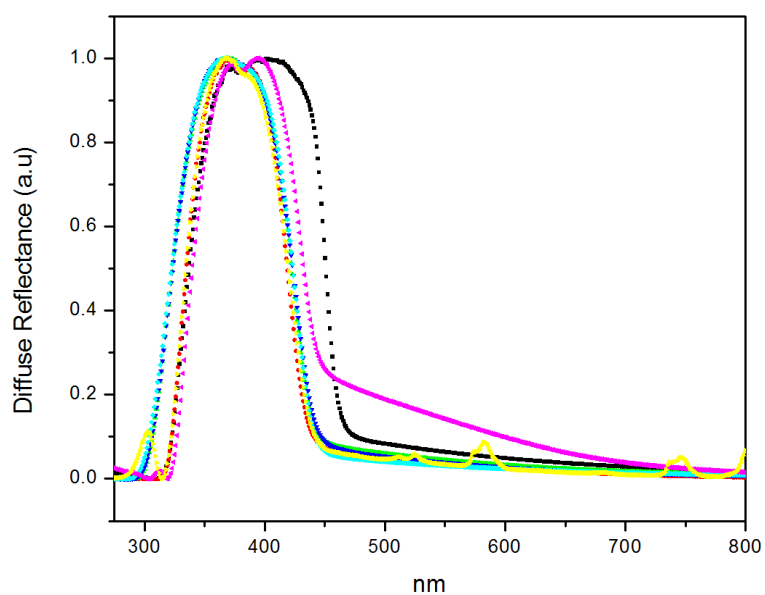


Figure S11- Diffuse reflectance spectra of Ce-to-Yb-SION-2. Colour scheme: black, ligand; light blue, Ce; yellow, Nd; dark blue, Eu; magenta, Gd; red, Tb; neon green, Yb.

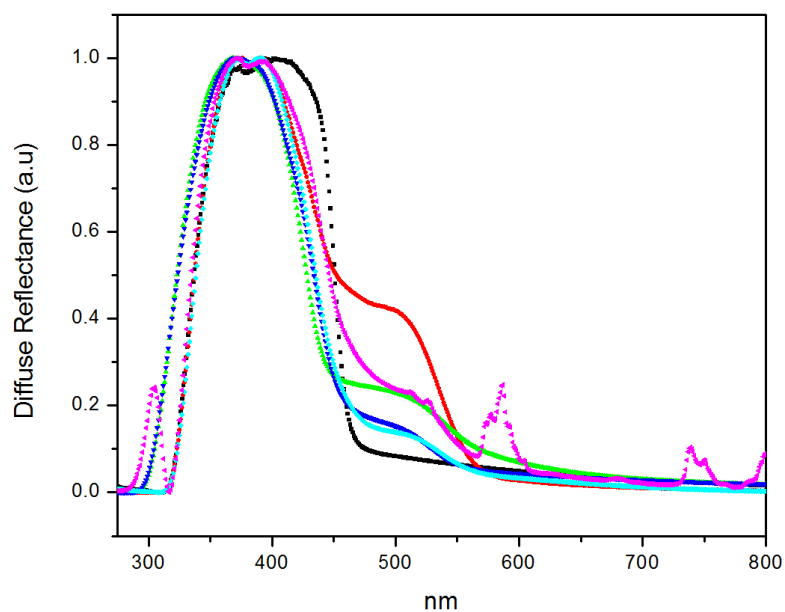


Figure S12- Diffuse reflectance spectra of Ce-to-Tb-SION-1. Colour scheme: black, ligand; dark blue, Ce; magenta, Nd; lime green, Eu; neon blue, Gd; red, Tb.

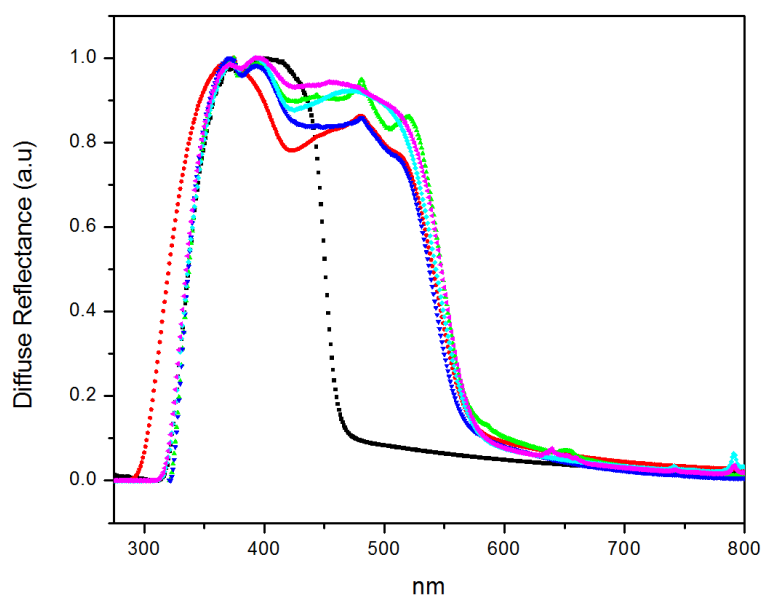


Figure S13- Diffuse reflectance spectra of Dy-to-Lu-SION-1. Colour scheme: black, ligand; neon blue, Dy; magenta, Ho; lime green, Er; red, Yb; dark blue, Lu.

S3.4 Computational Details for Ln-SION-1 and Ln-SION-2

All the calculations were done using the solid-state quantum chemical code Quantum Espresso (version 6.0). All the geometries were performed at the gamma point using the semi-local PBEsol exchange correlation functional, using norm-conserving pseudopotentials with a cut-off of 170 Ry. Dispersion force corrections were also employed. The force and energy thresholds were set to 1E-05 Ry and 1E-04 Ry, respectively, while the pressure convergence was set to 1E-01 Kbar. The spin state of single atoms were allowed to relax during the optimization with an SCF convergence threshold of 1E-09. The Density of State were calculated performing single point calculations at the PBEsol optimized geometries using the non-local hybrid GAUPBE functional. The Brillouin zone for these calculations were sampled using a Monkhorst-Pack grid of 2x3x2 and 2x2x2 k-points for **SION-1** and **SION-2** respectively. Here, the calculations have been performed after solvent removal.

It should be noted that for spin-orbit coupling (and correction) (SO), while it is relevant for the description of the 4f energy level in Ln-based materials, the **SION-1** and **SION-2** electronic structures (top VB and bottom CB) and their related properties (optical transitions) are characterized by π and π^* organic orbitals and 5d metal state, for whose SO coupling (and correction) is negligible. More information on the different spin configurations can be found in the following sections (SI sections 5-7).

S3.5 Electronic Transition

Table S1- DFT GAUPBE direct band gap: calculated Ln(5d)/ligand(π^*) and measured electronic transition for **Ln-SION-1**, and dispersion of the LUCOs through the b-axis. All data in eV.

M	Calculated Band Gap	Calculated L(π) \rightarrow Ln(5d)/L(π^*)	Measured L(π) \rightarrow Ln(5d)/L(π^*)	Calculated LUCO dispersion
Ce	1.63	2.08	2.18	0.04
Nd	0.43	2.10	2.21	0.04
Eu	2.75	2.75	2.10	0.04
Gd	2.15	2.15	2.18	0.05
Tb	2.13	2.13	2.11	0.05
Er	2.17	2.17	2.14	0.10
Yb	2.34	2.34	2.18	0.25
Lu	1.88	1.88	2.18	0.18

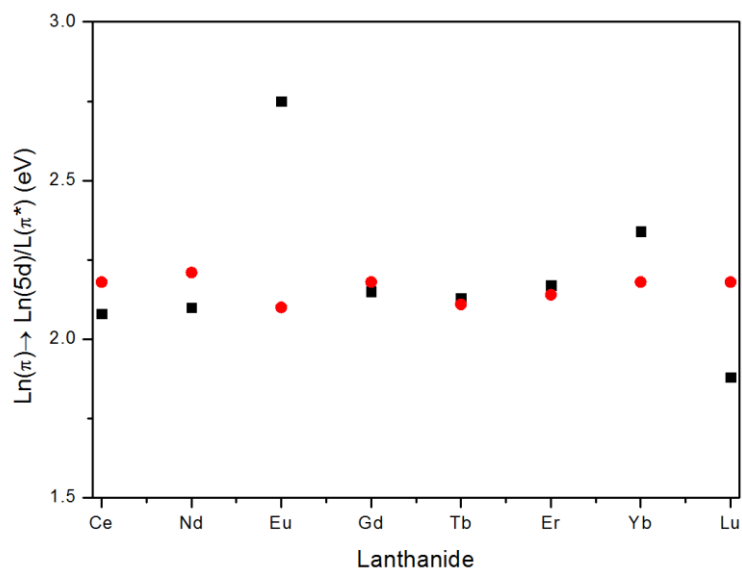


Figure S14- Plotted $L(\pi) \rightarrow Ln(5d)/L(\pi^*)$. Calculated (red dots) and measured (black squares).

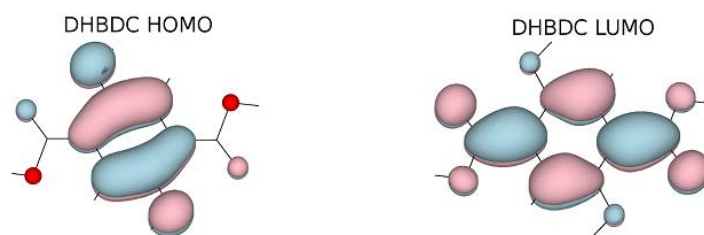


Figure S15- Frontier orbitals for the isolated in vacuum DHBDC. Atoms scheme colour: red, O; dark grey, C. The electronic transition is $\pi \rightarrow \pi^*$ with a band gap of 3.40 eV.

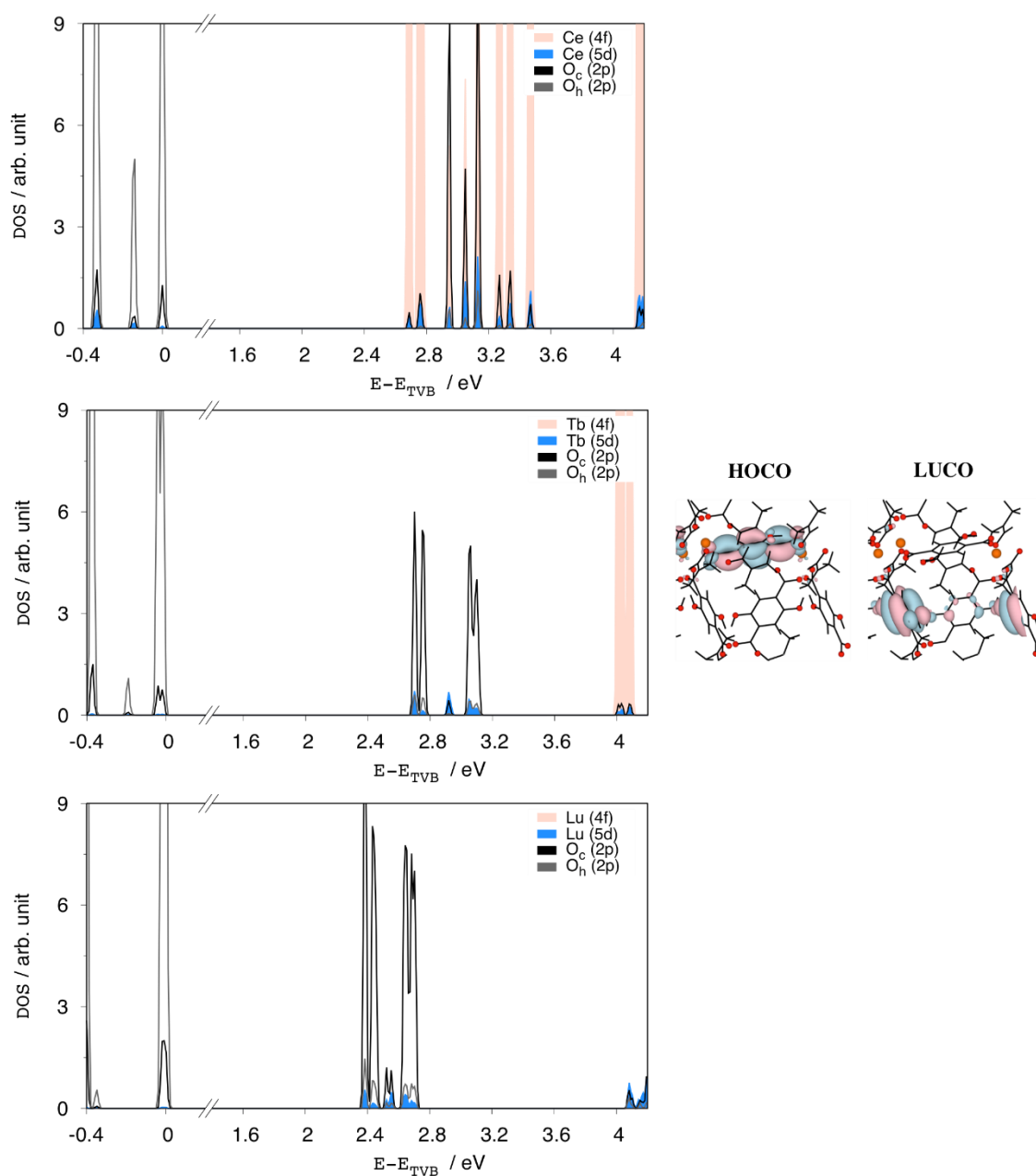


Figure S16- GAUPBE partial Density of State and frontier orbitals. The GAUPBE partial Density of State (left) and the corresponding frontier orbitals (right) for the isolated in vacuum **Ce-**, **Tb-** and **Lu-SION-2**. For the DOS the Fermi level was aligned to the HOCOs. Color scheme for pDOS plots: grey, carboxylate O 2p; black, oxido O 2p orbitals; pale orange, Ln 4f orbitals; blue, Ln 5d orbitals. Atoms color scheme: red, O; orange, Tb, dark grey, C.

S3.6 Density of State of Ln-SION-1

Ce-SION-1

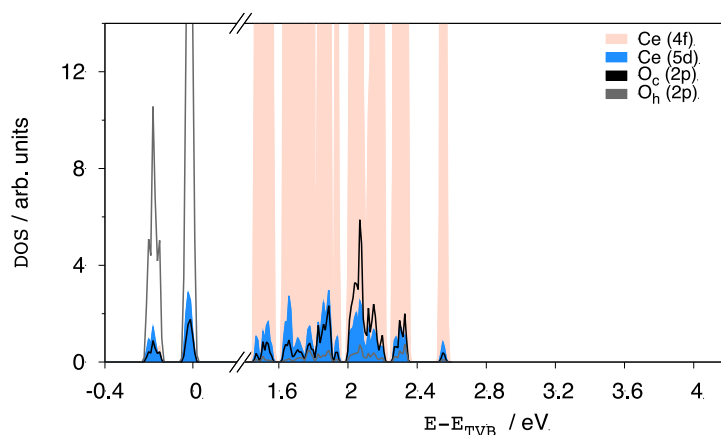


Figure S17- pDOS of Ce-SION-1. The valence of Ce(III) is $[\text{Xe}]4f^15d^0$. The HOCOs are mainly composed of the ligand π -orbitals whilst the LUCOs are made by the empty f-orbitals. Color scheme for pDOS plots: grey, carboxylate O 2p; black, oxido O 2p orbitals; pale orange, Ln 4f orbitals; blue, Ln 5d orbitals.

Nd-SION-1

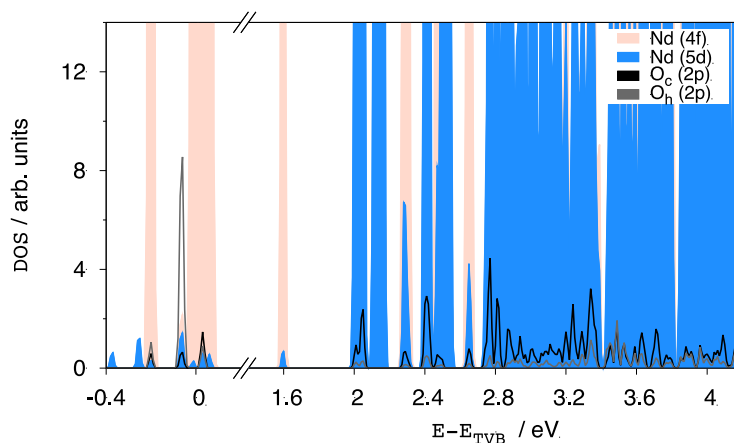


Figure S18- pDOS of Nd-SION-1. The valence of Nd(III) is $[\text{Xe}]4f^35d^0$. The HOCOs are mainly composed of the ligand π orbitals whilst the LUCOs are made by the empty f-orbitals. After the conduction band several mixed metal states are present – many absorption bands are observed in the UV/vis spectrum. Color scheme for pDOS plots: grey, carboxylate O 2p; black, oxido O 2p orbitals; pale orange, Ln 4f orbitals; blue, Ln 5d orbitals.

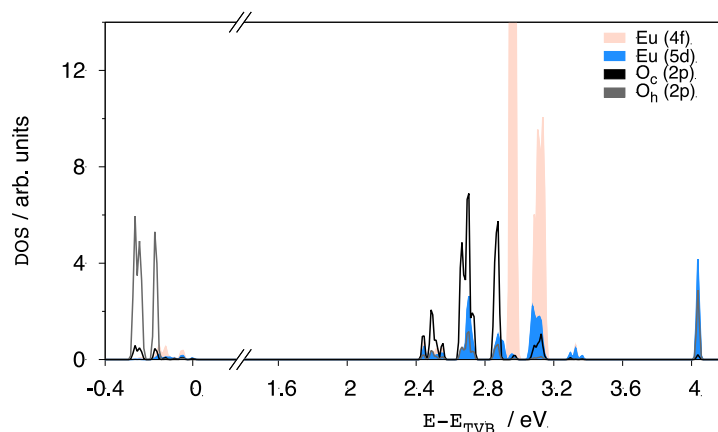
Eu-SION-1

Figure S19- pDOS of Eu-SION-1. The valence of Eu(III) is $[\text{Xe}]4f^65d^0$. The HOCOs are mainly composed of the ligand π -orbitals whilst the LUCOs are made by the ligand's π^* orbitals with only a small amount of state arising from the Eu(5d) orbitals. Color scheme for pDOS plots: grey, carboxylate O 2p; black, oxido O 2p orbitals; pale orange, Ln 4f orbitals; blue, Ln 5d orbitals.

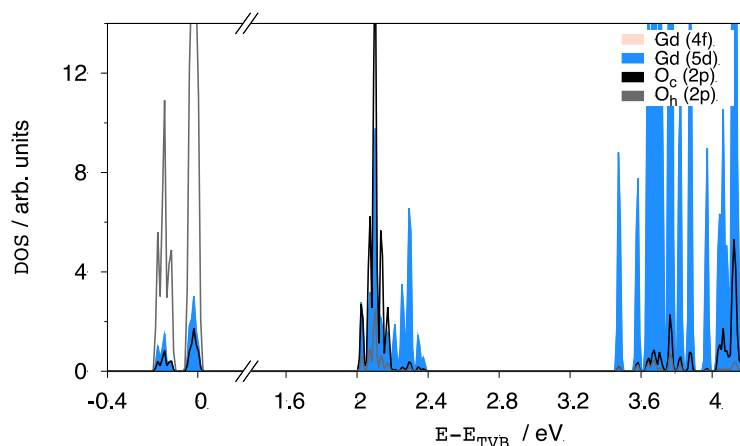
Gd-SION-1

Figure S20- pDOS of Gd-SION-1. The valence of Gd(III) is $[\text{Xe}]4f^75d^0$. The HOCOs are mainly composed of the ligand π -orbitals while the LUCOs are made by a mixture of Ln(5d)/ligand(π^*) orbitals. Color scheme for pDOS plots: grey, carboxylate O 2p; black, oxido O 2p orbitals; pale orange, Ln 4f orbitals; blue, Ln 5d orbitals.

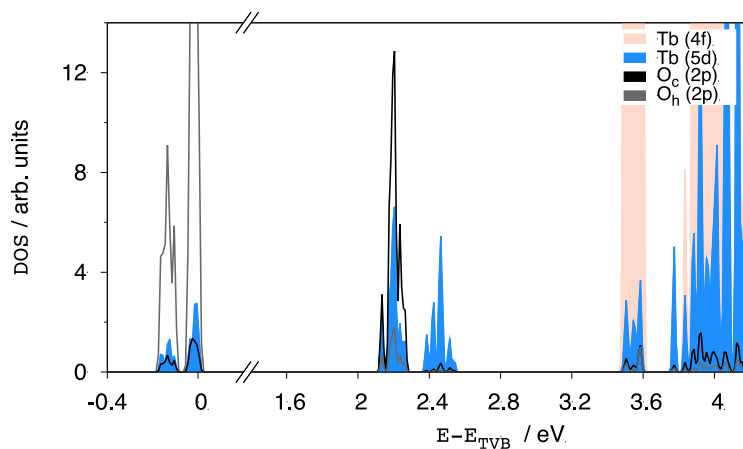
Tb-SION-1

Figure S21- pDOS of Tb-SION-1. The valence of Tb(III) is [Xe]4f⁸5d⁰. The HOCOs are mainly composed of the ligand π -orbitals whilst the LUCOs are made by a mixture of Ln(5d)/ligand(π^*) orbitals. Color scheme for pDOS plots: grey, carboxylate O 2p; black, oxido O 2p orbitals; pale orange, Ln 4f orbitals; blue, Ln 5d orbitals.

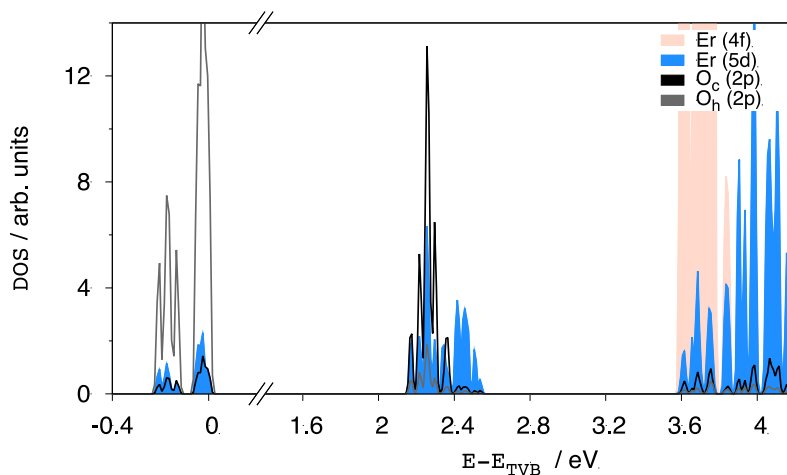
Er-SION-1

Figure S22- pDOS of Er-SION-1. The valence of Er(III) is [Xe]4f¹¹5d⁰. The HOCOs are mainly composed of the ligand π -orbitals whilst the LUCOs are made by a mixture of Ln(5d)/ligand(π^*) orbitals. Color scheme for pDOS plots: grey, carboxylate O 2p; black, oxido O 2p orbitals; pale orange, Ln 4f orbitals; blue, Ln 5d orbitals.

Yb-SION-1

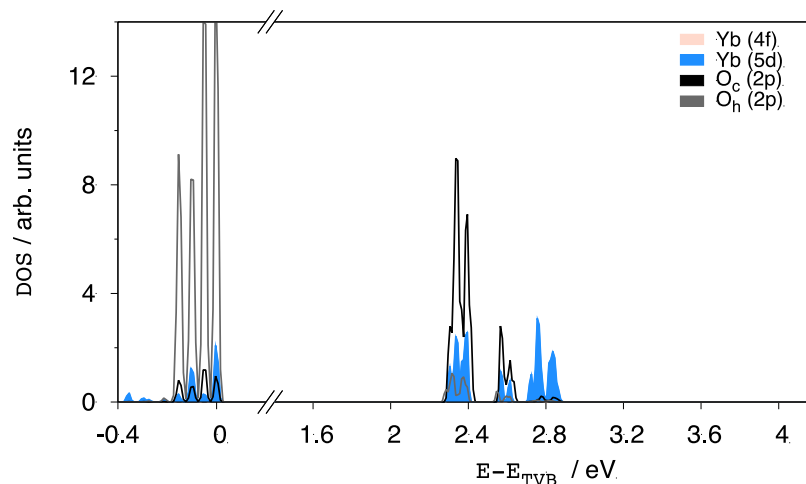


Figure S23- pDOS of Yb-SION-1. The valence of Yb(III) is $[Xe]4f^{13}5d^0$. The HOCOs are mainly composed of the ligand π -orbitals whilst the LUCOs are made by a mixture of Ln(5d)/ligand(π^*) orbitals. Color scheme for pDOS plots: grey, carboxylate O 2p; black, oxido O 2p orbitals; pale orange, Ln 4f orbitals; blue, Ln 5d orbitals.

Lu-SION-1

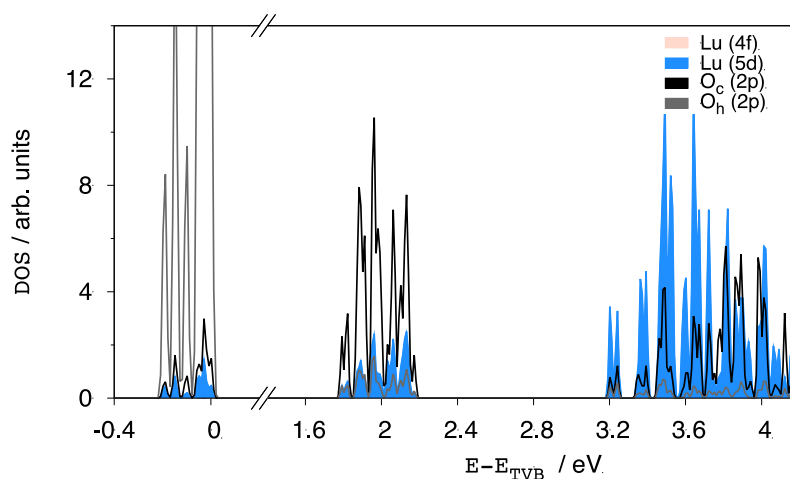


Figure S24- pDOS of Lu-SION-1. The valence of Lu(III) is $[Xe]4f^{14}5d^0$. The HOCOs are mainly composed of the ligand π -orbitals whilst the LUCOs is made by a mixture of Ln(5d)/ligand(π^*) orbitals. Color scheme for pDOS plots: grey, carboxylate O 2p; black, oxido O 2p orbitals; pale orange, Ln 4f orbitals; blue, Ln 5d orbitals.

S3.7 Optimized Bond Distances

Table S2- DFT PBEsol distances in Angstrom for Ln-SION-1. O_{ac} = Carboxylate Oxygen, O_{oxido} = Oxido Oxygen, O_{avg} = average distance.

Distance	Ce	Nd	Eu	Gd	Tb	Er	Yb	Lu
Ln-O _{ac1}	2.635	2.685	2.726	2.432	2.398	2.432	2.359	2.515
Ln-O _{ac2}	2.579	2.525	2.543	2.472	2.450	2.412	2.379	2.405
Ln-O _{ac3}	2.520	2.530	2.511	2.415	2.409	2.378	2.361	2.370
Ln-O _{ac4}	2.650	2.645	2.637	2.714	2.675	2.681	2.690	2.642
Ln-O _{ac5}	2.500	2.498	2.497	2.396	2.376	2.330	2.332	2.299
Ln-O _{ac6}	2.760	2.675	2.660	2.382	2.365	2.326	2.326	2.345
Ln-O_{oxido}	2.495	2.473	2.491	2.340	2.308	2.287	2.308	2.275
Ln-O _{dmf}	2.550	2.551	2.546	2.431	2.409	2.396	2.387	2.350
Ln-O _{avg}	2.589	2.573	2.576	2.448	2.424	2.406	2.393	2.366

Table S3- DFT PBEsol distances in Angstrom for CO of the oxido group in Ln-SION-1. O_{oxido} = Oxido Oxygen. A comparison with the CO_{oxido} bond distance of the ligand (DHBDC = 1.354), its anionic form (DOBDC = 1.270), its semiquinone (1,4-Cyclohexanedione-2,5-dicarboxylic radical = 1.252), and its quinone form (1,4-Cyclohexanedione-2,5-dicarboxylic acid = 1.229) reveal that the ligand it is always in its anionic state and that an interaction with the metal is present producing an of bond elongation.

M	C- O _{oxido}
Ce	1.302
Nd	1.282
Eu	1.274
Gd	1.313
Tb	1.321
Er	1.306
Yb	1.300
Lu	1.285

S3.8 Electron mobility (H₂ generation) and Current Voltage (I-V) Curves

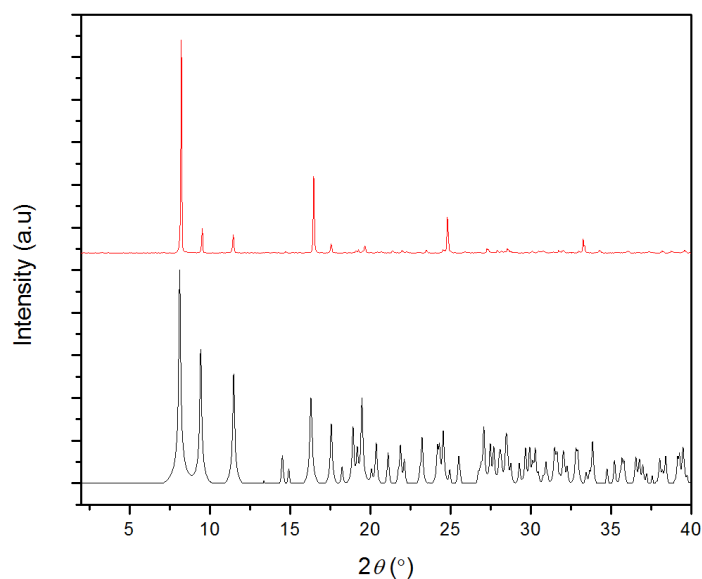


Figure S25- PXRD of Yb-SION-1 after following photocatalytic experiments. Color scheme: black, theory; red, experimental.

Based off of the calculated LUCO band dispersions of 0.04, 0.25 and 0.18 eV for **Ce-**, **Yb-**, and **Lu-SION-1**, electron mobility tests were performed (Table S4). For this, photocatalytic H₂ generation experiments were chosen to represent the potential for electron mobility because following light irradiation, electrons within the MOF have to move to the surface and interact with the co-catalyst and subsequently generate detectable amounts of H₂. From previous work published by our group, it is already known the co-catalysts under isolation do not generate H₂, and a blank with just the DHBDC ligand does not as well.⁸⁶

Hydrogen generation was not seen for **Ce-SION-1**, which is attributed to the low band dispersion. Whereas with **Yb-SION-1** (largest band dispersion) electrons have sufficient mobility to reach the surface, and through the process previously described generate detectable amounts of H₂. Following experiments it was further confirmed by PXRD that **Yb-SION-1** is stable (Figure S24), and does not undergo degradation.

Table S4- Electron mobility experiments of Yb-SION-1 and Ce-SION-1 via H₂ generation. Here, optimized **Yb-SION-1** conditions are highlighted in yellow, and we're applied to the Ce-SION-1 below.

Sample	Conditions	Co-Cat	Irradiation time (hrs)	Area of Peak (GC)
Yb-SION-1	CH ₃ CN: 81.96 v/v% H ₂ O: 1.64 v/v% TEA: 16.39 v/v% MOF: 17 mg Volume of solution: 17 mL	Ni ₂ P: 5.8 wt %	3	162.8
Yb-SION-1	CH ₃ CN: 70 v/v% H ₂ O: 15 v/v% TEA: 15 v/v% MOF: 50 mg Volume of solution: 20 mL	Ni ₂ P: 9.4 wt %	24	549
Yb-SION-1	CH ₃ CN: 70 v/v% H ₂ O: 15 v/v% TEA: 15 v/v% MOF: 50 mg Volume of solution: 20 mL	Ni ₂ P: 9.4 wt %	40	383
Yb-SION-1	CH ₃ CN: 64.70 v/v% H ₂ O: 17.64 v/v% TEA: 11.76 v/v% MOF: 20 mg Volume of solution: 17 mL	Pt: 0.8 wt %	40	240
Yb-SION-1	CH ₃ CN: 81.96 v/v% H ₂ O: 1.64 v/v% TEA: 16.39 v/v% MOF: 17 mg Volume of solution: 17 mL	Ni ₂ P: 5.8 wt %	20	612
Ce-SION-1	CH ₃ CN: 81.96 v/v% H ₂ O: 1.64 v/v% TEA: 16.39 v/v% MOF: 17 mg Volume of solution: 17 mL	Ni ₂ P: 5.8 wt %	24	0

Following electron mobility experiments, we further invested the **Ln-SION-1** series through current-voltage (I-V) curves to determine if electron mobility in **Ce-SION-1** is present, however only isolated to the 1-dimension chains within the structure and cannot move freely within the MOF (**Yb-SION-1**). **Ln-SION-1** samples (10 mg) were first ground for 10 minutes in a Agate mortar, followed by dispersion in acetone via a sonicating bath (10 minutes). The samples were prepared by drop-casting the **Ln-SION-1** dispersed samples on F:SnO₂ (FTO). By varying the concentration of acetone, we were able to control the thickness of the samples.

The current-voltage (I-V) profile for the FTO/**Ln-SION-1** samples were measured by using In-Ga drop for the top-contact. Here, a Ga-In eutectic mixture was drop casted on the active layer and

used as an electrode. A micromanipulator was used to form an electrical contact with the respective electrodes to measure the I-V characteristics of the photovoltaic device under a nitrogen atmosphere using a custom-built probe station and a Keithley 2612A dual-channel source measure unit under simulated AM1.5G irradiation from a 300 W Xe arc lamp set to 100 mW cm^{-2} with a calibrated Si photodiode. For each measurements, scans of voltage from -20V to 20V (**Yb-SION-1**) and -10V to 10V (**Ce-SION-1**) was swept while measuring the current to obtain the respective I-V curves. Various different locations on the active layer films were measure by moving the In-Ga bead with the micromanipulator. Dark measurements were first performed followed by illumination under simulated AM1.5G irradiation.

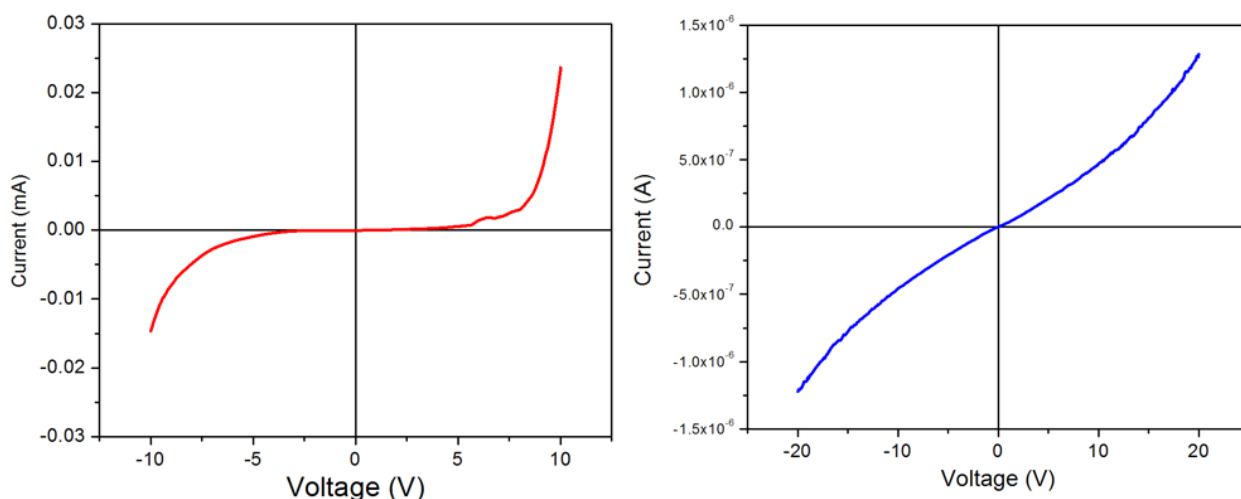


Figure S26- Current-Voltage (I-V) curves. Here, these I-V curves were measured from of device using ITO/PEDOT.PSS/Active Layer/InGa in the dark: left, **Ce-SION-1**; right, **Yb-SION-1**.

Deposition of **Ce-**, and **Yb-SION-1** were done on either bare or PEDOT-PSS-coated FTO using the same procedure previously described. These I-V measurements demonstrate the qualitative semi-conductor-like behavior of both the **Ce-SION-1** and **Yb-SION-1** MOFs.

S4 Supplementary Information for SION-19

Please note that the supporting information for this chapter can be found in our publication:

Anderson, L. Samantha; Boyd, G. Peter; Gładysiak, Andrzej, Nguyen, N. Tu; Palgrave, G. Robert; Kubicki, Dominik; Emsley, Lyndon; Bradshaw, Darren; Rosseinsky, J. Matthew, Berend; Stylianou, C. Kyriakos. Nucleobase Pairing and Photodimerization in a Biologically Derived Metal-Organic Framework Nanoreactor, *Nat. Commun.* **2019**, 10, 1612

S5 Supplementary Information for SION-9

S5.1 Synthesis of SION-9

SION-9 was synthesized through the combination of $\text{Zn}(\text{NO}_3)_2 \cdot 6(\text{H}_2\text{O})$ (17 mg, 0.057 mmols), TCPP (10 mg, 0.0126 mmols) and Ade (8 mg, 0.059 mmols), in an acidic DMF/ H_2O / HNO_3 solution (5.5 mL: 0.5 mL: 4 drops) (Scheme S1). The vial is capped and placed in the oven for 72 hrs at 120°C with a temperature ramp of 2.0°C, and cooling ramp of 0.2°C, affording red square like crystals in a 75% yield (based off of Zn). The formula of **SION-9** was determined to be $[\text{Zn}_8(\text{TCPP})_2(\text{Ade})_3]$ on the basis of the combined results of single-crystal X-ray diffraction (SCXRD), thermogravimetric analysis (TGA) and elemental analysis (EA). Anal. Calcd for $[\text{Zn}_8(\text{TCPP})_2(\text{Ade})_3]$: C 50.45, H 2.75, N 10.55. Experimental: C 49.15, H 4.25, N 12.54

S5.2 Crystal Structure

A high-quality single crystal of **SION-9** was isolated from the mother liquor, and mounted onto the PILATUS@SNBL diffractometer at the BM01 beamline (European Synchrotron Radiation Facility, Grenoble, France).²⁷⁵ The crystal was probed with X-rays, and the intensities of Bragg reflections were recorded with the PILATUS2M detector. Raw data were processed with CrysAlisPro (v. 1.171.38.43) program suite,²⁷⁶ and the empirical absorption correction was performed using spherical harmonics, implemented in SCALE3 ABSPACK scaling algorithm. Crystal structure was solved with the SHELXT structure solution program using Intrinsic Phasing,²⁷⁷ and refined with the SHELXL refinement package using least-squares minimization,²⁷⁸ implemented in the Olex2 program suite.²⁷⁹ Contribution of the disordered solvent molecules found in the structural voids to the measured structure factors was quantified with the SQUEEZE procedure of the PLATON program suite.²⁸⁰ Solvent accessible volume was calculated with the program MERCURY (v. 3.10.1).²⁸¹ Structure simplification and net classification was performed using the TOPOS Pro program suite.²⁸²

Table S5. Crystal data and structure refinement for **SION-9**.

Identification code	SION9
Empirical formula	C ₁₁₀ H ₆₀ N ₂₃ O ₁₇ Zn ₈
Formula weight	2498.77
Temperature/K	100.0
Crystal system	monoclinic
Space group	<i>C2/c</i>
<i>a</i> /Å	23.3855(9)
<i>b</i> /Å	23.6171(5)
<i>c</i> /Å	34.8208(11)
α /°	90
β /°	92.989(3)
γ /°	90
Volume/Å ³	19205.3(10)
<i>Z</i>	4
ρ_{calc} g/cm ³	0.864
μ /mm ⁻¹	1.024
<i>F</i> (000)	5028.0
Crystal size/mm ³	0.03 × 0.02 × 0.02
Radiation	synchrotron (λ = 0.7129 Å)
2 θ range for data collection/°	3.338 to 46.664
Index ranges	$-25 \leq h \leq 25$, $-26 \leq k \leq 26$, $-36 \leq l \leq 36$
Reflections collected	42176
Independent reflections	12741 [R_{int} = 0.0711, R_{sigma} = 0.0669]
Data/restraints/parameters	12741/155/741
Goodness-of-fit on F^2	1.009
Final <i>R</i> indexes [$I \geq 2\sigma(I)$]	R_1 = 0.0723, wR_2 = 0.2150
Final <i>R</i> indexes [all data]	R_1 = 0.0930, wR_2 = 0.2342
Largest diff. peak/hole / e Å ⁻³	1.19/−0.84

S5.3 Solid State Characterization

S5.3.1 SION-9 Characterization

The phase purity of **SION-9** and **SION-9'** were confirmed by the comparison of the experimental PXRD pattern with the simulated generated from the single crystal structure. **SION-9** was found to be air stable over a period of 6 months at ambient temperature while stored in a vial.

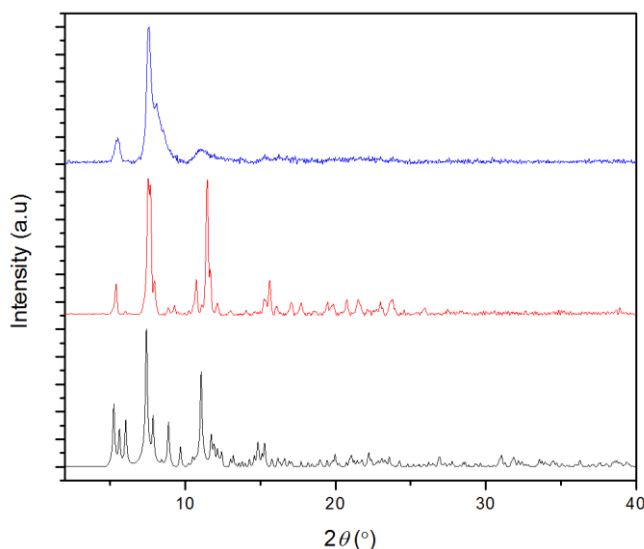


Figure 27- PXRD of SION-9. Color scheme: black, theory; red, **SION-9** experimental powder pattern taken at the ESRF; blue, **SION-9** experimental powder pattern taken at EPFL Valais/Wallis Switzerland.

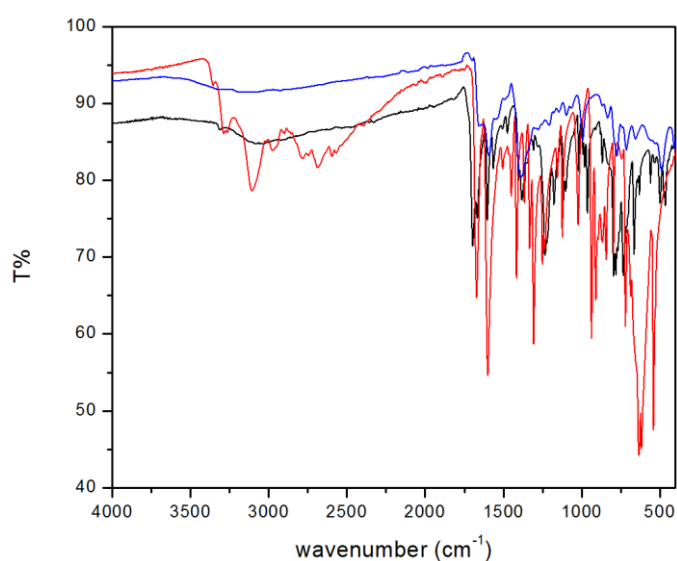


Figure S28- IR. Colour scheme: blue, **SION-9**; red, Ade; black, TCPP.

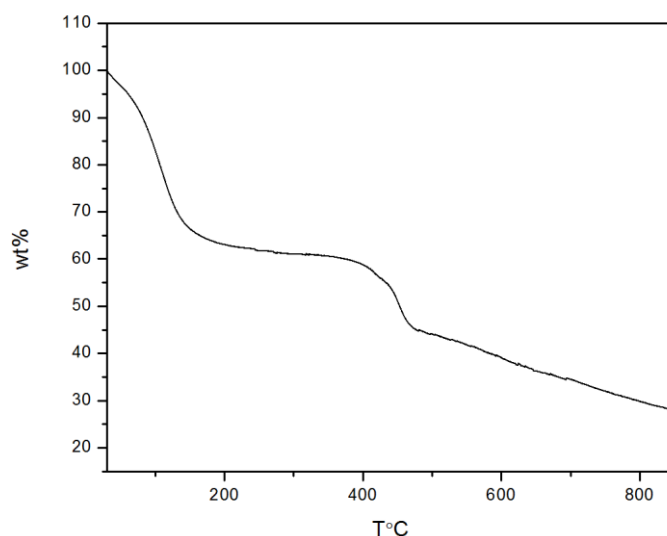


Figure S29- TGA analysis of SION-9.

EA of the bulk phase reveals that the overall structure of **SION-9**, $[\text{Zn}_8(\text{TCPP})_2(\text{Ade})_3]$, is comprised of only guest molecules in the pores. Here, the TGA profile shows one plateau occurring between 175-375°C and has a 38.9% weight loss attributed to the removal of guest molecules. At temperatures >375°C the framework begins to decompose.

Desolvation of **SION-9'** was carried out under at 120°C under vacuum for 72 hrs. Anal. Calcd for $[\text{Zn}_8(\text{TCPP})_2(\text{Ade})_3]$: C 50.45, H 2.75, N 10.55. Experimental: C 50.33, H 2.88, N 10.56

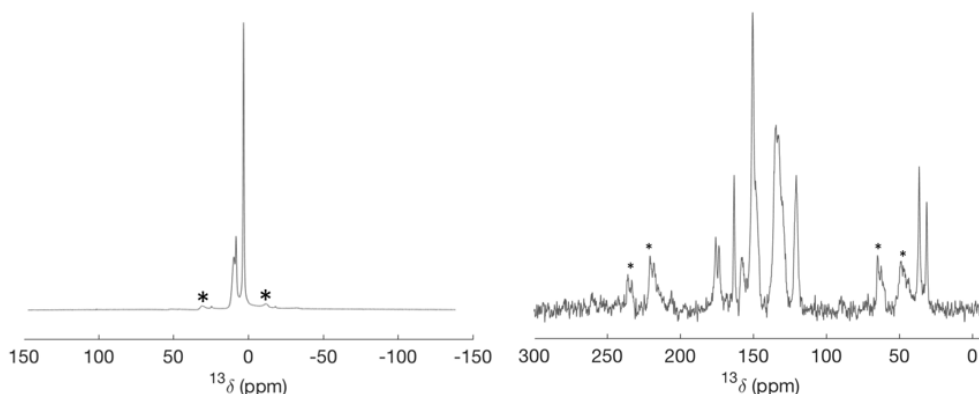


Figure S30- SION-9 ^{13}C CP-MAS. These spectra were recorded at 700MHz proton frequency. Rotor spinning at 15 kHz, contact time 4ms. Left: expanded spectrum; right: spectra from 0-300 ppm. Spinning sidebands indicated with a star.

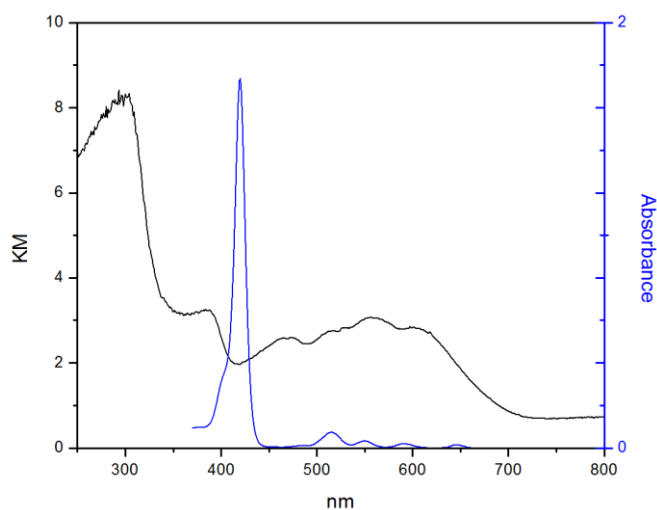


Figure S31- UV-vis of SION-9 (black) and free TCPP (blue).

S5.3.2 SION-9' Characterization

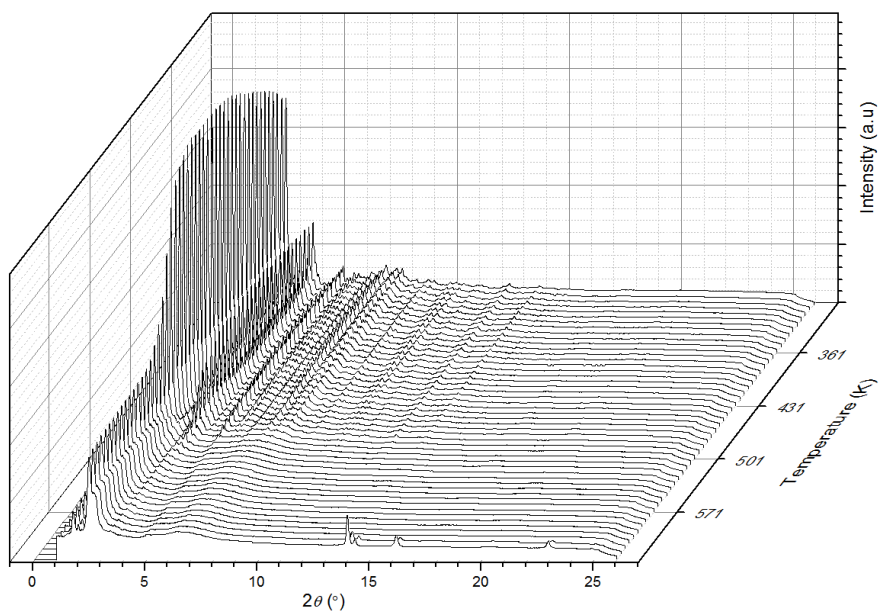


Figure S32- Variable Temperature PXRD of SION-9 to SION-9'.

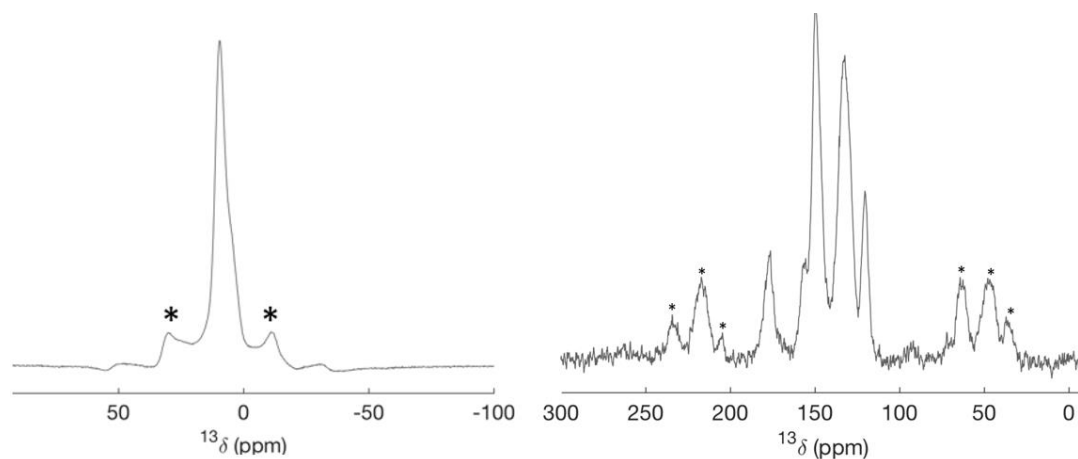


Figure S33- SION-9' ^{13}C CP-MAS. These spectra were recorded at 700 MHz proton frequency. Rotor spinning at 15 kHz, contact time 4ms. Left: expanded spectrum; right: spectra from 0-300 ppm. Spinning sidebands indicated with a star.

S5.3.3 EPR and Solid State NMR Experiments

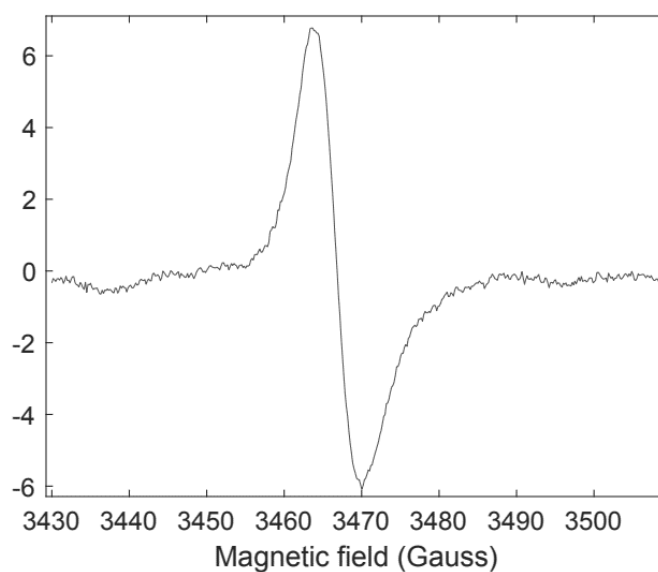


Figure S34- EPR of SION-9. This spectra confirms the presence of an unpaired electron in the material.

S5.4 Conductivity of SION-9

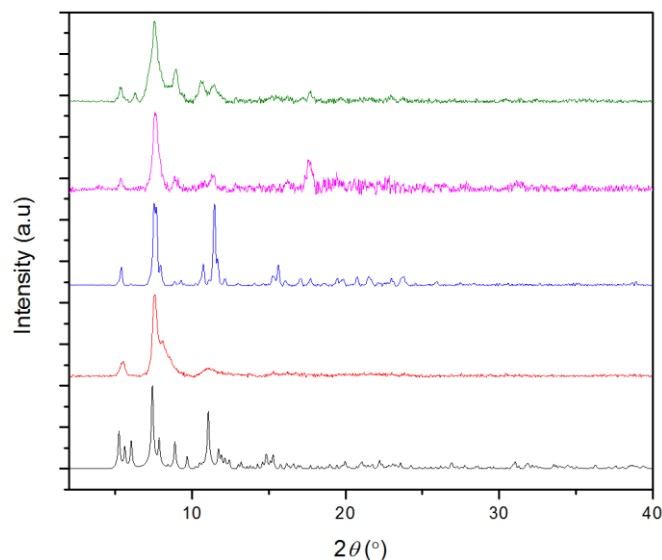


Figure S35- PXRD patterns of SION-9 after conductivity measurements. All material were measured at EPFL Valais/Walais. Color Scheme: **SION-9** Theory, black; **SION-9** before EIS measurements, red; **SION-9** before EIS measurements (ESRF), blue; **SION-9** pellet (whole), pink; **SION-9** crushed pellet, green.

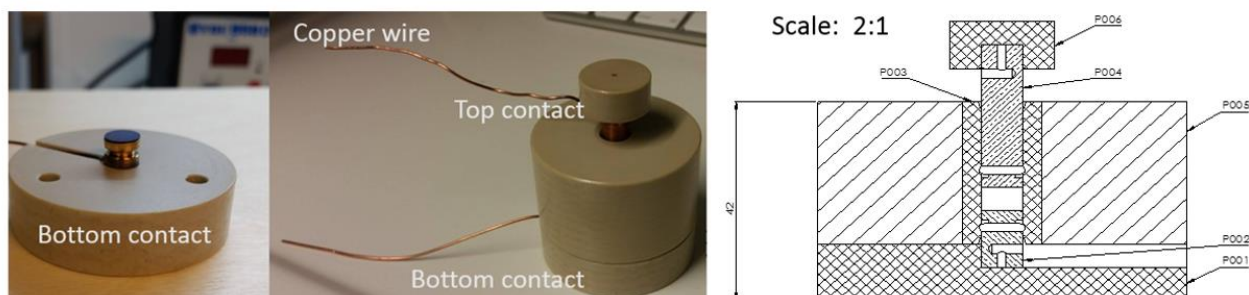


Figure S36- Cell set up and conductivity measurement set up. Right top: **SION-9** pressed pellet on top of gold contact; Middle: The cell used is comprised of two contacts (top and bottom). Left: Schematic of cell used.

Conductivity of **SION-9** MOF crystals and powders was investigated by means of electrochemical impedance spectroscopy (EIS). The measurements were performed using a potentiostat/galvanostat PGSTAT302N with FRA module (Metrohm Autolab). Impedance spectra of the pressed into 8 mm diameter pellet samples were measured in the range of working frequencies from 1 Hz to 1 MHz. The frequency range is built using a logarithmic distribution. The voltage modulation amplitude was set to 10 mV. Pressed powder samples were investigated under pressure of 500-

2000 kg/cm² in special home-designed conductivity cell with gold contacts (diameter of 8 mm). The spectra were obtained in the range of temperatures 5-60 °C.

Each Nyquist plot was fit with the equivalent circuit model:

$$(L_1 + R_1 + (Q_2/R_2) + Q_3/(R_3 + W_3))$$

where:

L= inductor

R= resistor

Q= constant phase element

W= Warburg element

The model circuit was chosen when the standard deviation of each element was less than 5% as can be seen in [Table S6](#).

Table S6: Equivalent circuit parameters for fitting **SION-9** at 1000 kg with a $(L_1 + R_1 + (Q_2/R_2) + Q_3/(R_3 + W_3))$ model.

Temp./ Param.	5 °C	10 °C	25 °C	40 °C	45 °C	50 °C	55 °C
L1 (H)	0.14×10^{-3} $\pm 73 \times 10^{-9}$	0.81×10^{-3} $\pm 2.0 \times 10^{-6}$	0.12×10^{-3} $\pm 0.16 \times 10^{-6}$	40×10^{-6} $\pm 0.37 \times 10^{-6}$	8.9×10^{-6} $\pm 0.14 \times 10^{-6}$	53×10^{-6} $\pm 0.29 \times 10^{-6}$	-17×10^{-6} $\pm 0.25 \times 10^{-6}$
R1 (Ohms)	772.5 ± 3.635	-13385 ± 6.791	-1860 ± 10.87	-1145 ± 22.83	-246.7 ± 13.64	-1619 ± 16.67	306.5 ± 8.518
Q2	6.3×10^{-9} $\pm 1.4 \times 10^{-12}$	-1.9×10^{-9} $\pm 2.8 \times 10^{-12}$	5.0×10^{-9} $\pm 5.6 \times 10^{-12}$	3.4×10^{-6} $\pm 4.3 \times 10^{-9}$	4.6×10^{-9} $\pm 7.5 \times 10^{-12}$	8.5×10^{-9} $\pm 13.5 \times 10^{-12}$	6.4×10^{-9} $\pm 7.4 \times 10^{-12}$
R2 (Ohms)	400549 ± 92.94	-23536 ± 42.02	58800 ± 9.765	151041 ± 461.5	42497 ± 12.72	39411 ± 16.70	54393 ± 6.769
Q3	0.47×10^{-9} $\pm 0.21 \times 10^{-12}$	5.3×10^{-9} $\pm 0.23 \times 10^{-12}$	1.7×10^{-6} $\pm 1.0 \times 10^{-9}$	9.3×10^{-9} $\pm 25 \times 10^{-12}$	3.5×10^{-6} $\pm 3.1 \times 10^{-9}$	0.45×10^{-6} $\pm 0.69 \times 10^{-9}$	2.5×10^{-6} $\pm 2.4 \times 10^{-9}$
R3 (Ohms)	262294 ± 91.44	673713 ± 21.9	138166 ± 168.6	33552 ± 22.46	282511 ± 651.8	2991 ± 30.02	377225 ± 3240

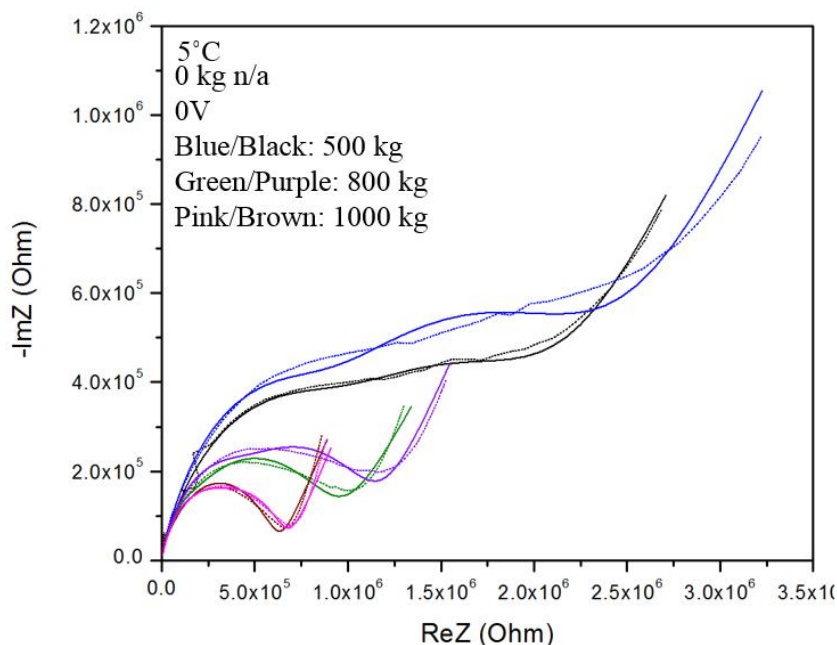


Figure S37- EIS for a SION-9 pellet at 5°C under different pressures. At 0 kg the material was not conductive. Here, experimental results are dots, and solid lines represent the fitted circuit. 0-1000 kg corresponds to 0-1990 kg/cm² of pressure.

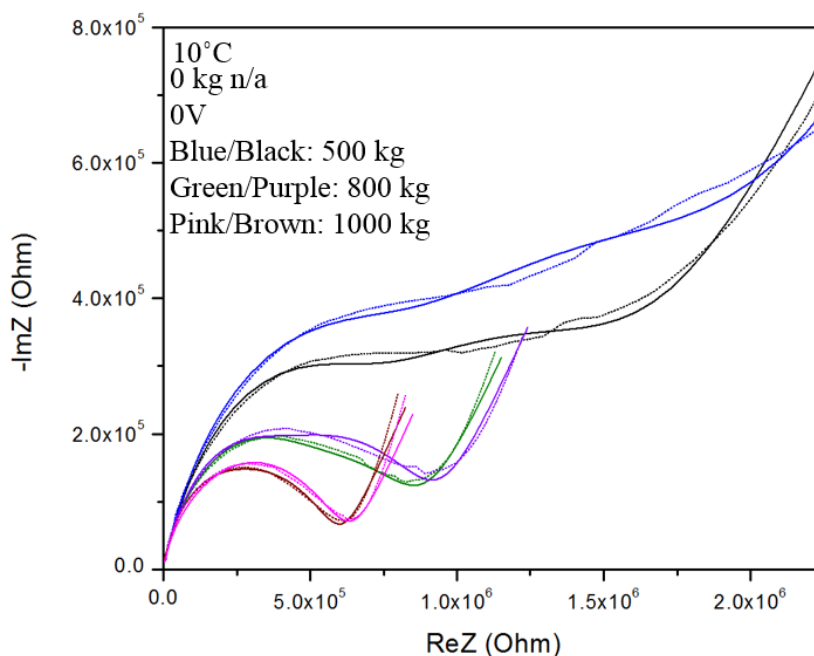


Figure S38- EIS for a SION-9 pellet at 10°C under different pressures. At 0 kg the material was not conductive. Here, experimental results are dots, and solid lines represent the fitted circuit. 0-1000 kg corresponds to 0-1990 kg/cm² of pressure.

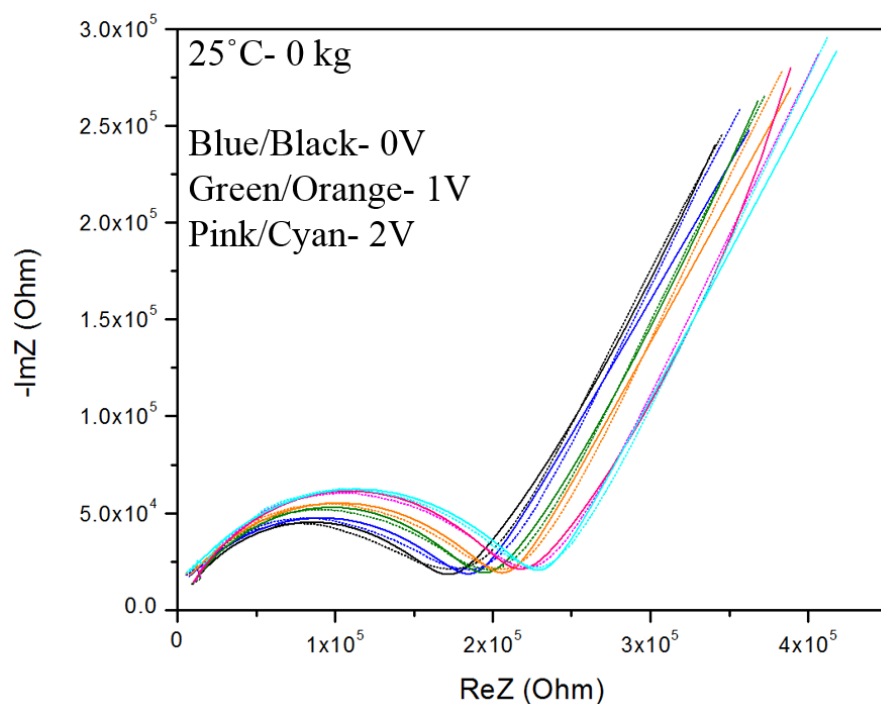


Figure S39- EIS for a SION-9 pellet at 25°C at 0 kg. Here, experimental results are dots, and solid lines represent the fitted circuit. 0 kg corresponds to 0 kg/cm² of pressure.

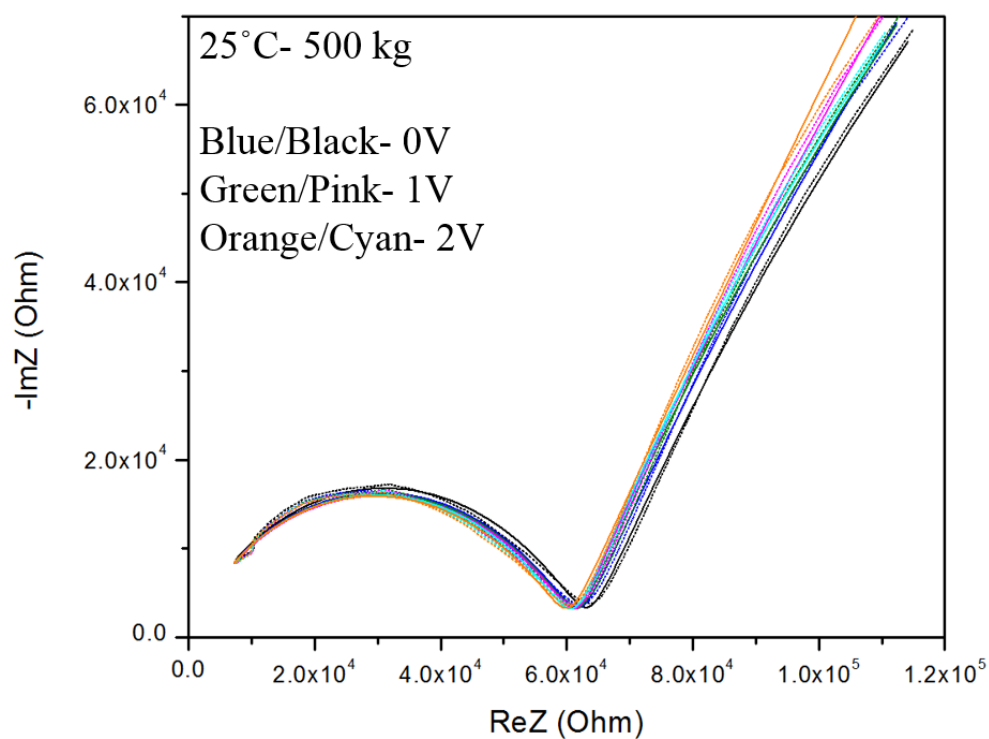


Figure S40- EIS for a SION-9 pellet at 25°C at 500 kg. Here, experimental results are dots, and solid lines represent the fitted circuit. 500 kg corresponds to 995 kg/cm² of pressure.

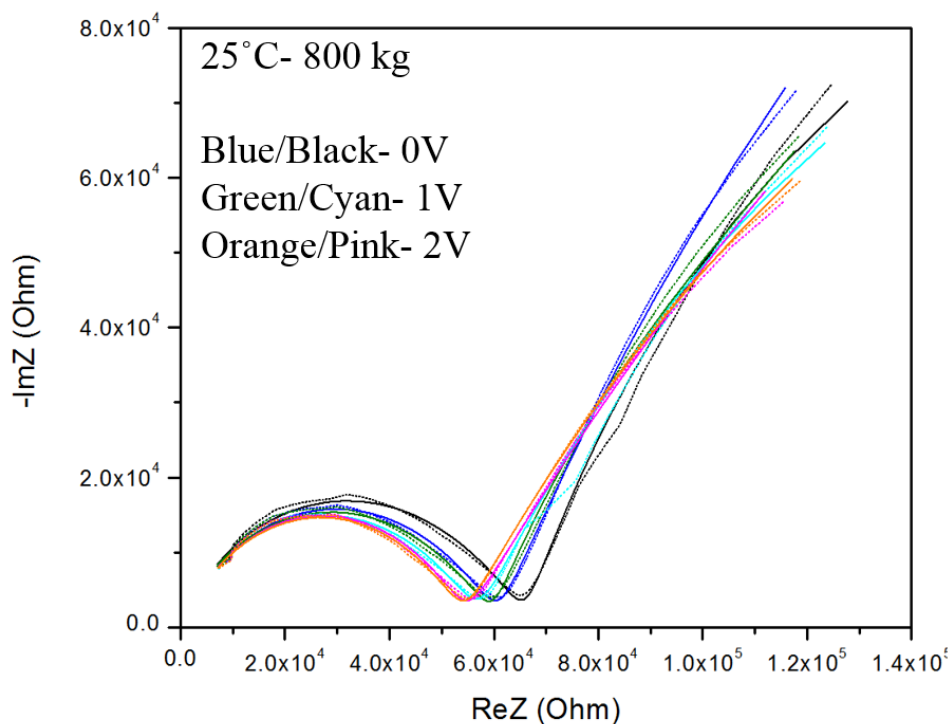


Figure S41- EIS for a SION-9 pellet at 25°C at 800 kg. Here, experimental results are dots, and solid lines represent the fitted circuit. 800 kg corresponds to 1592 kg/cm^2 of pressure.

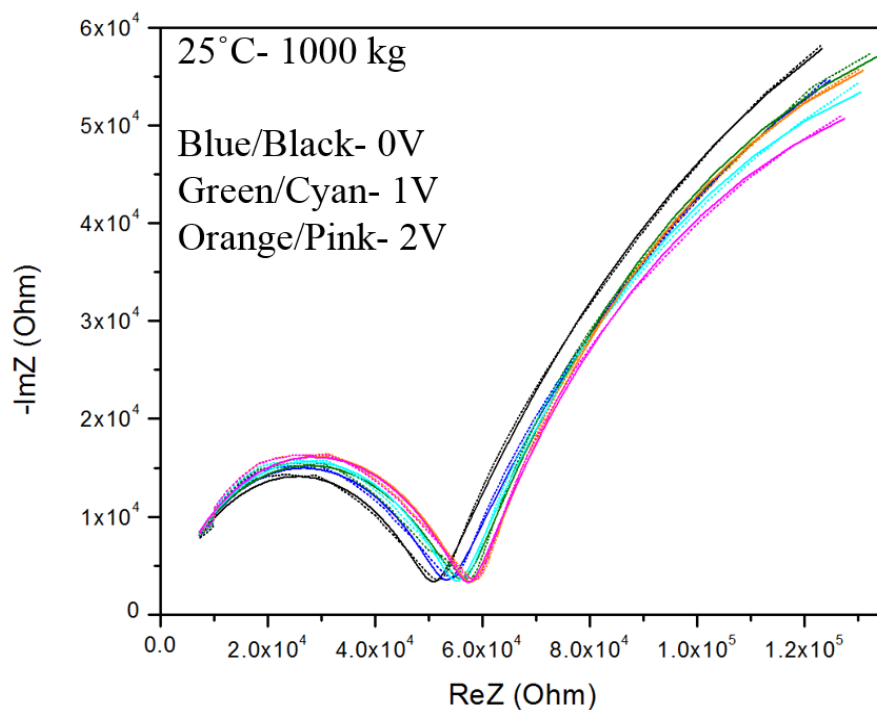


Figure S42- EIS for a SION-9 pellet at 25°C at 1000 kg. Here, experimental results are dots, and solid lines represent the fitted circuit. 1000 kg corresponds to 1990 kg/cm^2 of pressure.

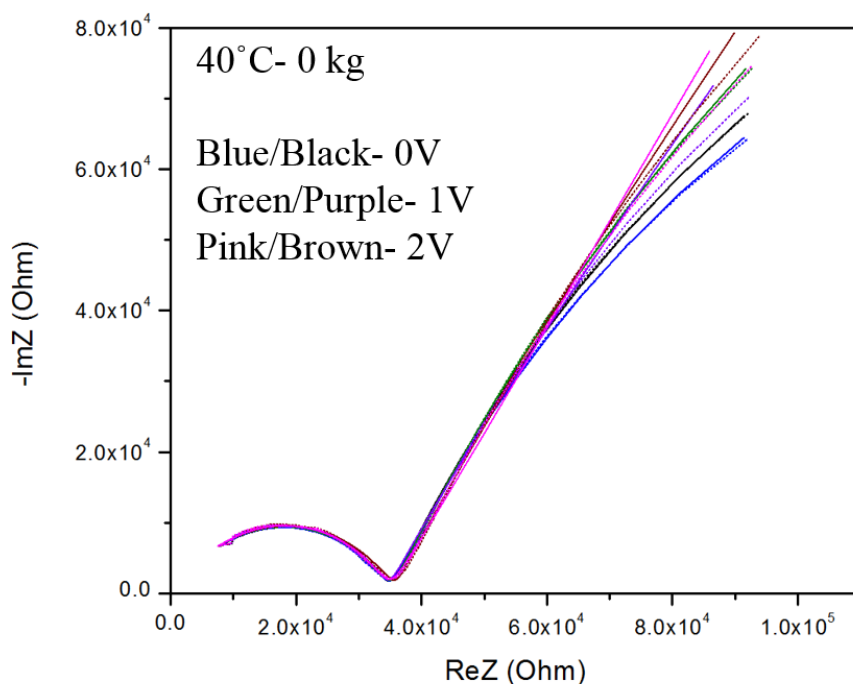


Figure S43- EIS for a SION-9 pellet at 40°C at 0 kg. Here, experimental results are dots, and solid lines represent the fitted circuit. 0 kg corresponds to 0 kg/cm² of pressure.

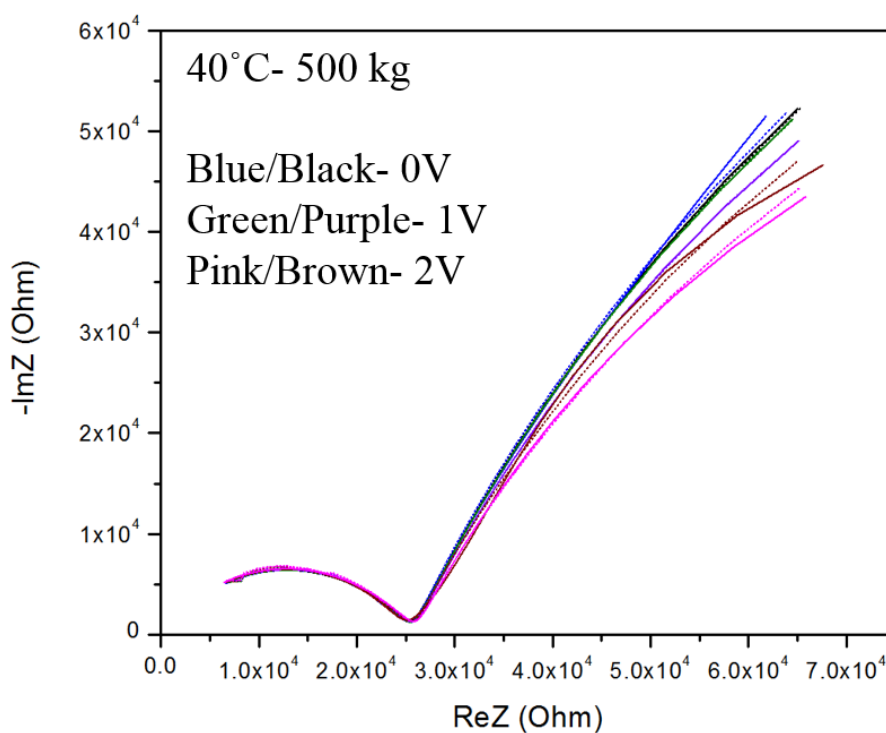


Figure S44- EIS for a SION-9 pellet at 40°C at 500 kg. Here, experimental results are dots, and solid lines represent the fitted circuit. 500 kg corresponds to 995 kg/cm² of pressure.

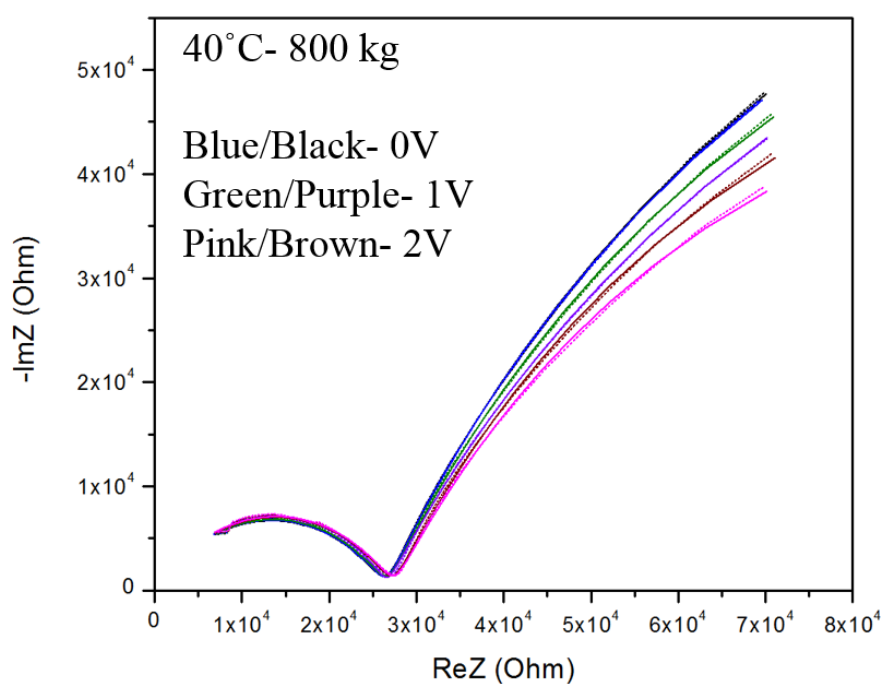


Figure S45- EIS for a SION-9 pellet at 40°C at 800 kg. Here, experimental results are dots, and solid lines represent the fitted circuit. 800 kg corresponds to 1592 kg/cm² of pressure

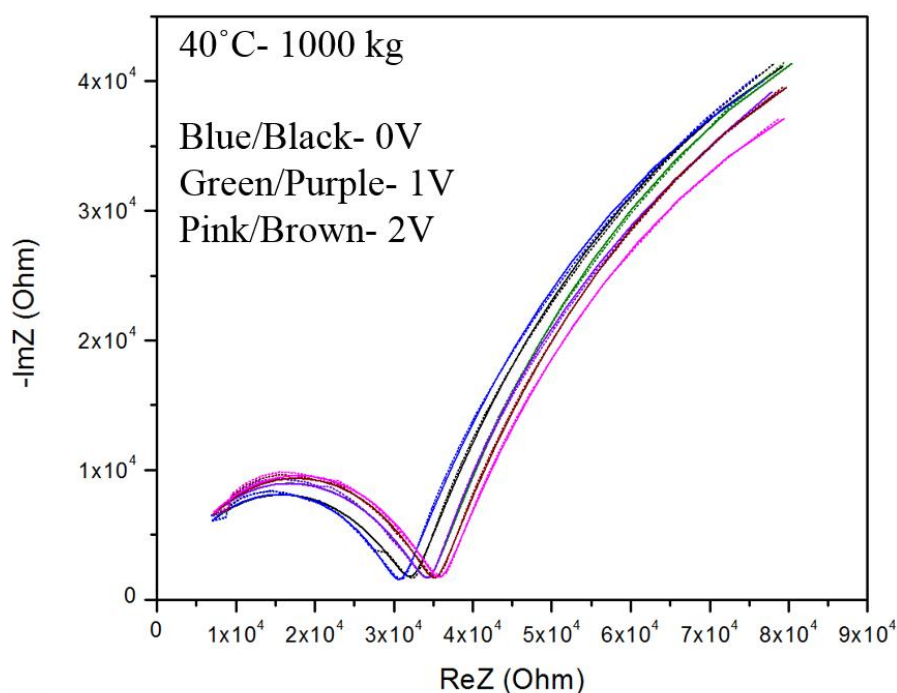


Figure S46- EIS for a SION-9 pellet at 40°C at 1000 kg. Here, experimental results are dots, and solid lines represent the fitted circuit. 1000 kg corresponds to 1990 kg/cm² of pressure.

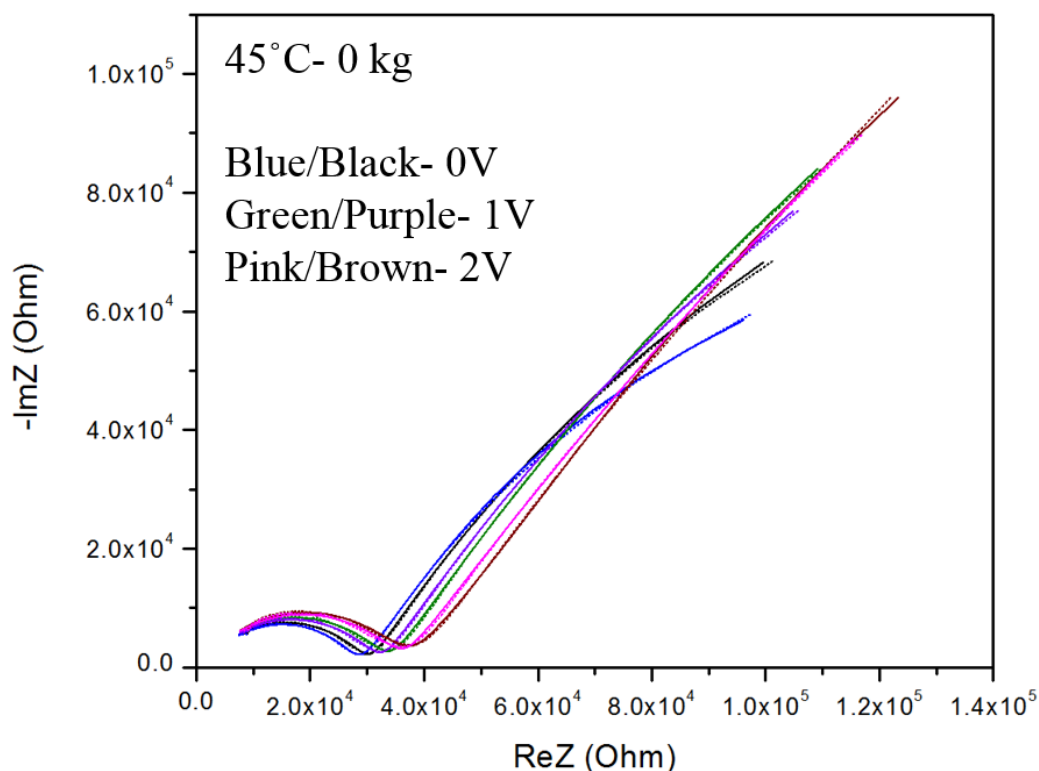


Figure S47- EIS for a SION-9 pellet at 45°C at 0 kg. Here, experimental results are dots, and solid lines represent the fitted circuit. 0 kg corresponds to 0 kg/cm² of pressure.

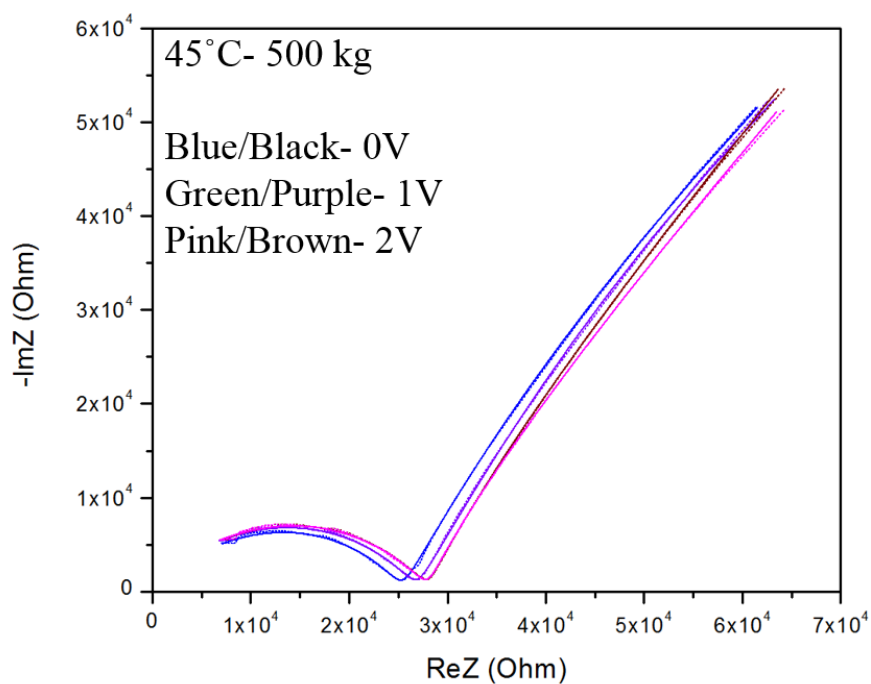


Figure S48- EIS for a SION-9 pellet at 45°C at 500 kg. Here, experimental results are dots, and solid lines represent the fitted circuit. 500 kg corresponds to 995 kg/cm² of pressure.

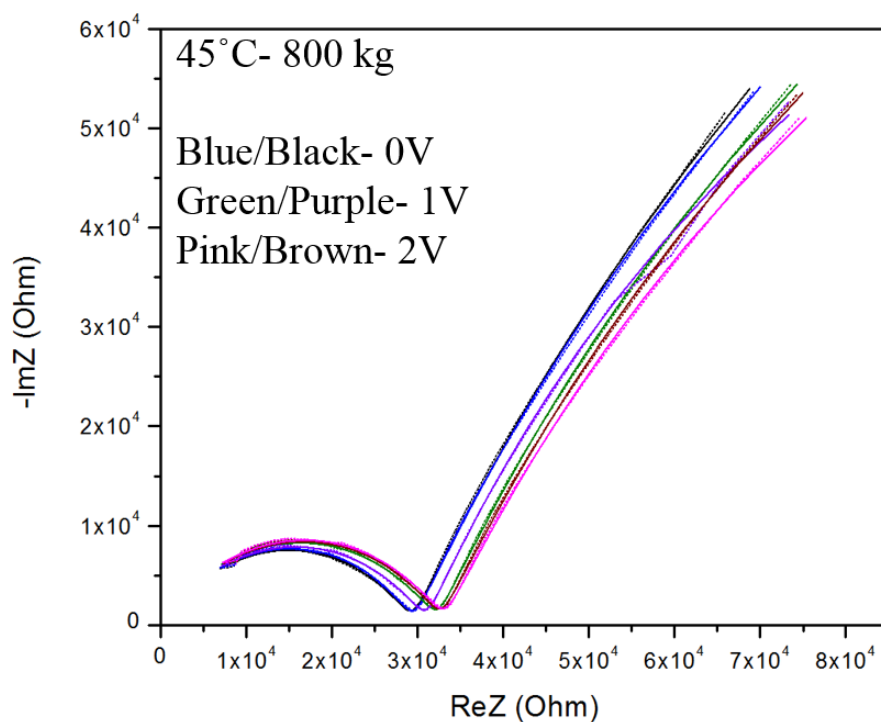


Figure S49- EIS for a SION-9 pellet at 45°C at 800 kg. Here, experimental results are dots, and solid lines represent the fitted circuit. 800 kg corresponds to 1592 kg/cm^2 of pressure.

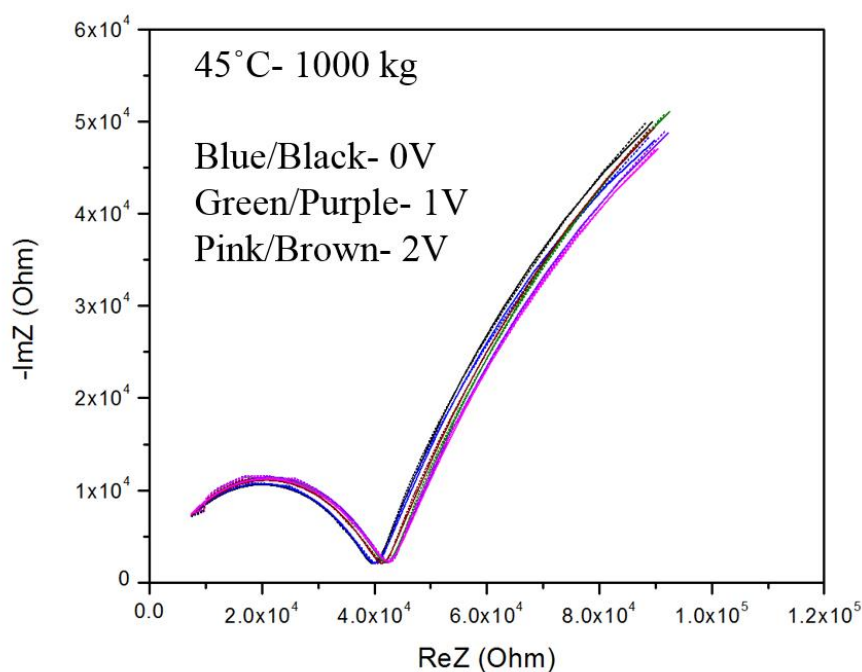


Figure S50- EIS for a SION-9 pellet at 45°C at 1000 kg. Here, experimental results are dots, and solid lines represent the fitted circuit. 1000 kg corresponds to 1990 kg/cm^2 of pressure.

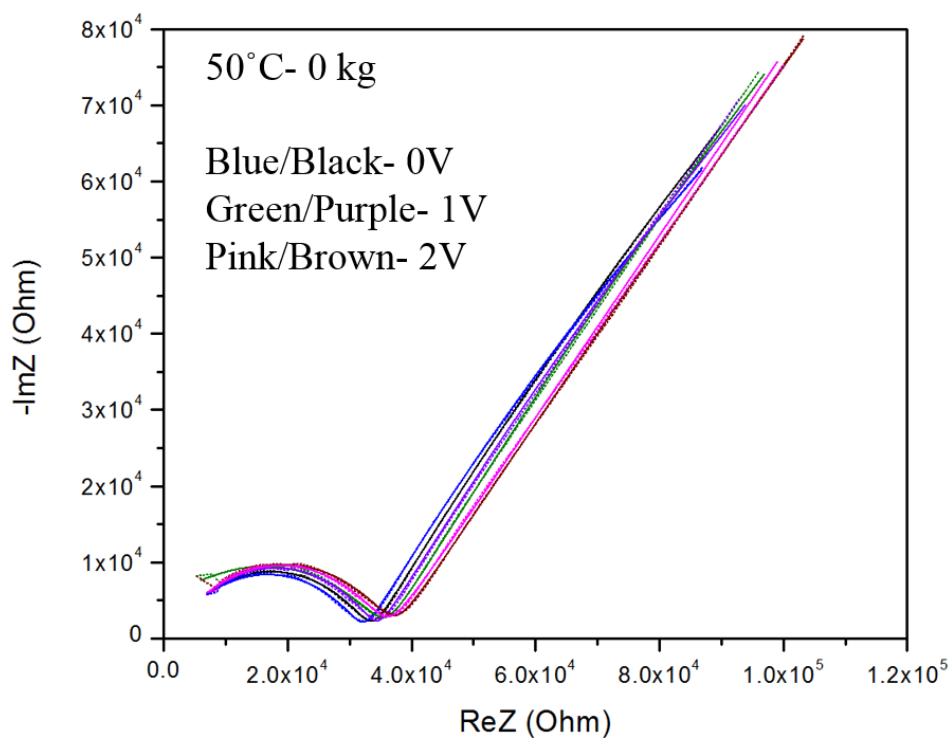


Figure S51- EIS for a SION-9 pellet at 50°C at 0 kg. Here, experimental results are dots, and solid lines represent the fitted circuit. 0 kg corresponds to 0 kg/cm² of pressure.

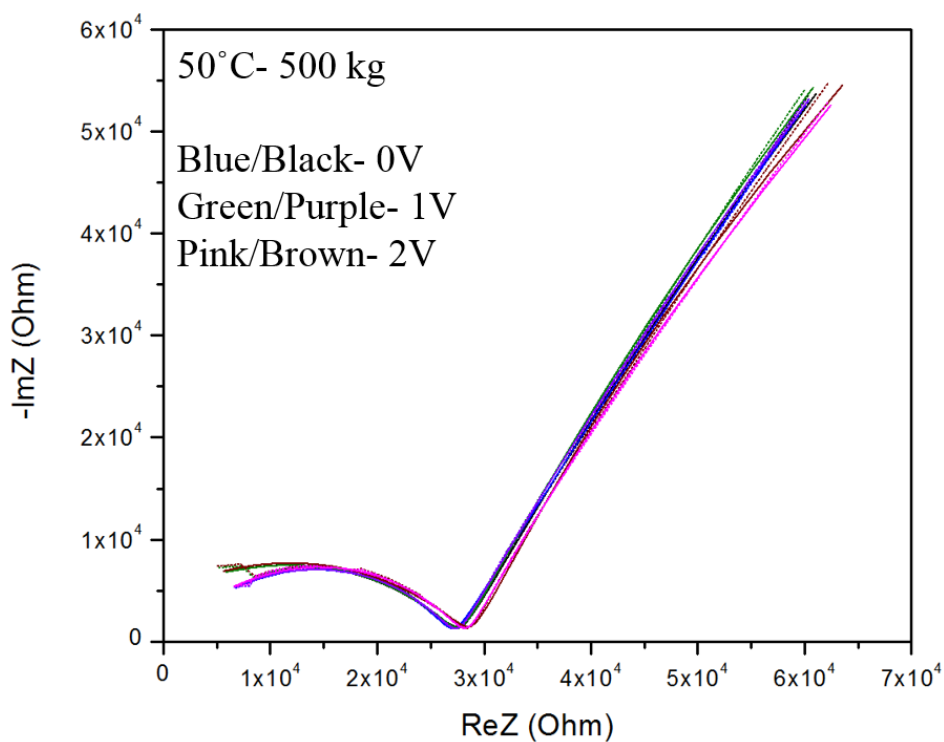


Figure S52- EIS for a SION-9 pellet at 50°C at 500 kg. Here, experimental results are dots, and solid lines represent the fitted circuit. 500 kg corresponds to 995 kg/cm² of pressure.

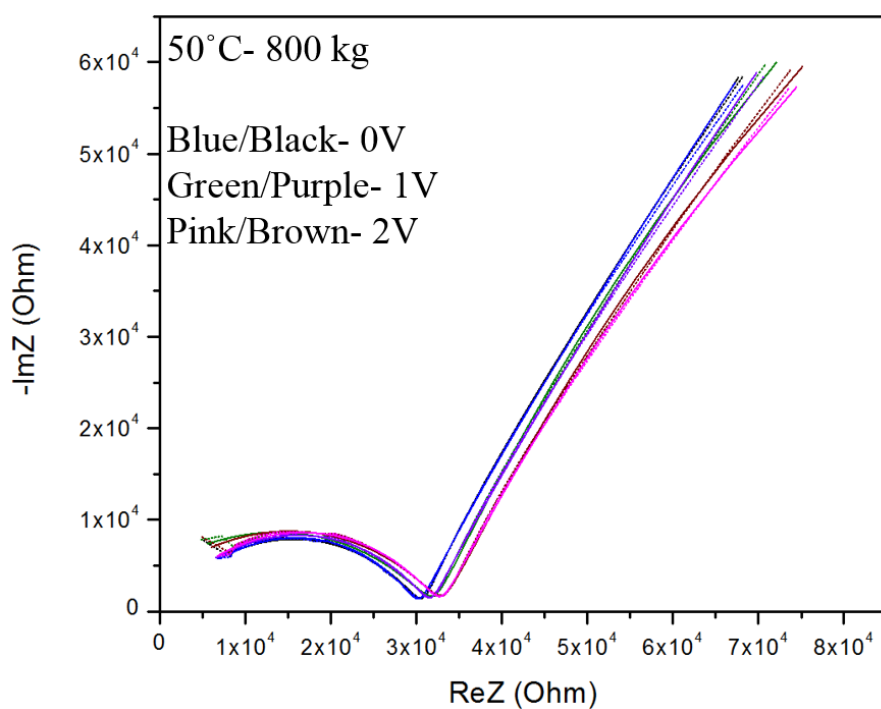


Figure S53- EIS for a SION-9 pellet at 50°C at 800 kg. Here, experimental results are dots, and solid lines represent the fitted circuit. 800 kg corresponds to 1592 kg/cm² of pressure.

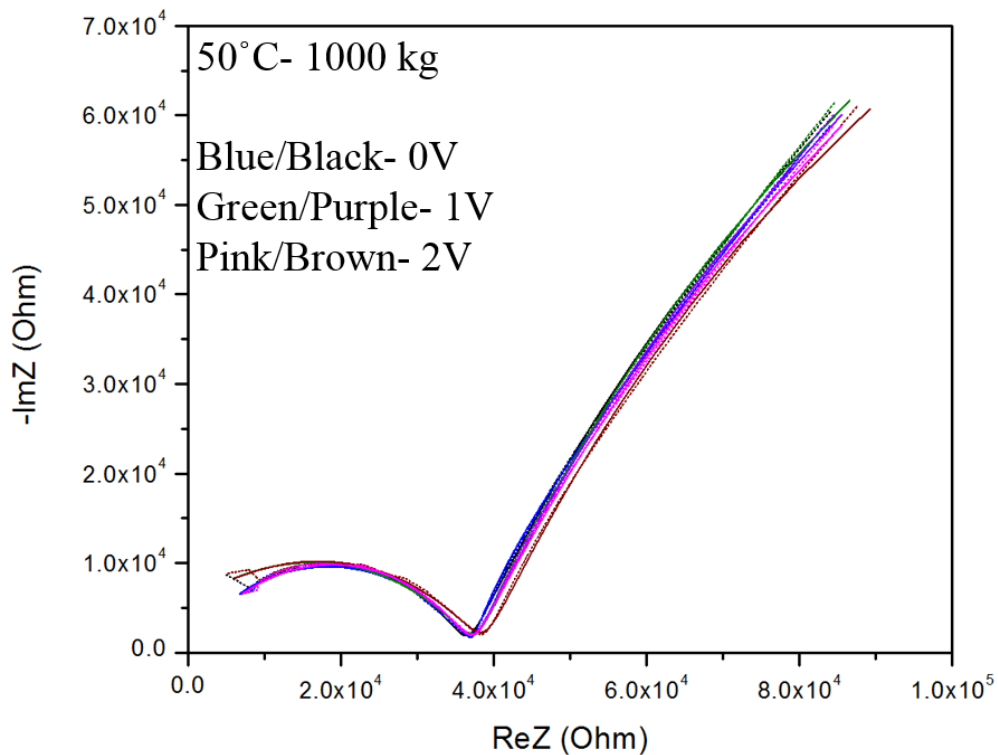


Figure S54- EIS for a SION-9 pellet at 50°C at 1000 kg. Here, experimental results are dots, and solid lines represent the fitted circuit. 1000 kg corresponds to 1990 kg/cm² of pressure.

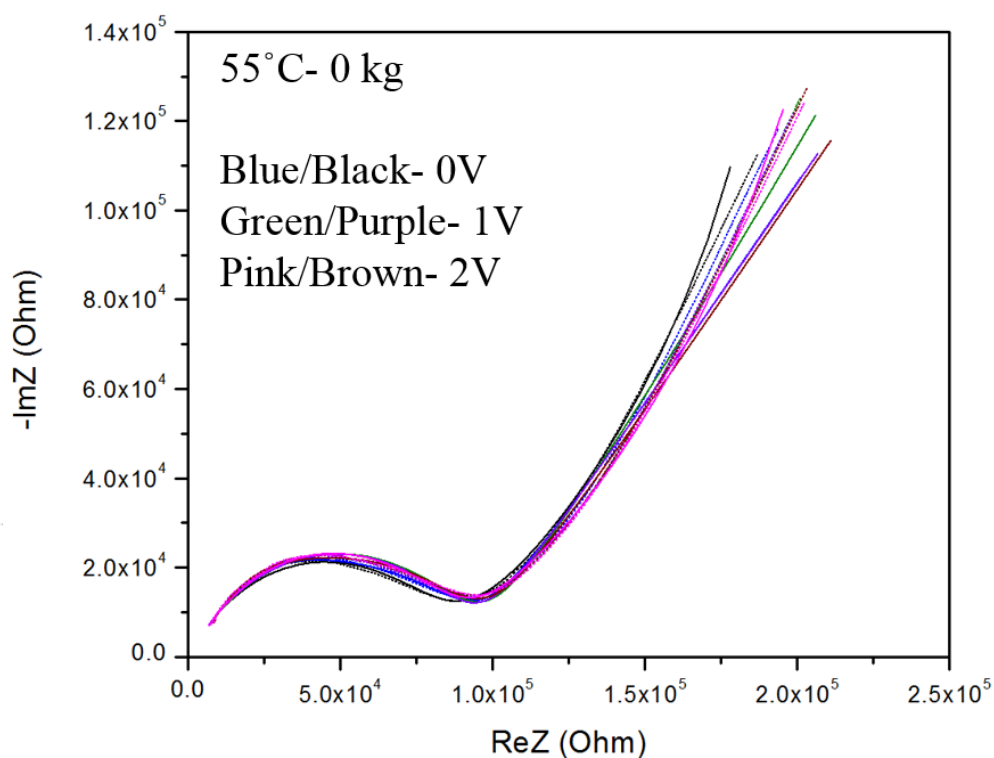


Figure S55- EIS for a SION-9 pellet at 55°C at 0 kg. Here, experimental results are dots, and solid lines represent the fitted circuit. 0 kg corresponds to 0 kg/cm² of pressure.

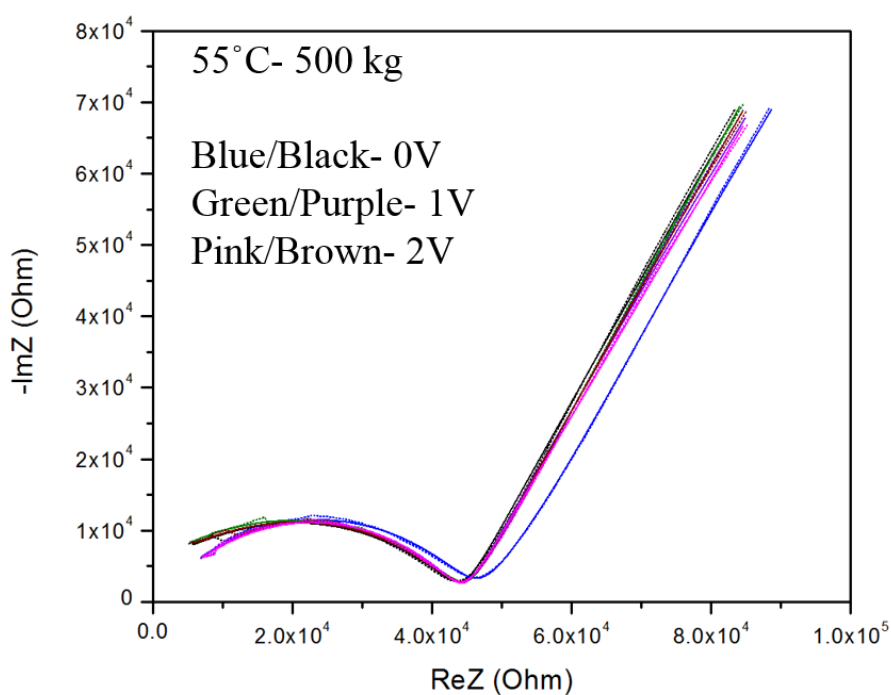


Figure S56- EIS for a SION-9 pellet at 55°C at 500 kg. Here, experimental results are dots, and solid lines represent the fitted circuit. 500 kg corresponds to 995 kg/cm² of pressure.

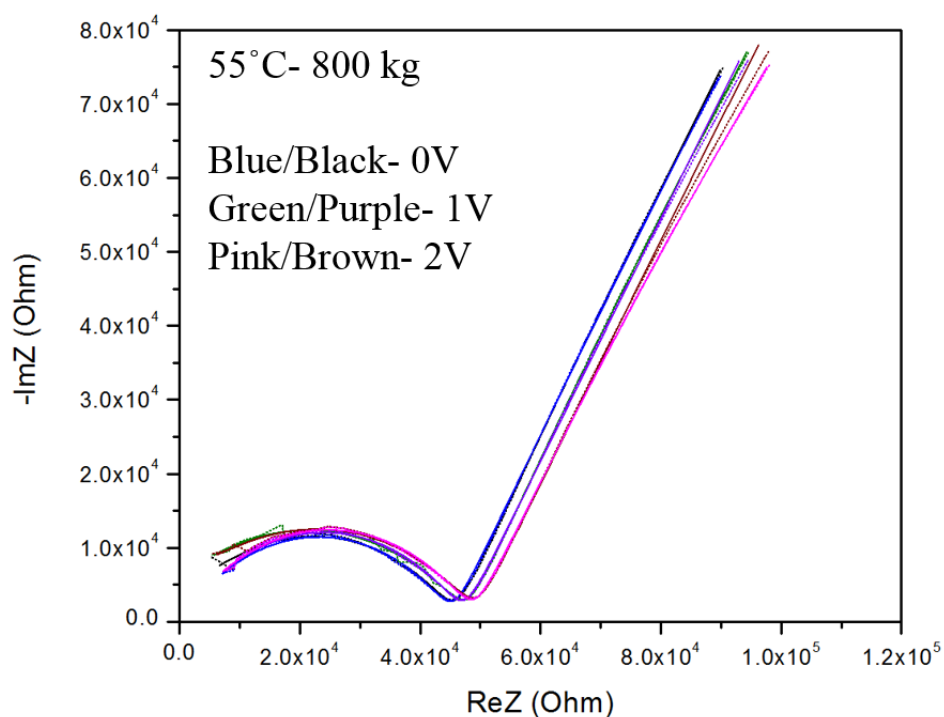


Figure S57- EIS for a SION-9 pellet at 55°C at 800 kg. Here, experimental results are dots, and solid lines represent the fitted circuit. 800 kg corresponds to 1592 kg/cm² of pressure.

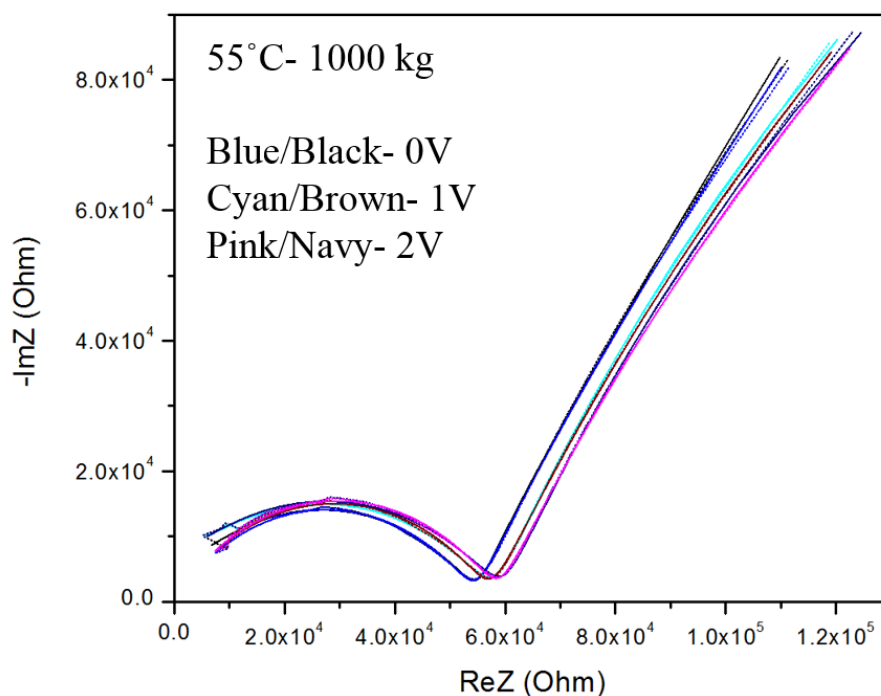


Figure S58- EIS for a SION-9 pellet at 55°C at 1000 kg. Here, experimental results are dots, and solid lines represent the fitted circuit. 1000 kg corresponds to 1990 kg/cm² of pressure.

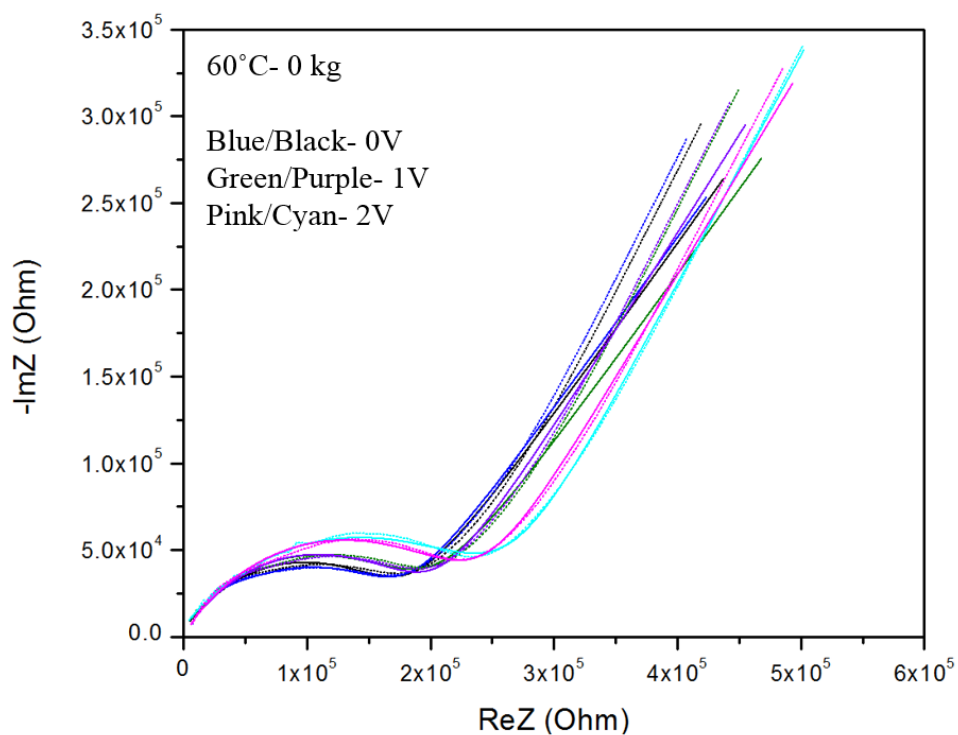


Figure S59- EIS for a SION-9 pellet at 60°C at 0 kg. Here, experimental results are dots, and solid lines represent the fitted circuit. 0 kg corresponds to 0 kg/cm² of pressure. 1000 kg corresponds to 1990 kg/cm² of pressure.

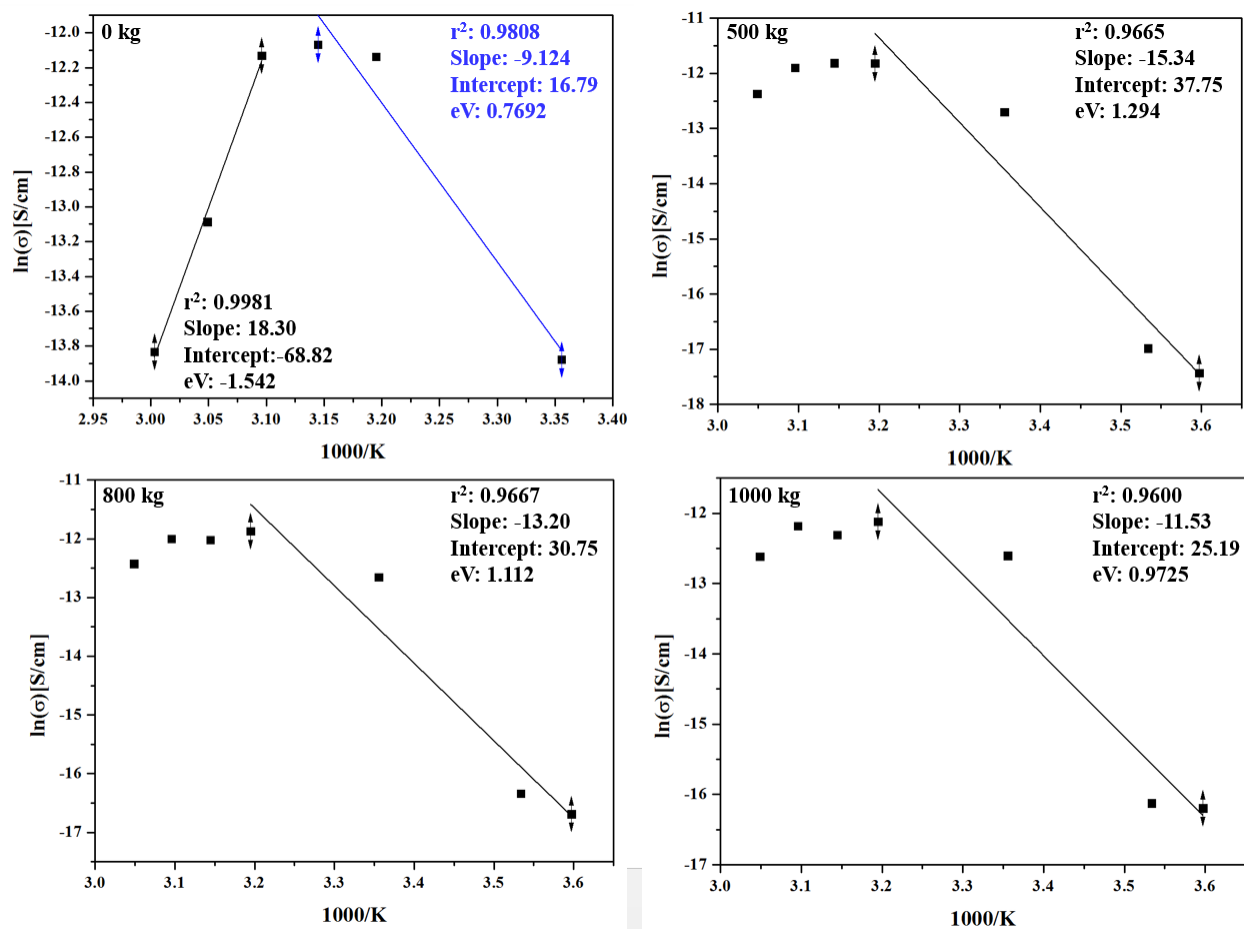


Figure S60- Arrhenius plots and eV of SION-9 pellets at different pressures and temperatures. 0-1000 kg corresponds to 0-1990 kg/cm² of pressure.

S5.5 Device Fabrication

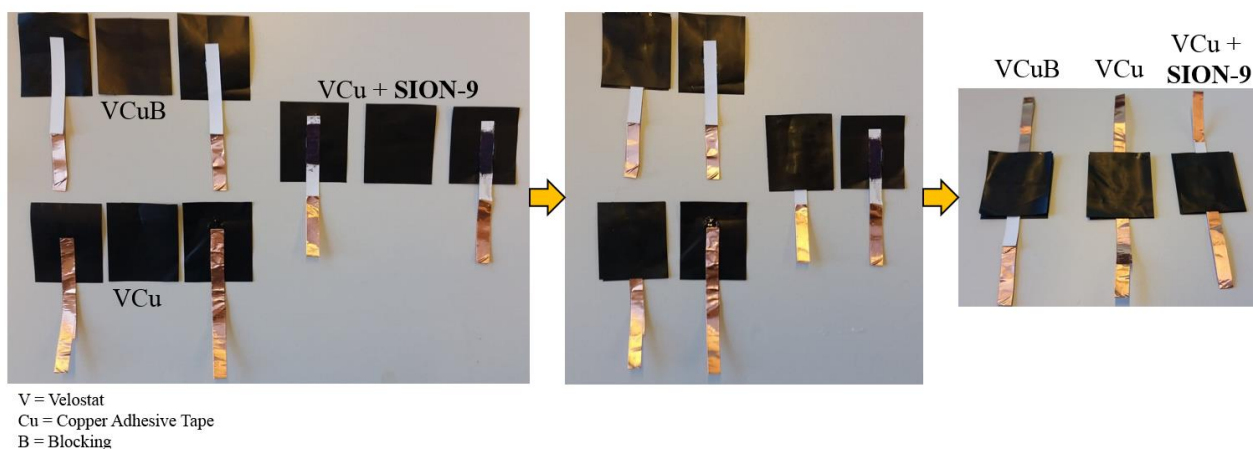


Figure S61- Device Fabrication: Device construction step by step, showing all three devices tested during this study.

Following conductivity studies, two pieces of 4 cm Cu tape were cut, and the non-adhesive sides were adhered to the center of two different 4 cm x 3.5 cm pieces of Velostat using Cemedine paste (Figure S61 Left). A 6 mm x 20 mm portion in the center of the adhesive Cu tape was removed, and covered with ground SION-9. Overall, two portions of the original adhesive backing remained to block any potential Cu-Velostat-Cu interactions and artificially increase the signal strength. Each component was oriented so that the hanging pieces of Cu were oriented opposite to each other (Figure S61 Middle), but that the **SION-9** portion overlapped in the center. Before finally assembling the device, a third piece of Velostat (4 cm x 3.5 cm) was placed between the two VCu-**SION-9** components, and all components were adhered with Cemedine paste (Figure S61 Right). The measurements were performed using a potentiostat/galvanostat PGSTAT302N with chronoamperometry module (Metrohm Autolab), and 3 V were applied for each measurement.

References

1. Ferey, G., *Chem. Soc. Rev.* **2008**, 37, 191-214.
2. Yaghi, O. M.; O'Keeffe, M.; Ockwig, N. W.; Chae, H. K.; Eddaoudi, M.; Kim, J., *Nature* **2003**, 423, 705-714.
3. Farha, O. K.; Eryazici, I.; Jeong, N. C.; Hauser, B. G.; Wilmer, C. E.; Sarjeant, A. A.; Snurr, R. Q.; Nguyen, S. T.; Yazaydin, A. Ö.; Hupp, J. T., *J. Am. Chem. Soc.* **2012**, 134, 15016-15021.
4. Furukawa, H.; Ko, N.; Go, Y. B.; Aratani, N.; Choi, S. B.; Choi, E.; Yazaydin, A. Ö.; Snurr, R. Q.; O'Keeffe, M.; Kim, J.; Yaghi, O. M., *Science* **2010**, 329, 424-428.
5. Furukawa, H.; Go, Y. B.; Ko, N.; Park, Y. K.; Uribe-Romo, F. J.; Kim, J.; O'Keeffe, M.; Yaghi, O. M., *Inorg. Chem.* **2011**, 50, 9147-9152.
6. Zhang, M.; Bosch, M.; Gentle Iii, T.; Zhou, H.-C., *CrystEngComm* **2014**, 16, 4069-4083.
7. Corma, A.; García, H.; Llabrés i Xamena, F. X., *Chem. Rev.* **2010**, 110, 4606-4655.
8. Fujii, K.; Garay, A. L.; Hill, J.; Sbircea, E.; Pan, Z.; Xu, M.; Apperley, D. C.; James, S. L.; Harris, K. D. M., *Chem. Commun.* **2010**, 46, 7572-7574.
9. Forster, P. M.; Thomas, P. M.; Cheetham, A. K., *Chem. Mater.* **2002**, 14, 17-20.
10. Chui, S. S.-Y.; Lo, S. M.-F.; Charmant, J. P. H.; Orpen, A. G.; Williams, I. D., *Science* **1999**, 283, 1148-1150.
11. Jhung, S. H.; Lee, J.-H.; Forster, P. M.; Férey, G.; Cheetham, A. K.; Chang, J.-S., *Chem. Eur. J.* **2006**, 12, 7899-7905.
12. Biemmi, E.; Christian, S.; Stock, N.; Bein, T., *Micropor. Mesopor. Mat.* **2009**, 117, 111-117.
13. Stock, N.; Bein, T., *Angew. Chem. Int. Ed.* **2004**, 43, 749-752.
14. Bauer, S.; Bein, T.; Stock, N., *Inorg. Chem.* **2005**, 44, 5882-5889.
15. Reinsch, H.; Stock, N., *Microporous Mesoporous Mater.* **2013**, 171, 156-165.
16. Sumida, K.; Horike, S.; Kaye, S. S.; Herm, Z. R.; Queen, W. L.; Brown, C. M.; Grandjean, F.; Long, G. J.; Dailly, A.; Long, J. R., *Chem. Sci.* **2010**, 1, 184-191.
17. Deng, H.; Grunder, S.; Cordova, K. E.; Valente, C.; Furukawa, H.; Hmadeh, M.; Gándara, F.; Whalley, A. C.; Liu, Z.; Asahina, S.; Kazumori, H.; O'Keeffe, M.; Terasaki, O.; Stoddart, J. F.; Yaghi, O. M., *Science* **2012**, 336, 1018-1023.
18. Witman, M.; Ling, S.; Anderson, S.; Tong, L.; Stylianou, K. C.; Slater, B.; Smit, B.; Haranczyk, M., *Chem. Sci.* **2016**, 7, 6263-6272.
19. Tranchemontagne, D. J.; Mendoza-Cortés, J. L.; O'Keeffe, M.; Yaghi, O. M., *Chem. Soc. Rev.* **2009**, 38, 1257-1283.
20. Cantu, D. C.; McGrail, B. P.; Glezakou, V.-A., *Chem. Mater.* **2014**, 26, 6401-6409.
21. Goesten, M. G.; Kapteijn, F.; Gascon, J., *CrystEngComm* **2013**, 15, 9249-9257.
22. Tzeng, B.-C.; Yeh, H.-T.; Chang, T.-Y.; Lee, G.-H., *Cryst. Growth Des.* **2009**, 9, 2552-2555.
23. Kumar, D. K.; Das, A.; Dastidar, P., *Cryst. Growth Des.* **2007**, 7, 2096-2105.
24. Wu, Y.; Breeze, M. I.; Clarkson, G. J.; Millange, F.; O'Hare, D.; Walton, R. I., *Angew. Chem. Int. Ed.* **2016**, 55, 4992-4996.
25. Bellarosa, L.; Brozek, C. K.; García-Melchor, M.; Dincă, M.; López, N., *Chem. Mater.* **2015**, 27, 3422-3429.
26. Brozek, C. K.; Michaelis, V. K.; Ong, T.-C.; Bellarosa, L.; López, N.; Griffin, R. G.; Dincă, M., *ACS Cent. Sci.* **2015**, 1, 252-260.
27. Wei, W.; Yu, H.; Jiang, F.; Liu, B.; Ma, J.; Hong, M., *CrystEngComm* **2012**, 14, 1693-1700.
28. Notash, B.; Safari, N.; Khavasi, H. R., *CrystEngComm* **2012**, 14, 6788-6796.
29. Loiseau, T.; Ferey, G., *J. Fluorine Chem.* **2007**, 128, 413-422.
30. Min, K. S.; Suh, M. P., *J. Am. Chem. Soc.* **2000**, 122, 6834-6840.
31. Zhang, Y.; Cremer, P. S., *Curr. Opin. Chem. Biol.* **2006**, 10, 658-663.

32. Custelcean, R.; Moyer, B. A., *Eur. J. Inorg. Chem.* **2007**, 2007, 1321-1340.
33. Haouas, M.; Volkringer, C.; Loiseau, T.; Férey, G.; Taulelle, F., *Chem. Mater.* **2012**, 24, 2462-2471.
34. Mitsuru, K.; Tomomichi, Y.; Hiroyuki, M.; Susumu, K.; Kenji, S., *Angew. Chem. Int. Ed.* **1997**, 36, 1725-1727.
35. Ayyappan, P.; Evans, O. R.; Lin, W., *Inorg. Chem.* **2002**, 41, 3328-3330.
36. Vaidhyanathan, R.; Iremonger, S. S.; Dawson, K. W.; Shimizu, G. K. H., *Chem. Commun.* **2009**, 5230-5232.
37. Li, H.; Eddaoudi, M.; Groy, T. L.; Yaghi, O. M., *J. Am. Chem. Soc.* **1998**, 120, 8571-8572.
38. Serre, C.; Stock, N.; Bein, T.; Férey, G., *Inorg. Chem.* **2004**, 43, 3159-3163.
39. Bao-Qing, M.; Da-Shun, Z.; Song, G.; Tian-Zhu, J.; Chun-Hua, Y.; Guang-Xian, X., *Angew. Chem. Int. Ed.* **2000**, 39, 3644-3646.
40. Hayashi, H.; Cote, A. P.; Furukawa, H.; O'Keeffe, M.; Yaghi, O. M., *Nat. Mater.* **2007**, 6, 501-506.
41. Park, K. S.; Ni, Z.; Côté, A. P.; Choi, J. Y.; Huang, R.; Uribe-Romo, F. J.; Chae, H. K.; O'Keeffe, M.; Yaghi, O. M., *PNAS* **2006**, 103, 10186-10191.
42. Janosch, C.; A., S. C.; Roman, N.; Jeremie, G.; Klaus, H.; Michael, W., *Angew. Chem. Int. Ed.* **2011**, 50, 8067-8071.
43. Hawxwell, S. M.; Espallargas, G. M.; Bradshaw, D.; Rosseinsky, M. J.; Prior, T. J.; Florence, A. J.; van de Streek, J.; Brammer, L., *Chem. Commun.* **2007**, 1532-1534.
44. Black, C. A.; Hanton, L. R.; Spicer, M. D., *Chem. Commun.* **2007**, 3171-3173.
45. Ren, P.; Liu, M.-L.; Zhang, J.; Shi, W.; Cheng, P.; Liao, D.-Z.; Yan, S.-P., *Dalton Trans.* **2008**, 4711-4713.
46. Shen, K.; Zhang, M.; Zheng, H., *CrystEngComm.* **2015**, 17, 981-991.
47. Almeida Paz, F. A.; Klinowski, J.; Vilela, S. M. F.; Tome, J. P. C.; Cavaleiro, J. A. S.; Rocha, J., *Chem. Soc. Rev.* **2012**, 41, 1088-1110.
48. Poloni, R.; Smit, B.; Neaton, J. B., *J. Am. Chem. Soc.* **2012**, 134, 6714-6719.
49. Horcajada, P.; Chalati, T.; Serre, C.; Gillet, B.; Sebrie, C.; Baati, T.; Eubank, J. F.; Heurtaux, D.; Clayette, P.; Kreuz, C.; Chang, J.-S.; Hwang, Y. K.; Marsaud, V.; Bories, P.-N.; Cynober, L.; Gil, S.; Férey, G.; Couvreur, P.; Gref, R., *Nat. Mater.* **2010**, 9, 172-178.
50. Imaz, I.; Rubio-Martinez, M.; An, J.; Sole-Font, I.; Rosi, N. L.; Maspocho, D., *Chem. Commun.* **2011**, 47, 7287-7302.
51. An, J.; Geib, S. J.; Rosi, N. L., *J. Am. Chem. Soc.* **2009**, 131, 8376-8377.
52. An, J.; Farha, O. K.; Hupp, J. T.; Pohl, E.; Yeh, J. I.; Rosi, N. L., *Nat. Commun.* **2012**, 3, 604.
53. Sletten, E., *Acta Crystallogr. B* **1969**, 25, 1480-1491.
54. Rojas-González, P. X.; Castiñeiras, A.; González-Pérez, J. M.; Choquesillo-Lazarte, D.; Niclós-Gutiérrez, J., *Inorg. Chem.* **2002**, 41, 6190-6192.
55. García-Terán, J. P.; Castillo, O.; Luque, A.; García-Couceiro, U.; Román, P.; Lezama, L., *Inorg. Chem.* **2004**, 43, 4549-4551.
56. Yang, E.-C.; Zhao, H.-K.; Ding, B.; Wang, X.-G.; Zhao, X.-J., *New J. Chem.* **2007**, 31, 1887-1890.
57. Zhang, M.; Gu, Z.-Y.; Bosch, M.; Perry, Z.; Zhou, H.-C., *Coord. Chem. Rev.* **2015**, 293-294, 327-356.
58. Anderson, S. L.; Stylianou, K. C., *Coord. Chem. Rev.* **2017**, 349, 102-128.
59. Cai, H.; Li, M.; Lin, X.-R.; Chen, W.; Chen, G.-H.; Huang, X.-C.; Li, D., *Angew. Chem. Int. Ed.* **2015**, 127, 10600-10605.
60. Thomas-Gipson, J.; Beobide, G.; Castillo, O.; Fröba, M.; Hoffmann, F.; Luque, A.; Pérez-Yáñez, S.; Román, P., *Cryst. Growth Des.* **2014**, 14, 4019-4029.

61. Burneo, I.; Stylianou, K. C.; Rodríguez-Hermida, S.; Juanhuix, J.; Fontrodona, X.; Imaz, I.; Maspoch, D., *Cryst. Growth Des.* **2015**, *15*, 3182-3189.
62. García-Terán, J. P.; Castillo, O.; Luque, A.; García-Couceiro, U.; Román, P.; Lloret, F., *Inorg. Chem.* **2004**, *43*, 5761-5770.
63. Garcia-Teran, J. P.; Castillo, O.; Luque, A.; Garcia-Couceiro, U.; Beobide, G.; Roman, P., *Dalton Trans.* **2006**, 902-911.
64. Wang, F.; Tan, Y.-X.; Yang, H.; Zhang, H.-X.; Kang, Y.; Zhang, J., *Chem. Commun.* **2011**, *47*, 5828-5830.
65. Das, S.; Madhavaiah, C.; Verma, S.; Bharadwaj, P. K., *Inorg. Chim. Acta* **2005**, *358*, 3236-3240.
66. Huang, H.-X.; Tian, X.-Z.; Song, Y.-M.; Liao, Z.-W.; Sun, G.-M.; Luo, M.-B.; Liu, S.-J.; Xu, W.-Y.; Luo, F., *Aust. J. Chem.* **2012**, *65*, 320-325.
67. Bux, H.; Feldhoff, A.; Cravillon, J.; Wiebcke, M.; Li, Y.-S.; Caro, J., *Chem. Mater.* **2011**, *23*, 2262-2269.
68. Charland, J.-P., *Inorg. Chim. Acta.* **1987**, *135*, 191-196.
69. Charland, J. P.; Beauchamp, A. L., *Inorg. Chem.* **1986**, *25*, 4870-4876.
70. Gładysiak, A.; Nguyen, T. N.; Anderson, S. L.; Boyd, P. G.; Palgrave, R. G.; Bacsa, J.; Smit, B.; Rosseinsky, M. J.; Stylianou, K. C., *Inorg. Chem.* **2018**, *57*, 1888-1900.
71. An, J.; Geib, S. J.; Rosi, N. L., *J. Am. Chem. Soc.* **2010**, *132*, 38-39.
72. Thomas-Gipson, J.; Beobide, G.; Castillo, O.; Cepeda, J.; Luque, A.; Pérez-Yáñez, S.; Aguayo, A. T.; Román, P., *CrystEngComm* **2011**, *13*, 3301-3305.
73. Wang, F.; Kang, Y., *Inorg. Chem. Commun.* **2012**, *20*, 266-268.
74. Zhang, M.; Lu, W.; Li, J.-R.; Bosch, M.; Chen, Y.-P.; Liu, T.-F.; Liu, Y.; Zhou, H.-C., *Inorg. Chem. Front.* **2014**, *1*, 159-162.
75. An, J.; Shade, C. M.; Chengelis-Czegán, D. A.; Petoud, S.; Rosi, N. L., *J. Am. Chem. Soc.* **2011**, *133*, 1220-1223.
76. Shen, X.; Yan, B., *J. Mater. Chem. C* **2015**, *3*, 7038-7044.
77. Li, T.; Rosi, N. L., *Chem. Commun.* **2013**, *49*, 11385-11387.
78. An, J.; Rosi, N. L., *J. Am. Chem. Soc.* **2010**, *132*, 5578-5579.
79. Nugent, P. S.; Rhodus, V. L.; Pham, T.; Forrest, K.; Wojtas, L.; Space, B.; Zaworotko, M. J., *J. Am. Chem. Soc.* **2013**, *135*, 10950-10953.
80. Li, T.; Sullivan, J. E.; Rosi, N. L., *J. Am. Chem. Soc.* **2013**, *135*, 9984-9987.
81. Li, T.; Chen, D.-L.; Sullivan, J. E.; Kozłowski, M. T.; Johnson, J. K.; Rosi, N. L., *Chem. Sci.* **2013**, *4*, 1746-1755.
82. Pérez-Yáñez, S.; Beobide, G.; Castillo, O.; Cepeda, J.; Luque, A.; Aguayo, A. T.; Román, P., *Inorg. Chem.* **2011**, *50*, 5330-5332.
83. Li, T.; Kozłowski, M. T.; Doud, E. A.; Blakely, M. N.; Rosi, N. L., *J. Am. Chem. Soc.* **2013**, *135*, 11688-11691.
84. Stylianou, K. C.; Warren, J. E.; Chong, S. Y.; Rabone, J.; Bacsa, J.; Bradshaw, D.; Rosseinsky, M. J., *Chem. Commun.* **2011**, *47*, 3389-3391.
85. Fu, H.-R.; Zhang, J., *Chem. Eur. J.* **2015**, *21*, 5700-5703.
86. Kampouri, S.; Nguyen, T. N.; Ireland, C. P.; Valizadeh, B.; Ebrahim, F. M.; Capano, G.; Ongari, D.; Mace, A.; Guijarro, N.; Sivula, K.; Sienkiewicz, A.; Forro, L.; Smit, B.; Stylianou, K. C., *J. Mater. Chem. A* **2018**.
87. Anderson, S. L.; Boyd, P. G.; Gładysiak, A.; Nguyen, T. N.; Palgrave, R. G.; Kubicki, D.; Emsley, L.; Bradshaw, D.; Rosseinsky, M. J.; Smit, B.; Stylianou, K. C., *Nat. Commun.* **2019**, *10*, 1612.
88. Nguyen, T. N.; Ebrahim, F. M.; Stylianou, K. C., *Coord. Chem. Rev.* **2018**, *377*, 259-306.

89. Allendorf, M. D.; Bauer, C. A.; Bhakta, R. K.; Houk, R. J. T., *Chem. Soc. Rev.* **2009**, *38*, 1330-1352.
90. Heine, J.; Muller-Buschbaum, K., *Chem. Soc. Rev.* **2013**, *42*, 9232-9242.
91. Cui, Y.; Yue, Y.; Qian, G.; Chen, B., *Chem. Rev.* **2012**, *112*, 1126-1162.
92. Stylianou, K. C.; Heck, R.; Chong, S. Y.; Bacsá, J.; Jones, J. T. A.; Khimyak, Y. Z.; Bradshaw, D.; Rosseinsky, M. J., *J. Am. Chem. Soc.* **2010**, *132*, 4119-4130.
93. Huo, P.; Chen, T.; Hou, J.-L.; Yu, L.; Zhu, Q.-Y.; Dai, J., *Inorg. Chem.* **2016**, *55*, 6496-6503.
94. Miyasaka, H., *Acc. Chem. Res.* **2013**, *46*, 248-257.
95. Huo, P.; Li, Y.-H.; Xue, L.-J.; Chen, T.; Yu, L.; Zhu, Q.-Y.; Dai, J., *CrystEngComm* **2016**, *18*, 1904-1910.
96. Chen, L.; Wang, H.; Zhang, D. W.; Zhou, Y.; Li, Z. T., *Angew. Chem. Int. Ed.* **2015**, *54*, 4028-4031.
97. Lee, C. Y.; Farha, O. K.; Hong, B. J.; Sarjeant, A. A.; Nguyen, S. T.; Hupp, J. T., *J. Am. Chem. Soc.* **2011**, *133*, 15858-15861.
98. Chen, W.; Wang, J.-Y.; Chen, C.; Yue, Q.; Yuan, H.-M.; Chen, J.-S.; Wang, S.-N., *Inorg. Chem.* **2003**, *42*, 944-946.
99. Frisch, M.; Cahill, C. L., *Dalton Trans.* **2005**, 1518-1523.
100. Colacio, E.; Kivekäs, R.; Lloret, F.; Sunberg, M.; Suarez-Varela, J.; Bardají, M.; Laguna, A., *Inorg. Chem.* **2002**, *41*, 5141-5149.
101. Vogler, A.; Nikol, H., *pac* **1992**, *64*, 1311-1317.
102. Wibowo, A. C.; Smith, M. D.; zur Loye, H.-C., *Chem. Commun.* **2011**, *47*, 7371-7373.
103. Huang, Y.; Yan, B.; Shao, M.; Chen, Z., *J. Mol. Struct.* **2007**, *871*, 59-66.
104. Wang, Y.; Huang, R.; Zhang, J.; Cheng, G.; Yang, H., *Polyhedron* **2018**, *148*, 178-183.
105. Park, Y. K.; Choi, S. B.; Kim, H.; Kim, K.; Won, B. H.; Choi, K.; Choi, J. S.; Ahn, W. S.; Won, N.; Kim, S., *Angew. Chem. Int. Ed.* **2007**, *119*, 8378-8381.
106. Cornil, J.; Dos Santos, D.; Crispin, X.; Silbey, R.; Brédas, J., *J. Am. Chem. Soc.* **1998**, *120*, 1289-1299.
107. McManus, G. J.; Perry, M.; Perry, M.; Wagner, B. D.; Zaworotko, M. J., *J. Am. Chem. Soc.* **2007**, *129*, 9094-9101.
108. Wagner, B. D.; McManus, G. J.; Moulton, B.; Zaworotko, M. J., *Chem. Commun.* **2002**, 2176-2177.
109. Rieter, W. J.; Taylor, K. M.; Lin, W., *Journal of the American Chemical Society* **2007**, *129*, 9852-9853.
110. Rosen, D. L.; Sharpless, C.; McGown, L. B., *Anal. Chem.* **1997**, *69*, 1082-1085.
111. Bauer, C. A.; Timofeeva, T. V.; Settersten, T. B.; Patterson, B. D.; Liu, V. H.; Simmons, B. A.; Allendorf, M. D., *J. Am. Chem. Soc.* **2007**, *129*, 7136-7144.
112. Knoll, G. F., *Radiation detection and measurement*. John Wiley & Sons: 2010.
113. Moore, E. G.; Samuel, A. P.; Raymond, K. N., *Acc. Chem. Res.* **2009**, *42*, 542-552.
114. Marques, L. F.; Correa, C. C.; Ribeiro, S. J. L.; dos Santos, M. V.; Dutra, J. D. L.; Freire, R. O.; Machado, F. C., *J. Solid State Chem.* **2015**, *227*, 68-78.
115. Wu, L.-L.; Zhao, J.; Wang, H.; Wang, J., *CrystEngComm* **2016**, *18*, 4268-4271.
116. Rocha, J.; Carlos, L. D.; Paz, F. A. A.; Ananias, D., *Chem. Soc. Rev.* **2011**, *40*, 926-940.
117. Seitz, M.; Oliver, A. G.; Raymond, K. N., *J. Am. Chem. Soc.* **2007**, *129*, 11153-11160.
118. Harris, D. C.; Bertolucci, M. D., *Symmetry and spectroscopy: an introduction to vibrational and electronic spectroscopy*. Courier Corporation: 1989.
119. Nasalevich, M. A.; van der Veen, M.; Kapteijn, F.; Gascon, J., *CrystEngComm* **2014**, *16*, 4919-4926.
120. Sun, L.; Campbell, M. G.; Dincă, M., *Angew. Chem. Int. Ed.* **2016**, *55*, 3566-3579.

121. Yoon, M.; Suh, K.; Natarajan, S.; Kim, K., *Angewandte Chemie International Edition* **2013**, 52, 2688-2700.
122. Grosso, G.; Parravicini, G. P., Chapter 11 - Optical and Transport Properties of Metals. In *Solid State Physics (Second Edition)*, Academic Press: Amsterdam, 2014; pp 483-528.
123. Grosso, G.; Parravicini, G. P., Chapter 12 - Optical Properties of Semiconductors and Insulators. . In *Solid State Physics (Second Edition)*, Academic Press: Amsterdam, 2014; pp 529-576.
124. Mott, N. F., *Philos. Mag.* **1969**, 19, 835-852.
125. Hoffmann, R., *Acc. Chem. Res.* **1971**, 4, 1-9.
126. Takaishi, S.; Hosoda, M.; Kajiwar, T.; Miyasaka, H.; Yamashita, M.; Nakanishi, Y.; Kitagawa, Y.; Yamaguchi, K.; Kobayashi, A.; Kitagawa, H., *Inorg. Chem.* **2009**, 48, 9048-9050.
127. Kobayashi, Y.; Jacobs, B.; Allendorf, M. D.; Long, J. R., *Chem. Mater.* **2010**, 22, 4120-4122.
128. Hao, Z.; Yang, G.; Song, X.; Zhu, M.; Meng, X.; Zhao, S.; Song, S.; Zhang, H., *J. Mater. Chem. A* **2014**, 2, 237-244.
129. Chae, S. H.; Kim, H.-C.; Lee, Y. S.; Huh, S.; Kim, S.-J.; Kim, Y.; Lee, S. J., *Cryst. Growth Des.* **2014**, 15, 268-277.
130. Rosi, N. L.; Kim, J.; Eddaoudi, M.; Chen, B.; O'Keeffe, M.; Yaghi, O. M., *J. Am. Chem. Soc.* **2005**, 127, 1504-1518.
131. Dietzel, P. D. C.; Blom, R.; Fjellvåg, H., *Eur. J. Inorg. Chem.* **2008**, 2008, 3624-3632.
132. Bloch, E. D.; Murray, L. J.; Queen, W. L.; Chavan, S.; Maximoff, S. N.; Bigi, J. P.; Krishna, R.; Peterson, V. K.; Grandjean, F.; Long, G. J., *J. Am. Chem. Soc.* **2011**, 133, 14814-14822.
133. Sanz, R.; Martínez, F.; Orcajo, G.; Wojtas, L.; Briones, D., *Dalton Trans.* **2013**, 42, 2392-2398.
134. Sun, L.; Miyakai, T.; Seki, S.; Dincă, M., *J. Am. Chem. Soc.* **2013**, 135, 8185-8188.
135. Talin, A. A.; Centrone, A.; Ford, A. C.; Foster, M. E.; Stavila, V.; Haney, P.; Kinney, R. A.; Szalai, V.; El Gabaly, F.; Yoon, H. P.; Léonard, F.; Allendorf, M. D., *Science* **2013**.
136. Erickson, K. J.; Léonard, F.; Stavila, V.; Foster, M. E.; Spataru, C. D.; Jones, R. E.; Foley, B. M.; Hopkins, P. E.; Allendorf, M. D.; Talin, A. A., *Adv. Mater.* **2015**, 27, 3453-3459.
137. Gładysiak, A.; Nguyen, T. N.; Spodaryk, M.; Lee, J.-H.; Neaton, J. B.; Züttel, A.; Stylianou, K. C., *Chem. Eur. J.* **2019**, 25, 501-506.
138. Ferraris, J.; Cowan, D.; Walatka, V. t.; Perlstein, J., *J. Am. Chem. Soc.* **1973**, 95, 948-949.
139. Sirringhaus, H.; Brown, P.; Friend, R.; Nielsen, M. M.; Bechgaard, K.; Langeveld-Voss, B.; Spiering, A.; Janssen, R. A.; Meijer, E.; Herwig, P., *Nature* **1999**, 401, 685.
140. Alvarez, S., *Dalton Trans.* **2013**, 42, 8617-8636.
141. Narayan, T. C.; Miyakai, T.; Seki, S.; Dincă, M., *J. Am. Chem. Soc.* **2012**, 134, 12932-12935.
142. Park, S. S.; Hontz, E. R.; Sun, L.; Hendon, C. H.; Walsh, A.; Van Voorhis, T.; Dincă, M., *J. Am. Chem. Soc.* **2015**, 137, 1774-1777.
143. Panda, T.; Banerjee, R., *Proc. Natl. Acad. Sci. India. Sect. A* **2014**, 84, 331-336.
144. Hmadeh, M.; Lu, Z.; Liu, Z.; Gándara, F.; Furukawa, H.; Wan, S.; Augustyn, V.; Chang, R.; Liao, L.; Zhou, F.; Perre, E.; Ozolins, V.; Suenaga, K.; Duan, X.; Dunn, B.; Yamamoto, Y.; Terasaki, O.; Yaghi, O. M., *Chem. Mater.* **2012**, 24, 3511-3513.
145. Kambe, T.; Sakamoto, R.; Hoshiko, K.; Takada, K.; Miyachi, M.; Ryu, J.-H.; Sasaki, S.; Kim, J.; Nakazato, K.; Takata, M., *J. Am. Chem. Soc.* **2013**, 135, 2462-2465.
146. Cui, J.; Xu, Z., *Chem. Commun.* **2014**, 50, 3986-3988.
147. Sheberla, D.; Sun, L.; Blood-Forsythe, M. A.; Er, S. I.; Wade, C. R.; Brozek, C. K.; Aspuru-Guzik, A. n.; Dincă, M., *J. Am. Chem. Soc.* **2014**, 136, 8859-8862.
148. Campbell, M. G.; Liu, S. F.; Swager, T. M.; Dincă, M., *J. Am. Chem. Soc.* **2015**, 137, 13780-13783.

149. Millikan, R. A.; Bishop, E. S., *Elements of electricity: a practical discussion of the fundamental laws and phenomena of electricity and their practical applications in the business and industrial world*. American Technical Society: 1917.
150. Macdonald, J. R.; Barsoukov, E., *Impedance spectroscopy: theory, experiment, and applications*. 2005; Vol. 1.
151. Perić, J.; Vučak, M.; Krstulović, R.; Brečević, L.; Kralj, D., *Thermochimica Acta* **1996**, 277, 175-186.
152. Hanaor, D. A. H.; Sorrell, C. C., *J. Mater. Sci.* **2011**, 46, 855-874.
153. Zhang, M.; Chen, T.; Wang, Y., *RSC Adv.* **2017**, 7, 52755-52761.
154. Gándara, F.; de la Peña-O'Shea, V. A.; Illas, F.; Snejko, N.; Proserpio, D. M.; Gutiérrez-Puebla, E.; Monge, M. A., *Inorg. Chem.* **2009**, 48, 4707-4713.
155. Taouti, M. B.; Suffren, Y.; Leynaud, O.; Benbortal, D.; Brenier, A.; Gautier-Luneau, I., *Inorg. Chem.* **2015**, 54, 3608-3618.
156. Whitlam, S.; Jack, R. L., *Annu. Rev. Phys. Chem.* **2015**, 66, 143-163.
157. Ostwald, W., *Z. Phys. Chem* **1897**, 22, 289-330.
158. Rein ten Wolde, P.; Frenkel, D., *Phys. Chem. Chem. Phys.* **1999**, 1, 2191-2196.
159. Cardew, P. T.; Davey, R. J., *Proc. R. Soc. Lond. A* **1985**, 398, 415-428.
160. Desgranges, C.; Delhommelle, J., *Phys. Rev. Lett.* **2007**, 98, 235502.
161. Zhu, N.; Lennox, M. J.; Duren, T.; Schmitt, W., *Chem. Commun.* **2014**, 50, 4207-4210.
162. Yan, Z.; Li, M.; Gao, H.-L.; Huang, X.-C.; Li, D., *Chem. Commun.* **2012**, 48, 3960-3962.
163. Frahm, D.; Hoffmann, F.; Fröba, M., *Cryst. Growth Des.* **2014**, 14, 1719-1725.
164. Morris, R. E., *ChemPhysChem* **2009**, 10, 327-329.
165. O'Brien, M. G.; Beale, A. M.; Weckhuysen, B. M., *Chem. Soc. Rev.* **2010**, 39, 4767-4782.
166. Jensen, K. M. Ø.; Tyrsted, C.; Bremholm, M.; Iversen, B. B., *ChemSusChem* **2014**, 7, 1594-1611.
167. Goesten, M. G.; Kapteijn, F.; Gascon, J., *CrystEngComm.* **2013**, 15, 9249-9257.
168. Yeung, H. H. M.; Wu, Y.; Henke, S.; Cheetham, A. K.; O'Hare, D.; Walton, R. I., *Angew. Chem. Int. Ed.* **2016**, 55, 2012-2016.
169. Nayak, S.; Nayek, H. P.; Pietzonka, C.; Novitchi, G.; Dehnen, S., *J. Mol. Struct.* **2011**, 1004, 82-87.
170. Wang, Y.-L.; Jiang, Y.-L.; Liu, Q.-Y.; Tan, Y.-X.; Wei, J.-J.; Zhang, J., *CrystEngComm.* **2011**, 13, 4981-4987.
171. Delgado Friedrichs, O.; O'Keeffe, M.; Yaghi, O. M., *Acta Crystallogr. Sect. A* **2003**, 59, 22-27.
172. O'Keeffe, M.; Yaghi, O. M., *Chem. Rev.* **2012**, 112, 675-702.
173. Majano, G.; Martin, O.; Hammes, M.; Smeets, S.; Baerlocher, C.; Pérez-Ramírez, J., *Adv. Funct. Mater.* **2014**, 24, 3855-3865.
174. Piguet, C.; Geraldès, C. F. G. C., Paramagnetic NMR Lanthanide Induced Shifts for Extracting Solution Structures. In *Handbook on the Physics and Chemistry of Rare Earths*, K.A. Gschneidner, J. C. G. B.; Pecharsky, V. K., Eds. Elsevier: 2003; Vol. Volume 33, pp 353-463.
175. Krumpel, A. H., *Locating Energy Levels of Lanthanide Ions in Inorganic Ionic Compounds*. Shaker Publishing: 2009.
176. Nguyen, T. N.; Capano, G.; Gladysiak, A.; Ebrahim, F. M.; Eliseeva, S. V.; Chidambaram, A.; Valizadeh, B.; Petoud, S.; Smit, B.; Stylianou, K. C., *Chemical Communications* **2018**.
177. Pereira, C. C. L.; Coutinho, J. T.; Pereira, L. C. J.; Leal, J. P.; Laia, C. A. T.; Monteiro, B., *Polyhedron* **2015**, 91, 42-46.
178. A. W. Fan, A. L. L.-M., *Beijing, CHINE, 2002. Vol. 60, C*
179. Armelao, L.; Quici, S.; Barigelletti, F.; Accorsi, G.; Bottaro, G.; Cavazzini, M.; Tondello, E., *Coord. Chem. Rev.* **2010**, 254, 487-505.

180. Hendon, C. H.; Tiana, D.; Fontecave, M.; Sanchez, C.; D'arras, L.; Sassoye, C.; Rozes, L.; Mellot-Draznieks, C.; Walsh, A., *Journal of the American Chemical Society* **2013**, *135*, 10942-10945.
181. Hendon, C. H.; Walsh, A.; Dincă, M., *Inorganic Chemistry* **2016**, *55*, 7265-7269.
182. Komatsu, T.; Taylor, J. M.; Kitagawa, H., *Inorganic Chemistry* **2016**, *55*, 546-548.
183. Dolgoplova, E. A.; Brandt, A. J.; Ejegbavwo, O. A.; Duke, A. S.; Maddumapatabandi, T. D.; Galhenage, R. P.; Larson, B. W.; Reid, O. G.; Ammal, S. C.; Heyden, A.; Chandrashekhar, M.; Stavila, V.; Chen, D. A.; Shustova, N. B., *Journal of the American Chemical Society* **2017**, *139*, 5201-5209.
184. Kampouri, S.; Nguyen, T. N.; Ireland, C. P.; Valizadeh, B.; Ebrahim, F. M.; Capano, G.; Ongari, D.; Mace, A.; Guijarro, N.; Sivula, K.; Sienkiewicz, A.; Forro, L.; Smit, B.; Stylianou, K. C., *Journal of Materials Chemistry A* **2018**, *6*, 2476-2481.
185. Ahn, D. Y.; Lee, D. Y.; Shin, C. Y.; Bui, H. T.; Shrestha, N. K.; Giebeler, L.; Noh, Y.-Y.; Han, S.-H., *ACS Applied Materials & Interfaces* **2017**, *9*, 12930-12935.
186. Lee, C.-H.; Podraza, N. J.; Zhu, Y.; Berger, R. F.; Shen, S.; Sestak, M.; Collins, R. W.; Kourkoutis, L. F.; Mundy, J. A.; Wang, H.; Mao, Q.; Xi, X.; Brillson, L. J.; Neaton, J. B.; Muller, D. A.; Schlom, D. G., *Appl. Phys. Lett.* **2013**, *102*, 122901.
187. Taddei, M.; Tiana, D.; Casati, N.; van Bokhoven, J. A.; Smit, B.; Ranocchiari, M., *Phys. Chem. Chem. Phys.* **2017**, *19*, 1551-1559.
188. Tiana, D.; Hendon, C. H.; Walsh, A.; Vaid, T. P., *Phys. Chem. Chem. Phys.* **2014**, *16*, 14463-14472.
189. Hendon, C. H.; Tiana, D.; Fontecave, M.; Sanchez, C.; D'arras, L.; Sassoye, C.; Rozes, L.; Mellot-Draznieks, C.; Walsh, A., *J. Am. Chem. Soc.* **2013**, *135*, 10942-10945.
190. Bernales, V.; Yang, D.; Yu, J.; Gümüslü, G.; Cramer, C. J.; Gates, B. C.; Gagliardi, L., *ACS Appl. Mater. Interfaces* **2017**, *3*, 734-742.
191. Anderson, S. L.; Gladysiak, A.; Boyd, P. G.; Ireland, C. P.; Mieville, P.; Tiana, D.; Vlaisavljevich, B.; Schouwink, P.; van Beek, W.; Gagnon, K. J.; Smit, B.; Stylianou, K. C., *CrystEngComm* **2017**.
192. Paolo, G.; Stefano, B.; Nicola, B.; Matteo, C.; Roberto, C.; Carlo, C.; Davide, C.; Guido, L. C.; Matteo, C.; Ismaila, D.; Andrea Dal, C.; Stefano de, G.; Stefano, F.; Guido, F.; Ralph, G.; Uwe, G.; Christos, G.; Anton, K.; Michele, L.; Layla, M.-S.; Nicola, M.; Francesco, M.; Riccardo, M.; Stefano, P.; Alfredo, P.; Lorenzo, P.; Carlo, S.; Sandro, S.; Gabriele, S.; Ari, P. S.; Alexander, S.; Paolo, U.; Renata, M. W., *Journal of Physics: Condensed Matter* **2009**, *21*, 395502.
193. Perdew, J. P.; Ruzsinszky, A.; Csonka, G. I.; Vydrov, O. A.; Scuseria, G. E.; Constantin, L. A.; Zhou, X.; Burke, K., *Phys. Rev. Lett.* **2008**, *100*, 136406.
194. Park, I.-H.; Lee, S. S.; Vittal, J. J., *Chem. Eur. J.* **2013**, *19*, 2695-2702.
195. Warren, J. E.; Perkins, C. G.; Jelfs, K. E.; Boldrin, P.; Chater, P. A.; Miller, G. J.; Manning, T. D.; Briggs, M. E.; Stylianou, K. C.; Claridge, J. B.; Rosseinsky, M. J., *Angew. Chem.* **2014**, *126*, 4680-4684.
196. Eddaoudi, M.; Kim, J.; Rosi, N.; Vodak, D.; Wachter, J.; O'Keeffe, M.; Yaghi, O. M., *Science* **2002**, *295*, 469-472.
197. Kong, X.; Deng, H.; Yan, F.; Kim, J.; Swisher, J. A.; Smit, B.; Yaghi, O. M.; Reimer, J. A., *Science* **2013**, *341*, 882-885.
198. Lyndon, R.; Konstas, K.; Ladewig, B. P.; Southon, P. D.; Kepert, P. C. J.; Hill, M. R., *Angew. Chem. Int. Ed.* **2013**, *52*, 3695-3698.
199. Chen, G.; Fang, X. a.; Chen, Q.; Zhang, J. g.; Zhong, Z.; Xu, J.; Zhu, F.; Ouyang, G., *Adv. Funct. Mater.* **2017**, *27*, 1702126-1702126.
200. Deleu, W. P.; Rivero, G.; Teixeira, R. F.; Du Prez, F. E.; De Vos, D. E., *Chem. Mater.* **2015**, *27*, 5495-5502.

201. Chen, W.-M.; Meng, X.-L.; Zhuang, G.-L.; Wang, Z.; Kurmoo, M.; Zhao, Q.-Q.; Wang, X.-P.; Shan, B.; Tung, C.-H.; Sun, D., *Journal of Materials Chemistry A* **2017**, *5*, 13079-13085.
202. Chen, J.-M.; Hou, Y.-X.; Zhou, Q.-K.; Zhang, H.; Liu, D., *Dalton Trans.* **2017**, *46*, 9755-9759.
203. Martí Gastaldo, C.; Antypov, D.; Warren, J. E.; Briggs, M. E.; Chater, P. A.; Wiper, P. V.; Miller, G. J.; Khimyak, Y. Z.; Darling, G. R.; Berry, N. G.; Rosseinsky, M. J., *Nat. Chem.* **2014**, *6*, 343-351.
204. Rabone, J.; Yue, Y.-F.; Chong, S. Y.; Stylianou, K. C.; Bacsá, J.; Bradshaw, D.; Darling, G. R.; Berry, N. G.; Khimyak, Y. Z.; Ganin, A. Y.; Wiper, P.; Claridge, J. B.; Rosseinsky, M. J., *Science* **2010**, *329*, 1053-1057.
205. Wright, P. A., *Science* **2010**, *329*, 1025-1026.
206. Beobide, G.; Castillo, O.; Luque, A.; Pérez-Yáñez, S., *CrystEngComm* **2015**, *17*, 3051-3059.
207. Beobide, G.; Castillo, O.; Cepeda, J.; Luque, A.; Pérez-Yáñez, S.; Román, P.; Thomas-Gipson, J., *Coord. Chem. Rev.* **2013**, *257*, 2716-2736.
208. Navarro-Sánchez, J.; Argente-García, A. I.; Moliner-Martínez, Y.; Roca-Sanjuán, D.; Antypov, D.; Campíns-Falcó, P.; Rosseinsky, M. J.; Martí-Gastaldo, C., *J. Am. Chem. Soc.* **2017**, *139*, 4294-4297.
209. Mohideen, M. I. H.; Xiao, B.; Wheatley, P. S.; McKinlay, A. C.; Li, Y.; Slawin, A. M. Z.; Aldous, D. W.; Cessford, N. F.; Düren, T.; Zhao, X.; Gill, R.; Thomas, K. M.; Griffin, J. M.; Ashbrook, S. E.; Morris, R. E., *Nat. Chem.* **2011**, *3*, 304.
210. Stylianou, K. C.; Gómez, L.; Imaz, I.; Verdugo-Escamilla, C.; Ribas, X.; MasPOCH, D., *Chem. Eur. J.* **2015**, *21*, 9964-9969.
211. Ingleson, M. J.; Barrio, J. P.; Bacsá, J.; Dickinson, C.; Park, H.; Rosseinsky, M. J., *Chem. Commun.* **2008**, 1287-1289.
212. Sapchenko Sergey, A.; Dybtsev Danil, N.; Fedin Vladimir, P., *pac* **2017**, *89*, 1049.
213. Todorova, T. K.; Rozanska, X.; Gervais, C.; Legrand, A.; Ho, L. N.; Berruyer, P.; Lesage, A.; Emsley, L.; Farrusseng, D.; Canivet, J.; Mellot-Draznieks, C., *Chemistry – A European Journal* **2016**, *22*, 16531-16538.
214. Pfeifer, G. P.; Besaratinia, A., *Photochemical & photobiological sciences : Official journal of the European Photochemistry Association and the European Society for Photobiology* **2012**, *11*, 90-97.
215. Juan-Alcaniz, J.; Ramos-Fernandez, E. V.; Kapteijn, F.; Gascon, J., CHAPTER 10 MOFs as Nano-reactors. In *Metal Organic Frameworks as Heterogeneous Catalysts*, The Royal Society of Chemistry: 2013; pp 310-343.
216. Rauer, C.; Nogueira, J. J.; Marquetand, P.; González, L., *J. Am. Chem. Soc.* **2016**, *138*, 15911-15916.
217. Hoffmann, R.; Woodward, R. B., *Acc. Chem. Res.* **1968**, *1*, 17-22.
218. Schmidt, G. M. J., *pac* **1971**, *27*, 647.
219. Füchtbauer, W.; Mazur, P., *J. Photochem. Photobiol.* **1966**, *5*, 323-335.
220. Cuquerella, M. C.; Lhiaubet-Vallet, V.; Bosca, F.; Miranda, M. A., *Chem. Sci.* **2011**, *2*, 1219-1232.
221. Schreier, W. J.; Schrader, T. E.; Koller, F. O.; Gilch, P.; Crespo-Hernández, C. E.; Swaminathan, V. N.; Carell, T.; Zinth, W.; Kohler, B., *Science (New York, N.Y.)* **2007**, *315*, 625-629.
222. Stylianou, K. C., *PhD thesis, University of Liverpool* **2011**.
223. Blatov, V. A.; Shevchenko, A. P.; Proserpio, D. M., *Cryst. Growth Des.* **2014**, *14*, 3576-3586.
224. Schmuck, C.; Wienand, W., *Angew. Chem. Int. Ed.* **2001**, *40*, 4363-4369.
225. Seeman, N. C.; Rosenberg, J. M.; Suddath, F. L.; Kim, J. J. P.; Rich, A., *J. Mol. Biol.* **1976**, *104*, 109-144.
226. Tang, W.; Sanville, E.; Henkelman, G., *J. Phys. Condens. Matter* **2009**, *21*, 084204.

227. Fonseca Guerra, C.; Bickelhaupt, F. M.; Snijders, J. G.; Baerends, E. J., *J. Am. Chem. Soc.* **2000**, *122*, 4117-4128.
228. Espejo, C.; Rey-González, R., *Rev. Mex. Fis.* **2007**, *53*, 212-216.
229. Liu, Y.; Bryantsev, V. S.; Diallo, M. S.; Goddard III, W. A., *J. Am. Chem. Soc.* **2009**, *131*, 2798-2799.
230. Law, Y. K.; Azadi, J.; Crespo-Hernández, C. E.; Olmon, E.; Kohler, B., *Biophys. J.* **2008**, *94*, 3590-3600.
231. Kaur, G.; Adhikari, R.; Cass, P.; Bown, M.; Gunatillake, P., *RSC Adv.* **2015**, *5*, 37553-37567.
232. Tien, N. T.; Jeon, S.; Kim, D. I.; Trung, T. Q.; Jang, M.; Hwang, B. U.; Byun, K. E.; Bae, J.; Lee, E.; Tok, J. B. H.; Bao, Z.; Lee, N. E.; Park, J. J., *Adv. Mater.* **2014**, *26*, 796-804.
233. Hou, C.; Wang, H.; Zhang, Q.; Li, Y.; Zhu, M., *Adv. Mater.* **2014**, *26*, 5018-5024.
234. Lou, Z.; Chen, S.; Wang, L.; Shi, R.; Li, L.; Jiang, K.; Chen, D.; Shen, G., *Nano Energy* **2017**, *38*, 28-35.
235. Trung, T. Q.; Ramasundaram, S.; Hwang, B. U.; Lee, N. E., *Adv. Mater.* **2016**, *28*, 502-509.
236. Zhao, X.-H.; Ma, S.-N.; Long, H.; Yuan, H.; Tang, C. Y.; Cheng, P. K.; Tsang, Y. H., *ACS Appl. Mater. Interfaces* **2018**, *10*, 3986-3993.
237. Yang, Y.-J.; Cheng, M.-Y.; Chang, W.-Y.; Tsao, L.-C.; Yang, S.-A.; Shih, W.-P.; Chang, F.-Y.; Chang, S.-H.; Fan, K.-C., *Sens. Actuators A* **2008**, *143*, 143-153.
238. Ebrahim, F. M.; Nguyen, T. N.; Shyshkanov, S.; Gładysiak, A.; Favre, P.; Zacharia, A.; Itskos, G.; Dyson, P. J.; Stylianou, K. C., *J. Am. Chem. Soc.* **2019**, *141*, 3052-3058.
239. Park, S. S.; Hontz, E. R.; Sun, L.; Hendon, C. H.; Walsh, A.; Van Voorhis, T.; Dincă, M., *J. Am. Chem. Soc.* **2015**, *137*, 1774-1777.
240. Fu, X.; Dong, H.; Zhen, Y.; Hu, W., *Small* **2015**, *11*, 3351-3356.
241. Allendorf, M. D.; Schwartzberg, A.; Stavila, V.; Talin, A. A., *Chem. Eur. J.* **2011**, *17*, 11372-11388.
242. Stavila, V.; Talin, A. A.; Allendorf, M. D., *Chem. Soc. Rev.* **2014**, *43*, 5994-6010.
243. Yang, T.; Jiang, X.; Zhong, Y.; Zhao, X.; Lin, S.; Li, J.; Li, X.; Xu, J.; Li, Z.; Zhu, H., *ACS sens.* **2017**, *2*, 967-974.
244. Liu, Y.; Tao, L.-Q.; Wang, D.-Y.; Zhang, T.-Y.; Yang, Y.; Ren, T.-L., *Appl. Phys. Lett.* **2017**, *110*, 123508.
245. Lan, M.; Zhao, H.; Yuan, H.; Jiang, C.; Zuo, S.; Jiang, Y., *Dyes Pigm.* **2007**, *74*, 357-362.
246. Chen, X.; Wang, Y.; Zhou, J.; Yan, W.; Li, X.; Zhu, J.-J., *Anal. Chem.* **2008**, *80*, 2133-2140.
247. Mikhailenko, S. D.; Afsahi, F.; Kaliaguine, S., *J. Phys. Chem. C* **2014**, *118*, 9165-9175.
248. Wu, W.; Wen, X.; Wang, Z. L., *Science* **2013**, 1234855.
249. Dagdeviren, C.; Su, Y.; Joe, P.; Yona, R.; Liu, Y.; Kim, Y.-S.; Huang, Y.; Damadoran, A. R.; Xia, J.; Martin, L. W., *Nat. Commun.* **2014**, *5*, 4496.
250. Pang, C.; Lee, G.-Y.; Kim, T.-i.; Kim, S. M.; Kim, H. N.; Ahn, S.-H.; Suh, K.-Y., *Nat. Mater.* **2012**, *11*, 795.
251. Alametsä, J.; Viik, J.; Alakare, J.; Värri, A.; Palomäki, A., *Physiol. Meas.* **2008**, *29*, 1071-87.
252. Vashisth, S.; Khan, M.; Vijay, R.; Salhan, A., *Int. J. Bioinformatics Research and Applications* **2012**, *12*, 227-237.
253. Joseph, J.; Jayashankar, V., *J. Med. Devices* **2010**, *4*, 045004.
254. Joseph, J.; Nabeel, P.; Shah, M. I.; Sivaprakasam, M., *PloS one* **2018**, *13*, e0202480.
255. Feyer, V.; Plekan, O.; Prince, K. C.; Šutara, F.; Skála, T.; Cháb, V.; Matolín, V.; Stenuit, G.; Umari, P., *Phys. Rev. B* **2009**, *79*, 155432.
256. Kresse, G.; Furthmüller, J., *Phys. Rev. B* **1996**, *54*, 11169-11186.
257. Kresse, G.; Furthmüller, J., *Comput. Mater. Sci.* **1996**, *6*, 15-50.
258. Kresse, G.; Hafner, J., *Phys. Rev. B* **1994**, *49*, 14251-14269.
259. Kresse, G.; Hafner, J., *Phys. Rev. B* **1993**, *47*, 558-561.

260. Perdew, J. P.; Burke, K.; Ernzerhof, M., *Phys. Rev. Lett.* **1997**, *78*, 1396-1396.
261. Perdew, J. P.; Burke, K.; Ernzerhof, M., *Phys. Rev. Lett.* **1996**, *77*, 3865-3868.
262. Blöchl, P. E., *Phys. Rev. B* **1994**, *50*, 17953-17979.
263. Ongari, D.; Boyd, P. G.; Barthel, S.; Witman, M.; Haranczyk, M.; Smit, B., *Langmuir* **2017**, *33*, 14529-14538.
264. Campaña, C.; Mussard, B.; Woo, T. K., *J. Chem. Theory Comput.* **2009**, *5*, 2866-2878.
265. Plimpton, S., *J. Comput. Phys.* **1995**, *117*, 1-19.
266. Mayo, S. L.; Olafson, B. D.; Goddard, W. A., *J. Phys. Chem.* **1990**, *94*, 8897-8909.
267. Willems, T. F.; Rycroft, C. H.; Kazi, M.; Meza, J. C.; Haranczyk, M., *Micropor. Mesopor. Mat.* **2012**, *149*, 134-141.
268. Pinheiro, M.; Martin, R. L.; Rycroft, C. H.; Jones, A.; Iglesia, E.; Haranczyk, M., *J. Mol. Graph. Model.* **2013**, *44*, 208-219.
269. Pinheiro, M.; Martin, R. L.; Rycroft, C. H.; Haranczyk, M., *CrystEngComm* **2013**, *15*, 7531-7538.
270. Michaud-Agrawal, N.; Denning, E. J.; Woolf, T. B.; Beckstein, O., *J. Comput. Chem.* **2011**, *32*, 2319-2327.
271. J Gowers, R.; Linke, M.; Barnoud, J.; J E Reddy, T.; N Melo, M.; Seyler, S.; L Dotson, D.; Domanski, J.; Buchoux, S.; M Kenney, I.; Others, *MDAnalysis: a Python package for the rapid analysis of molecular dynamics simulations*. 2016.
272. Beukers, R.; Berends, W., *Biochim. Biophys. Acta* **1961**, *49*, 181-189.
273. Cadet, J.; Voituriez, L.; Hruska, F. E.; Kan, L.-S.; Leeuw, F. A. A. M. d.; Altona, C., *Can. J. Chem.* **1985**, *63*, 2861-2868.
274. Burdi, D.; Hoyt, S.; Begley, T. P., *Tetrahedron Lett.* **1992**, *33*, 2133-2136.
275. Dyadkin, V.; Pattison, P.; Dmitriev, V.; Chernyshov, D., *J. Synchrotron Rad.* **2016**, *23*, 825-829.
276. RigakuOxfordDiffraction *CrysAlisPro*, 1.171.38.43; 2015.
277. Sheldrick, G., *Acta Cryst. Sect. A* **2015**, *71*, 3-8.
278. Sheldrick, G., *Acta Crystallographica Section C* **2015**, *71*, 3-8.
279. Dolomanov, O. V.; Bourhis, L. J.; Gildea, R. J.; Howard, J. A. K.; Puschmann, H., *J. Appl. Cryst.* **2009**, *42*, 339-341.
280. Spek, A., *Acta Cryst. Sect. C* **2015**, *71*, 9-18.
281. Macrae, C. F.; Bruno, I. J.; Chisholm, J. A.; Edgington, P. R.; McCabe, P.; Pidcock, E.; Rodriguez-Monge, L.; Taylor, R.; van de Streek, J.; Wood, P. A., *J. Appl. Cryst.* **2008**, *41*, 466-470.
282. Blatov, V. A.; Shevchenko, A. P.; Proserpio, D. M., *Crystal Growth & Design* **2014**, *14*, 3576-3586.

SAMANTHA LYNN ANDERSON

Ave. de Lavaux 81, Pully

Switzerland

+41 076 814 38 36

email: samantha.anderson@epfl.ch

Maiden name: Voth

EDUCATION

Ph.D Chemistry 2019

Ecole Polytechnique Fédérale de Lausanne - Valais

[Dissertation: "Synthesis, Characterization, and Applications of Visible Light Active Metal-Organic Frameworks"]

M.Sc Chemistry 2015

Queen's University, Kingston ON, Canada

[Dissertation: "Chemoselective Cross Coupling of Boronic Esters"]

B.Sc. Honours in Chemistry 2012

University of Winnipeg, Winnipeg MB, Canada

[Honours Thesis: "Rearrangement/Diels-Alder sequence for stereoselective formation of bi- and tricyclic ring systems"]

RESEARCH EXPERIENCE

Department of Chemistry and Chemical Engineering, EPFL, Sion/Lausanne, Switzerland 2015-2019Doctoral Assistant, LSMO group

Rational design, synthesis and characterization of visible light active MOFs for various applications.

This includes ligand design and synthesis for the LSMO group.

Instrument specialization: High throughput MW/Chemspeed robot, SCXRD, PXRD, TGA, IR, NMR,

Fluorescence, UV/vis, sorption.

Department of Chemistry, Queen's University, Kingston ON, CanadaGraduate Research Assistant

2012-2015

Developed synthetic strategies for selective cross coupling of tris boronic ester substrates.

Completed project of selective coupling for bis boronic ester substrates.

All reactions performed using Schlenk Line techniques or a glove box. Instrument specialization:

SFC, GCMS, LC/HPLC, EA, NMR.

Department of Chemistry, University of Winnipeg, Winnipeg MB, CanadaUndergraduate Research Assistant

2010-2012

1. Dr. Adam McCubbin: Completed project on metal free tunable catalysts for allylic alcohol rearrangements.

2. Dr. Ernest Prokopchuk: Completed project on Oxidation of dibenzothiophene by hydrogen peroxide in the presence of bis(acetylacetonato)oxovanadium(IV).

Experience based in both labs involved experimental set up, purification and data analysis.

Instrument specialization: IR, MS

TEACHING EXPERIENCE

Ecole Polytechnique Fédérale de LausanneTeaching Assistant

2015-2019

Courses taught: Experimental Analytical Chemistry (CH-309a)

Chemical Engineering Practice (ChE-309)

Queen's University, Kingston ON, CanadaTeaching Assistant

2012-2015

Courses taught: Organic Chemistry (Life Science) Help Desk (281).
Engineering Chemistry/Chemistry (212)

University Of Winnipeg, Winnipeg MB, Canada

Teaching Assistant/Lab Demonstrator/Marker,

2010-2012

Courses taught: Introductory Chemistry (1111 and 1112).

Organic Chemistry (2202 and 2203)

PUBLICATIONS AND PATENTS

1. **Samantha L. Anderson**, Christopher P. Ireland, Kyriakos C. Stylianou, Berend Smit. Radically Enhanced Room Temperature Degradation of PET. (2019) Provisional patent.
2. **Samantha L. Anderson**, Peter G. Boyd, Andrzej Gładysiak, Tu N. Nguyen, Robert G. Palgrave, Dominik Kubicki, Lyndon Emsley, Darren Bradshaw, Matthew J. Rosseinsky, Berend Smit, Kyriakos C. Stylianou*. Nucleobase Pairing and Photodimerization in a Biologically Derived Metal-Organic Framework Nanoreactor. (2019) *Nat. Commun.* 10, 1612.
3. Andrzej Gładysiak, Tu N. Nguyen, **Samantha L. Anderson**, Peter G. Boyd, Robert G. Palgrave, John Bacsá, Berend Smit, Matthew J. Rosseinsky, Kyriakos C. Stylianou*. Shedding Light on the Protonation States and Location of Protonated N Atoms of Adenine in Metal-Organic Frameworks. (2018) *Inorg. Chem.* 57, 1888-1900
4. **Samantha L. Anderson**, Kyriakos C. Stylianou*. Biologically Derived Metal-Organic Frameworks. (2017) *Coord. Chem. Rev.* 349, 102-128.
5. **Samantha L. Anderson**, Andrzej Gładysiak, Peter G. Boyd, Christopher P. Ireland, Pascal Miéville, Davide Tiana, Bess Vlasisavljevich, Pascal Schouwink, Wouter van Beek, Kevin J. Gagnon, Berend Smit, Kyriakos C. Stylianou*. (2017) *Crys-EngComm*, 19, 3407-3413.
6. Matthew Witman, Sanliang Ling, **Samantha Anderson**, Lianheng Tong, Kyriakos C. Stylianou, Ben Slater, Berend Smit, Maciej Haranczyk*. (2016) *Chem. Sci.* 7, 6263-6272.
7. C.M. Crudden, C. Ziebenhaus, J. P. G. Rygus, K. Ghazati, P. J. Unsworth, M. Nambo, **S. Anderson (Voth)**, M. Hutchinson, V. S. Laberge, Y. Maekawa, D. Imao. Iterative protecting group-free cross-coupling leading to chiral multiply arylated structures. (2016) *Nat. Commun.* 7, 11065-110.
8. **Anderson (Voth), S**; Hollett, J; McCubbin, J. A.* Transition Metal Free Access to Primary Anilines from Boronic Acids and a Common NH_2 Equivalent. (2015) *J. Org. Chem.* 80, 2545-2553.
9. McCubbin, J.A*., **Anderson (Voth), S.**, and Krokhin, O.V. Mild and Tunable Benzoic Acid Catalysts for Rearrangement Reactions of Allylic Alcohols. (2011) *J. Org. Chem.* 76, 8537-8542.
10. Silva, G., **Anderson (Voth), S.**, Szymanski, P., and Prokopchuk, E.M*. Oxidation of dibenzothiophene by hydrogen peroxide in the presence of bis(acetylacetonato)oxovanadium(IV). (2011) *Fuel Processing Technology*, 92, 1656-1661.

CONTRIBUTIONS TO RESEARCH AND DEVELOPMENT (NON REFEREED)

1. **Samantha L. Anderson**, et al. (2019) A Multimodal Metal-Organic Framework Sensor for Real Time Carotid Artery Pulse Monitoring. Oral presentations at the 2019 Canadian Chemistry Conference and Exhibition.
2. **Samantha L. Anderson**, Andrzej Gładysiak, Peter G. Boyd, Christopher P. Ireland, Pascal Miéville, Davide Tiana, Bess Vlasisavljevich, Pascal Schouwink, Wouter van Beek, Kevin J. Gagnon, Berend Smit, Kyriakos C. Stylianou*. (2017) Formation Pathways of Metal Organic Frameworks Proceeding Through Partial Dissolution of the Metastable Phase. Oral presentation at the 2017 Canadian Chemistry Conference and Exhibition.
3. **Anderson (Voth), S**; Ghazati, K; Ziebenhaus, C; Hutchinson, M; Crudden, C*. (2014) Chemoselective Suzuki-Miyaura Cross-Coupling of Bis and Tris Boronic Ester Substrates. Poster Presented at the 2014 International Symposium on Homogenous Catalysis.
4. Ghazati, K; **Anderson (Voth), S**, Hutchinson, M; Crudden, C. (2013) Chemoselective Suzuki-Miyaura Cross-Coupling of Bis and Tris Boronic Ester Substrates. Poster presented at the 2013 Canadian Chemistry Conference and Exhibition.
5. **Anderson (Voth), S.**, Fainman, S., and McCubbin, J.A*. (2012) Boronic Acid Catalyzed [4+3] Cycloadditions of Furfuryl Alcohols. Poster presented at the 2012 Canadian Chemistry Conference and Exhibition.
6. McCubbin, J.A.,* **Anderson (Voth), S.**, and Krokhin, O.V. (2011) Mild and Tunable Benzoic Acid Catalysts for Rearrangement Reactions of Allylic Alcohols. Poster presented at the 2011 Canadian Chemistry Conference and Exhibition.

